PLASMONIC METAMATERIALS AND ELECTROMAGNETIC DEVICES

EDITED BY: Zhen Liao, Kai-Da Xu, Hui Feng Ma and Zhewang Ma
PUBLISHED IN: Frontiers in Physics

frontiers Research Topics

ISSN 1664-8714
ISBN 978-2-88976-832-5
DOI 10.3389/978-2-88976-832-5

About Frontiers

Frontiers is more than just an open-access publisher of scholarly articles: it is a pioneering approach to the world of academia, radically improving the way scholarly research is managed. The grand vision of Frontiers is a world where all people have an equal opportunity to seek, share and generate knowledge. Frontiers provides immediate and permanent online open access to all its publications, but this alone is not enough to realize our grand goals.

Frontiers Journal Series

The Frontiers Journal Series is a multi-tier and interdisciplinary set of open-access, online journals, promising a paradigm shift from the current review, selection and dissemination processes in academic publishing. All Frontiers journals are driven by researchers for researchers; therefore, they constitute a service to the scholarly community. At the same time, the Frontiers Journal Series operates on a revolutionary invention, the tiered publishing system, initially addressing specific communities of scholars, and gradually climbing up to broader public understanding, thus serving the interests of the lay society, too.

Dedication to Quality

Each Frontiers article is a landmark of the highest quality, thanks to genuinely collaborative interactions between authors and review editors, who include some of the world's best academicians. Research must be certified by peers before entering a stream of knowledge that may eventually reach the public - and shape society; therefore, Frontiers only applies the most rigorous and unbiased reviews.
Frontiers revolutionizes research publishing by freely delivering the most outstanding research, evaluated with no bias from both the academic and social point of view. By applying the most advanced information technologies, Frontiers is catapulting scholarly publishing into a new generation.

What are Frontiers Research Topics?

Frontiers Research Topics are very popular trademarks of the Frontiers Journals Series: they are collections of at least ten articles, all centered on a particular subject. With their unique mix of varied contributions from Original Research to Review Articles, Frontiers Research Topics unify the most influential researchers, the latest key findings and historical advances in a hot research area! Find out more on how to host your own Frontiers Research Topic or contribute to one as an author by contacting the Frontiers Editorial Office: frontiersin.org/about/contact

PLASMONIC METAMATERIALS AND ELECTROMAGNETIC DEVICES

Topic Editors:
Zhen Liao, Hangzhou Dianzi University, China
Kai-Da Xu, Xi'an Jiaotong University, China
Hui Feng Ma, Southeast University, China
Zhewang Ma, Saitama University, Japan

Citation: Liao, Z., Xu, K.-D., Ma, H. F., Ma, Z., eds. (2022). Plasmonic Metamaterials and Electromagnetic Devices. Lausanne: Frontiers Media SA.
doi: 10.3389/978-2-88976-832-5

Table of Contents

frontiers | Frontiers in Physics

EDITORIAL
published: 22 July 2022
doi: 10.3389/fphy.2022.955715

Editorial: Plasmonic Metamaterials and Electromagnetic Devices

Zhen Liao[1], *Kai-Da Xu*[2]*, *Huifeng Ma*[3] *and Zhewang Ma*[4]

[1]College of Electronic Information, Hangzhou Dianzi University, Hangzhou, China, [2]School of Information and Communications Engineering, Xi'an Jiaotong University, Xi'an, China, [3]State Key Laboratory of Millimeter Waves, Southeast University, Nanjing, China, [4]Graduate School of Science and Engineering, Saitama University, Saitama University, Saitama, Japan

Keywords: plasmonic metamateials, electromagnetic device, filter, antenna, metasurafce

Editorial on the Research Topic

Plasmonic Metamaterials and Electromagnetic Devices

Plasmonic metamaterials, relying on surface plasmons, exhibit novel optical properties that don't exist in natural materials. The rise of plasmonic metamaterials has revolutionized the entire field of optics and photonics, owing to the impacts that they bring to both the fundamental physics and practical applications. Moreover, the recent emerging spoof surface plasmons (SSPs) have extended the plasmonic metamaterials to lower frequency band, enabling intriguing applications ranged from microwave and terahertz devices. Their spatial confinement features have contributed to the development of the miniaturization of electromagnetic devices. The present Research Topic on plasmonic metamaterials compiles work on several of these aspects including plasmonic sensor, antenna, filters, and thus highlights current new interesting developments:

Spoof surface plasmon polaritons (SSPPs) are novel guiding modes excited on the surface of periodic metamaterial structures. A series of passive and active functional devices based on SSPPs were reported. Pan et al. studied a high-efficient leaky-wave antenna based on SSPPs loaded with parasitic patch array is proposed. Sinusoidal modulation is used for the radiation of SSPPs, while parasitic array mitigates the open stopband (OSB) effect. The device shows stable gain distribution within the whole operating band, which is available for conformal applications and other kinds of radiation systems. Pan et al. also explored a novel unequal bandpass filtering power divider based on hybrid mode of half mode substrate integrated waveguide (HMSIW) and SSPPs. In addition, defected ground structures (DGSs) are etched on the bottom of the substrate to improve out-of-band suppression. The design provides a stable power division within wide frequency range from 6.5 to 9. 5 GHz. Another paper in this Research Topic by Chen et al. presented a wideband controllable band-pass filter based on the SSPPs and slip ring resonators (SRR). The reconfigurable passband can be controlled by using varactor diode. Besides SSPPs, spoof localized surface plasmons (SLSPs) is another kind of SSPs, which mimic the localized oscillations of electrons in the lower frequency band. Due to the strong confinement of the electromagnetic fields, the SLSPs are sensitive to the surrounding environment. Wang et al. presented a high-Q-factor and high-sensitivity hybridized SLSPs sensor and a mixed-resolution algorithm. This may open new directions for generation of future high-frequency on-chip resonators and sensors.

Plasmonic materials and their emerging applications serve as a starting point for this Research Topic. Many efforts have also been devoted to the development of metasurfaces. Metasurfaces are thin-films composed of individual elements that provide a solution to the limitation of the conventional metamaterials. Over the past few years, metasurfaces have been employed for the design and fabrication of electromagnetic elements and systems with abilities that surpass the performance of conventional diffractive electromagnetic elements. An et al. presented a double-layer complementary transmitarray structure for linear and circular polarizations. Combining the cross

OPEN ACCESS

Edited and reviewed by:
Nicholas X. Fang, Massachusetts Institute of Technology, United States

***Correspondence:**
Kai-Da Xu
kaidaxu@ieee.org

Specialty section:
This article was submitted to Optics and Photonics, a section of the journal Frontiers in Physics

Received: *29 May 2022*
Accepted: *17 June 2022*
Published: *22 July 2022*

Citation:
Liao Z, Xu K-D, Ma H and Ma Z (2022) Editorial: Plasmonic Metamaterials and Electromagnetic Devices. Front. Phys. 10:955715. doi: 10.3389/fphy.2022.955715

and slot-type structure, a double-layer frequency-selective element has been designed, which should have broad application prospects in the future. Dong et al.proposed a novel low-profile broadband polarization conversion metasurface antenna using a partially chamfered symmetric triangular unit structure. In this paper, the resonance characteristics and radiation characteristics of the metasurface antenna are analyzed by characteristic mode analysis (CMA). Moreover, the characteristics of simple structure and easy processing is suitable for C-band satellite communications. Yang et al. found that the active control to the local resonant mode of metasurface is a promising route for improving the operation bandwidth limitation of metasurface. They have experimentally demonstrated the active tunabilities in a frequency-agile Fano-resonant metasurface, which may facilitate the development of high-performance active photonic applications. Metasurface is also an important route of optical manipulation in far-infrared range. Tamim et al. proposed an anisotropic metasurface for efficient polarization conversion, which is a potential candidate for advanced THz applications.

Increasing demand for the high-performance telecommunication system is mainly boosting technical innovation. The development of electromagnetic devices for high performance, compact size, low-consumption and low-cost systems such as filters, and antennas are urgent. Shen et al. presented a comprehensive design of dual-band filtering power dividers (FPDs) with arbitrary phase distribution based on the topology of inverter-coupled L/C resonators, which will be very attractive in future multi-functional wireless communication systems. Zhang et al. studied a tunable low pass filter adopting tunable input/output impedance technology, which can be generalized to other types of filters and filter designs with other properties. Wang et al. proposed a novel dual-band bandpass filter (BPF) with independently controllable transmission zeros (TZs), which is attractive for application in high-selectivity filter designs. In telecommunications, millimeter wave is used for a variety of services on mobile and wireless networks, as it enables higher data rates than at lower frequencies. Liu et al. presented a compact 60-GHz on-chip BPF using gallium arsenide (GaAs) technology. The miniaturization is achieved by the (HMSIW) structure. The proposed HMSIW BPF can be easily integrated with other GaAs components and circuits in millimeter-wave (mmW) systems such as vehicle-mounted radar and 5G communications. Li et al. explored a new triple-band four-way filtering power divider (FPD) with greatly improved frequency selectivity and in-band isolation.

In parallel to filter, antenna also plays a vital role in many fields such as communications, military applications, wearable systems, and power industry. A number of articles present recent advances in antennas in this Research Topic. Xiao et al. presented a dual-polarized corrugated horn antenna using turnstile orthomode transducer (OMT) operating within the full Ka-band, which can realize dual-linear polarization and provide high isolation. The proposed antenna system is a promising candidate for future 5G applications. In recent years, antennas with a wideband low radar cross section (RCS) have drawn significant attention in the low-observable needed platforms, such as military aircraft and missiles. By combing of a e circularly polarized (CP) antenna with a chessboard polarization conversion metasurface, Zhou et al. designed a low-profile CP meta-antenna with a broadband low-RCS feature. Wang et al. proposed a dual-band flexible antenna using a combined technique of liquid metal (LM) filling and polydimethylsiloxane substrate for wearable applications. To realize a resource-saving and environment-friendly society, it is preferable to combine solar cells and antennas for green communication. An et al. reported a single-port dual-band antenna integrated with solar cells for wireless local area network (WLAN) applications. As the RF energy around us increases sharply, the rectenna becomes one of the key devices for harvesting RF energy. Wang et al.studied an output power reconfigurable rectenna array, which can be used to capture abundant RF energy with high conversion efficiency in a wide range of input power levels.

With regards to optimizing design process in this ongoing field, predictive analytics have been always mentioned. Analogously, Peng proposes a universal approach to alleviate the problem of individual variability in epileptic seizure prediction.

This Research Topic contains 19 articles devoted to the recent progress in plasmonic metamaterials and electromagnetic devices. Much more efforts are still ongoing in this fascinating area. We expect that this field will attract more and more attentions and benefit potential electromagnetic applications.

AUTHOR CONTRIBUTIONS

All authors listed have made a substantial, direct and intellectual contribution to the work, and approved it for publication.

FUNDING

This work has received funding in part from the National Natural Science Foundation of China under Grant 62071159, the Zhejiang Provincial Natural Science Foundation under Grant No. LY22F010021.

Conflict of Interest: The authors declare that the research was conducted in the absence of any commercial or financial relationships that could be construed as a potential conflict of interest.

Publisher's Note: All claims expressed in this article are solely those of the authors and do not necessarily represent those of their affiliated organizations, or those of the publisher, the editors and the reviewers. Any product that may be evaluated in this article, or claim that may be made by its manufacturer, is not guaranteed or endorsed by the publisher.

frontiers in Physics

ORIGINAL RESEARCH
published: 03 September 2021
doi: 10.3389/fphy.2021.739465

Actively Controlled Frequency-Agile Fano-Resonant Metasurface for Broadband and Unity Modulation

Ruisheng Yang, Quanhong Fu, Yuancheng Fan*, Jing Xu, Wei Zhu, Weiqi Cai and Fuli Zhang**

Key Laboratory of Light Field Manipulation and Information Acquisition, Ministry of Industry and Information Technology and School of Physical Science and Technology, Northwestern Polytechnical University, Xi'an, China

The active control to the local resonant mode of metasurface is a promising route for improving the operation bandwidth limitation of metasurface. Here, we propose and experimentally demonstrated the active tunabilities in a frequency-agile Fano-resonant metasurface. The metasurface with a pair of asymmetric split ring resonators is integrated with double varactor diodes for active control of the sharp Fano resonance. It is found that the sharp Fano-type spectrum appears due to the near-field interferences between the collective electric and magnetic dipole modes. The physical insight is revealed through local field analysis, multipole decomposition and temporal coupled-mode theory. It is also found that the metasurface can be employed as a broadband and unity modulator. Hopefully, our results could inspire sophisticated electrically controlled photonic devices with novel functions.

Keywords: frequency-agile metasurfaces, fano resonance, varactor diodes, temporal coupled-mode theory, modulator

OPEN ACCESS

Edited by:
Zhewang Ma,
Saitama University, Japan

Reviewed by:
Weiren Zhu,
Shanghai Jiao Tong University, China
Sunil Kumar,
Indian Institute of Technology Delhi, India

****Correspondence:***
Quanhong Fu
fuquanhong@nwpu.edu.cn
Yuancheng Fan
phyfan@nwpu.edu.cn
Fuli Zhang
fuli.zhang@nwpu.edu.cn

Specialty section:
This article was submitted to Optics and Photonics, a section of the journal Frontiers in Physics

Received: *11 July 2021*
Accepted: *23 August 2021*
Published: *03 September 2021*

Citation:
Yang R, Fu Q, Fan Y, Xu J, Zhu W, Cai W and Zhang F (2021) Actively Controlled Frequency-Agile Fano-Resonant Metasurface for Broadband and Unity Modulation. Front. Phys. 9:739465. doi: 10.3389/fphy.2021.739465

INTRODUCTION

Metamaterials are artificial engineered subwavelength structures with tailorable properties superior to the natural materials, which have shown unprecedented capability in exterior light manipulations [1–5]. Since three-dimensional metamaterials are difficult to design and fabricate, their two-dimensional (2D) counterpart, metasurfaces [6–10], constructed by subwavelength metallic or dielectric particles in a planar platform, have attracted considerable attention in recent years for the arbitrary control of electromagnetic waves [11–13]. Metasurfaces have inspired extraordinary light manipulations such as invisibility cloak [14], broadband achromatic metalens [15], arbitrary orbital angular momentum generation [16], enhanced nonlinear photonics [17], and meta-hologram [18]. Compared with 3D complex metamaterials, planar metasurfaces with subwavelength-thickness monolayer or few functional layers [19, 20] are easier to fabricate by utilizing sophisticated processing techniques. Besides, the subwavelength thickness of metasurfaces along the propagating direction is beneficial for miniaturizing optical systems and improving working efficiency [21, 22].

Fano resonance appears when a discrete localized state interferences with a continuum band of states [23]. In general, Fano resonance is always accompanied by a high-Q factor and significant local field enhancement, showing a sharp transmission or reflection curves [24, 25]. Recently, metasurfaces with so-called bright and dark modes are designed to resemble the original physical mechanism of Fano resonance [26–28], i.e., interference between a narrow discrete resonance with a broadband spectral line in a quantum system. The bright and dark modes

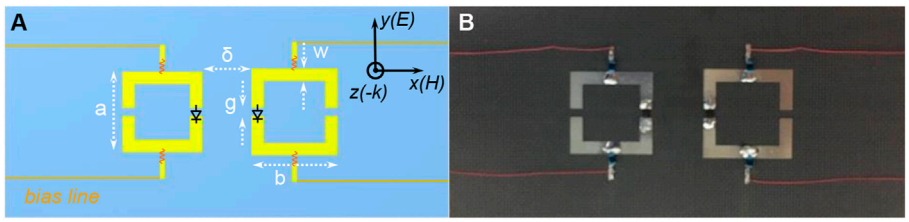

FIGURE 1 | Front view of the frequency-agile Fano-resonant metasurface. Schematic diagram **(A)** and photograph **(B)** of the fabricated sample. The metasurface is composed of a pair of asymmetric split ring resonators (ASRRs) on a Teflon substrate. Double varactor diodes are soldered in the middle gap of the asymmetric rings. Four inductors and four bias copper wires are integrated into the metasurface. The geometric parameters are: a = 13 mm, b = 14 mm, w = 2 mm, g = 1.3 mm, and δ = 8 mm.

have different scattering pathways for the incident waves. The bright mode can be directly excited by incident waves in free space, while the dark mode is weakly coupled to incident waves and can be excited through near field coupling with the bright mode by breaking the geometric symmetry [29–31]. Fano resonances with high quality factors can be generated through the interference between the new-emergent narrow dark mode and the original continuum mode [32–34]. The Fano metasurfaces are generally accompanied with extremely sharp reflection or transmission curves and are widely studied due to the attractive feature of high-Q response [35–38].

Fano metasurfaces have been proven and considered as a very promising platform for the high-Q response with enhanced light-matter interactions, but the intrinsic narrow operation bandwidth may significantly hinder them towards practical applications due to their resonant natures. Although it can be optimized by incorporating changeable materials [39–42] or employing reconfigurable structures [43, 44] to extend the bandwidth, this greatly complicates the manufacturing process and also makes it more expensive/difficult to embed into increasingly integrated photonic systems. Here in this paper, we experimentally demonstrated an electrically tunable frequency-agile Fano-resonant metasurface with a pair of asymmetric split ring resonators (ASRRs) configuration. The ASRRs metasurface is integrated with double varactor diodes for active control of the sharp Fano resonance. Remarkable blue shift on the Fano resonance frequency was demonstrated by increasing the bias voltage from 0 to 8 V to electrically tune the capacitances of the varactor diodes. The sharp Fano-type spectrum appears due to the near-field couplings between the collective electric and magnetic dipole modes, and its physical insight is revealed through local field analysis, multipole decomposition and temporal coupled-mode theory (TCMT). Moreover, we also found that the metasurface can be employed as a broadband and unity modulator. The proposed strategy provides an alternative way to overcome the limited bandwidth of conventional meta-devices, which may facilitate the development of low-cost and high-performance active photonic applications.

RESULTS AND DISCUSSION

The schematic of our designed metasurface is shown in **Figure 1A**. It consists of a pair of asymmetric split ring resonators (ASRRs) with different side lengths. To realize the electrically tunable frequency-agile Fano resonance, double varactor diodes (BBY52-02W, Infineon) are soldered at the middle gap of the ASRRs pair and are biased through four copper wires. The varactor diodes have a series resistance of 0.9 Ω and inductance of 0.6 nH, respectively. Four inductors are located between the bias wires and ASRRs to effectively avoid the cross talk. By applying external bias voltage on the varactor diodes, their capacitance can be significantly changed and the Fano resonance can be dynamically modulated accordingly. The photograph of a fabricated sample is shown in **Figure 1B**. The metallic pattern is 0.035 mm thick copper on a 1 mm thick Teflon base and is fabricated through standard printed circuit board (PCB) technology. The Teflon substrate was cut to a dimension of $72.14 \times 34.04\ mm^2$ corresponding to the cross-section of a standard waveguide WR284, and simultaneously ensuring the metallic patterns at the center of the substrate. In our experiments, the scattering parameters of the metasurface are measured inside a standard waveguide of WR284, where the TE_{10} mode with an electric field polarizing along the y direction is normally incident on the metasurface, and are recorded through a vector network analyzer (AV3629D).

To understand the design strategy of the Fano-resonant metasurface, we would like to firstly consider the spectral response of the coupled metasurface design (see **Figure 2A**). The calculations were carried out within a perfect electric conductor (PEC) around an air box to simulate a standard waveguide of WR284. In the simulations, PEC boundaries are set along x and y directions, and open boundaries are set along z direction. An excitation source is applied at the boundary of z direction. For a metasurface with only left split ring resonator (SRR), a typical symmetric Lorentz-type resonance dip appears at f_1 (2.99 GHz), while for a metasurface with only right SRR, another typical symmetric Lorentz-type resonance dip occurs at frequency f_2 (2.77 GHz). These resonators show electric dipolar resonances arising from the current induced by the incident electric field in the asymmetric metallic sides of SRR, which are further confirmed by the electric field and surface current distributions shown in **Figures 2C,D**. Since their resonant frequencies are close to each other, we may expect some interesting phenomena when we set the asymmetric SRRs in a close proximity, resulting from the near-field interference.

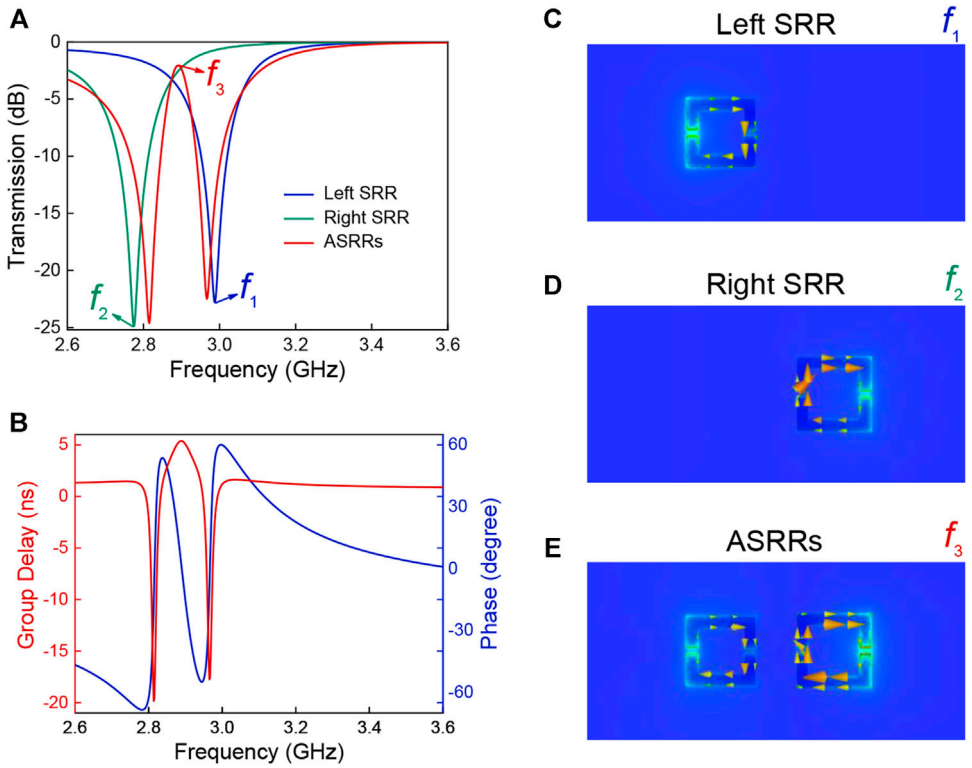

FIGURE 2 | (A) Calculated transmission spectra of the left SRR only (blue curve), right SRR only (green curve), and the asymmetric SRR pair (red curve). **(B)** Calculated transmission group delay (red curve) and phase (blue curve) of the metasurface. **(C–E)** Instantaneous distributions of the out-of-plane electric field and the induced surface current corresponding to the resonant frequencies at f_1, f_2, and f_3 in section **(A)**. Arrows indicate the instantaneous directions of the current flow. All these results are obtained when the capacitance of varactor diodes is 2.63 pF.

The red curve in **Figure 2A** shows the calculated transmission spectrum of the ASRRs metasurface. The near field coupling between the ASRRs leads to an asymmetric Fano-shaped profile with a sharp change between the dip and peak. The destructive interference between the ASRRs also results in a sharp transparency window around frequency f_3 (2.89 GHz), which is similar to the analogy of the electromagnetically induced transparency [28]. Note that the transparency peak of the metasurface is quite sharp with a full width at half-maximum (FWHM) of 0.0558 GHz, reaching a high quality factor of 52. The calculated transmission group delay and phase are shown in **Figure 2B**, from which we can see that around the transparency peak, the transmission phase experiences an abrupt variation, leading to strong dispersion of the effective parameters and a large group delay of 5.4 ns. To explore the underlying mechanism of the Fano-type resonance and the sharp transmission window, we calculated the surface current and electric field distribution at the transmission peak f_3 (see **Figure 2E**). The induced surface currents on the ASRRs are oscillating in-phase, forming a collective magnetic mode $\boldsymbol{M}_z$. This new emergent mode $\boldsymbol{M}_z$, as a non-radiative dark state (sharp discrete mode), is weakly coupling with the incident electromagnetic field, and destructively interfering with the background electric dipole mode $\boldsymbol{P}_y$ (broadband continuum mode), resulting in the sharp transparency window.

To further understand the near-field coupling mechanism of the metasurface, we calculated the contributions of various multipole moments induced in the metasurface. The electric and magnetic dipole moments of the metasurface can be quantitatively evaluated with the following formula [45].

$$\mathbf{P} = \frac{1}{i\omega}\int \mathbf{j}d^3\mathbf{r} \tag{1}$$

$$\mathbf{M} = \frac{1}{2c}\int (\mathbf{r}\times\mathbf{j})d^3\mathbf{r} \tag{2}$$

where $\boldsymbol{j}$ is the current density, ω is the angular frequency, and c is the speed of light in vacuum. The multipole moments can be calculated by integrating spatially distributed current density extracted from the simulation. The calculated normalized magnitude and the corresponding phase of the electric dipole moment $\boldsymbol{P}_y$ and the magnetic dipole moment $\boldsymbol{M}_z$ are presented in **Figures 3A,B**, respectively.

We can find that the electric dipole $\boldsymbol{P}_y$, as a bright mode resonance, shows strong scattering over the entire interesting frequency band, indicating that the ASRRs metasurface strongly couples to the *y*-polarized electric field component in the waveguide. The collective oscillations of the electric dipoles can be considered as a broadband continuum mode. Around the transparency peak frequency f_3, the $\boldsymbol{P}_y$ is significantly

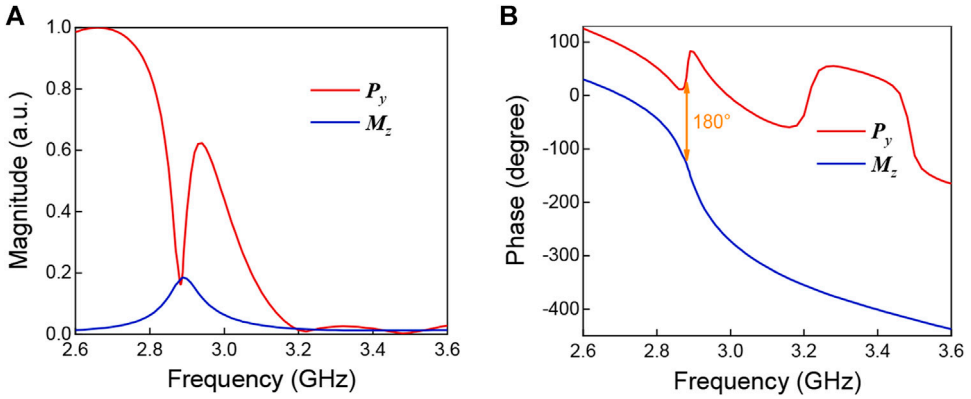

FIGURE 3 | Normalized magnitude **(A)** of multipole moments $\boldsymbol{P}_y$ and $\boldsymbol{M}_z$, and their corresponding phase **(B)** induced in the ASRRs metasurface with the capacitance 2.63 pF: the electric dipole (red curve), and magnetic dipole (blue curve).

suppressed, while the $\boldsymbol{M}_z$ is excited and enhanced to a similar magnitude as $\boldsymbol{P}_y$, and the phase difference between the $\boldsymbol{P}_y$ and $\boldsymbol{M}_z$ is about 180°, which further confirms the fact that these two modes interference destructively, and their scattering cancellation results in the non-radiating configuration and the sharp transparency window. We notice that the collective magnetic dipole mode cannot be directly excited by the incident wave, as the metasurface is placed in a standard rectangular waveguide where only the fundamental TE_{10} mode can propagate in the frequency band of interest. However, the collective magnetic dipole mode can be excited through near-field coupling, leading to the collective oscillation of the ASRRs and the suppression of electric dipolar mode, and forming the dark mode resonance.

To quantitatively evaluate the interaction between the incident wave and the metasurface, we also employed TCMT to analyze the mode coupling between the collective electric and magnetic dipoles. The transmission spectrum of the metasurface excited by a monochromatic wave can be expressed as below [46, 47].

$$t = \frac{(j\omega - j\omega_1 + \Gamma_{i1})(j\omega - j\omega_2 + \Gamma_{i2}) + k^2}{(j\omega - j\omega_1 + \Gamma_{i1} + \Gamma_{e1})(j\omega - j\omega_2 + \Gamma_{i2})k^2}. \quad (3)$$

where ω_1, Γ_{e1}, and Γ_{i1} (or ω_2, Γ_{e2}, and Γ_{i2}) are the resonant frequency, radiative decay rate, and non-radiative decay rate of the bright (or dark) resonator, respectively, and κ is the coupling coefficient. We can obtain the characteristic parameters of the resonator system through fitting the expression of $|t|$ to the simulated transmission spectrum of the metasurface (red curve in **Figure 2A**), as follows:

$$\begin{aligned}
\omega_1 &= 2\pi \times 2.88 \times 10^9 rad/s,\\
\omega_{12} &= 2\pi \times 2.891 \times 10^9 rad/s,\\
\Gamma_{e1} &= 2\pi \times 0.197 \times 10^9 rad/s,\\
\Gamma_{i1} &= 2\pi \times 0.0035 \times 10^9 rad/s,\\
\Gamma_{i2} &= 2\pi \times 0.009 \times 10^9 rad/s,\\
k &= 2\pi \times 0.076 \times 10^9 rad/s.
\end{aligned}$$

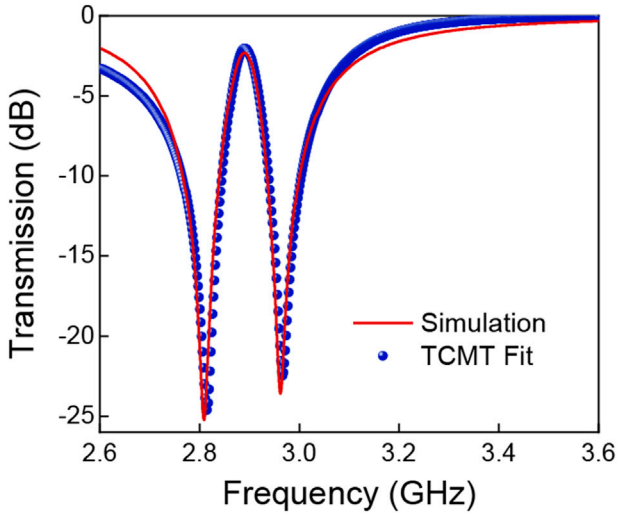

FIGURE 4 | Transmission spectra of the metasurface predicted by the TCMT (blue points) and simulated through FDTD (red curve) with the capacitance 2.63 pF.

It can be found that the ω_1 and ω_2 correspond to the dip of electric dipole moment $\boldsymbol{P}_y$ (as bright mode) and the peak of magnetic dipole moment of $\boldsymbol{M}_z$ (as dark mode), respectively, (**Figure 3A**), indicating that our metasurface systems are dominated by these two modes. For the collective electric dipole mode, the radiative decay rate, Γ_{e1}, is about 56 times larger than the non-radiative decay rate, Γ_{i1}. Both the radiative and non-radiative decay rate of collective magnetic dipole mode, Γ_{e2} and Γ_{i2} are much less than Γ_{e1} and Γ_{i1}, so they are negligible. The frequency interval between the two transmission dips of our metasurface is only 0.15 GHz, since the coupling coefficient κ is much less than the resonant frequencies, ω_1 and ω_2, and even the radiative decay rate, Γ_{e1}. The TCMT accurately predicts the transmission spectrum of the metasurface, as shown in **Figure 4**.

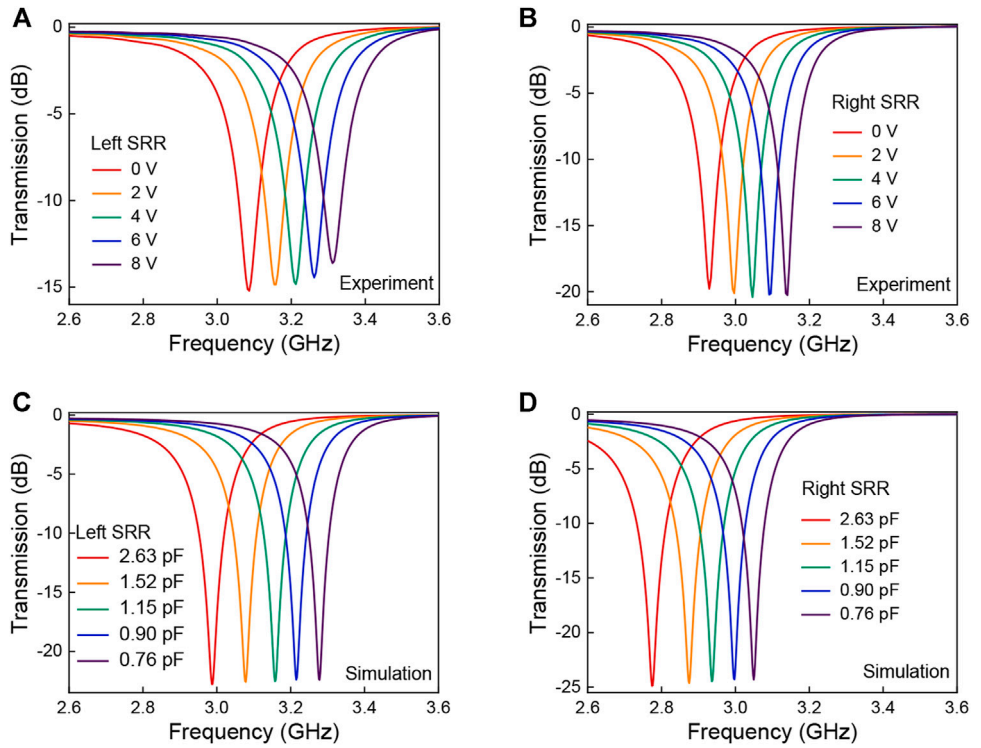

FIGURE 5 | Measured **(A)**, **(B)** and calculated **(C)**, **(D)** transmission spectra of the SRR alone with different bias voltages (from 0 to 8 V) and corresponding capacitances (from 2.63 to 0.76 pF): the left SRR alone **(A)**, **(C)**, and right SRR alone **(B)**, **(D)**.

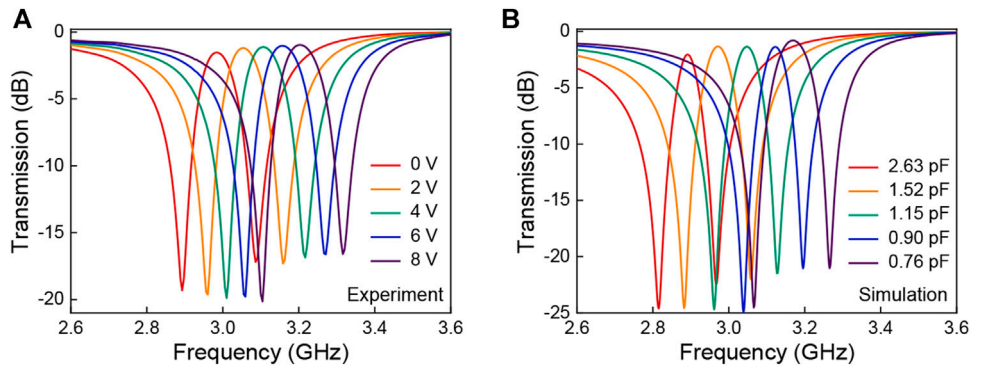

FIGURE 6 | Measured **(A)** and calculated **(B)** transmission spectra of the frequency-agile metasurface with different bias voltages (from 0 to 8 V) and corresponding capacitances (from 2.63 to 0.76 pF).

The tunabilities of the metasurface can be understood as a LC circuit with changeable capacitances. The electric resonance frequency is determined by $\omega = (LC)^{-1/2}$. So the resonance frequency of SRR and the Fano-type resonance frequency can be manipulated significantly by applying voltage to alter the capacitance of varactor diodes. Next, the transmission properties of the SRR alone under different bias voltages are investigated. The measured and calculated transmission spectra of the single SRR with different voltages (capacitances in simulations) are shown in **Figure 5**. As the bias voltage gradually increases from 0 to 8 V, the capacitance of the varactor diode decreases from 2.63 to 0.76 pF, and the corresponding transmission spectrum undergoes a remarkable blue shift; the experimental resonant frequency of the left SRR alone undergoes a blue shift of 0.22 GHz from 3.09 to 3.31 GHz (see **Figure 5A**), and similarly, the experimental resonant frequency of the right SRR alone undergoes a blue shift of 0.21 GHz from 2.93 to 3.14 GHz (see **Figure 5B**). The

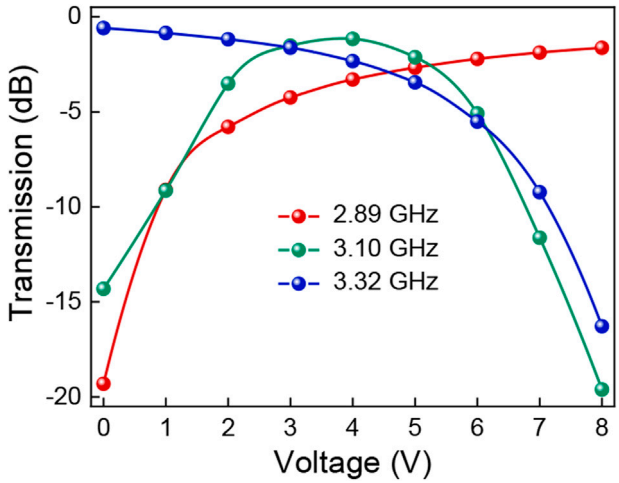

FIGURE 7 | Measured transmission of the metasurface with different bias voltages ranging from 0 to 8 V at 2.89 GHz (red), 3.10 GHz (green), and 3.32 GHz (blue).

calculated trend (**Figures 5C,D**) agrees well with the measured results, implying the effective frequency-agile tunability by the integrated varactor diodes.

To actively control the Fano-type resonance, double varactor diodes are then integrated into the ASRRs metasurface system. The dynamic modulation on Fano resonance of the frequency-agile metasurface is illustrated in **Figure 6**. When no voltage is applied, the measured Fano resonance peak occurs at 2.98 GHz (see **Figure 6A**). As the bias voltage gradually increases from 0 to 8 V, the Fano resonance peak gradually shifts from 2.98 to 3.2 GHz, exhibiting a blue shift of 0.22 GHz. Although there is a small amplitude variation, the significant sharp transmission feature is preserved. Meanwhile, the transmission dips of the Fano resonance also exhibit blue shifts of 0.2 and 0.22 GHz, respectively. The calculated results (**Figure 6B**) show good agreement with our measured results. It is worth mentioning that the lower frequency dip completely exceeds the upper frequency dip when the applied voltage is changed from 0 to 8 V, thanks to the sharp dispersion characteristic of Fano resonance. It indicates that our metasurface can be employed not only for a frequency-agile device, but also for a broadband and unity amplitude modulator.

To show the amplitude modulation performance of our metasurface, we here plot the transmission with different bias voltages, as shown in **Figure 7**. Remarkable modulation on transmission can be realized through electric biasing at several frequency points. For example, the measured transmission curves at three selected frequencies of 2.89, 3.10 and 3.32 GHz with different voltages are plotted. As the voltage changes from 0 to 8 V, the transmittance at 2.89 GHz monotonously increases from −19.31 dB to −1.63 dB (red curve), while at 3.32 GHz monotonously decreases from −0.59 dB to −16.29 dB (blue curve), showing a remarkable modulation performance. In particular, the transmittance at 3.10 GHz (green curve), shows a growing trend from −14.31 dB to −1.16 dB with the voltage increased from 0 to 4 V, while a downward trend from −1.16 dB to −19.62 dB when further increasing the voltage to 8 V. Note that although our results were obtained in a waveguide system, the similar modulation performance can also be achieved with periodic structures in free space.

CONCLUSION

In conclusion, we have experimentally demonstrated the active tunabilities in a frequency-agile Fano-resonant metasurface. The sharp Fano resonance can be dynamically modulated by integrating a pair of varactor diodes in the metasurface. We found that the non-radiative collective magnetic dipole mode was excited in our metasurface and its physical insight is uncovered through local field analysis, multipole decomposition and TCMT. We also found significant manipulation on both frequency tuning and amplitude modulation by applying bias voltage on the varactor diodes. The demonstrated frequency-agile Fano-resonant metasurface is promising for realizing sophisticated electrically controlled microwave devices with novel functions, which may facilitate the development of high-performance active photonic applications in, e.g., smart sensing or signal processing.

METHODS

Numerical Simulation: Numerical simulations are carried out using the finite-element frequency-domain solver. The metallic pattern with a conductivity of 5.8×10^7 S/m is standing on a Teflon substrate with a relative permittivity of 2.65 and a tangent loss of 0.0004. In the simulations, PEC conditions are applied in both the x and y directions and open boundaries are set along z direction. An excitation source is applied at the boundary of z direction. The multipole moments $\boldsymbol{P}_y$ and $\boldsymbol{M}_z$ can be calculated by integrating spatially distributed current density extracted from the simulation utilizing the commonly used formulas (**Eqs. 1**, **2**).

Experiments: The printed circuit board (PCB) technique was used to fabricate the metallic ASRRs pattern. The Teflon substrate was cut to a dimension of 72.14×34.04 mm^2 corresponding to the cross-section of a standard waveguide WR284, and simultaneously ensuring the metallic patterns at the center of the substrate. In the measurements, the sample was placed inside a WR284 rectangular waveguide, and was measured through a vector network analyzer (AV3629D).

DATA AVAILABILITY STATEMENT

The original contributions presented in the study are included in the article/Supplementary Material, further inquiries can be directed to the corresponding authors.

AUTHOR CONTRIBUTIONS

QF, YF, and FZ conceived the idea and guided the research. RY designed the metasurface, characterized the samples, and wrote the article. JX, WZ and WC contributed to the final version of the article. All authors discussed the results and commented on the paper.

FUNDING

The authors would like to acknowledge financial support from Natural Science Foundation of China (NSFC) (Grants No. 12074314, 11774057, 11674266, 61771402), NPU AoXiang New Star program, Science, Technology and Innovation Commission of Shenzhen Municipality (JCYJ20170817162221169), Shaanxi Province Postdoctoral Science Foundation (No. 2018BSHEDZZ64), and Natural Science Basic Research Plan in Shaanxi Province of China (Nos. 2018JM6024, 2020JM-145).

REFERENCES

1. Linden S, Enkrich C, Wegener M, Zhou J, Koschny T, and Soukoulis CM. Magnetic Response of Metamaterials at 100 Terahertz. *Science* (2004) 306: 1351–3. doi:10.1126/science.1105371
2. Smith DR, Pendry JB, and Wiltshire MC. Metamaterials and Negative Refractive Index. *Science* (2004) 305:788–92. doi:10.1126/science.1096796
3. Chen H-T, Padilla WJ, Zide JMO, Gossard AC, Taylor AJ, and Averitt RD. Active Terahertz Metamaterial Devices. *Nature* (2006) 444:597–600. doi:10.1038/nature05343
4. Zhao Q, Zhou J, Zhang F, and Lippens D. Mie Resonance-Based Dielectric Metamaterials. *Mater Today* (2009) 12:60–9. doi:10.1016/S1369-7021(09)70318-9
5. Yang R, Xu J, Shen NH, Zhang F, Fu Q, Li J, et al. Subwavelength Optical Localization With Toroidal Excitations in Plasmonic and Mie Metamaterials. *InfoMat* (2021) 3:577–97. doi:10.1002/inf2.12174
6. Yu N, Genevet P, Kats MA, Aieta F, Tetienne J-P, Capasso F, et al. Light Propagation With Phase Discontinuities: Generalized Laws of Reflection and Refraction. *Science* (2011) 334:333–7. doi:10.1126/science.1210713
7. Sun S, He Q, Xiao S, Xu Q, Li X, and Zhou L. Gradient-Index Meta-Surfaces as a Bridge Linking Propagating Waves and Surface Waves. *Nat Mater* (2012) 11: 426–31. doi:10.1038/NMAT3292
8. Glybovski SB, Tretyakov SA, Belov PA, Kivshar YS, and Simovski CR. Metasurfaces: From Microwaves to Visible. *Phys Rep* (2016) 634:1–72. doi:10.1016/j.physrep.2016.04.004
9. Ding F, Pors A, and Bozhevolnyi SI. Gradient Metasurfaces: a Review of Fundamentals and Applications. *Rep Prog Phys* (2017) 81:026401. doi:10.1088/1361-6633/aa8732
10. Shaltout AM, Shalaev VM, and Brongersma ML. Spatiotemporal Light Control with Active Metasurfaces. *Science* (2019) 364:eaat3100. doi:10.1126/science.aat3100
11. Kildishev AV, Boltasseva A, and Shalaev VM. Planar Photonics With Metasurfaces. *Science* (2013) 339:1232009. doi:10.1126/science.1232009
12. Chen H-T, Taylor AJ, and Yu N. A Review of Metasurfaces: Physics and Applications. *Rep Prog Phys* (2016) 79:076401. doi:10.1088/0034-4885/79/7/076401
13. Chen WT, Zhu AY, and Capasso F. Flat Optics With Dispersion-Engineered Metasurfaces. *Nat Rev Mater* (2020) 5:604–20. doi:10.1038/s41578-020-0203-3
14. Zhang F, Li C, Fan Y, Yang R, Shen NH, Fu Q, et al. Phase-Modulated Scattering Manipulation for Exterior Cloaking in Metal-Dielectric Hybrid Metamaterials. *Adv Mater* (2019) 31:1903206. doi:10.1002/adma.201903206
15. Chen WT, Zhu AY, Sanjeev V, Khorasaninejad M, Shi Z, Lee E, et al. A Broadband Achromatic Metalens for Focusing and Imaging in the Visible. *Nat Nanotech* (2018) 13:220–6. doi:10.1038/s41565-017-0034-6
16. Devlin RC, Ambrosio A, Rubin NA, Mueller JPB, and Capasso F. Arbitrary Spin-To-Orbital Angular Momentum Conversion of Light. *Science* (2017) 358: 896–901. doi:10.1126/science.aao5392
17. Koshelev K, Kruk S, Melik-Gaykazyan E, Choi J-H, Bogdanov A, Park H-G, et al. Subwavelength Dielectric Resonators for Nonlinear Nanophotonics. *Science* (2020) 367:288–92. doi:10.1126/science.aaz3985
18. Wen D, Yue F, Li G, Zheng G, Chan K, Chen S, et al. Helicity Multiplexed Broadband Metasurface Holograms. *Nat Commun* (2015) 6:8241. doi:10.1038/ncomms9241
19. Cheng H, Liu Z, Chen S, and Tian J. Emergent Functionality and Controllability in Few-Layer Metasurfaces. *Adv Mater* (2015) 27:5410–21. doi:10.1002/adma.201501506
20. Chen S, Li Z, Liu W, Cheng H, and Tian J. From Single-Dimensional to Multidimensional Manipulation of Optical Waves with Metasurfaces. *Adv Mater* (2019) 31:1802458. doi:10.1002/adma.201802458
21. Khorasaninejad M, Chen WT, Devlin RC, Oh J, Zhu AY, and Capasso F. Metalenses at Visible Wavelengths: Diffraction-Limited Focusing and Subwavelength Resolution Imaging. *Science* (2016) 352:1190–4. doi:10.1126/science.aaf6644
22. Zhu W, Yang R, Geng G, Fan Y, Guo X, Li P, et al. Titanium Dioxide Metasurface Manipulating High-Efficiency and Broadband Photonic Spin Hall Effect in Visible Regime. *Nanophotonics* (2020) 9:4327–35. doi:10.1515/nanoph-2020-0290
23. Fano U. Effects of Configuration Interaction on Intensities and Phase Shifts. *Phys Rev* (1961) 124:1866–78. doi:10.1103/PhysRev.124.1866
24. Luk'yanchuk B, Zheludev NI, Maier SA, Halas NJ, Nordlander P, Giessen H, et al. The Fano Resonance in Plasmonic Nanostructures and Metamaterials. *Nat Mater* (2010) 9:707–15. doi:10.1038/NMAT2810
25. Limonov MF, Rybin MV, Poddubny AN, and Kivshar YS. Fano Resonances in Photonics. *Nat Photon* (2017) 11:543–54. doi:10.1038/NPHOTON.2017.142
26. Liu N, Langguth L, Weiss T, Kästel J, Fleischhauer M, Pfau T, et al. Plasmonic Analogue of Electromagnetically Induced Transparency at the Drude Damping Limit. *Nat Mater* (2009) 8:758–62. doi:10.1038/NMAT2495
27. Gu J, Singh R, Liu X, Zhang X, Ma Y, Zhang S, et al. Active Control of Electromagnetically Induced Transparency Analogue in Terahertz Metamaterials. *Nat Commun* (2012) 3:1151. doi:10.1038/ncomms2153
28. Yang Y, KravchenkoII, Briggs DP, and Valentine J. All-dielectric Metasurface Analogue of Electromagnetically Induced Transparency. *Nat Commun* (2014) 5:5753. doi:10.1038/ncomms6753
29. Fedotov VA, Rose M, Prosvirnin SL, Papasimakis N, and Zheludev NI. Sharp Trapped-Mode Resonances in Planar Metamaterials With a Broken Structural Symmetry. *Phys Rev Lett* (2007) 99:147401. doi:10.1103/PhysRevLett.99.147401
30. Wu C, Khanikaev AB, Adato R, Arju N, Yanik AA, Altug H, et al. Fano-Resonant Asymmetric Metamaterials for Ultrasensitive Spectroscopy and Identification of Molecular Monolayers. *Nat Mater* (2012) 11:69–75. doi:10.1038/NMAT3161
31. Cui C, Zhou C, Yuan S, Qiu X, Zhu L, Wang Y, et al. Multiple Fano Resonances in Symmetry-Breaking Silicon Metasurface for Manipulating Light Emission. *ACS Photon* (2018) 5:4074–80. doi:10.1021/acsphotonics.8b00754
32. Zhang F, Huang X, Zhao Q, Chen L, Wang Y, Li Q, et al. Fano Resonance of an Asymmetric Dielectric Wire Pair. *Appl Phys Lett* (2014) 105:172901. doi:10.1063/1.4900757
33. Fu Q, Zhang F, Fan Y, He X, Qiao T, and Kong B. Electrically Tunable Fano-type Resonance of an Asymmetric Metal Wire Pair. *Opt Express* (2016) 24: 11708–15. doi:10.1364/OE.24.011708
34. Fan Y, Qiao T, Zhang F, Fu Q, Dong J, Kong B, et al. An Electromagnetic Modulator Based on Electrically Controllable Metamaterial Analogue to Electromagnetically Induced Transparency. *Sci Rep* (2017) 7:40441. doi:10.1038/srep40441
35. Lassiter JB, Sobhani H, Fan JA, Kundu J, Capasso F, Nordlander P, et al. Fano Resonances in Plasmonic Nanoclusters: Geometrical and Chemical Tunability. *Nano Lett* (2010) 10:3184–9. doi:10.1021/nl102108u
36. Khanikaev AB, Wu C, and Shvets G. Fano-resonant Metamaterials and Their Applications. *Nanophotonics* (2013) 2:247–64. doi:10.1515/nanoph-2013-0009
37. Yang Y, Wang W, Boulesbaa A, Kravchenko II, Briggs DP, Puretzky A, et al. Nonlinear Fano-Resonant Dielectric Metasurfaces. *Nano Lett* (2015) 15: 7388–93. doi:10.1021/acs.nanolett.5b02802
38. Lou J, Liang J, Yu Y, Ma H, Yang R, Fan Y, et al. Silicon-Based Terahertz Meta-Devices for Electrical Modulation of Fano Resonance and Transmission Amplitude. *Adv Opt Mater.* (2020) 8:2000449. doi:10.1002/adom.202000449
39. Zhu W, Fan Y, Li C, Yang R, Yan S, Fu Q, et al. Realization of a Near-Infrared Active Fano-Resonant Asymmetric Metasurface by Precisely Controlling the Phase Transition of Ge2Sb2Te5. *Nanoscale* (2020) 12:8758–67. doi:10.1039/c9nr09889e

40. Gupta M, Srivastava YK, and Singh R. A Toroidal Metamaterial Switch. *Adv Mater* (2018) 30:1704845. doi:10.1002/adma.201704845
41. Fan Y, Shen NH, Zhang F, Zhao Q, Wu H, Fu Q, et al. Graphene Plasmonics: A Platform for 2D Optics. *Adv Opt Mater* (2019) 7:1800537. doi:10.1002/adom.201800537
42. Gholipour B, Zhang J, MacDonald KF, Hewak DW, and Zheludev NI. An All-Optical, Non-Volatile, Bidirectional, Phase-Change Meta-Switch. *Adv Mater* (2013) 25:3050–4. doi:10.1002/adma.201300588
43. Manjappa M, Pitchappa P, Singh N, Wang N, Zheludev NI, Lee C, et al. Reconfigurable MEMS Fano Metasurfaces With Multiple-Input-Output States for Logic Operations at Terahertz Frequencies. *Nat Commun* (2018) 9:4056. doi:10.1038/s41467-018-06360-5
44. Ren Z, Chang Y, Ma Y, Shih K, Dong B, and Lee C. Leveraging of MEMS Technologies for Optical Metamaterials Applications. *Adv Opt Mater*. (2020) 8:1900653. doi:10.1002/adom.201900653
45. Fan Y, Zhang F, Shen N-H, Fu Q, Wei Z, Li H, et al. Achieving a High- Q Response in Metamaterials by Manipulating the Toroidal Excitations. *Phys Rev A* (2018) 97:033816. doi:10.1103/PhysRevA.97.033816
46. Fu Q, Zhang F, Fan Y, Dong J, Cai W, Zhu W, et al. Weak Coupling Between Bright and Dark Resonators With Electrical Tunability and Analysis Based on Temporal Coupled-Mode Theory. *Appl Phys Lett* (2017) 110:221905. doi:10.1063/1.4984596
47. Yang R, Fu Q, Fan Y, Cai W, Qiu K, Zhang W, et al. Active Control of EIT-like Response in a Symmetry-Broken Metasurface With Orthogonal Electric Dipolar Resonators. *Photon Res* (2019) 7:955–60. doi:10.1364/PRJ.7.000955

Conflict of Interest: The authors declare that the research was conducted in the absence of any commercial or financial relationships that could be construed as a potential conflict of interest.

Publisher's Note: All claims expressed in this article are solely those of the authors and do not necessarily represent those of their affiliated organizations, or those of the publisher, the editors and the reviewers. Any product that may be evaluated in this article, or claim that may be made by its manufacturer, is not guaranteed or endorsed by the publisher.

frontiers in Physics

ORIGINAL RESEARCH
published: 08 October 2021
doi: 10.3389/fphy.2021.775214

Dual-Band Antenna Integrated With Solar Cells for WLAN Applications

*Wenxing An, Hui Wang and Yu Luo**

The Tianjin Key Laboratory of Imaging and Sensing Microelectronic Technology, School of Microelectronics, Tianjin University, Tianjin, China

A single-port dual-band antenna integrated with solar cells is reported for the 2.4/5-GHz wireless local area network (WLAN) applications. Thirty solar cells are adopted and integrated into the antenna structure for both energy harvesting and wireless communication. The solar cells can act as a director for the lower band, and the main radiation structure for the higher band. The slot and microstrip antennas are incorporated into the compact structure and multiple resonant modes are utilized for dual-band performance. The measurement results show that the lower band is from 2.27 to 2.5 GHz with an omnidirectional radiation pattern and the upper band is from 4.8 to 6.9 GHz with a directional radiation pattern. The proposed solar cell antenna can provide a dual-band performance with the ability of DC power generation, which can be a potential candidate for future green low-carbon communication.

Keywords: microstrip antenna, slot antenna, dual-function device, solar cell, dual-band

OPEN ACCESS

Edited by:
Kai-Da Xu,
Xi'an Jiaotong University, China

Reviewed by:
Liuge Du,
Shandong University, China
Wang Kai Xu,
Harbin Institute of Technology, Shenzhen, China

****Correspondence:***
Yu Luo
yluo@tju.edu.cn

Specialty section:
This article was submitted to Optics and Photonics, a section of the journal Frontiers in Physics

Received: *13 September 2021*
Accepted: *23 September 2021*
Published: *08 October 2021*

Citation:
An W, Wang H and Luo Y (2021) Dual-Band Antenna Integrated With Solar Cells for WLAN Applications. Front. Phys. 9:775214. doi: 10.3389/fphy.2021.775214

INTRODUCTION

The IEEE 802.11 wireless local area network (WLAN) standards have been used worldwide in these bands of 2.4~2.4835, 5.15~5.35, and 5.725~5.875 GHz. The higher band is also applied for 5G WiFi. Many extensive explorations have been carried out including dipole, slot, and microstrip antennas [1–4]. To cover these frequency bands, the dual-band and multiband antennas are much desired with favorable characteristics such as compact size, low cost, and easy integration with the RF circuit. Many dual-band antennas have been investigated, such as monopole, dipole, slot, and PIFA antennas with an omnidirectional radiation pattern [5–9].

To realize a resource-saving and environment-friendly society, it is preferable to combine solar cells and antennas for green communication. Based on the published researches, the solar-cell antenna can be categorized into at least three types. The first type is that the solar cells are treated as a parasitic structure, which includes the slot antenna [10, 11], PIFA [12–14], substrate integrated waveguide antenna [15], patch antenna [16, 17]. In the second type, the solar cells are treated as the ground or reflector [18–21]. The disadvantage is that the radiator will cause certain optical blockages. For the third type, the solar cells are adopted for the radiation structure directly [22–27]. It contains the dipole [22], shorted patch [23, 24], microstrip [25, 26], slot [27, 28], and Vivaldi antennas [29].

Although there are many designs of antenna integrated with solar cells, few studies can cover the 2.4/5-GHz WLAN bands simultaneously. To realized a compact design, the solar cells are expected to be both radiator/director and DC generator. However, the solar cells are with regular shapes of squares and rectangles, which would impose certain difficulty on the dual-band and wideband designs. For the dual-band design, the receiving band prefers an omnidirectional radiation pattern that can receive signals from all directions while the transmitting band desires a directional radiation pattern with a higher gain for long-distance transmission. So, some novel dual-band solar cell antennas are expected for the WLAN.

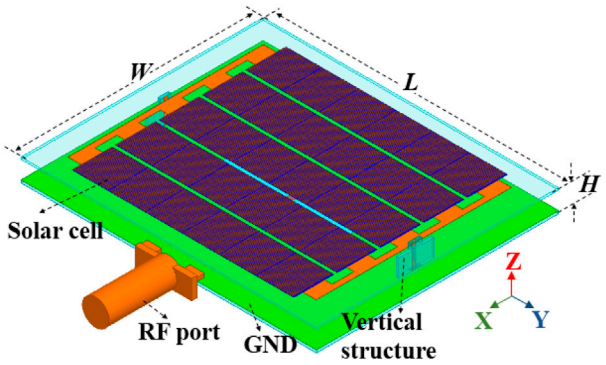

FIGURE 1 | The proposed dual-band solar cell antenna.

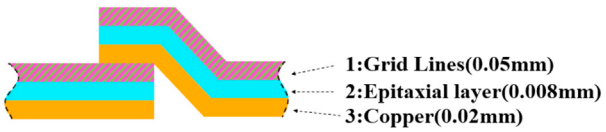

FIGURE 2 | The multi-layer structure and connection of the adopted solar cell.

A dual-band solar cell antenna is proposed for the WLAN applications. Thirty solar cells are employed to form the radiation structure for the upper band. The aperture coupling method is adopted with a coupling slot on the ground, which works at 2.4 GHz for the lower band. Relative bandwidth of 9.6 and 35.9% are obtained for the lower and higher bands, respectively. This dual-band antenna can achieve a measured gain of 5.69 dBi at 2.4 GHz with an omnidirectional radiation pattern and an average measured gain of 10.58 dBi for the upper band with a directional radiation pattern. Its DC performance is also tested through an optical experiment.

DUALBAND SOLAR CELL ANTENNA STRUCTURE

The proposed dual-band antenna integrated with solar cells is shown in **Figure 1** with a dimension of $83 \times 68 \times 3.4$ mm^3. Relong and FR4 laminates are adopted for the top, bottom, and vertical substrates. The Relong substrate has a thickness of 0.762 mm with a relative dielectric constant of 2.55, and a loss tangent of 0.0009 while the FR4 substrate has a thickness of 0.6 mm with a relative dielectric constant of 4.4, and loss tangent of 0.02. An air gap of 2 mm separates the bottom and top substrates.

One type of solar cell with the size of 11.2 mm × 11.5 mm is chosen for the dual-function design. Its multi-layer structure is depicted in **Figure 2**, which is similar to that in [22]. As the size of a single solar cell is relatively small compared with the wavelength of its working frequency, six solar cells are in a serial connection with every two adjacent solar cells overlapped along the long edge.

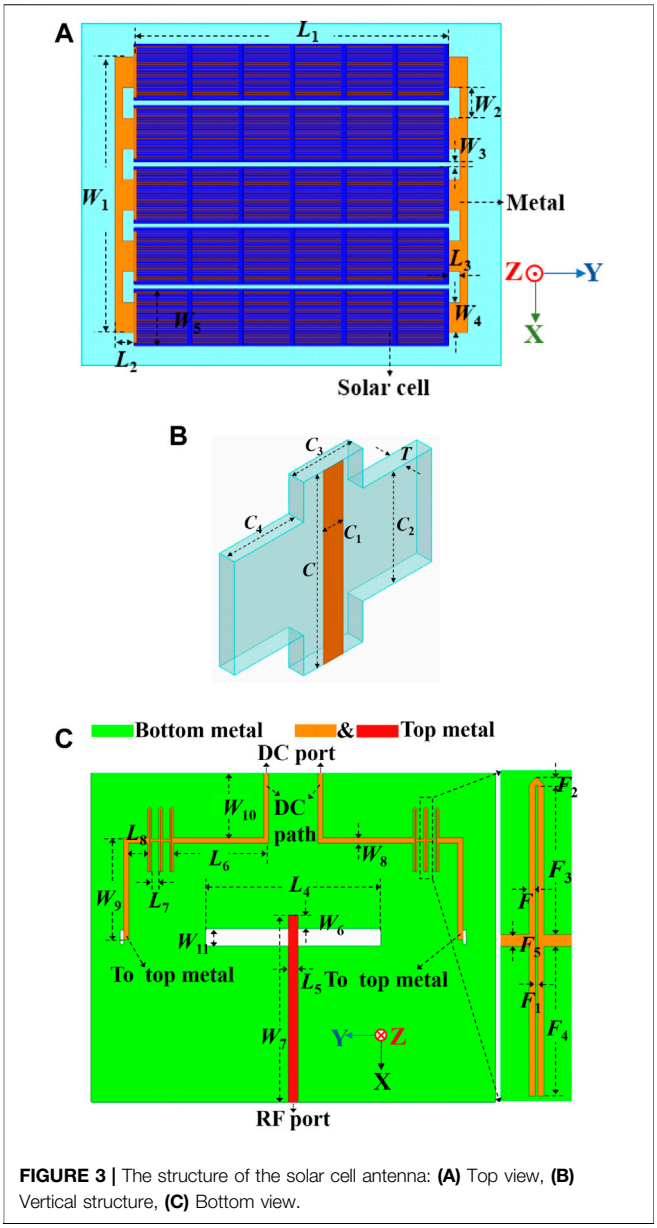

FIGURE 3 | The structure of the solar cell antenna: **(A)** Top view, **(B)** Vertical structure, **(C)** Bottom view.

TABLE 1 | Antenna parameters (mm).

Para.	W	W1	W2	W3	W4	W5	W6
Value	68	54.8	6.2	1	6	11.5	4.5
Para.	W7	W8	W9	W10	W11	L	L1
Value	38.5	1	21	13.5	3.6	83	62.25
Para.	L2	L3	L4	L5	L6	L7	L8
Value	3.7	2.2	36	1.95	19.6	1.5	4
Para	F	F1	F2	F3	F4	F5	C
Value	0.3	0.15	0.3	6.5	6.5	0.5	5.5
Para.	C1	C2	C3	C4	H	T	—
Value	1	2	3	3.5	2.6	0.6	—

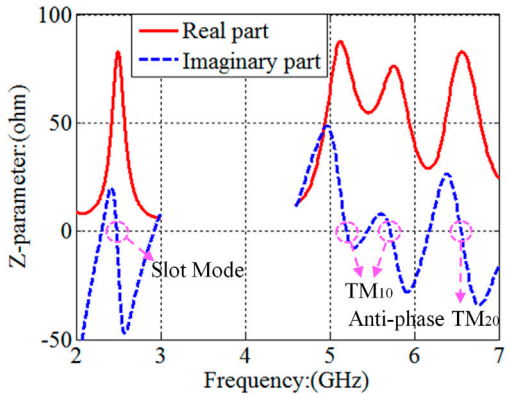

FIGURE 4 | The *Z*-parameter of the dual-band solar cell antenna.

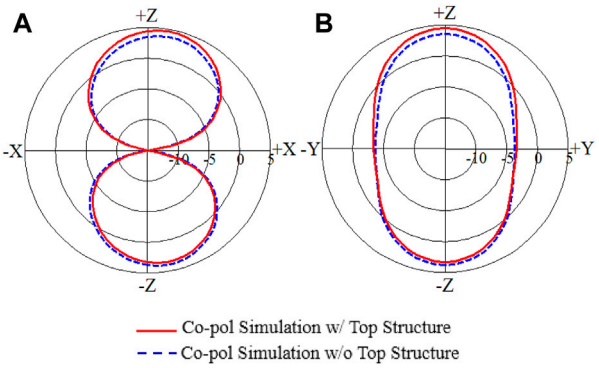

FIGURE 6 | The influence of top metal and solar cells on the radiation patterns at 2.4 GHz: **(A)** E-plane, **(B)** H-plane.

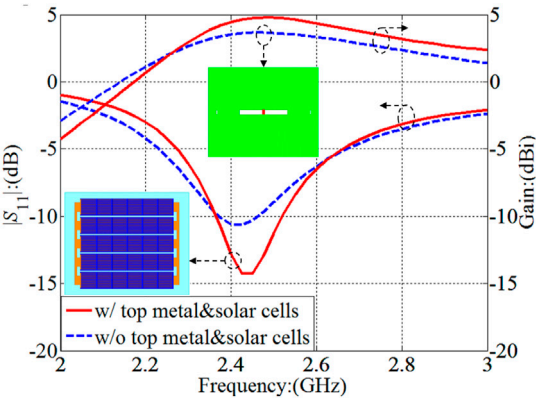

FIGURE 5 | The influence of top metal and solar cells on the antenna performance of the lower band.

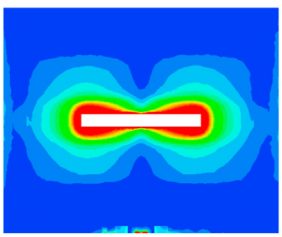

FIGURE 7 | Effective current distribution at 2.4 GHz.

The antenna structure is in **Figure 3** with detailed parameters in **Table 1**. It has the same polarization for two bands in the X-direction.

In **Figure 3A**, five rectangular patches made of solar cells are placed on the FR4 substrate. Each solar cell strip has a length of L_1 and a width of W_5. The anode and cathode of five solar cell strips are connected to the copper structures with the sizes of L_2, L_3, W_1, W_2, and W_4. In **Figure 3C**, the ground plane is printed on the top of the Relong substrate while the feeding strip and the DC path are printed on the bottom. The aperture coupling method is adopted for the excitation with a coupling slot at the center of the ground plane. Electromagnetic coupling is also an effective way to prevent the DC energy from the RF port. To block the RF current to the DC port, microstrip bandstop filters are added at the DC path [30].

The DC transmission line includes the top copper structures, DC path with filters on the bottom substrate, and vertical strips printed on the vertical substrate to connect the bottom DC path and top metallic structure, as shown in **Figures 1**, **3B**. The vertical substrate is also used to support the top structure.

ANTENNA ANALYSIS

To clarify the working mechanism of the dual-band antenna, *Z*-parameters are depicted in **Figure 4** and its working modes are investigated. It is observed from **Figure 4** that there are one resonant frequency point at the lower band and three resonant frequency points at the higher band. The current and E-field distributions are plotted for the lower and upper bands to analyze these resonant modes.

For the lower band, to analyze the influence of the top structure on the antenna performance, the *S*-parameter and gain with and without top structure are plotted in **Figure 5**. It is observed that the top structure has certain effects on the antenna performance at the lower band. The -10-dB bandwidth can be barely maintained at 2.4 GHz without top structure. After loading top structure, the impedance matching has been improved and the gain in the normal direction is 0.93 dB higher than that without top structure. The radiation patterns with and without top structure are plotted in **Figure 6** at 2.4 GHz. It is noticed that the front-to-back ratio is about 0.5 dB higher after loading the top structure. So, it can be concluded that the resonant mode at 2.4 GHz is independent of the top structure. Furthermore, the effective current distribution of the ground plane is also plotted in **Figure 7** and the antenna is with the slot mode at 2.4 GHz.

For the higher band, the instantaneous E-field distribution is plotted in **Figures 8A,B,C**. Based on the E-field distribution, it is

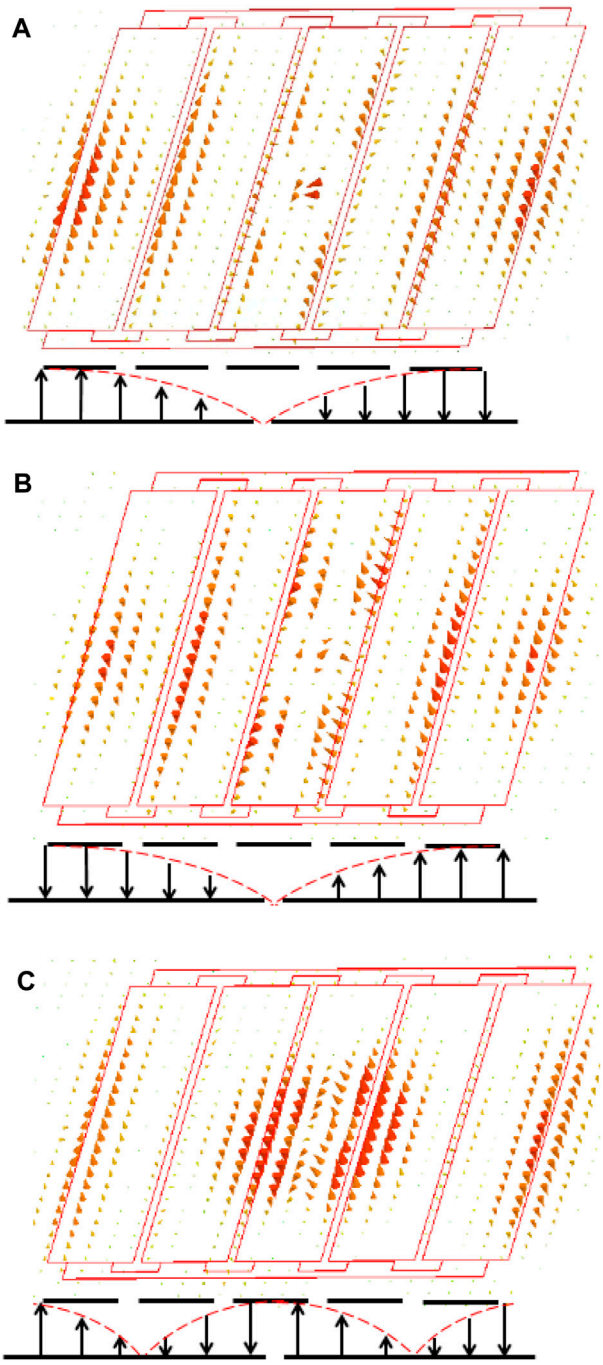

FIGURE 8 | Instantaneous E-field distribution at higher band: **(A)** 2.4 GHz, **(B)** 5.2 GHz, **(C)** 5.7 GHz, **(D)** 6.5 GHz.

clear that TM_{10} modes are excited at 5.2 and 5.7 GHz, and the antiphase TM_{20} mode is stimulated at 6.5 GHz. The slot structure on the ground acts as the excitation for the microstrip antenna at the upper band. To sum up, the proposed antenna has different resonant modes for dual-band performance. It is with the slot mode at the lower band and the cavity mode (TM_{10} and antiphase TM_{20}) at the higher band.

EXPERIMENTAL VERIFICATION

To verify the proposed dual-band design integrated with solar cells, a prototype is fabricated and thirty solar cells are assembled on the top structure, as shown in **Figure 9**. The *S*-parameter is measured by the Rohde and Schwarz ZVA24 network analyzer and the radiation performance is tested in an anechoic chamber. The software High-Frequency Structure Simulator (HFSS) is adopted for the numerical simulation.

The simulation and measurement results of the *S*-parameter and gain are plotted in **Figure 9**. The simulated −10-dB bandwidth is from 2.37 to 2.51 GHz at the lower band and from 5.1 to 6.7 GHz at the higher band. The measured −10-dB bandwidth is from 2.27 to 2.5 GHz at the lower band and from 4.8 to 6.9 GHz at the higher band. The target bands of 2.4, 5.2, and 5.8 GHz have been entirely covered.

For the lower band, the measured gain is 5.25 dBi at 2.4 GHz, while the simulated gain is 4.45 dBi. For the higher band, the measured gains at 5.2 and 5.8 GHz are 12.2 and 12 dBi, respectively. The simulated gains at 5.2 and 5.8 GHz are 11 and 12.67 dBi, respectively. An average measured gain of 10.58 dBi is realized at the higher band. The radiation patterns are plotted in **Figure 10**. It is observed that an omnidirectional radiation pattern is achieved at 2.4 GHz in **Figure 10A** with the measured cross-polarization levels of less than −15 dB. Unidirectional radiation patterns are obtained at 5.2 and 5.8 GHz, as shown in **Figures 10B,C**. The measured cross-polarization levels are less than −21 dB with the measured back-lobe level better than −10 dB.

It is observed that certain differences exist between the simulation and measurement results, which is mainly due to the assembly error. In the fabrication procedure, the solar cells are overlapped and soldered together, the anode and cathode of each solar strip are soldered to the metallic structure. All these processes are conducted manually and the actual size is larger than the design, so the measured performance is shifted to the lower band slightly.

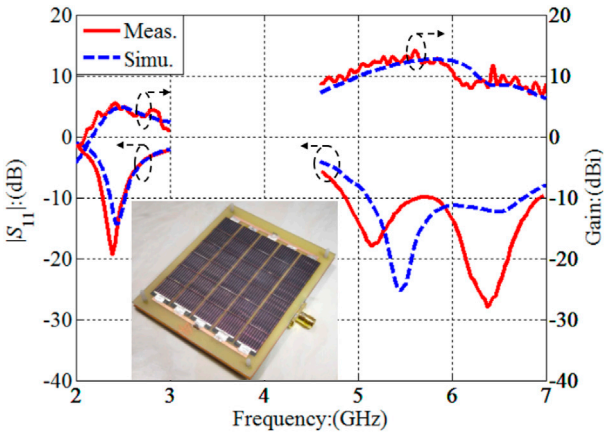

FIGURE 9 | The measured and simulated *S*-parameters and gains of the prototype.

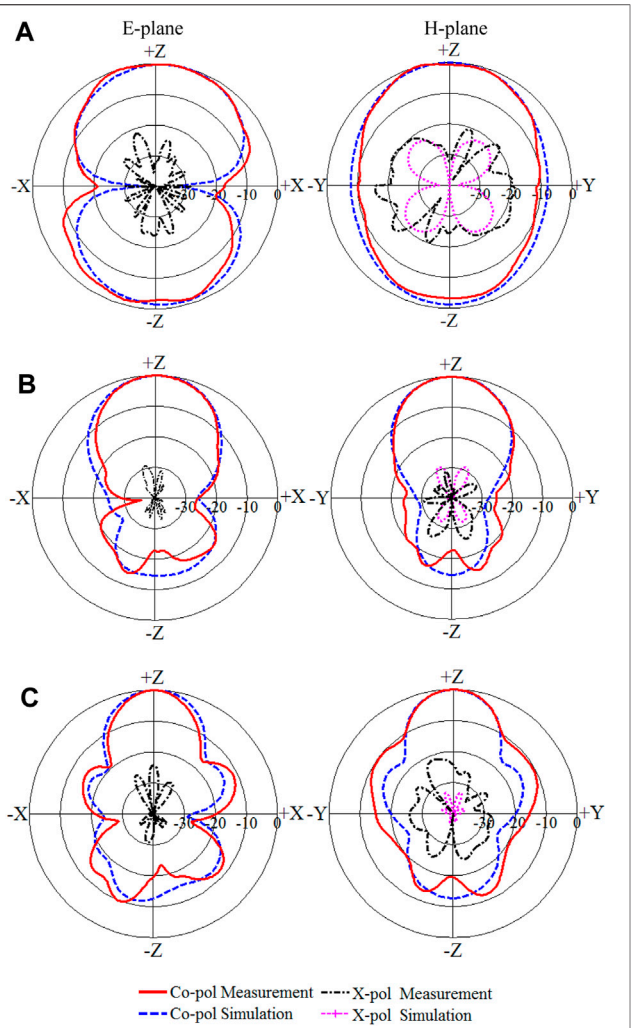

FIGURE 10 | Measured and simulated radiation patterns: **(A)** 2.4 GHz, **(B)** 5.2 GHz, **(C)** 5.8 GHz.

The proposed antenna integrated with solar cells is compared with some published solar cell antennas in **Table 2**. The solar cells are treated as a parasitic structure in [10, 12]. A slot antenna was reported in [10] with a measured gain of 6.62 dBi at 5.8 GHz. A low-profile multiband PIFA integrated with solar cells was presented in [12]. Measured gains of 4.7 and 5.5 dBi have been realized at 2.4 and 5.8 GHz, respectively. Using the solar cells as a radiation structure, a single-band low-profile antenna was investigated at 2.4 GHz with

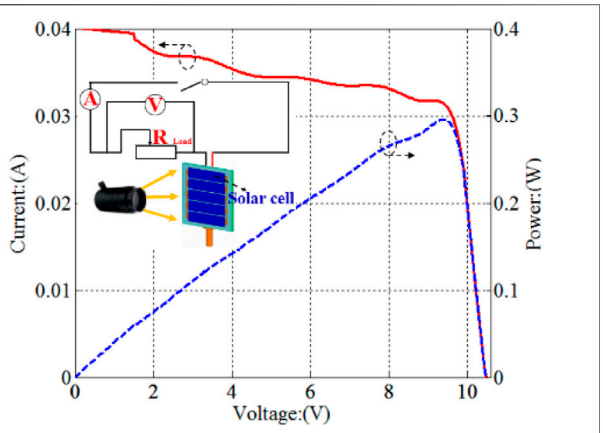

FIGURE 11 | The setup and measured results of the optical experiment.

measured gain of 8.55 dBi at 2.4 GHz [26]. A slot antenna integrated with solar cells was discussed in [27]. Dualband performance is obtained at 2.4 and 5.2 GHz with the measured gains of 3.5 and 3.1 dBi. To enhance the bandwidth, a novel dual-band solar cell antenna is designed in this work. The aforementioned frequency bands of 2.4, 5.2 and 5.8 GHz have been fully covered with enhanced gains at both bands.

OPTICAL EXPERIMENT

To test its ability of DC power generation, an optical experiment is conducted and the experimental setup is depicted in **Figure 11**. A light source with a light intensity of 1000 W/m^2 is adopted to illuminate the solar cells, which can be treated as a voltage source with certain inner resistance. A variable resistor acts as the load, which is connected to the anode and cathode of the DC port of the solar cell antenna. Voltmeter and ammeter are employed to measure the voltage and current of the resistance load so that the output power can be calculated.

The results of the optical experiment are also plotted in **Figure 11**. The value of the variable resistor increases from zero, it is observed that the load voltage starts to rise and the current starts to decrease due to the increased resistance. The output power also begins to increase, it reaches the maximum point when the resistor is 299.5 Ω, then starts to decrease when the resistor continues to increase. The output power can peak when the load resistance is equal to the inner source resistance

TABLE 2 | Comparison of the proposed antenna with existing designs.

Ref	2.4 GHz	5.2 GHz	5.8 GHz	Solar cell as radiator	Gain (dBi)	Antenna type
[10]	No	N. A	Yes	No	6.62	Slot
[12]	Yes	No	Yes	No	4.7/5.5	PIFA
[26]	Yes	No	No	Yes	8.55	Microstrip
[27]	Yes	Yes	No	Yes	3.5/3.1	Slot
This work	Yes	Yes	Yes	Yes	5.69/11.5/12.6	Slot and Microstrip

based on the circuit theory. So, the resistance of the equivalent source is obtained when the light intensity is 1000 W/m^2.

CONCLUSION

A dual-band antenna integrated with solar cells is designed for the WLAN. The one-wavelength slot mode is excited for the lower band while the cavity modes of TM_{10} and antiphase TM_{20} are stimulated for the higher band. Relative bandwidths of 9.6 and 35.9% have been achieved for the lower and higher bands, respectively. The lower band has an omnidirectional radiation pattern, which is proper for receiving while the higher band has a unidirectional radiation pattern, which is suitable for transmitting. Furthermore, this solar cell antenna with the ability of DC power generation makes it preferable for the outdoor anonymous platform and green communication. With these favorable characteristics, this dual-band antenna integrated with solar cells should find extensive applications in the future.

DATA AVAILABILITY STATEMENT

The original contributions presented in the study are included in the article/Supplementary Material, further inquiries can be directed to the corresponding author.

AUTHOR CONTRIBUTIONS

WA provides the idea and fabrication, HW conducts the simulation and measurement, YL provides the optimization and instruction. WA and YL prepare the original manuscript.

REFERENCES

1. Lai HW, and Wong H. Substrate Integrated Magneto-Electric Dipole Antenna for 5G Wi-Fi. *IEEE Trans Antennas Propagat* (2015) 63(2):870–4. doi:10.1109/tap.2014.2384015
2. Hu H-T, Chen F-C, and Chu Q-X. A Compact Directional Slot Antenna and its Application in MIMO Array. *IEEE Trans Antennas Propagat* (2016) 64(12):5513–7. doi:10.1109/tap.2016.2621021
3. Sun W, Li Y, Zhang Z, and Chen P-Y. Low-Profile and Wideband Microstrip Antenna Using Quasi-Periodic Aperture and Slot-To-CPW Transition. *IEEE Trans Antennas Propagat* (2019) 67(1):632–7. doi:10.1109/tap.2018.2874801
4. Sun W, Li Y, Zhang Z, and Feng Z. Broadband and Low-Profile Microstrip Antenna Using Strip-Slot Hybrid Structure. *Antennas Wirel Propag Lett* (2017) 16:3118–21. doi:10.1109/lawp.2017.2763987
5. Sim C-Y -D, Chen C-C, Zhang XY, Lee Y-L, and Chiang C-Y. Very Small-Size Uniplanar Printed Monopole Antenna for Dual-Band WLAN Laptop Computer Applications. *IEEE Trans Antennas Propagat* (2017) 65(6):2916–22. doi:10.1109/tap.2017.2695528
6. Sun XL, Liu L, Cheung SW, and Yuk TI. Dual-band Antenna with Compact Radiator for 2.4/5.2/5.8 GHz WLAN Applications. *IEEE Trans Antennas Propagat* (2012) 60(12):5924–31. doi:10.1109/tap.2012.2211322
7. Sim C-Y -D, Chien H-Y, and Lee C-H. Dual-/Triple-Band Asymmetric Dipole Antenna for WLAN Operation in Laptop Computer. *IEEE Trans Antennas Propagat* (2013) 61(7):3808–13. doi:10.1109/tap.2013.2257648
8. Lee C-T, Su S-W, Chen S-C, and Fu C-S. Low-cost, Direct-Fed Slot Antenna Built in Metal Cover of Notebook Computer for 2.4-/5.2-/5.8-GHz WLAN Operation. *IEEE Trans Antennas Propagat* (2017) 65(5):2677–82. doi:10.1109/tap.2017.2679070
9. Sim D-U, and Choi J-I. A Compact Wideband Modified Planar Inverted F Antenna (PIFA) for 2.4/5-GHz WLAN Applications. *Antennas Wirel Propag Lett* (2006) 5:391–4. doi:10.1109/lawp.2006.881914
10. Zhang Z, Bai B, Li X, Liu Y, Sun C, and Zhang Y. Integration of Circularly Polarized Microstrip Slot Array Antenna with Amorphous Silicon Solar Cells. *Antennas Wirel Propag Lett* (2020) 19(12):2320–3. doi:10.1109/lawp.2020.3031608
11. Vaccaro S, Pereira C, Mosig JR, and de Maagt P. In-Flight experiment for Combined Planar Antennas and Solar Cells (SOLANT). *IET Microw Antennas Propag* (2009) 3(8):1279–87. doi:10.1049/iet-map.2008.0410
12. Yurduseven O, and Smith D. A Solar Cell Stacked Multi-Slot Quad-Band PIFA for GSM, WLAN and WiMAX Networks. *IEEE Microw Wireless Compon Lett* (2013) 23(6):285–7. doi:10.1109/lmwc.2013.2258006
13. O'Conchubhair O, McEvoy P, and Ammann MJ. Integration of Antenna Array with Multicrystalline Silicon Solar Cell. *IEEE Antennas Wireless Propag Lett* (2015) 14:1231–4. doi:10.1109/LAWP.2015.2399652
14. O'Conchubhair O, Narbudowicz A, McEvoy P, and Ammann MJ. Circularly Polarised Solar Antenna for Airborne Communication Nodes. *Electron Lett* (2015) 51(9):667–9. doi:10.1049/el.2015.0201
15. Lemey S, Declercq F, and Rogier H. Dual-band Substrate Integrated Waveguide Textile Antenna with Integrated Solar Harvester. *IEEE Antennas Wireless Propag Lett* (2016) 13:269–72. doi:10.1109/LAWP.2014.2303573
16. Virili M, Georgiadis A, Collado A, Mezzanotte P, and Roselli L. EM Characterization of a Patch Antenna with Thermo Electric Generator and Solar Cell for Hybrid Energy Harvesting. In: Proceedings of the IEEE Radio and Wireless Symposium; 25 Jan 2015; San Diego, CA, USA. IEEE (2015). p. 44–6.
17. Virili M, Georgiadis A, Mira F, Collado A, Alimenti F, Mezzanotte P, and Roselli L. EH Performance of an Hybrid Energy Harvester for Autonomous Nodes. In: Proc. IEEE Topical Conf. Wireless Sensors Sensor Netw; 24 Jan 2016; Austin, TX, USA. IEEE (2016). p. 71–4. doi:10.1109/wisnet.2016.7444325
18. Yurduseven O, Smith D, Pearsall N, and Forbes I. A Transparent Solar Patch Antenna for 2.4/2.5 GHz WLAN-WiMAX Applications. In: Proceedings of the 2nd International Symposium On Environment Friendly Energies And Applications; 25 June 2012; Newcastle Upon Tyne, UK. IEEE (2012). p. 614–7.
19. Ta SX, and Park I. A Circularly Polarized Antenna Integrated with a Solar Cell Metasurface for CubeSat. In: Proceedings of the Asia-Pacific Microwave Conference; 6 November 2018; Kyoto, Japan. IEEE (2018). p. 696–8.
20. An W, Xu S, Yang F, and Gao J. A Ka-Band Reflectarray Antenna Integrated with Solar Cells. *IEEE Trans Antennas Propagat* (2014) 62(11):5539–46. doi:10.1109/tap.2014.2354424
21. An W, Xiong L, Xu S, Yang F, Fu H-P, and Ma J-G. A Ka-Band High-Efficiency Transparent Reflectarray Antenna Integrated with Solar Cells. *IEEE Access* (2018) 6:60843–51. doi:10.1109/access.2018.2875359
22. An W, Hong L, Luo Y, Ma K, Ma J, and Huang X. A Wideband Dual-Function Solar Cell Dipole Antenna for Both Energy Harvesting and Wireless Communications. *IEEE Trans Antennas Propagat* (2021) 69(1):544–9. doi:10.1109/tap.2020.3005250
23. Yurduseven O, Smith D, Pearsall N, and Forbes I. A Triband Short-Circuited Suspended Solar Patch Antenna. Propagation and EM Theory. In: Proceedings of the International Symposium on Antennas; 22 Oct 2012; Xi'an, China. IEEE (2012). p. 294–7.
24. Yurduseven O, Smith D, and Elsdon M. Cross-coax Fed Wideband Solar Patch Antenna. In: Proceedings of the Conference on Microwave Techniques; 17 April 2013; Pardubice, Czech Republic. IEEE (2013). p. 25–30.
25. Yurduseven O, Smith D, Pearsall N, and Forbes I. Design of a Highly Efficient Wideband Suspended Solar Array Antenna. In: Proceedings of the IEEE International Symposium on Antennas and Propagation; 8 July 2012; Chicago, IL, USA. IEEE (2012). p. 1–2. doi:10.1109/aps.2012.6348555

26. Zhao Y, An W, Luo Y, Li S, Xiong L, and Yu S. Low-Profile Antenna Integrated with Solar Cells for the 2.4 GHz Band. *Antennas Wirel Propag Lett* (2021) 20(4):443–7. doi:10.1109/lawp.2021.3051795
27. Shynu SV, Ons MJR, Ammann MJ, McCormack SJ, and Norton B. Dual Band A-Si:H Solar-Slot Antenna for 2.4/5.2 GHz WLAN Applications. In: Proc. 3rd Eur. Conf. Antennas Propag.; 23 March 2009; Berlin, Germany. IEEE (2009). p. 408–10.
28. An W, Zhao W, Wang H, Luo Y, Wang J, and Huang X. Dual-Function Slot Antenna Integrated with Solar Cells for the 1.575-GHz Band. *IEICE Electron Express* (2016) 17(21):1–6. doi:10.1587/elex.17.20200322
29. O'Conchubhair O, Yang K, McEvoy P, and Ammann MJ. Amorphous Silicon Solar Vivaldi Antenna. *IEEE Antennas Wireless Propag Lett* (2020) 15:893–6. doi:10.1109/LAWP.2015.2479189
30. Luo S, Zhu L, and Sun S. Stopband-Expanded Low-Pass Filters Using Microstrip Coupled-Line Hairpin Units. *IEEE Antennas Wireless Compon Lett* (2008) 18(8):506–8. doi:10.1109/LMWC.2008.2001004

Conflict of Interest: The authors declare that the research was conducted in the absence of any commercial or financial relationships that could be construed as a potential conflict of interest.

frontiers in Physics

ORIGINAL RESEARCH
published: 24 November 2021
doi: 10.3389/fphy.2021.774338

60-GHz Half-Mode Substrate-Integrated Waveguide Bandpass Filter in 0.15-μm GaAs Technology

Xu-Juan Liu[1], *Wen Wu*[2], *Kai-Da Xu*[3]*, *Ying-Jiang Guo*[4] and *Qiang Chen*[2]

[1]School of Vehicle Engineering, Xi'an Aeronautical University, Xi'an, China, [2]Department of Communications Engineering, Tohoku University, Sendai, Japan, [3]School of Information and Communications Engineering, Xi'an Jiaotong University, Xi'an, China, [4]Microsystem and Terahertz Research Center, China Academy of Engineering Physics, Chengdu, China

A compact 60-GHz on-chip bandpass filter (BPF) is presented using gallium arsenide (GaAs) technology. The miniaturization is achieved by the half-mode substrate-integrated waveguide (HMSIW) structure. Finally, a prototype of the BPF is fabricated and tested to validate the proposed idea, whose simulated and measured results are in good agreement. The measurements show that it has a center frequency at 58.6 GHz with a bandwidth of 17.9%, and the minimum insertion loss within the passband is 1.2 dB. The chip, excluding the feedings, is only about $0.38\lambda_g \times 0.58\lambda_g$, where λ_g is the guided wavelength at the center frequency.

Keywords: bandpass filters, GaAs-based circuits, on-chip devices, millimeter wave devices, half-mode substrate-integrated waveguide

OPEN ACCESS

Edited by:
Jifeng Liu,
Dartmouth College, United States

Reviewed by:
Haozhe Wang,
Massachusetts Institute of Technology, United States

***Correspondence:**
Kai-Da Xu
kaidaxu@ieee.org

Specialty section:
This article was submitted to Optics and Photonics, a section of the journal Frontiers in Physics

Received: *11 September 2021*
Accepted: *03 November 2021*
Published: *24 November 2021*

Citation:
Liu X-J, Wu W, Xu K-D, Guo Y-J and Chen Q (2021) 60-GHz Half-Mode Substrate-Integrated Waveguide Bandpass Filter in 0.15-μm GaAs Technology. Front. Phys. 9:774338. doi: 10.3389/fphy.2021.774338

INTRODUCTION

Recent developments in semiconductor technology have enabled the pursuit of miniaturized applications based on on-chip millimeter-wave (mmW) devices and systems to become popular, such as automotive mmW radar. The on-chip bandpass filter (BPF) design for millimeter-wave transceivers has, thus, attracted more attention and has made numerous breakthroughs. Abundant investigations have been oriented based on the conventional silicon-based semiconductor technology–integrated circuit process (e.g., CMOS, SiGe, etc.) pursuing low cost with compact physical occupation [1–9]. But meanwhile, the low loss of BPF is also very demanding. The Gallium arsenide (GaAs) process is a desirable candidate for lower in-band insertion loss and higher steep edge with high-operating frequency. Consequently, some works on GaAs–based BPFs have been reported in recent years [10–14]. However, the design of GaAs–based BPFs that consider both size and loss has still not been proposed. In our previous work [13], the proposed BPF achieves bandwidth of over 50% based on the spoof surface plasmon polaritons transmission line theory, but the size is bulky, reaching $1.95\boldsymbol{\lambda_g}\times0.37\boldsymbol{\lambda_g}$. In [14], the BPF structure is based on planar resonant circuits with metal strips, and the LC equivalent circuit model theory is used for the design. The miniaturized size is achieved but at the expense of insertion loss, larger than 2.4 dB.

Considering compatibility with the integrated circuit system, a BPF based on substrate-integrated waveguide (SIW) technology is introduced with high-Q factor, low loss, and easy fabrication [15]. Furthermore, half-mode SIW (HMSIW) saves about half of the SIW dimension with almost same performance for the design of BPFs. The HMSIW BPF implemented based on GaAs technology is expected to balance the size and loss. However, few BPF works are explored using HMSIW in GaAs technology at the millimeter-wave frequencies.

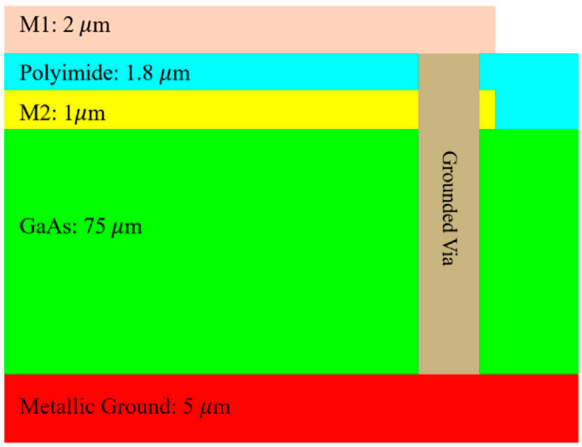

FIGURE 1 | Stack-up of the employed 0.15-μm GaAs pHEMT technology.

In this article, for the first time, we implement the HMSIW structure based on the GaAs standard process. A compact 60-GHz on-chip BPF is proposed based on HMSIW with the 0.15-μm GaAs pHEMT process, and the stack-up is shown in **Figure 1**. Two metal layers M1 and M2 are thinned to 2 μm and 1 μm, respectively, with a conductivity of 4×10^7 S/m. The thicknesses of GaAs and polyimide are 75 μm and 1.8 μm, respectively, and their relative permittivity are 12.9 and 2.9, respectively. A 5-μm metal layer beneath the GaAs substrate is coated as the ground. The proposed BPF circuit is designed on the M1 layer having square vias to the ground. By optimizing the dimensions of the aligned component on the M1 layer, the BPF can be adjusted to achieve the desired values of the passband and insertion loss. Compared with the previous SIW/HMSIW BPFs [16–23], this design has relatively small insertion loss and size.

DESIGN METHOD AND ANALYSIS

A pair of HMSIW cavity resonators is employed to realize BPF response and miniaturized size. The compact structure is constructed with transition from the microstrip line to HMSIW for further layout size saving. The detailed configuration of the slotted HMSIW BPF is demonstrated in **Figure 2**, which consists of an input/output microstrip line and slotted HMSIW structure. The HMSIW cavity is divided into two symmetrical cavity resonators, A and B, by the transversal slot. Therefore, each resonator's boundary is constructed by one electric wall (EW) and three magnetic walls (MWs), as shown in **Figure 3A**. The EW is formed by rows of metal vias, as the tangential component of the electric field is almost zero near the surface of these via holes. In contrast, the other three side edges are used as MWs because the tangential component of the magnetic field is zero. Therefore, the resonator cavity can be approximately equivalent to a segment of the microstrip line propagating along the x-axis which is open-circuited at one end and short-circuited at the other end. Moreover, the resonator length along x-axis is $\lambda_g/4$ (where λ_g is the guide wavelength), and λ_g is approximately equal to $\lambda/\sqrt{\varepsilon_r}$, where ε_r is the relative permittivity of GaAs dielectric and λ is the free-space wavelength at the operating frequency.

The standard microstrip propagation mode is the quasi-transversal electromagnetic (TEM) wave. The TEM mode indicates that both the electric field and magnetic field are perpendicular to the direction of electromagnetic wave propagation. In the resonator cavity, the electric field is along y-axis, while the magnetic field is along z-axis. The fields are mostly within the GaAs dielectric of the cavity and partly in the air region adjacent to the edge of the cavity. The phase speed of TEM fields in the GaAs region would be $c/\sqrt{\varepsilon_r}$ (where c is the light velocity in free-space), while the phase speed of TEM fields in the air region would be c. As a result, phase-mismatching conditions are unavoidable at the GaAs–air boundaries of the cavity.

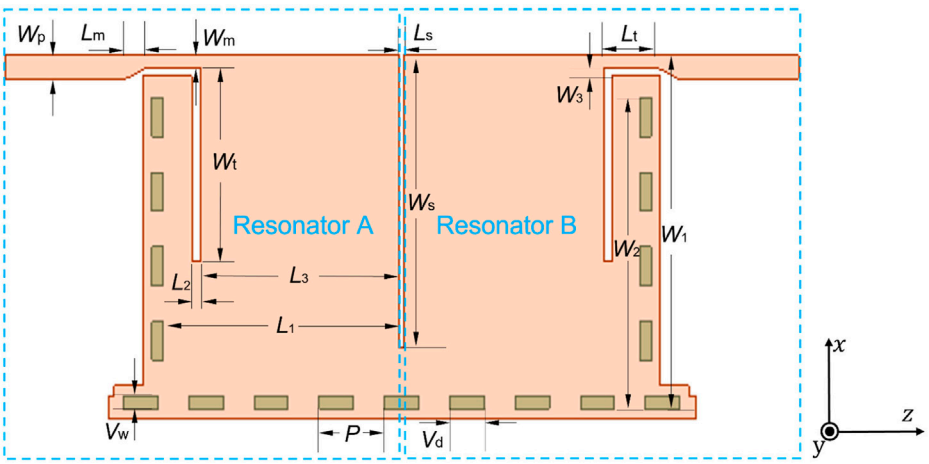

FIGURE 2 | Configuration of the proposed HMSIW BPF (Only top view of the TM1 layer is shown).

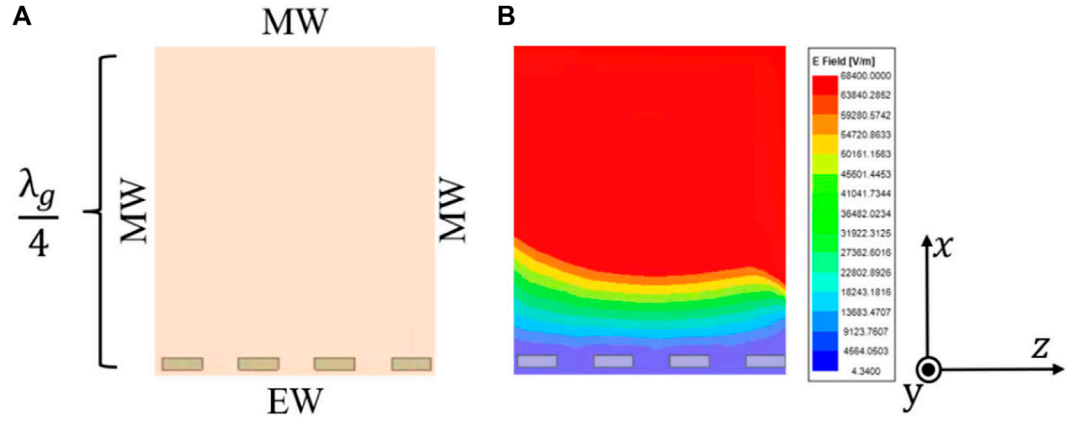

FIGURE 3 | (A) HMSIW resonator and **(B)** electric field distribution of the quasi-TEM mode of the HMSIW resonator.

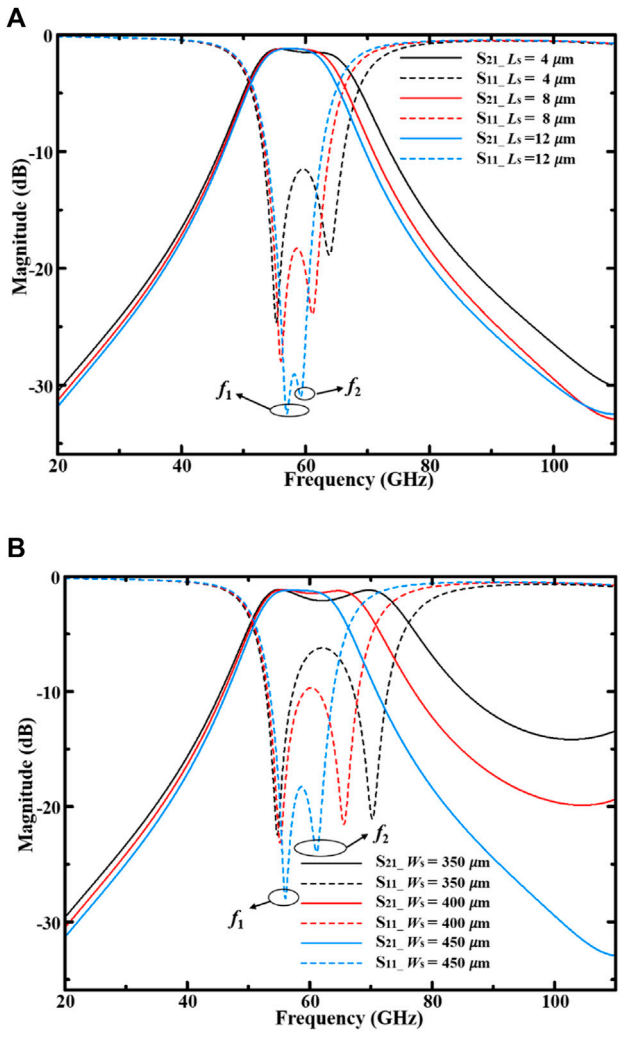

FIGURE 4 | S_{21} of the HMSIW BPF with **(A)** varied *Ls* at *Ws* = 450 μm and **(B)** varied *Ws* at *Ls* = 8 μm

Therefore, the resonant mode of the cavity is referred as the quasi-TEM mode, as shown in **Figure 3B**. The color from blue to red represents the electric field intensity from weak to strong. The resonant frequency (f_c) of the single cavity with the quasi-TEM mode can be evaluated based on classical transmission line theory:

$$f_c = \frac{c}{4W_2\sqrt{\varepsilon_r}}, \tag{1}$$

where W_2 is the width of the HMSIW shown in **Figure 2**.

The mutual coupling between two identical HMSIW resonators A and B is defined as inter-coupling. One more resonant frequency will be generated because of the inter-coupling scheme [24]. Therefore, the resonant frequency f_c of the HMSIW cavity will be split into two resonant frequencies, represented by f_1 and f_2, respectively. Thus, these two frequencies are controlled by the inter-coupling between two HMSIW resonators. The inter-coupling coefficient k can be acquired by simulation from ANSYS HFSS and can be evaluated as [24]:

$$k = \frac{f_2^2 - f_1^2}{f_2^2 + f_1^2}. \tag{2}$$

It can be seen that the coupling coefficient k is proportional to the separation between the resonant frequency points f_1 and f_2. As a result, the tighter the coupling is, the wider will be the separation of f_1 and f_2, and the bandwidth of the BPF is thus expanded. On the other hand, the coupling strength can be tuned by changing the length *Ls* and width *Ws* of the transversal slot inserted between the two HMSIW cavity resonators. When these values increase, the gap between HMSIW resonators will be increased, and the coupling strength will be reduced, resulting in decreased bandwidth and lower insertion loss. **Figure 4** shows the simulated results using the Ansys HFSS simulator to verify the relationships between slot size variation and BPF frequency response. The *S*-parameters are used to evaluate the electromagnetic (EM) performance. S_{11} and S_{21} represent the reflection and transmission coefficients of the EM wave, respectively.

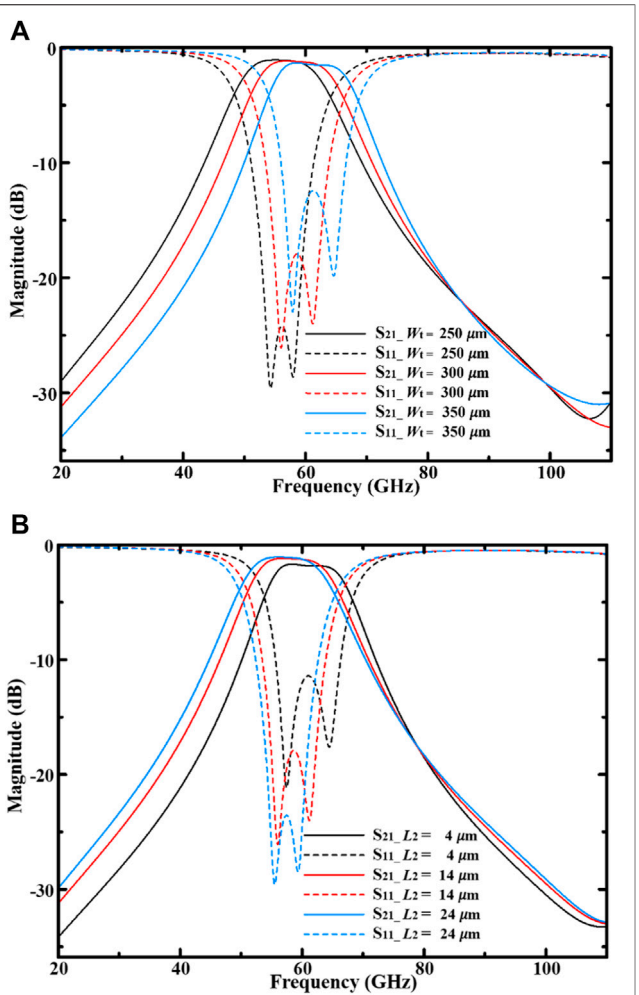

FIGURE 5 | S-parameters of the HMSIW BPF with **(A)** varied W_t at L_2 = 14 μm and **(B)** varied L_2 at W_t = 318 μm.

When choosing the final values of *L*s and *W*s, both bandwidth and loss requirements should be considered to make a balance. Usually, the value of $|S_{11}|$ should be lower than -10 dB in the passband, but the ultra-low $|S_{11}|$ value would result in bandwidth reduction. The value of $|S_{21}|$ represents the insertion loss (IL) within the passband of the filter and the suppression at the stopband. Considering the fringing field effect, the values 8 μm and 450 μm of *L*s and *W*s are chosen, respectively. The maximum $|S_{11}|$ is about -17 dB. The IL at the center frequency is less than 1.1 dB, and 10 GHz of bandwidth is achieved.

The external coupling between the HMSIW resonator and input/output feed line can be defined by the external quality factor Q_e, and its value can be calculated by the equation [25]:

$$Q_e = \frac{2\pi \cdot f_0 \cdot \tau_{S_{11}}(f_0)}{4}, \tag{3}$$

where τ_{S11} is the group delay of S_{11} at resonant frequency; f_0 is the center frequency of the BPF passband.

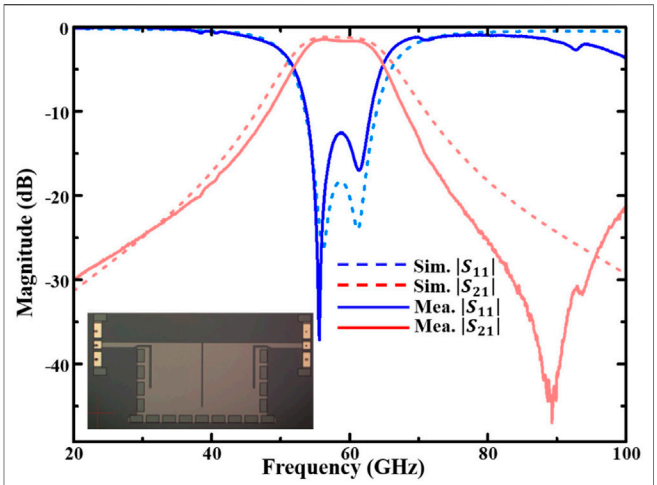

FIGURE 6 | Simulated and measured results of the proposed GaAs–based BPF.

TABLE 1 | Configuration parameters of the HMSIW BPF.

Parameter	Value (μm)	Parameter	Value (μm)
P	115	L_m	35
V_d	60	W_m	18
V_w	20	L_1	416
L_t	94	L_2	14
W_t	318	L_3	352
L_s	8	W_1	545
W_s	450	W_2	480
W_p	35	W_3	14

In this work, the value of Q_e is 7.8 which is extracted by the Ansys HFSS simulator. It can be tuned by changing the dimension of the structure which transfers from the microstrip line to HMSIW. To miniaturize the overall size, direct connection is proposed instead of the traditional gradual changing structure. The corresponding impedance matching can be performed by the slot between the feeding port and HMSIW. The length of the slot is W_t, while the width is L_2. Therefore, the values of $|S_{11}|$ and $|S_{21}|$ can be also adjusted by W_t and L_2, as shown in **Figure 5**. As discussed before, the $|S_{11}|$ is suggested to be about −17 dB, and the center frequency should be near 60 GHz. Consequently, W_t and L_2 are selected as 300 μm and 14 μm, respectively.

RESULTS

The prototype of the designed HMSIW BPF filter is fabricated as shown in the inset of **Figure 6**. The overall size excluding two Ground–Signal–Ground (GSG) pads is $0.38\lambda_g \times 0.58\lambda_g$. The detailed parameter information is shown in **Table 1**. The filter is measured through an on-wafer probe using the Keysight Vector Network Analyzer. Comparisons between the simulated and measured S-parameters are shown in **Figure 6**. The minimum insertion loss (IL) of the measured passband is about 1.2 dB, and

TABLE 2 | Performance comparisons with some reported SIW/HMSIW BPFs.

Reference	Δf (%)	IL (dB)	Size ($\lambda_g \times \lambda_g$)	Q_u	Center Frequency (GHz)	Technology
[11]	3.4	4.3	2.31 × 1.57	130	93	GaAs
[13]	50.5	1.4	1.95 × 0.37	NA	65	GaAs
[14]	18.4	2.42	0.07 × 0.16	52	58.7	GaAs
[16]	17	4.1	0.25 × 2.2	NA	10	PCB
[17]	40	1.2	0.31 × 1.1	NA	8.79	PCB
[22]	10.8	1.45	0.45 × 0.67	NA	3	PCB
[23]	40	0.7	0.86 × 0.91	NA	40	LTCC
This work	**17.9**	**1.2**	**0.38 × 0.58**	**135**	**58.6**	**GaAs**

the return loss is better than −10 dB. The center frequency is at 58.6 GHz, 3-dB passband is ranged from 53.3 to 63.8 GHz, and the relative bandwidth is 17.9%. The calculated unloaded quality factor Q_u [24] is 135. The deviation of the measured and simulated passband loss is within 0.5 dB, whose error may be introduced by the GSG probe measurement system. It is noticed that there is a spurious transmission zero near 90 GHz which does not match with the simulation. This may be caused by the modeling deviation of via holes. The frequency response of the resonant cavity is sensitive to the row of these vias at higher frequency.

Table 2 shows the characteristic comparisons with some other reported SIW/HMSIW BPFs. The results demonstrate that both IL and size of our proposed HMSIW filter are better than those of the SIW filter in [11] using the same GaAs technology. Compared with our previous work [14], the IL of 1.2 dB has been improved. The IL of the filter using LTCC in [23] is lower than the proposed work, but its size is bulky, increased by more than 6 times. Moreover, the solution in [23] is not too easy to integrate with other active devices which require to be designed on the same wafer.

CONCLUSION

The bandwidth and insertion loss of the passband can be easily tuned by adjusting the dimension of the slot between the two HMSIW cavity resonators. The center frequency can be evaluated by the single HMSIW resonator. The direct connection structure is deployed for the transition from the microstrip line to HMSIW considering size saving. The fabricated BPF prototype centered at 58.6 GHz has a broadband filtering response with very good insertion loss and return loss. The measurement results agree well with the simulation results. The HMSIW and compact feeding configuration for the design of the BPF are useful to improve the circuit occupation on the chip. At the same time, performance has been not deteriorated compared with other traditional SIW/HMSIW BPFs. It also illustrates that the energy leakage, bandgap effect, etc. of the HMSIW with the period square vias in the GaAs process is also applicable. Owing to these virtues, the proposed HMSIW BPF can be easily integrated with other GaAs components and circuits in mmW systems such as vehicle-mounted radar and 5G communications.

DATA AVAILABILITY STATEMENT

The original contributions presented in the study are included in the article/Supplementary Material; further inquiries can be directed to the corresponding author

AUTHOR CONTRIBUTIONS

X-JL and WW contributed to this work equally. All authors listed have made a substantial, direct, and intellectual contribution to the work and approved it for publication.

FUNDING

This work was supported in part by the NSAF Joint Fund under Grant U2130102, in part by the Natural Science Foundation of Shaanxi Province under Grant 2021JQ-060, and in part by the “Siyuan Scholar” Fellowship of XJTU.

REFERENCES

1. HsuCheng-Ying C, ChuangHuey-Ru C, Chuang H. A 60-GHz Millimeter-Wave Bandpass Filter Using 0.18-μm CMOS Technology. *IEEE Electron Device Lett* (2008) 29(3):246–8. doi:10.1109/LED.2007.915369
2. Franc A-L, Pistono E, Gloria D, Ferrari P. High-Performance Shielded Coplanar Waveguides for the Design of CMOS 60-GHz Bandpass Filters. *IEEE Trans Electron Devices* (2012) 59(5):1219–26. doi:10.1109/TED.2012.2186301
3. Yang Y, Liu H, Hou ZJ, Zhu X, Dutkiewicz E, Xue Q. Compact On-Chip Bandpass Filter with Improved In-Band Flatness and Stopband Attenuation in 0.13-μm (Bi)-CMOS Technology. *IEEE Electron Device Lett* (2017) 38(10): 1359–62. doi:10.1109/LED.2017.2739186
4. El-Hameed ASA, Barakat A, Abdel-Rahman AB, Allam A, Pokharel RK. Ultracompact 60-GHz CMOS BPF Employing Broadside-Coupled Open-Loop Resonators. *IEEE Microw Wireless Compon Lett* (2017) 27(9):818–20. doi:10.1109/LMWC.2017.2734771
5. Zhu H, Yang Y, Zhu X, Sun Y, Wong S-W. Miniaturized Resonator and Bandpass Filter for Silicon-Based Monolithic Microwave and Millimeter-

Wave Integrated Circuits. *IEEE Trans Circuits Syst* (2018) 65(12):4062–71. doi:10.1109/TCSI.2018.2839701
6. Li M, Yang Y, Xu KD, Zhu X, Wong SW. Microwave On-Chip Bandpass Filter Based on Hybrid Coupling Technique. *IEEE Trans Electron Devices* (2018) 65(12):5453–9. doi:10.1109/TED.2018.2876324
7. Luo C, Wong SW, Chen RS, Zhu X, Yang Y, Lin JY, et al. Compact On-Chip Millimetre Wave Bandpass Filters with Meandered Grounding Resonator in 0.13-μm (Bi)-CMOS Technology. *IET Microwaves, Antennas & Propagation* (2020) 14(6):559–65. doi:10.1049/iet-map.2019.0192
8. Xu K-D, Zhu X, Yang Y, Chen Q. A Broadband On-Chip Bandpass Filter Using Shunt Dual-Layer Meander-Line Resonators. *IEEE Electron Device Lett* (2020) 41(11):1617–20. doi:10.1109/LED.2020.3027734
9. Ge Z, Chen L, Yang L, Gómez-García R, Zhu X. On-Chip Millimeter-Wave Integrated Absorptive Bandstop Filter in (Bi)-CMOS Technology. *IEEE Electron Device Lett* (2021) 42(1):114–7. doi:10.1109/LED.2020.3036036
10. Li L-P, Shen W, Ding J-Y, Sun X-W. Compact 60-GHz On-Chip Bandpass Filter with Low Insertion Loss. *IEEE Electron Device Lett* (2018) 39(1):12–4. doi:10.1109/LED.2017.2778714
11. Xiao Y, Shan P, Zhao Y, Sun H, Yang F. Design of a W -Band GaAs-Based SIW Chip Filter Using Higher Order Mode Resonances. *IEEE Microw Wireless Compon Lett* (2019) 29(2):104–6. doi:10.1109/LMWC.2018.2890265
12. Guo Y-J, Xu K-D, Deng X, Cheng X, Chen Q. Millimeter-Wave On-Chip Bandpass Filter Based on Spoof Surface Plasmon Polaritons. *IEEE Electron Device Lett* (2020) 41(8):1165–8. doi:10.1109/LED.2020.3003804
13. Xu K-D, Guo Y-J, Yang Q, Zhang Y-L, Deng X, Zhang A, et al. On-Chip GaAs-Based Spoof Surface Plasmon Polaritons at Millimeter-Wave Regime. *IEEE Photon Technol Lett* (2021) 33(5):255–8. doi:10.1109/LPT.2021.3054962
14. Xu K-D, Guo Y-J, Liu Y, Deng X, Chen Q, Ma Z. 60-GHz Compact Dual-Mode On-Chip Bandpass Filter Using GaAs Technology. *IEEE Electron Device Lett* (2021) 42(8):1120–3. doi:10.1109/LED.2021.3091277
15. Hong W, Liu B, Wang Y, Lai Q, Tang H, Yin XX, et al. Half Mode Substrate Integrated Waveguide: A New Guided Wave Structure for Microwave and Millimeter Wave Application. In: 2006 Joint 31st International Conference on Infrared Millimeter Waves and 14th International Conference on Teraherz Electronics; 2006 Sept 18-22; Shanghai, China (2006), p. 219. doi:10.1109/ICIMW.2006.368427
16. Zhou S, Wang Z, Xu R, Shen D, Zhan M. A Novel X-Band Half Mode Substrate Integrated Waveguide (HMSIW) Bandpass Filter. In: 2009 Asia Pacific Microwave Conference; 2009 Dec 7-10; Singapore (2009), p. 1387–9. doi:10.1109/APMC.2009.5384496
17. Wang Y, Hong W, Dong Y, Liu B, Tang HJ, Chen J, et al. Half Mode Substrate Integrated Waveguide (HMSIW) Bandpass Filter. *IEEE Microw Wireless Compon Lett* (2007) 17(4):265–7. doi:10.1109/LMWC.2007.892958
18. Zhang Q-L, Wang B-Z, Zhao D-S, Wu K. A Compact Half-Mode Substrate Integrated Waveguide Bandpass Filter with Wide Out-Of-Band Rejection. *IEEE Microw Wireless Compon Lett* (2016) 26(7):501–3. doi:10.1109/LMWC.2016.2574997
19. Jones TR, Daneshmand M. Miniaturized Slotted Bandpass Filter Design Using a Ridged Half-Mode Substrate Integrated Waveguide. *IEEE Microw Wireless Compon Lett* (2016) 26(5):334–6. doi:10.1109/LMWC.2016.2549000
20. Cheng F, Lin X, Song K, Jiang Y, Fan Y. Compact Diplexer with High Isolation Using the Dual-Mode Substrate Integrated Waveguide Resonator. *IEEE Microw Wireless Compon Lett* (2013) 23(9):459–61. doi:10.1109/LMWC.2013.2274036
21. Zhang-Cheng Hao H, Wei Hong W, Ji-Xin Chen J-X, Ke Wu X-P, Wu K. Compact Super-wide Bandpass Substrate Integrated Waveguide (SIW) Filters. *IEEE Trans Microwave Theor Techn.* (2005) 53(9):2968–77. doi:10.1109/TMTT.2005.854232
22. Chen F, Song K, Hu B, Fan Y. Compact Dual-Band Bandpass Filter Using HMSIW Resonator and Slot Perturbation. *IEEE Microw Wireless Compon Lett* (2014) 24(10):686–8. doi:10.1109/LMWC.2014.2342883
23. Wong SW, Wang K, Chen Z-N, Chu Q-X. Electric Coupling Structure of Substrate Integrated Waveguide (SIW) for the Application of 140-GHz Bandpass Filter on LTCC. *IEEE Trans Compon., Packag Manufact Technol* (2014) 4(2):316–22. doi:10.1109/TCPMT.2013.2285388
24. Hong J-S, Lancaster MJ. *Microstrip Filters for RF/Microwave Applications*. New York: Wiley (2001). p. 235–61. doi:10.1002/0471221619
25. Ness JB. A Unified Approach to the Design, Measurement, and Tuning of Coupled-Resonator Filters. *IEEE Trans Microwave Theor Techn.* (1998) 46(4): 343–51. doi:10.1109/22.664135

Conflict of Interest: The authors declare that the research was conducted in the absence of any commercial or financial relationships that could be construed as a potential conflict of interest.

Publisher's Note: All claims expressed in this article are solely those of the authors and do not necessarily represent those of their affiliated organizations, or those of the publisher, the editors, and the reviewers. Any product that may be evaluated in this article, or claim that may be made by its manufacturer, is not guaranteed or endorsed by the publisher.

frontiers in Physics

ORIGINAL RESEARCH
published: 03 January 2022
doi: 10.3389/fphy.2021.811681

Seizure Prediction With HIVE-CODAs: The Hierarchical Vote Collective of Domain Adaptation Methods

*Peizhen Peng**

Key Laboratory of Measurement and Control of CSE, Ministry of Education, School of Automation, Southeast University, Nanjing, China

Epileptic seizure prediction is one of the most used therapeutic adjuvant strategies for drug-resistant epilepsy. Conventional methods are usually trained and tested on the same patient due to the interindividual variability. However, the challenging problem of the domain shift between different subjects remains unsolved, resulting in low prevalence of clinical application. In this study, a generic model based on the domain adaptation (DA) technique is proposed to alleviate such problems. Ensemble learning is employed by developing a hierarchical vote collective of seven DA modules over multi-modality data, such that the predictive performance is improved by training multiple models. Moreover, to increase the feasibility of its implementation, this study mimics the data distribution of clinical sampling and tests the model under this simulated realistic condition. Based on the performance of seven subnetworks, the applicability of each DA algorithm for seizure prediction is evaluated, which is the first study that provides the assessment. Experimental results on both intracranial and scalp EEG databases demonstrate that this method can reduce the domain gap effectively compared with previous studies.

Keywords: seizure prediction, domain adaptation, ensemble learning, EEG, time series classification

OPEN ACCESS

Edited by:
Kai-Da Xu,
Xi'an Jiaotong University, China

Reviewed by:
Bin Chen,
Yangzhou University, China
Liangyu Ma,
North China Electric Power University, China

***Correspondence:**
Peizhen Peng
zpeng0714@gmail.com

Specialty section:
This article was submitted to Optics and Photonics, a section of the journal Frontiers in Physics

Received: *09 November 2021*
Accepted: *01 December 2021*
Published: *03 January 2022*

Citation:
Peng P (2022) Seizure Prediction With HIVE-CODAs: The Hierarchical Vote Collective of Domain Adaptation Methods. Front. Phys. 9:811681. doi: 10.3389/fphy.2021.811681

1 INTRODUCTION

1.1 Epilepsy Background

Epilepsy is a cerebral anomaly with the transient occurrence of unexpected seizures caused by excessive or hypersynchronous neuronal activities [1]. It is the second most clinically significant neurological disorder, which affects approximately 1.0% of the world's population [2]. The reliable seizure prediction device, which refers to anticipating an upcoming seizure based on continuous electroencephalogram (EEG) signals, is an emerging and important demand for drug-resistant individuals accounting for about 30% of the epileptic [3, 4]. The early warning device could significantly prevent the injury of epileptic coma, or even death.

EEG is a commonly used type of physiological signal that measures the epileptic brain activity, which records rhythmic information induced by coordinated neuronal firing with characteristic periodicity. The first-in-man forecast study was reported in 2013 [5], which offered the convincing proof of the predictability of seizure. Since then, many EEG-based algorithms adopting the data-driven technique have been presented.

1.2 Related Work

Current research studies regarding seizure prediction can be mainly categorized into two streams. The first stream typically follows a binary classification scheme, which assumes that a difference exists between the interictal and preictal stages. The ictal and postictal sequences are discarded during the data processing due to the futility of their contribution to forecast. The second stream is to detect the fluctuation of a specific index during the preictal period, such as the spike rate [6–8], zero-crossing intervals [9], and phase/amplitude locking value [10]. If the observed indicator exceeds the previously set threshold, an early warning would be declared. Owing to the multiplicity of multichannel EEG recordings, the first stream is more widely recognized than the second one. This study also adopts the strategy that distinguishes preictal states from interictal states, which is depicted in **Figure 1**.

Approaches using the binary classification scheme commonly adopt machine learning techniques like support vector machines [11–13], random forests [14], and *k*-nearest neighbor [15]. For the past few years, many deep learning frameworks, including convolutional neural network (CNN) [16–19], 3D CNN [20], long short-term memory (LSTM) network [21–23], and cascades of DNN [24], have been exploited to analyze continuously acquired epileptic EEG signals. However, there are still many promising algorithms to be developed and applied further. Ensemble learning is considered the state-of-the-art solution for many challenging problems?. For instance, several representative approaches, including HIVE-COTE [25], boosting, bagging, and stacking?, have achieved high performance for time series classification. Such methods are appealing because it has stronger generalization ability than a single model by training multiple subnetworks and combining their predictions. For this reason, we attempt to probe into its effectiveness for seizure prediction.

Most recently, various machine learning–based studies have achieved high performance. However, these methods are not yet in widespread use. Most of these research studies only provide patient-specific results, namely, both training and testing sets are collected from one subject. The reason for adopting this strategy is that large interindividual variability is ubiquitous among patients with epilepsy [26–28]. Therefore, an ensemble that contains a number of domain adaptation modules is developed in this study to reduce the impact of epileptic individual variability.

1.3 Significance

Although conventional studies achieve encouraging successes in seizure prediction task, their translation to the application remains challenging, in part due to their limited domain adaptability across different subjects. EEG patterns vary significantly from patient to patient as shown in **Figure 2**, and the issue regarding the model generalization ability remains unsolved. In previous studies, the training and testing sets are from the same patients, which can obtain a very high sensitivity (< 85% on average). Although such trials are important for personalized medicine, they are inconsistent with the clinical scenario in most cases. In other words, conventional models may

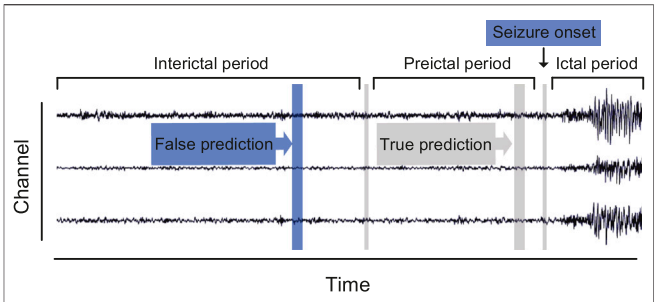

FIGURE 1 | Definition of three brain states in continuous epileptic EEG recordings.

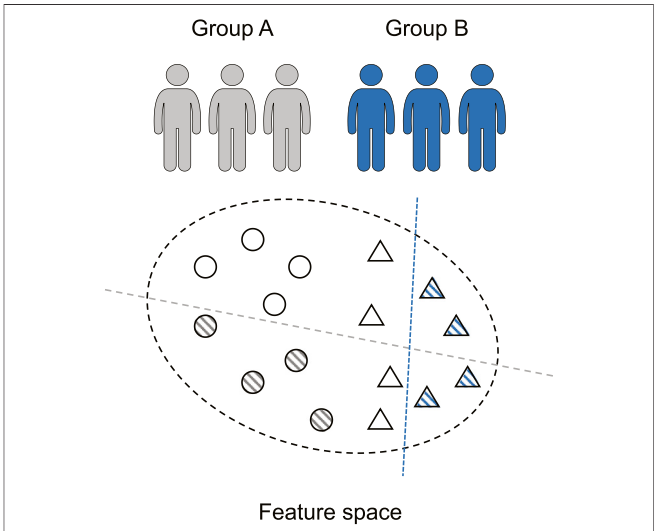

FIGURE 2 | Seizure prediction is a patient-specific problem. The discriminative models (dashed line) of various individuals (circle and triangle) differ significantly.

perform well in one patient but be less effective in another, since the domain gap between different subjects is partly ignored. In practice, the training set is mainly composed of the previous patient data, and only a small amount of user samples can be used for training. The training set consisted of various subjects is the source domain. The "unseen" user is the target domain. In the existing literature, few research studies explore the domain shift issue. Therefore, a general seizure prediction model that is similar to clinical situation remains to explore and perfect further.

To alleviate the low popularization of clinical application and circumvent the impact of interindividual variability, domain adaptation (DA) is introduced for seizure prediction. However, few studies aim at using these techniques in epileptic EEG. In the fields such as image recognition and emotion-related EEG, successful applications of domain adaptation approaches have been reported [29, 30]. There are three main streams of DA algorithms. The first stream exploits adversarial learning to extract invariant information among source and target domains. The second stream extends sample size with data augmentation to access the target domain pattern in advance.

The third stream establishes general features based on specific prior knowledge.

Inspired by the success in other areas, we hope to extend DA to the field of seizure prediction. Since many DA techniques [31–33] have been provided, an ensemble learning–based model, the hierarchical vote collective of DA subnetworks (HIVE-CODAs), is proposed in this study. HIVE-CODAs combine the advantages of various DA methods. Besides, it can evaluate the applicability of each DA algorithm. In general, the main contributions of this study are summarized as follows:

- A generic model, HIVE-CODA, is proposed to tackle the DA problem for seizure prediction. It is the first attempt to reduce the domain disparity between different patients and to test the model under simulated clinical sampling conditions.
- Ensemble learning is introduced into this model by developing a hierarchical vote collective. Such a framework can improve the predictive performance and generalization ability due to the combination of multiple DA subnetworks.
- This study is the first study to evaluate the applicability of different DA algorithms for seizure prediction, which is crucial for follow-up studies.

Based on DA techniques and ensemble learning, the proposed model provides an above par disturbance rejection property, making the model more robust and practical for clinical application. Experiments on two public databases, the Freiburg Hospital EEG database and the CHB-MIT EEG database [34, 35], are conducted for model evaluation. Results indicate that HIVE-CODA achieves better domain adaptability compared with other state-of-the-art baselines.

2 DATA ACQUISITION AND PREPROCESSING

2.1 Patients

Two public EEG datasets, the Freiburg Hospital Intracranial EEG database [34] and the CHB-MIT scalp EEG database [35], are adopted to evaluate the generalization capability of HIVE-CODAs. The Freiburg Hospital EEG database includes time series of 87 seizures from 21 people with medically intractable focal epilepsy, ranging from 10 to 50 years old (8 male and 13 female patients). EEG signals are recorded invasively with six electrodes (3 near the epileptic focus and the other three distal to the epileptogenic zone). The sampling rate for all patients is 256 Hz (data of Patient No. 12 are sampled at 512 Hz but are down-sampled to 256 Hz).

The CHB-MIT database consists of scalp EEG sequences of 22 epileptic subjects, including five male patients ranging from 3 to 22 years and 17 female patients from 1.5 to 19 years. The EEG signals are recorded at a 256 Hz sampling rate with 16-bit analog-to-digital converters. Most samples are acquired from surface electrodes of 23 channels following the 10–20 standard system for electrodes placement. Each patient has a subfolder that contains 9 to 42 recordings.

2.2 Data Selection and Labeling

Power line noise removal is implemented to denoise the data. We discarded the frequency bands of 47–53 and 97–103 Hz in the intracranial EEG set and the frequency bands of 57–63 and 117–123 Hz in the scalp EEG set. It is because noise commonly appears at 50 Hz for the Freiburg database and 60 Hz for the CHB-MIT database. Moreover, a subject selection is performed. Only patients with at least two seizures but fewer than 15 seizures per day are used for prediction, since less than two seizures are not enough to support training and more than 15 seizures make the forecast purportless. The chosen subjects are listed in **Tables 1**, **2**.

A prerequisite for seizure prediction is the reliable distinction between preictal and interictal samples. We set 30 min before seizure onset as the seizure prediction horizon (SPH), which follows empirical evidence of comparison tests as applied multiple preictal lengths, and the seizure occurrence period is set to 0. A seizure should occur within 30 min after the predictor returns a positive. The raw EEG recordings are then divided into continuous, non-overlapping fragments by a 5-s time window. The sample number for each subject is sufficient (>7,200) to support training. Besides, we remarked that the amount of interictal samples is much larger than preictal samples. To remedy the sample imbalance, a random subsample on the interictal signals is performed to make an equal quantity of preictal and interictal training samples.

3 METHODS

To learn the domain-invariant representation, we proposed a generic seizure prediction model: the hierarchical vote collective of DA subnetworks (HIVE-CODAs). HIVE-CODA is an ensemble that combines 7 DA modules over multi-modality data. Each subnetwork is assigned a weight *via* the probabilistic voting scheme to equilibrate its value. By analyzing the most contributive DA component and its feature space, we provided a preliminary conclusion about the generalized information during the preictal period among various individuals.

3.1 Clinical Situation Simulation

Conventional approaches only provide the patient-specific results. Such frameworks may obtain high precision but are not consistent with the signal recording situation in real life. It is difficult to collect a large number of long-term EEG samples from one specific patient during clinical treatment, such that the sample size is unable to support the training process. Therefore, we considered using DA technology to apply data from other subjects to predictor training for the particular subject.

The training and testing strategy is depicted in **Figure 3**. The training and validation sets consist of existing patient data and one seizure of the target subject, while the remaining target seizures served as the testing set. The selection of seizure for

TABLE 1 | Details of the Freiburg Hospital test set.

Patient	Gender	Age (years)	Seizure type	No. of seizures
Pt 1	F	15	SP	4
Pt 2	M	38	SP, CP, GTC	3
Pt 3	M	14	SP, CP	5
Pt 4-	F	26	SP, CP, GTC	5
Pt 5	F	16	SP, CP, GTC	5
Pt 6	F	31	CP, GTC	3
Pt 8	F	32	SP, CP	2
Pt 9	M	44	CP, GTC	4
Pt 10	M	47	SP, CP, GTC	5
Pt 11	F	10	SP, CP, GTC	4
Pt 12	F	42	SP, CP, GTC	3
Pt 13	F	22	SP, CP, GTC	2
Pt 14	F	41	CP, GTC	4
Pt 15	M	31	SP, CP, GTC	4
Pt 16	F	50	SP, CP, GTC	5
Pt 17	M	28	SP, CP, GTC	5
Pt 18	F	25	SP, CP	5
Pt 19	F	28	SP, CP, GTC	4
Pt 20	M	33	SP, CP, GTC	5
Pt 21	M	13	SP, CP	5

F, female; M, male; SP, simple partial; CP, complex partial; and GTC, generalized tonic-clonic.

TABLE 2 | Details of the CHB-MIT test set.

Patient	Gender	Age (years)	Seizure type	No. of seizures
Pt 1	F	11	SP, CP	7
Pt 2	M	11	SP, CP, GTC	3
Pt 3	F	14	SP, CP	6
Pt 5	F	7	CP, GTC	5
Pt 6	F	2	CP, GTC	4
Pt 7	F	15	SP, CP, GTC	3
Pt 8	M	4	SP, CP, GTC	5
Pt 9	F	10	CP, GTC	4
Pt 10	M	3	SP, CP, GTC	6
Pt 13	F	3	SP, CP, GTC	5
Pt 14	F	9	CP, GTC	5
Pt 17	F	12	SP, CP, GTC	3
Pt 18	F	18	SP, CP	6
Pt 19	F	19	SP, CP, GTC	3
Pt 20	F	6	SP, CP, GTC	5
Pt 21	F	13	SP, CP	4

F, female; M, male; SP, simple partial; CP, complex partial; and GTC, generalized tonic-clonic.

training refers to the idea of the leave-one-out cross-validation (LOOCV) approach [36]. Moreover, the combined data are partitioned into five folds, and 80% of the samples are assigned to the training set, while the remaining 20% is named for the validation set to prevent overfitting.

3.2 Modular Hierarchical Structure

HIVE-CODAs include seven constituent modules: subject-invariant domain adaption (SIDA) [37], conditional deep convolutional generative adversarial networks (C-DCGANs) [38], plug-and-play domain adaptation (PPDA) [39], maximum independence domain adaptation (MIDA) [40], maximum mean discrepancy–adversarial autoencoders (MMD-AAEs) [41], model-agnostic learning of semantic features (MASF) [42], and cone manifold domain adaptation (CMDA) [43]. The modular hierarchical structure is depicted in **Figure 4**.

Since few domain adaptation techniques of epileptic EEG have been reported, we applied seven state-of-the-art approaches from the related fields to constitute the subnetworks of HIVE-CODAs. Several modules require images as inputs, instead of time series, such that we generate the spectrograms from EEG segments using the short-time Fourier transform (STFT) [44]. The raw EEG recordings are translated into two-dimensional matrices composed of frequency and time axes. Then the EEG fragments and their spectrograms will be sent forward to the corresponding modules depending on their modalities.

3.3 Modules Based on Adversarial Learning

1) MMD-AAE: We developed the MMD-AAE module referring to the study mentioned in reference [41], which aims at assessing the effectiveness of maximum mean discrepancy (MMD) measure and adversarial autoencoders (AAEs). An MMD-based regularization term is proposed to align the distributions among various subjects. The AAE architecture is applied to learn the latent codes that are universal to all domains. The sharable information is captured by matching the aligned distribution to an arbitrary prior distribution. Thus the MMD-AAE may circumvent the overfitting to source data.

2) SIDA: We also estimated the performance of SIDA on epileptic EEG, which combines power spectral density (PSD) features and adversarial learning [37]. SIDA focuses on the extraction of the invariant representations among different domains. The sharable information is jointly learned with the task loss $\mathcal{L}_{task}$ and subject confusion loss $\mathcal{L}_{subj}$. The training procedure adopts the adversarial strategy, which is implemented with a gradient reversal layer. Suppose that there are N source samples $\{x_i\}_{i=1}^{N}$, the process can be explicitly written as follows:

$$\begin{aligned}\mathcal{L} = &\frac{1}{N}\sum_{i=1}^{N}\mathcal{L}_{task}\left(h\left(f\left(x_i;\theta\right);\gamma\right),c_i\right)\\ &-\lambda\frac{1}{N}\sum_{i=1}^{N}\mathcal{L}_{subj}\left(g\left(f\left(x_i;\theta\right);\phi\right),s_i\right),\end{aligned} \tag{1}$$

$$\hat{\theta},\hat{\gamma} = \arg\min_{\theta,\gamma}\left(\mathcal{L}\left(\theta,\gamma,\hat{\phi}\right)\right), \tag{2}$$

$$\hat{\phi} = \arg\max_{\phi}\left(\mathcal{L}\left(\hat{\theta},\hat{\gamma},\phi\right)\right), \tag{3}$$

where θ, γ, ϕ represent the network parameters and $\hat{\theta},\hat{\gamma},\hat{\phi}$ are their updated forms. λ is the trade-off positive parameter. $h(\cdot)$ and $g(\cdot)$ are the classification task and subject discrimination outputs. c_i, s_i denote the corresponding labels for $\mathcal{L}_{task}$ and $\mathcal{L}_{subj}$, respectively. Note that, a specific feature extraction component is assembled in HIVE-CODAs since the inputs of SIDA are PSD features in accordance with the study mentioned in reference [37].

3.4 Modules Based on Data Augmentation

1) C-DCGANs: By introducing C-DCGANs [38], we tested the feasibility of using data augmentation and convolutional neural networks (CNN) to remedy the domain discrepancy. The main

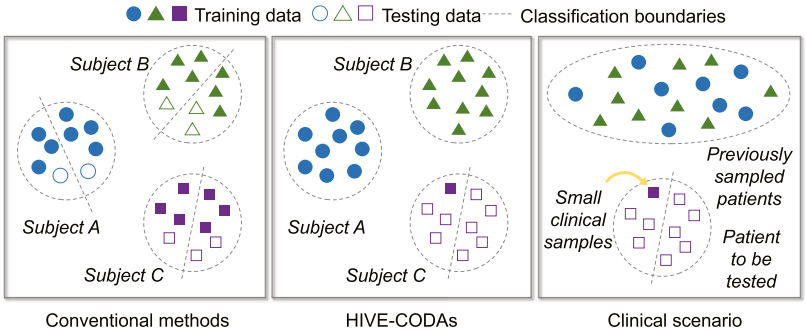

FIGURE 3 | Illustration of clinical situation simulation.

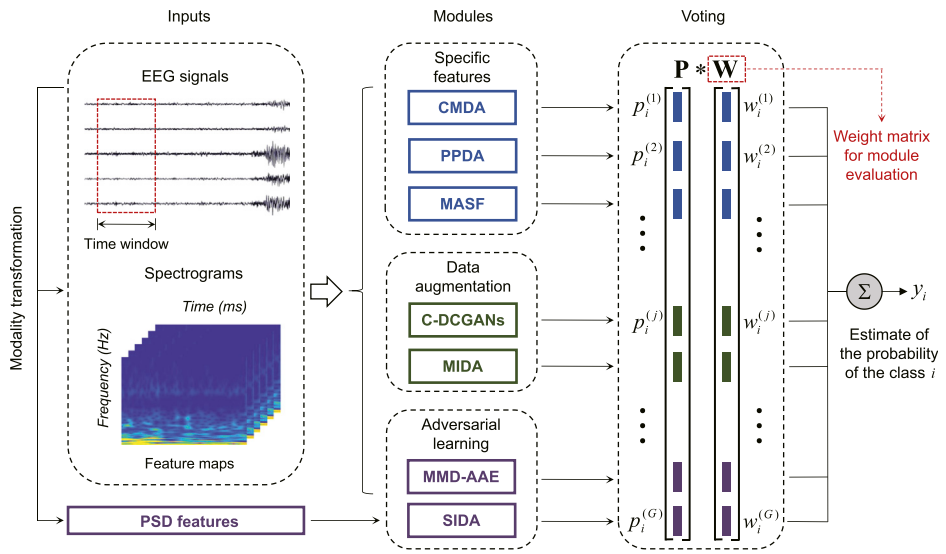

FIGURE 4 | Block diagram of HIVE-CODAs: the raw EEG recordings convert into multi-modality data to meet the input requirement of the corresponding module. The *j*th DA module outputs the voting vector $p_i^{(j)}$ to claim its decision. Then the voting vectors will be selected adaptively with the weight matrices to produce the probability of class *i*. Meanwhile, the weight layer will be exploited for DA subnetwork assessment.

idea of C-DCGANs is increasing generalization capability *via* artificial EEG data generation. A generative adversarial network (GAN) is exploited to expand the training set, and an end-to-end CNN is employed as the classifier. We remarked that C-DCGANs also involve the adversarial learning due to the application of GAN. However, the generation function of GAN is highlighted in HIVE-CODAs, instead of the minmax optimization, such that we placed emphasis on the assessment of data augmentation.

2) MIDA: MIDA subnetwork is developed to measure the importance of background information and feature augmentation. In MIDA framework, an inner product space is established, where feature vectors are maximally independent in the sense of a Hilbert–Schmidt independence criterion (HSIC) [40]. The feature augmentation is performed *via* generating latent representations based on the background knowledge like acquisition time. The original feature vectors are expanded by concatenating with the produced features. According to the study mentioned in reference [40], we exploited the domain label (which domain a sample belongs) as the background information since no device label and the acquisition time is provided in the epileptic EEG database.

3.5 Modules Based on Specific Features

1) CMDA: The CMDA module is adopted to evaluate the applicability of manifold on epileptic EEG. Referring to the study menitioned in reference [43], the latent feature space among various domains is regularized by modeling sharable information on the Riemannian cone manifold. Specifically, covariance matrices P of EEG segments are computed to constitute the manifold $\mathcal{M}$. The CMDS module leverages the global Riemannian mean $\hat{\boldsymbol{P}}$ and the local Riemannian mean $\bar{\boldsymbol{P}}^{(k)}$ to describe the cross-domain center and the centroid of the set $\{\boldsymbol{P}^{(k)} \mid \boldsymbol{P}^{(k)} \in \mathcal{M}\}$ for the kth-domain (cite). By using the parallel transport approach, the projections of $\{\boldsymbol{P}^{(k)}\}$ on the tangent space $\mathcal{T}_{\hat{\boldsymbol{P}}}\mathcal{M}$ can describe the invariant features among source domains as follows:

TABLE 3 | Results compared with conventional methods on the Freiburg Hospital database.

Source	Target	CNN		LSTM		HIVE-CODAs	
		S_n	FPR (/h)	S_n	FPR (/h)	S_n	FPR (/h)
S.C.	Pt 1	0.73	0.24	0.72	0.23	0.83	0.11
S.C.	Pt 2	0.58	0.31	0.66	0.30	0.85	0.09
S.C.	Pt 3	0.67	0.26	0.67	0.25	0.85	0.13
S.C.	Pt 4	0.67	0.27	0.71	0.16	0.84	0.12
S.C.	Pt 5	0.48	0.40	0.45	0.32	0.73	0.18
S.C.	Pt 6	0.75	0.27	0.58	0.38	0.86	0.11
S.C.*	Pt 8	0.55	0.34	0.53	0.29	0.66	0.32
S.C.	Pt 9	0.65	0.19	0.75	0.16	0.83	0.15
S.C.	Pt 10	0.51	0.37	0.58	0.26	0.79	0.24
S.C.	Pt 11	0.69	0.36	0.54	**0.21**	0.87	**0.22**
S.C.	Pt 12	0.66	0.18	0.65	0.24	0.84	0.17
S.C.*	Pt 13	0.56	0.31	0.52	0.23	0.68	0.27
S.C.	Pt 14	0.47	0.48	0.57	0.29	0.76	0.23
S.C.	Pt 15	0.66	0.19	0.70	0.17	0.88	0.12
S.C.	Pt 16	0.53	0.37	0.44	0.46	0.79	0.19
S.C.	Pt 17	**0.63**	0.36	0.42	0.41	**0.63**	0.28
S.C.	Pt 18	0.72	**0.18**	0.73	**0.20**	0.83	**0.20**
S.C.	Pt 19	0.44	**0.29**	0.47	**0.33**	0.75	0.14
S.C.	Pt 20	0.43	0.37	0.46	0.33	0.74	0.26
S.C.	Pt 21	0.64	0.32	0.50	0.28	0.84	0.12
Avg.		0.60	0.31	0.56	0.27	0.80	0.18

S.C., simulated clinical samples; S_n, sensitivity; FPR, false prediction rate; and Avg., average result. Note that S.C. uses NO samples of the predictor user.*
The bold values denote outliers.

TABLE 4 | Results compared with conventional methods on the CHB-MIT database.

Source	Target	CNN		LSTM		HIVE-CODAs	
		S_n	FPR (/h)	S_n	FPR (/h)	S_n	FPR (/h)
S.C.	Pt 1	0.57	0.36	0.55	0.28	0.72	0.16
S.C.	Pt 2	0.48	0.39	0.42	0.27	0.65	0.22
S.C.	Pt 3	0.64	0.30	0.58	0.32	0.75	0.27
S.C.	Pt 5	0.54	0.42	0.45	0.41	0.76	0.23
S.C.	Pt 6	0.66	0.31	0.62	0.32	0.72	0.15
S.C.	Pt 7	0.65	**0.25**	0.55	**0.25**	0.83	**0.28**
S.C.	Pt 8	0.64	0.28	0.57	0.20	0.74	0.20
S.C.	Pt 9	0.48	0.35	0.45	**0.26**	0.63	**0.31**
S.C.	Pt 10	0.47	0.32	0.51	**0.24**	0.62	**0.34**
S.C.	Pt 13	0.55	**0.22**	0.50	**0.23**	0.73	**0.26**
S.C.	Pt 14	0.55	0.42	0.44	**0.32**	0.72	**0.35**
S.C.	Pt 17	0.47	0.4	0.42	0.42	0.62	0.28
S.C.	Pt 18	0.58	0.32	0.45	0.34	0.73	0.29
S.C.	Pt 19	0.59	0.22	0.53	0.21	0.79	0.17
S.C.	Pt 20	0.60	0.25	0.57	0.27	0.77	0.22
S.C.	Pt 21	0.62	0.28	0.62	0.27	0.77	0.15
Avg.		0.53	0.32	0.51	0.29	0.72	0.24

S.C., simulated clinical samples; S_n, sensitivity; FPR, false prediction rate; and Avg., average result.
The bold values denote outliers.

$$\hat{\boldsymbol{S}}^{(k)} = \Gamma_{\bar{\boldsymbol{P}}^{(k)} \to \hat{\boldsymbol{P}}}\left(\boldsymbol{S}^{(k)}\right), \ \forall k, \tag{4}$$

$$\boldsymbol{S}^{(k)} = \mathrm{Log}_{\bar{\boldsymbol{P}}^{(k)}}\left(\boldsymbol{P}^{(k)}\right), \tag{5}$$

where $\hat{\boldsymbol{S}}^{(k)}$ denotes the generalized features, $\Gamma_{B \to A}(\cdot)$ represents the parallel transport from B to A, and $\boldsymbol{S}^{(k)}$ represents the projection of $\boldsymbol{P}^{(k)}$ on the tangent space $\mathcal{T}_{\bar{\boldsymbol{P}}^{(k)}}\mathcal{M}$ with the logarithm map (cite). In general, each domain feature is parallelly transported from $\bar{\boldsymbol{P}}^{(k)}$ to the global centroid $\hat{\boldsymbol{P}}$, and the transported point $\hat{\boldsymbol{S}}^{(k)}$ is embedded in the $\langle \cdot, \cdot \rangle_{\hat{\boldsymbol{P}}}$ inner product space to make the generalized features describable in the Euclidean space.

2) PPDA: The long short-term memory (LSTM) architecture and a peculiar learning strategy are evaluated by adding the PPDA module. PPDA divides the latent features into private portions specific to each subject and generalized components among all subjects. To leverage both the universal and private feature vectors, PPDA develops a learning procedure including the training phase, calibration phase, and test phase. Specially, the LSTM layer is adopted for encoding and decoding.

3) MASF: To assess the applicability of meta-learning and semantic features, the MASF module is employed in HIVE-CODAs. According to the study mentioned in reference [42], a model-agnostic learning paradigm is exploited to minimize the domain gap *via* using a global class alignment loss $\mathcal{L}_{global}$ and a local sample clustering loss $\mathcal{L}_{local}$. The knowledge about interclass relationships and the domain-independent class-specific cohesion/separation is captured by $\mathcal{L}_{global}$ and $\mathcal{L}_{local}$, respectively, which is given as follows:

$$(\psi, \theta) \leftarrow (\psi, \theta) - \eta \nabla_{\psi,\theta}(\mathcal{L}_{task} + \mathcal{L}_{meta}), \tag{6}$$

$$\mathcal{L}_{meta} \leftarrow \beta_1 \mathcal{L}_{global} + \beta_2 \mathcal{L}_{local}, \tag{7}$$

where ψ, θ are the network parameters, η is the learning rate, and β_1, β_2 denote the weighting coefficients. $\mathcal{L}_{task}$ represents the loss function of the predictive task. By introducing both global and local information, the semantic structure regarding the EEG feature space is regularized explicitly.

3.6 Weighted Voting Scheme

To evaluate the contribution of each subnetwork, a weighted voting structure is introduced at the end of the network. We assumed that there are G modules for the classification with C classes. For an arbitrary class $y = i$, we denote by $w_i^{(j)}$ the weight assigned to the jth module, where $i \in [1, \ldots, C]$ and $j \in [1, \ldots, G]$. Then the collective probability p_i for the ith class is the normalized weighted sum over modules:

$$p_i = \frac{\sum_{j=1}^{G} w_i^{(j)} p_i^{(j)}}{\sum_{i=1}^{C} \sum_{j=1}^{G} w_i^{(j)} p_i^{(j)}}. \tag{8}$$

The prediction result $\hat{y}$ can be given as follows:

$$\hat{y} = \arg\max_i \ p_i. \tag{9}$$

The applicability of each algorithm on epileptic EEG could be estimated *via* observing its weight unit. Besides, a more balanced and intuitive collective could be created as the subnetworks are trained adaptively.

TABLE 5 | Results compared with DA methods on the Freiburg Hospital database.

Source	Target	MIDA	MASF	PPDA	MMD-AAE	SAN	C-DCGANs	SIDA	CMDA	HIVE-CODAs
S.C.	Pt 1	0.59	0.63	0.74	0.78	0.78	0.80	0.81	0.80	0.86
S.C.	Pt 2	0.56	0.62	0.71	0.77	0.78	0.77	0.83	0.82	0.86
S.C.	Pt 3	0.55	0.62	0.67	0.74	0.75	0.80	0.77	0.83	0.84
S.C.	Pt 4	0.52	0.57	0.56	0.57	0.61	0.62	0.62	0.64	0.75
S.C.	Pt 5	0.60	0.63	0.72	0.79	0.79	0.80	0.80	0.82	0.85
S.C.	Pt 6	0.54	0.53	0.55	0.65	0.68	0.66	0.73	0.74	0.79
S.C.*	Pt 8	0.48	0.51	0.55	0.54	0.56	0.57	0.57	0.61	0.68
S.C.	Pt 9	0.50	0.55	0.61	0.69	0.68	0.70	0.70	0.73	0.80
S.C.	Pt 10	0.53	0.63	0.60	0.69	0.68	0.69	0.70	0.74	0.77
S.C.	Pt 11	0.62	0.65	0.70	0.77	0.81	0.73	0.83	0.82	0.87
S.C.	Pt 12	0.63	0.63	0.70	0.68	0.71	0.75	0.78	0.77	0.85
S.C.*	Pt 13	0.46	0.52	0.60	0.64	0.64	0.68	0.67	0.68	0.74
S.C.	Pt 14	0.48	0.55	0.63	0.65	0.66	0.69	0.68	0.71	0.78
S.C.	Pt 15	0.59	0.69	0.69	0.73	0.75	0.78	0.77	0.82	0.86
S.C.	Pt 16	0.45	0.48	0.58	0.62	0.67	0.69	0.67	0.70	0.76
S.C.	Pt 17	0.46	0.48	0.52	0.54	0.54	0.55	0.55	0.56	0.68
S.C.	Pt 18	0.61	0.64	0.68	0.75	0.77	0.79	0.78	0.81	0.86
S.C.	Pt 19	0.46	0.47	0.53	0.54	0.53	0.55	0.58	0.60	0.69
S.C.	Pt 20	0.50	0.55	0.60	0.67	0.69	0.68	0.71	0.70	0.78
S.C.	Pt 21	0.52	0.58	0.60	0.62	0.66	0.55	0.69	0.72	0.83
Avg.		0.53	0.58	0.63	0.64	0.65	0.69	0.71	0.73	0.80

S.C., simulated clinical samples. Note that S.C. uses NO samples of the predictor user.*

4 RESULTS AND DISCUSSION

In this section, the comparison results and weight matrix are provided to verify the generalization ability and evaluate the DA algorithms. HIVE-CODA is assessed on both intracranial and scalp EEGs. We adopted three common measures for evaluation: sensitivity, false alarm rate per hour (FPR), and area under the receiver operating characteristic curve (AUC).

4.1 Generalization Ability Analysis

The comparison experiments are conducted to demonstrate the advantages of HIVE-CODAs over other conventional methods. Many time/frequency domain–based approaches have been applied to predict upcoming seizures. Two classic deep neural networks, CNN and LSTM, are selected to assess the generalization ability of our method, which have achieved success in patient-specific forecast. We also attempted to find a generic algorithm across different subjects for comparison. However, little existing research considers the similarity of data acquisition to clinical situation and uses plenty of "unseen" patient's samples for training. The implementation details of CNN and LSTM refer to references [17] and [22], and the experimental results are listed in **Tables 3**, **4**.

The experiment regarding the intracranial EEG is performed based on the widely used Freiburg Hospital database. **Table 3** illustrates that HIVE-CODAs achieve a sensitivity of 80% and an FPR of 0.18/h on average, which outperforms other forecast models. For the outlier-like Pt 17, HIVE-CODAs do not produce the desired effectiveness, which might be caused by a larger domain gap existing in the sample space.

Evidently, performances of all these prediction approaches show a significant decline compared with the patient-specific results in their literature. This phenomenon is reasonable since the training and testing samples are collected from one same subject in prior studies, which consider little about the generalization ability. Conversely, our method is implemented based on the existing database and small amount of "unseen" patient's data, which is more coincident with the real clinical situations. Though the precision is not relative high, the model performance is sufficient for the daily needs of patients, as it approximates to the first-in-man trial [5].

In terms of scalp EEG, the experiment is conducted based on the public CHB-MIT database, produced by the Massachusetts Institute of Technology. As shown in **Table 4**, HIVE-CODAs achieve a sensitivity of 72% and an FPR of 0.24/h on average. Since the conventional algorithms consider little about the domain shift among different patients, HIVE-CODAs exhibit obvious advantages over other prediction models. Still, for several outliers like Pt 2, Pt 9, Pt 10, and Pt 17, the sensitivity of our approach is slightly higher than the lower bound of a random binary classifier. HIVE-CODA is a variation over deep learning models. As such, it carries with it the uncertainties associated to deep neural networks, in particular a lack of formal convergence guarantees.

Furthermore, experiments compared with DA algorithms are conducted. Results of AUC value are listed in **Tables 5**, **6**. For the Freiburg Hospital database, results indicate that HIVE-CODAs achieve higher generalization ability than the conventional algorithms. It also testifies to the application potential of integrated DA modules on processing epileptic EEG. To be specific, the interindividual variability could be alleviated, and the existing forecast systems could be transferred to the clinic due to the emerging technologies in DA.

For the CHB-MIT database, the conventional studies show a lower performance in a clear margin compared with their patient-specific results, which is consistent with the experiment

TABLE 6 | Results compared with DA methods on the CHB-MIT database.

Source	Target	MIDA	MASF	PPDA	MMD-AAE	SAN	C-DCGANs	SIDA	CMDA	HIVE-CODAs
S.C.	Pt 1	0.60	0.64	0.65	0.73	0.75	0.77	0.77	0.80	0.86
S.C.	Pt 2	0.48	0.52	0.46	0.64	0.66	0.70	0.69	0.82	0.86
S.C.	Pt 3	0.54	0.53	0.59	0.65	0.67	0.68	0.71	0.83	0.84
S.C.	Pt 5	0.52	0.56	0.62	0.70	0.75	0.74	0.74	0.82	0.85
S.C.	Pt 6	0.52	0.55	0.61	0.66	0.74	0.75	0.73	0.74	0.79
S.C.	Pt 7	0.59	0.61	0.64	0.70	0.72	0.75	0.76	0.74	0.79
S.C.	Pt 8	0.51	0.58	0.61	0.67	0.70	0.71	0.71	0.61	0.68
S.C.	Pt 9	0.47	0.49	0.52	0.58	0.60	0.61	0.64	0.73	0.80
S.C.	Pt 10	0.46	0.50	0.49	0.51	0.55	0.54	0.60	0.74	0.77
S.C.	Pt 13	0.49	0.53	0.46	0.58	0.62	0.63	0.62	0.68	0.74
S.C.	Pt 14	0.47	0.53	0.55	0.63	0.66	0.68	0.70	0.71	0.78
S.C.	Pt 17	0.51	0.54	0.52	0.61	0.63	0.62	0.64	0.56	0.68
S.C.	Pt 18	0.50	0.51	0.53	0.58	0.61	0.62	0.66	0.81	0.86
S.C.	Pt 19	0.51	0.53	0.56	0.63	0.66	0.66	0.69	0.60	0.69
S.C.	Pt 20	0.55	0.56	0.59	0.65	0.68	0.72	0.74	0.70	0.78
S.C.	Pt 21	0.51	0.53	0.60	0.66	0.71	0.73	0.77	0.72	0.83
Avg.		0.51	0.54	0.56	0.64	0.66	0.67	0.69	0.70	0.74

S.C., simulated clinical samples.

conducted on intracranial EEG. Moreover, all these model performances drop to a varying degree compared with the precisions on the Freiburg test set. It might be caused by the advantages of ensemble learning in analyzing low spatial resolution recordings, namely, the scalp EEG signals. In other words, intracranial EEG recordings have the high spatial resolution and SNR, and the artifacts are typically seen in scalp EEG [46, 47]. This result also illustrates that HIVE-CODAs have superiority for processing complex time series due to the diverse inner pattern of the collective structure.

4.2 Module Performance Analysis

As few studies evaluate the applicability of different DA algorithms for seizure prediction, this study provides an analysis based on the adaptively trained weight matrices. HIVE-CODAs introduce several successful machine learning models from related fields and assess their performance. The subnetworks are conducted *via* a statistical analysis of the weighted voting layer. The weight distributions are presented in **Figure 5**. The greater the normalized weight, the greater the contribution of the corresponding DA module. DA methods with high contributions are considered to have larger potential. This study also tests the predictive precision of each module running alone (with the other modules' weights reset to 0). The results of AUC values are illustrated in **Figure 6**. A detailed discussion regarding these DA techniques is provided as follows.

1) CMDA: CMDA relies on Riemannian manifold–based features to capture the characteristic scale of the neuronal events, which was proposed for motor imagery. As shown in **Figure 5**, CMDA surpasses the other approaches on both intracranial and scalp EEG datasets. We conjectured that the inner pattern of EEG sequences may obey a compact distribution in the embedding space, such that the manifold-based methods that capture continuous subspace might be applicable to such task. The experimental result indicates that the analytic Riemannian manifold can potentially be used to develop a robust seizure predictor.

2) SIDA: The SIDA module is an adversarial neural network from the area of emotion recognition. It uses EEG spectra as input to learn a new representation, minimizing loss of emotion recognition and subject confusion. As we can see, SIDA makes relatively larger contribution compared with other modules. It might be due to the combination of CNN and generative adversarial network (GAN), which have been exploited to extract invariant latent features successfully. The weight unit of SIDA module may suggest the potential effect of adversarial learning on generalization ability, since SIDA exploited the architecture of GAN. However, this conjecture needs to be further verified for the SIDA module as it adopts the power spectral density (PSD) features as inputs.

3) C-DCGANs: C-DCGANs use conditional GANs to generate EEG artificially, which is developed for the detection of subject's movement intention (MI). We noticed that the performance of data augmentation–based module is not desired compared with the specific features and adversarial learning–based subnetworks. The degradation might be caused by the limitation of EEG data augmentation. The fake data usually involve more artifacts [48] that may contaminate EEG data. Still, C-DCGANs provide a decent accuracy, which suggests that data augmentation still has potential in developing a generic seizure forecast model.

4) MMD-AAE: By matching the aggregated posterior with a prior distribution, the MMD-AAE module extracts the cross-domain features with adversarial learning. This scheme was originally used for image recognition. On both intracranial and scalp EEG datasets, MMD-AAE outperforms MIDA, MASFF, and PPDA modules and exhibits a slight decrease compared with the C-DCGAN module. Due to the above par performance of MMD-AAE, the conjecture in 2) about the superiority of adversarial learning is verified to some extent. This superiority may derive from the variational inference process of MMD-AAE, which alleviates the overfitting to the source domains effectively.

5) PPDA: PPDA is a technology applied to EEG-based emotion recognition. It uses LSTM-based encoder to

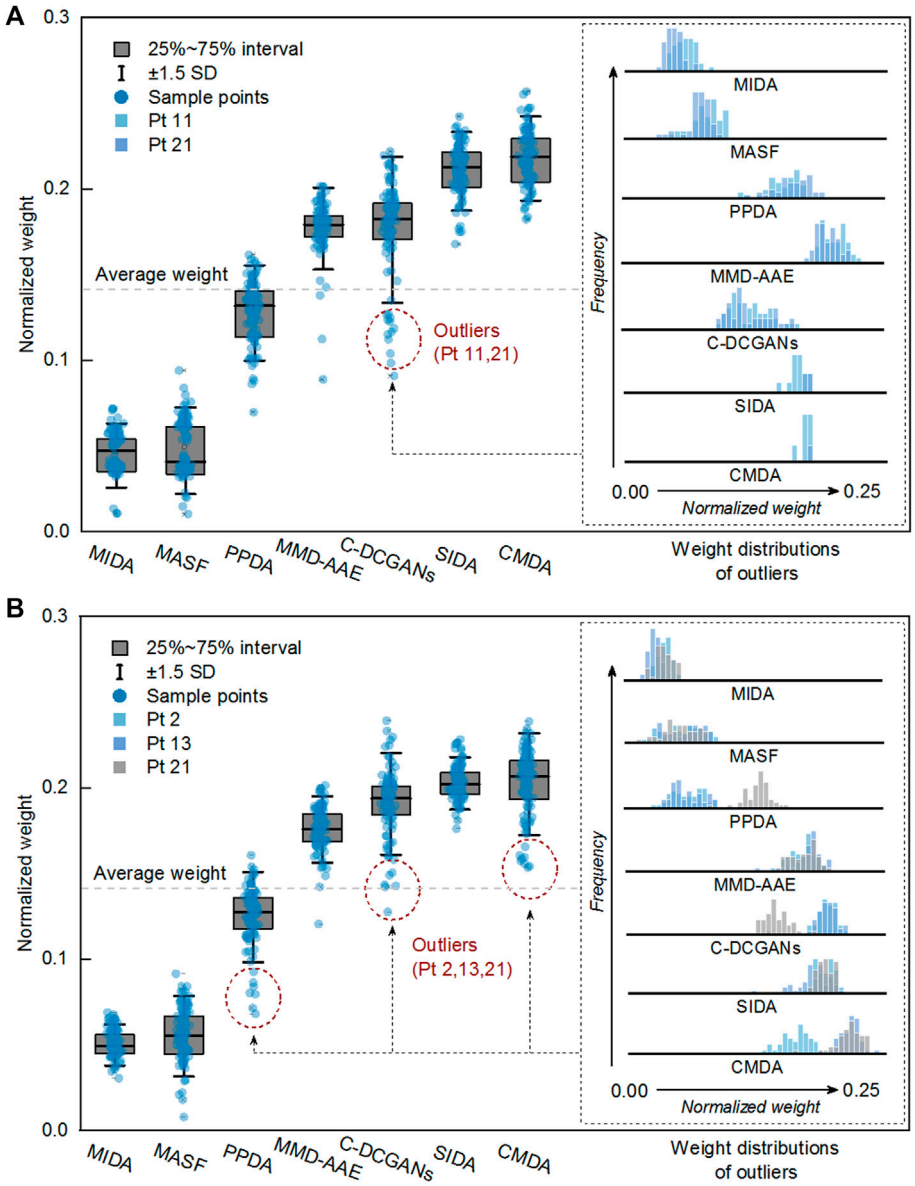

FIGURE 5 | Module performance analysis for the Freiburg Hospital **(A)** and CHB-MIT **(B)** database. It is calculated based on the learned weight vector of each DA subnetwork.

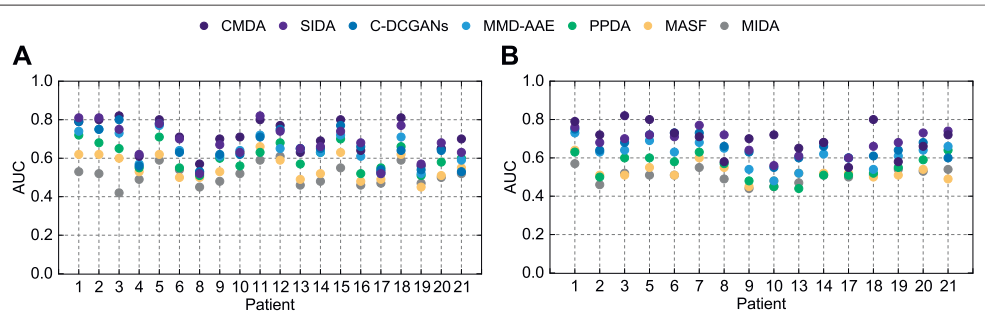

FIGURE 6 | AUC of different modules on the Freiburg Hospital test set **(A)** and the CHB-MIT test set **(B)**.

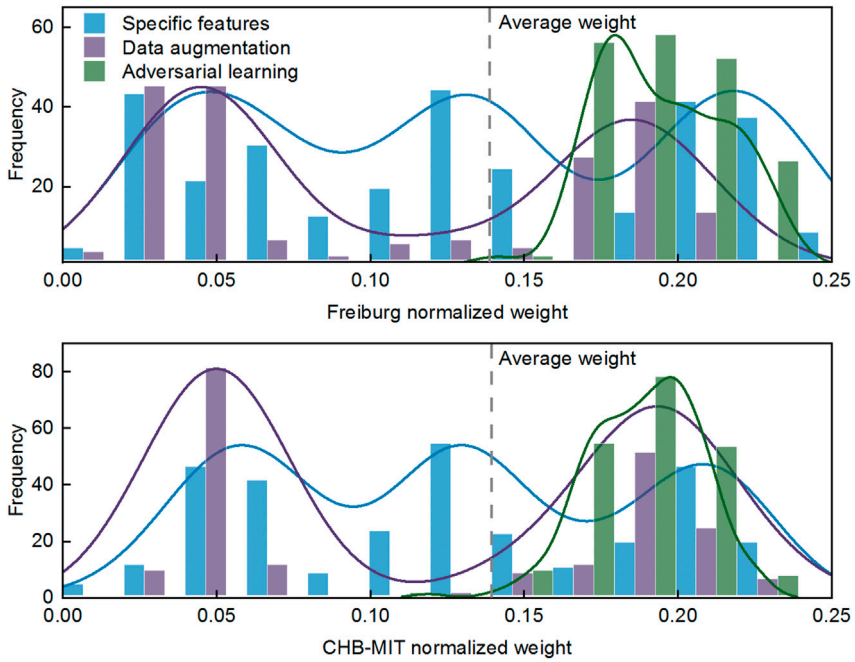

FIGURE 7 | Distribution of weight matrices of three types of DA algorithms.

decompose the features into general characteristics applicable to all individuals and personalized characteristics. Dividing the raw EEG data into subject-specific information and generalized information is a commonly-adopted strategy for domain adaptation. However, for seizure prediction, PPDA displays subpar performance, which we did not expect. Feature decomposition and the adoption of LSTM seem reasonable in these tasks. However, due to the few reports of relevant models, it cannot be absolutely determined that the decomposed features and LSTM are not suitable for epileptic signals.

6) MASF: MASF exploits semantic features and gradient-based meta-learning to establish a model-agnostic learning paradigm. In the field of image processing, successful application of MASF has been reported. Notably, the performance of the semantic feature–based method is unsatisfactory. We conjectured that the discriminant hyperplane in the feature space may be too complex to be adapted by the explicit semantic features. Moreover, the limitation of the initial neural architecture for meta-learning might also be a constraint of the search space.

7) MIDA: MIDA is originally applied in the emotion recognition field. The purpose of this model is to reduce differences in domain distributions by learning a subspace with maximum independence. **Figure 5** indicates that all the DA methods can outperform the MIDA module. This result was expected, given the limited background information on epileptic data. Obviously, the background-specific features are not valid characteristics.

Based on these results, we observed that adversarial learning and manifolds may achieve good performance in epilepsy prediction. In addition, CNN and PSD features may also have the potential to process epileptic signals. In the domain generalization field, CNN has gradually become one of the most popular algorithms. This also further echoes the conjecture about CNN in this experiment. Note that the module performance may be variable on some special cases, since several outliers (in the Freiburg dataset, Pt 11, 21 for the C-DCGAN module; in the CHB-MIT dataset, Pt 2, 13 for the PPDA module, Pt 21 for C-DCGANs module, and Pt 2 for CMDA module) have been observed.

4.3 Model Applicability Analysis

Here, we attempt to summarize the universal characteristics and architectures based on the observations of DA algorithms in **Section 4.2**. The weight vectors of three types of DA methods (specific features, data augmentation, and adversarial learning) are quantified in a statistical analysis, which is depicted in **Figure 7**.

As shown in **Figure 7**, the adversarial learning–based approaches exhibit obvious advantages over the other DA methods on both intracranial and scalp EEG. Meanwhile, the weight distribution indicates that model performance regarding the specific features and data augmentation is volatile. Comparing adversarial learning to specific features, we reckon that the amount of above par weights is about 64% up. Comparing adversarial learning to data augmentation, a further 61% benefit is obtained, for a total of about 125% margin over data augmentation–based methods. These observations give us confidence in the efficacy of adversarial learning for processing epileptic signals, and we conjecture that data augmentation is relatively inferior for alleviating individual variability.

In particular, the manifold feature of CMDA surpasses all the other methods, such that the effectiveness of manifold feature

TABLE 7 | *p* values on the Freiburg Hospital dataset.

Patient	Pt 1	Pt 2	Pt 3	Pt 4	Pt 5	Pt 6
Patient	Pt 1	Pt 2	Pt 3	Pt 4	Pt 5	Pt 6
p value	0.032	0.041	0.034	0.034	**0.052**	0.044
Patient	Pt 8	Pt 9	Pt 10	Pt 11	Pt 12	Pt 13
p value	0.037	0.032	0.038	0.028	0.032	0.032
Patient	Pt 14	Pt 15	Pt 16	Pt 17	Pt 18	Pt 19
p value	0.034	0.014	0.045	**0.062**	0.025	**0.055**
Patient	Pt 20	Pt 21	—	—	—	—
p value	0.047	0.041	—	—	—	—

The bold values denote outliers.

TABLE 8 | *p* values on the CHB-MIT dataset.

Patient	Pt 1	Pt 2	Pt 3	Pt 5	Pt 6	Pt 7
p value	0.046	**0.068**	0.038	**0.055**	0.028	0.033
Patient	Pt 8	Pt 9	Pt 10	Pt 13	Pt 14	Pt 17
p value	0.032	**0.056**	0.048	0.040	0.044	0.038
Patient	Pt 18	Pt 19	Pt 20	Pt 21	—	—
p value	0.035	0.025	0.028	0.028	—	—

The bold values denote outliers.

requires a further demonstration. The statistical significance of the manifold feature is assessed for discriminating preictal and interictal stages across different patients. The two-sample Kolmogorov–Smirnov test [49] at a 5% significance level ($p < 0.05$) is implemented during the evaluation.

The significance analysis for each patient is provided in **Tables 7**, **8**. The unqualified performance index is marked in bold format. For the manifold feature, 17 of 20 subjects in the Freiburg dataset and 13 of 16 subjects in the CHB-MIT dataset present an adequately distinguished ability. According to this observation, the manifold-based methods might be the promising techniques in developing a robust seizure predictor.

5 CONCLUSION

This study proposes a universal approach to alleviate the problem of individual variability in epileptic seizure prediction. By combining the DA and ensemble learning techniques, the proposed HIVE-CODA model mitigates the effects of epileptic individual variance and increases the generalization ability. Besides, a simulated clinical sampling scenario is adopted during training and testing periods, which is the first attempt to adopt this evaluating strategy. Compared with the patient-specific scheme in conventional studies, such an assessment model is relatively demanding and challenging. Nonetheless, HIVE-CODAs achieve high domain shift robustness and precision, which demonstrates its feasibility of real-world applications.

By analyzing the contributions of each module, the experimental results also demonstrate the effectiveness of adversarial learning and manifolds in epileptic seizure prediction. The underlying causes of this phenomenon remain unclear because there is no definitive explanation of the dynamics of epilepsy in the existing literature. However, the success of the manifold module in this experiment brings new inspiration. We speculate that the mapping of EEG in the high-dimensional space may follow a compact distribution, so the kernel-based method for searching hyperplanes may have potential in this task. The search for more powerful DA algorithms and the underlying reasons will be considered as part of our future research extension to achieve higher performance.

DATA AVAILABILITY STATEMENT

Publicly available datasets were analyzed in this study. These data can be found here: https://epilepsy.uni-freiburg.de/ freiburg-seizure-predictionproject/ eeg-database.

ETHICS STATEMENT

Written informed consent was obtained from the individual(s) and minor(s)' legal guardian/next of kin, for the publication of any potentially identifiable images or data included in this article.

AUTHOR CONTRIBUTIONS

PP contributed to conception and design of the study, analysis and/or interpretation of data, and drafting the manuscript.

REFERENCES

1. Fisher RS, Boas WVE, Blume W, Elger C, Genton P, Lee P, et al. Epileptic Seizures and Epilepsy: Definitions Proposed by the International League against Epilepsy (ILAE) and the International Bureau for Epilepsy (IBE). *Epilepsia* (2005) 46(4):470–2. doi:10.1111/j.0013-9580.2005.66104.x
2. Banerjee PN, Filippi D, Allen Hauser W. The Descriptive Epidemiology of Epilepsy-A Review. *Epilepsy Res* (2009) 85(1):31–45. doi:10.1016/j.eplepsyres.2009.03.003
3. Kwan P, Schachter SC, Brodie MJ. Drug-resistant Epilepsy. *N Engl J Med* (2011) 365(10):919–26. doi:10.1056/nejmra1004418
4. Lin L-C, Ouyang C-S, Chiang C-T, Yang R-C, Wu R-C, Wu H-C. Early Prediction of Medication Refractoriness in Children with Idiopathic Epilepsy Based on Scalp EEG Analysis. *Int J Neur Syst* (2014) 24(07):1450023. doi:10.1142/s0129065714500233
5. Cook MJ, O'Brien TJ, Berkovic SF, Murphy M, Morokoff A, Fabinyi G, et al. Prediction of Seizure Likelihood with a Long-Term, Implanted Seizure Advisory System in Patients with Drug-Resistant Epilepsy: a First-In-Man Study. *Lancet Neurol* (2013) 12(6):563–71. doi:10.1016/s1474-4422(13)70075-9
6. Li S, Zhou W, Yuan Q, Liu Y. Seizure Prediction Using Spike Rate of Intracranial EEG. *IEEE Trans Neural Syst Rehabil Eng* (2013) 21(6):880–6. doi:10.1109/tnsre.2013.2282153

7. Karoly PJ, Freestone DR, Boston R, Grayden DB, Himes D, Leyde K, et al. Interictal Spikes and Epileptic Seizures: Their Relationship and Underlying Rhythmicity. *Brain* (2016) 139(4):1066–78. doi:10.1093/brain/aww019
8. Guo L, Wang Z, Cabrerizo M, Adjouadi M. A Cross-Correlated Delay Shift Supervised Learning Method for Spiking Neurons with Application to Interictal Spike Detection in Epilepsy. *Int J Neur Syst* (2017) 27(03):1750002. doi:10.1142/s0129065717500022
9. Shahidi Zandi A, Tafreshi R, Javidan M, Dumont GA. Predicting Epileptic Seizures in Scalp EEG Based on a Variational Bayesian Gaussian Mixture Model of Zero-Crossing Intervals. *IEEE Trans Biomed Eng* (2013) 60(5):1401–13. doi:10.1109/tbme.2012.2237399
10. Myers MH, Padmanabha A, Hossain G, de Jongh Curry AL, Blaha CD. Seizure Prediction and Detection via Phase and Amplitude Lock Values. *Front Hum Neurosci* (2016) 10:80. doi:10.3389/fnhum.2016.00080
11. Mirowski P, Madhavan D, LeCun Y, Kuzniecky R. Classification of Patterns of EEG Synchronization for Seizure Prediction. *Clin Neurophysiol* (2009) 120(11):1927–40. doi:10.1016/j.clinph.2009.09.002
12. Direito B, Teixeira CA, Sales F, Castelo-Branco M, Dourado A. A Realistic Seizure Prediction Study Based on Multiclass SVM. *Int J Neur Syst* (2017) 27(03):1750006. doi:10.1142/s012906571750006x
13. Sun C, Cui H, Zhou W, Nie W, Wang X, Yuan Q. Epileptic Seizure Detection with EEG Textural Features and Imbalanced Classification Based on Easyensemble Learning. *Int J Neur Syst* (2019) 29(10):1950021. doi:10.1142/s0129065719500217
14. Brinkmann BH, Wagenaar J, Abbot D, Adkins P, Bosshard SC, Chen M, et al. Crowdsourcing Reproducible Seizure Forecasting in Human and Canine Epilepsy. *Brain* (2016) 139(6):1713–22. doi:10.1093/brain/aww045
15. Zhang T, Chen W, Li M. Fuzzy Distribution Entropy and its Application in Automated Seizure Detection Technique. *Biomed Signal Process Control* (2018) 39:360–77. doi:10.1016/j.bspc.2017.08.013
16. Peng P, Xie L, Wei H. A Deep Fourier Neural Network for Seizure Prediction Using Convolutional Neural Network and Ratios of Spectral Power. *Int J Neur Syst* (2021) 31:2150022. doi:10.1142/s0129065721500222
17. Zhang Y, Guo Y, Yang P, Chen W, Lo B. Epilepsy Seizure Prediction on Eeg Using Common Spatial Pattern and Convolutional Neural Network. *IEEE J Biomed Health Inform* (2020) 24(2):465–74. doi:10.1109/JBHI.2019.2933046
18. Liu G, Zhou W, Geng M. Automatic Seizure Detection Based on S-Transform and Deep Convolutional Neural Network. *Int J Neur Syst* (2020) 30(04):1950024. doi:10.1142/s0129065719500242
19. Lin L-C, Ouyang C-S, Wu R-C, Yang R-C, Chiang C-T. Alternative Diagnosis of Epilepsy in Children without Epileptiform Discharges Using Deep Convolutional Neural Networks. *Int J Neur Syst* (2020) 30(05):1850060. doi:10.1142/s0129065718500600
20. Ozcan AR, Erturk S. Seizure Prediction in Scalp EEG Using 3D Convolutional Neural Networks with an Image-Based Approach. *IEEE Trans Neural Syst Rehabil Eng* (2019) 27(11):2284–93. doi:10.1109/tnsre.2019.2943707
21. Daoud H, Bayoumi MA. Efficient Epileptic Seizure Prediction Based on Deep Learning. *IEEE Trans Biomed Circuits Syst* (2019) 13(5):804–13. doi:10.1109/tbcas.2019.2929053
22. Tsiouris KM, Pezoulas VC, Zervakis M, Konitsiotis S, Koutsouris DD, Fotiadis DI. A Long Short-Term Memory Deep Learning Network for the Prediction of Epileptic Seizures Using EEG Signals. *Comput Biol Med* (2018) 99:24–37. doi:10.1016/j.compbiomed.2018.05.019
23. Li Y, Yu Z, Chen Y, Yang C, Li Y, Allen Li X, et al. Automatic Seizure Detection Using Fully Convolutional Nested LSTM. *Int J Neural Syst* (2020) 30(4):2050019. doi:10.1142/S0129065720500197
24. Özcan AR, Ertürk S. Epileptic Seizure Prediction with Recurrent Convolutional Neural Networks. In: Signal Processing and Communications Applications Conference (2017). p. 1–4.
25. Peng P, Wei H, Xie L, Song Y. Epileptic Seizure Prediction in Scalp Eeg Using an Improved HIVE-COTE Model. In: Chinese Control Conference. IEEE (2020). p. 6450–7. doi:10.23919/ccc50068.2020.9188930
26. Jirsa VK, Proix T, Perdikis D, Woodman MM, Wang H, Gonzalez-Martinez J, et al. The Virtual Epileptic Patient: Individualized Whole-Brain Models of Epilepsy Spread. *Neuroimage* (2017) 145:377–88. doi:10.1016/j.neuroimage.2016.04.049
27. Kuhlmann L, Lehnertz K, Richardson MP, Schelter B, Zaveri HP. Seizure Prediction - Ready for a new era. *Nat Rev Neurol* (2018) 14(10):618–30. doi:10.1038/s41582-018-0055-2
28. Elger CE, Hoppe C. Diagnostic Challenges in Epilepsy: Seizure Under-reporting and Seizure Detection. *Lancet Neurol* (2018) 17(3):279–88. doi:10.1016/s1474-4422(18)30038-3
29. Samek W, Meinecke FC, Muller K-R. Transferring Subspaces between Subjects in Brain--Computer Interfacing. *IEEE Trans Biomed Eng* (2013) 60(8):2289–98. doi:10.1109/tbme.2013.2253608
30. Zhang L, Wang X, Yang D, Sanford T, Harmon S, Turkbey B, et al. Generalizing Deep Learning for Medical Image Segmentation to Unseen Domains via Deep Stacked Transformation. *IEEE Trans Med Imaging* (2020) 39(7):2531–40. doi:10.1109/tmi.2020.2973595
31. Pan SJ, Yang Q. A Survey on Transfer Learning. *IEEE Trans Knowledge Data Eng* (2009) 22(10):1345–59.
32. Long M, Cao Z, Wang J, Jordan MI, Conditional Adversarial Domain Adaptation, *Advances in Neural Information Processing Systems* (2018).
33. Combes RTd., Zhao H, Wang Y-X, Gordon G, Domain Adaptation with Conditional Distribution Matching and Generalized Label Shift, *Advances in Neural Information Processing Systems* (2020).
34. Zhou M, Tian C, Cao R, Wang B, Niu Y, Hu T, et al. Epileptic Seizure Detection Based on EEG Signals and CNN. *Front Neuroinform* (2018) 12:95. doi:10.3389/fninf.2018.00095
35. Goldberger AL, Amaral LA, Glass L, Hausdorff JM, Ivanov PC, Mark RG, et al. PhysioBank, PhysioToolkit, and PhysioNet: Components of a New Research Resource for Complex Physiologic Signals. *Circulation* (2000) 101(23):e215–20.E215. doi:10.1161/01.cir.101.23.e215
36. Peng L-H, Yin J, Zhou L, Liu M-X, Zhao Y. Human Microbe-Disease Association Prediction Based on Adaptive Boosting. *Front Microbiol* (2018) 9:2440. doi:10.3389/fmicb.2018.02440
37. Rayatdoost S, Yin Y, Rudrauf D, Soleymani M. Subject-invariant EEG Representation Learning for Emotion Recognition. In: IEEE International Conference on Acoustics, Speech and Signal Processing (2021). p. 3955–9. doi:10.1109/icassp39728.2021.9414496
38. Zhang W, Yan F, Han F, He R, Li E, Wu Z, et al. Auto Recognition of Solar Radio Bursts Using the C-DCGAN Method. *Front Microbiol* (2021) 9:646556. doi:10.3389/fphy.2021.646556
39. Zhao L-M, Yan X, Lyu B. Plug-and-play Domain Adaptation for Cross-Subject EEG-Based Emotion Recognition. In: Proceedings of the AAAI Conference on Artificial Intelligence (2021).
40. Yan K, Kou L, Zhang D. Learning Domain-Invariant Subspace Using Domain Features and independence Maximization. *IEEE Trans Cybern* (2018) 48(1):288–99. doi:10.1109/TCYB.2016.2633306
41. Li H, Pan SJ, Wang S, Kot AC. Domain Generalization with Adversarial Feature Learning. In: Proceedings of the IEEE Conference on Computer Vision and Pattern Recognition (2018). p. 5400–9. doi:10.1109/cvpr.2018.00566
42. Dou Q, Castro DC, Kamnitsas K, Glocker B. Domain Generalization via Model-Agnostic Learning of Semantic Features" in *Advances In Neural Information Processing Systems* (2019).
43. Yair O, Ben-Chen M, Talmon R. Parallel Transport on the Cone Manifold of SPD Matrices for Domain Adaptation. *IEEE Trans Signal Process* (2019) 67(7):1797–811. doi:10.1109/tsp.2019.2894801
44. Gill V, Singh J, Singh Y. Analytical Solution of Generalized Space-Time Fractional Advection-Dispersion Equation via Coupling of Sumudu and Fourier Transforms. *Front Phys* (2019) 6:151. doi:10.3389/fphy.2018.00151
46. Usman SM, Khalid S, Akhtar R, Bortolotto Z, Bashir Z, Qiu H. Using Scalp EEG and Intracranial EEG Signals for Predicting Epileptic Seizures: Review of Available Methodologies. *Seizure* (2019) 71:258–69. doi:10.1016/j.seizure.2019.08.006
47. Ramantani G, Maillard L, Koessler L. Correlation of Invasive Eeg and Scalp EEG. *Seizure* (2016) 41:196–200. doi:10.1016/j.seizure.2016.05.018
48. Fahimi F, Dosen S, Ang KK, Mrachacz-Kersting N, Guan C. Generative Adversarial Networks-Based Data Augmentation for Brain-Computer Interface. *IEEE Trans Neural Networks Learn Syst* (2020).

49. Xiao Y. A Fast Algorithm for Two-Dimensional Kolmogorov-Smirnov Two Sample Tests. *Comput Stat Data Anal* (2017) 105:53–8. doi:10.1016/j.csda.2016.07.014

Conflict of Interest: The author declares that the research was conducted in the absence of any commercial or financial relationships that could be construed as a potential conflict of interest.

Publisher's Note: All claims expressed in this article are solely those of the authors and do not necessarily represent those of their affiliated organizations, or those of the publisher, the editors, and the reviewers. Any product that may be evaluated in this article, or claim that may be made by its manufacturer, is not guaranteed or endorsed by the publisher.

frontiers in Physics

ORIGINAL RESEARCH
published: 03 January 2022
doi: 10.3389/fphy.2021.809752

Dual-Band Bandpass Filter With Controllable Stopband Bandwidth

*Nan Wang[1], Haokun Wei[1], Kun Gao[2], Xiting Ruan[2], Xiaojian Chen[3], Qian Xu[4], Qian Yang[5], Anxue Zhang[5] and Shuangyang Liu[5]**

[1]State Grid Shaanxi Electric Power Research Institute, Xi'an, China, [2]State Grid Xi'an Electric Power Corporation, Xi'an, China, [3]State Grid Shaanxi Maintenance Company, Xi'an, China, [4]State Grid Weinan Electric Power Corporation, Shangluo, China, [5]School of Information and Communications Engineering, Xi'an Jiaotong University, Xi'an, China

A novel dual-band bandpass filter (BPF) is proposed with independently controllable transmission zeros (TZs) which can realize widely tunable stopband bandwidth (BW). The planar microstrip filter consists of a three-degree L-C ladder lowpass filter loaded with two unsymmetrical shorted stubs which are used to produce different TZs. By tuning the parameters of the two unsymmetrical shorted stubs, the TZs can be independently controlled. Therefore, the BPF has independent controllable center frequencies (CFs), passband bandwidths, and stopband bandwidths between adjacent passbands. All the L-C values in the equivalent circuit of the proposed filter are optimized to fulfill the design specifications. For demonstration, a dual-band BPF is designed. The measured results show good agreement with the simulated ones.

Keywords: bandpass filter, dual-band, tunable stopband, wide upper stopband, transmission zeros, transmission poles

OPEN ACCESS

Edited by:
Zhewang Ma,
Saitama University, Japan

Reviewed by:
Weiren Zhu,
Shanghai Jiao Tong University, China
Yijun Cai,
Xiamen University of Technology, China

****Correspondence:***
Shuangyang Liu
lsy6820@stu.xjtu.edu.cn

Specialty section:
This article was submitted to Optics and Photonics, a section of the journal Frontiers in Physics

Received: *05 November 2021*
Accepted: *29 November 2021*
Published: *03 January 2022*

Citation:
Wang N, Wei H, Gao K, Ruan X, Chen X, Xu Q, Yang Q, Zhang A and Liu S (2022) Dual-Band Bandpass Filter With Controllable Stopband Bandwidth. Front. Phys. 9:809752. doi: 10.3389/fphy.2021.809752

INTRODUCTION

Modern wireless communication systems need high performance filters which have controllable CFs, passband bandwidths, stopband bandwidths, and sharp rejection. Different designing structures and methods have been greatly studied [1–17]. Generally, the dual-band bandpass filter (BPF) adjusts the CFs by changing transmission poles (TPs) [1, 2]. To suppress the harmonic responses, the multiple resonant modes excited by a stepped impedance stub-loaded resonator are used to design dual-band BPFs with a wide upper stopband [3]. However, there is only one transmission zero (TZ) in the stopband. Therefore, the stopband bandwidth is narrow. By introducing more TZs in the stopband, the performances of selectivity and stopband bandwidth can be enhanced. Signal-interference principles [4–6] are applied to design single- or dual-band BPFs with broad stopband bandwidths by creating multiple TZs. To design high performance filters with multiple passbands, the method of multiple mono-frequency resonators coupling to a non-resonating node is proposed in [7]. To have more TZs, couplings between the non-resonating nodes are introduced in [8], or couplings and more open/shorted-subs [9, 10] are applied in the configurations. However, it is difficult to realize the coupling for application when the number of passband increases. Moreover, TZs introduced by the coupling matrix need to change all the coupling coefficients, so it is also difficult to independently adjust the position of TZs [11].

This study presents a novel BPF loaded with two unsymmetrical shorted stubs to introduce two different TZs in the stopband to realize the controllable stopband bandwidth. Following our early work [12], the theoretical analysis of the TZs and TPs is shown in this study, which can demonstrate that the design method has advantages of simplicity and effectiveness. A three-degree lowpass filter

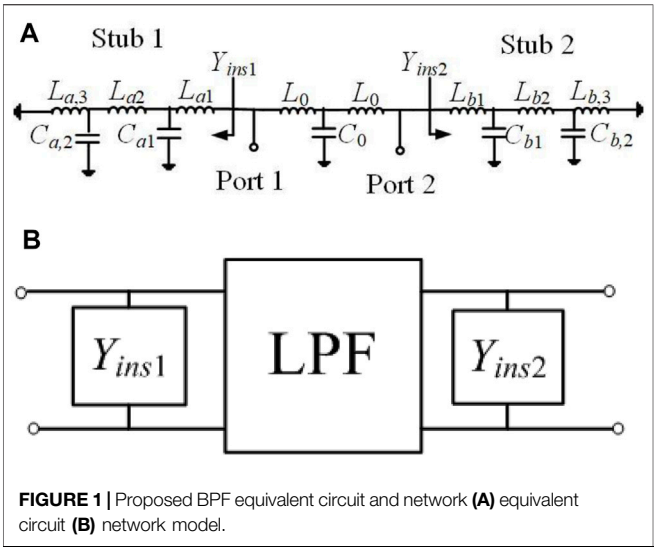

FIGURE 1 | Proposed BPF equivalent circuit and network **(A)** equivalent circuit **(B)** network model.

prototype is chosen for simplicity; the in-band performance will be improved when choosing more degrees of the lowpass filter prototype. A dual-band BPF has been designed and fabricated to verify the proposed concept.

ANALYSIS

The equivalent circuit and network of the proposed prototype are shown in **Figure 1**. The network can be divided into three subnetworks, as shown in **Figure 1B**, which are the lowpass filter (LPF) section in the middle and two unsymmetrical shunt admittance sections at the sides. The LPF section is also a symmetric network and has chosen a three order L-C ladder prototype for simplicity, as shown in **Figure 1A**.

From our early analysis in [12], the shorted stub with two equivalent capacitors will introduce two TZs. As shown in **Figure 1**, the configuration has two unsymmetrical shorted stubs; the shunt admittances of Stub1 and Stub 2 have different LC values, which will produce four different TZs.

The ABCD matrix of the transmission network in **Figure 1B** is expressed as follows, where M_{Y1} and M_{Y2} are the ABCD matrices of the Stub 1 and Stub 2, respectively. M_{LPF} is the ABCD matrix of the middle LPF section. According to the relationship of scattering parameters with the ABCD matrix, the TZs and the reflection zeros (TPs) are the roots of polynomials $P(s)$ and $F(s)$, respectively, where the impedance of the source/load is normalized to be 1. When the root of $F(s)$ is an imaginary number, the reflection zero related to the root represents a TP.

$$M_{Y1} = \begin{bmatrix} 1 & 0 \\ Y_{ins1} & 1 \end{bmatrix} = \begin{bmatrix} 1 & 0 \\ \dfrac{D_1(s)}{N_1(s)} & 1 \end{bmatrix} = \frac{1}{N_1(s)} \begin{bmatrix} N_1(s) & 0 \\ D_1(s) & N_1(s) \end{bmatrix}, \tag{1a}$$

$$N_1(s) = C_{a1}C_{a2}L_{a1}L_{a2}L_{a3}s^5 + [C_{a1}L_{a1}(L_{a2}+L_{a3}) + C_{a2}L_{a3}(L_{a1}+L_{a2})]s^3 + (L_{a1}+L_{a2}+L_{a3})s, \tag{1b}$$

$$D_1(s) = C_{a1}C_{a2}L_{a2}L_{a3}s^4 + (C_{a1}L_{a2} + C_{a1}L_{a3} + C_{a2}L_{a3})s^2 + 1, \tag{1c}$$

$$M_{Y2} = \begin{bmatrix} 1 & 0 \\ Y_{ins2} & 1 \end{bmatrix} = \begin{bmatrix} 1 & 0 \\ \dfrac{D_2(s)}{N_2(s)} & 1 \end{bmatrix} = \frac{1}{N_2(s)} \begin{bmatrix} N_2(s) & 0 \\ D_2(s) & N_2(s) \end{bmatrix}, \tag{2a}$$

$$N_2(s) = C_{b1}C_{b2}L_{b1}L_{b2}L_{b3}s^5 + [C_{b1}L_{b1}(L_{b2}+L_{b3}) + C_{b2}L_{b3}(L_{b1}+L_{b2})]s^3 + (L_{b1}+L_{b2}+L_{b3})s, \tag{2b}$$

$$D_2(s) = C_{b1}C_{b2}L_{b2}L_{b3}s^4 + (C_{b1}L_{b2} + C_{b1}L_{b3} + C_{b2}L_{b3})s^2 + 1, \tag{2c}$$

$$M_{LPF} = \begin{bmatrix} L_0C_0s^2+1 & L_0^2C_0s^3 + 2L_0s \\ C_0s & L_0C_0s^2+1 \end{bmatrix} = \begin{bmatrix} a(s) & b(s) \\ c(s) & d(s) \end{bmatrix}, \tag{3}$$

$$\begin{bmatrix} A & B \\ C & D \end{bmatrix} = M_{Y1} \times M_{LPF} \times M_{Y2} = \frac{1}{N_1(s)N_2(s)} \begin{bmatrix} A'(s) & B'(s) \\ C'(s) & D'(s) \end{bmatrix} = \frac{1}{P(s)} \begin{bmatrix} A'(s) & B'(s) \\ C'(s) & D'(s) \end{bmatrix}, \tag{4a}$$

$$P(s) = N_1(s)N_2(s), \tag{4b}$$

$$F(s) = A'(s) + B'(s) - C'(s) - D'(s) = N_1(s)N_2(s)[b(s)-c(s)] - [N_1(s)D_2(s) + D_1(s)N_2(s)]a(s) - D_1(s)D_2(s)b(s). \tag{5}$$

From (**Eq. 4b**), polynomial $P(s)$ has $4n+2$ roots (n = 2), of which 2 roots are at the origin and others are conjugate and symmetrical on the imaginary axis. Therefore, each shorted stub produces n TZs and the two unsymmetrical shorted stubs produce $2n$ different TZs on the imaginary axis. From (**Eq. 5**), the degree of polynomial $F(s)$ is $4n+5$. $N_1(s)$, $N_2(s)$, $b(s)$, and $c(s)$ have odd terms only, while $D_1(s)$, $D_2(s)$, and $a(s)$ have constant terms. Therefore, polynomial $F(s)$ has one root at the origin; two real roots and the remaining $4n+2$ roots are conjugate and symmetrical on the imaginary axis or in four quadrants. The optimization algorithm is used to obtain the required lumped element values for independently controlling the TZs and the return losses, such as genetic algorithm and so on.

Since one of the two shorted stubs can tune two TZs, a dual-band BPF is presented for demonstration. The optimized L-C values are shown in **Table 1**. The S-parameters of the circuit with different parameters of the shorted stub are shown in **Figures 2**, **3**. The parameter L_{a1} of the shorted stub 1 can tune TZ_1 and TZ_4, which means the first passband CF and stopband bandwidth can

TABLE 1 | Optimized L-C values for a dual-band BPF (*L* unit in nH, *C* unit in pF).

L_{a1}	L_{a2}	L_{a3}	L_{b1}	L_{b2}	L_{b3}
0.6923	2.1267	2.2803	0.6053	2.6080	2.0501
C_{a1}	C_{a2}	C_{b1}	C_{b2}	C_0	L_0
0.9256	2.0160	1.4576	1.3815	0.9321	1.7690

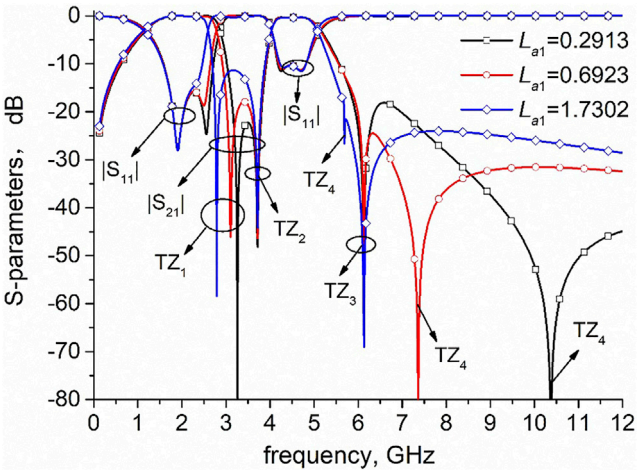

FIGURE 2 | Tunable TZ_1 and TZ_4 versus different L_{a1}.

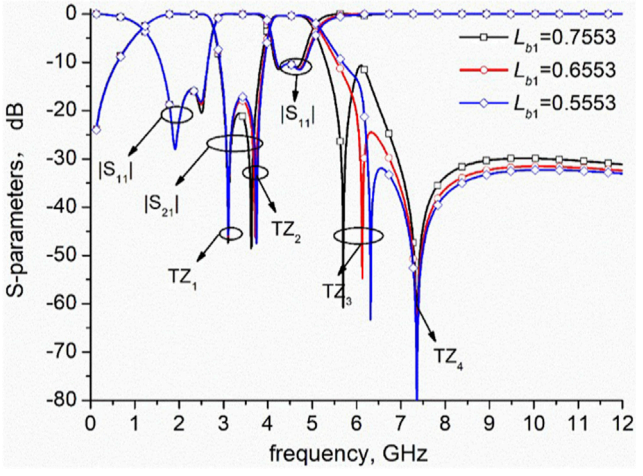

FIGURE 3 | Tunable TZ_2 and TZ_3 versus different L_{b1}.

be tuned independently, while the second passband width, TZ_2 and TZ_3 keep unchanged. The larger the value of L_{a1}, the smaller will be the frequencies of TZ_1 and TZ_4. Meanwhile, when the parameter L_{b1} of the shorted stub 2 changes, the frequencies of TZ_2 and TZ_3 vary simultaneously. As shown in **Figure 3**, the value of L_{b1} gets large and the frequencies of TZ_2 and TZ_3 decrease, which move at the same direction as that of TZ_1 and TZ_4. Therefore, the bandwidth of the second passband can be

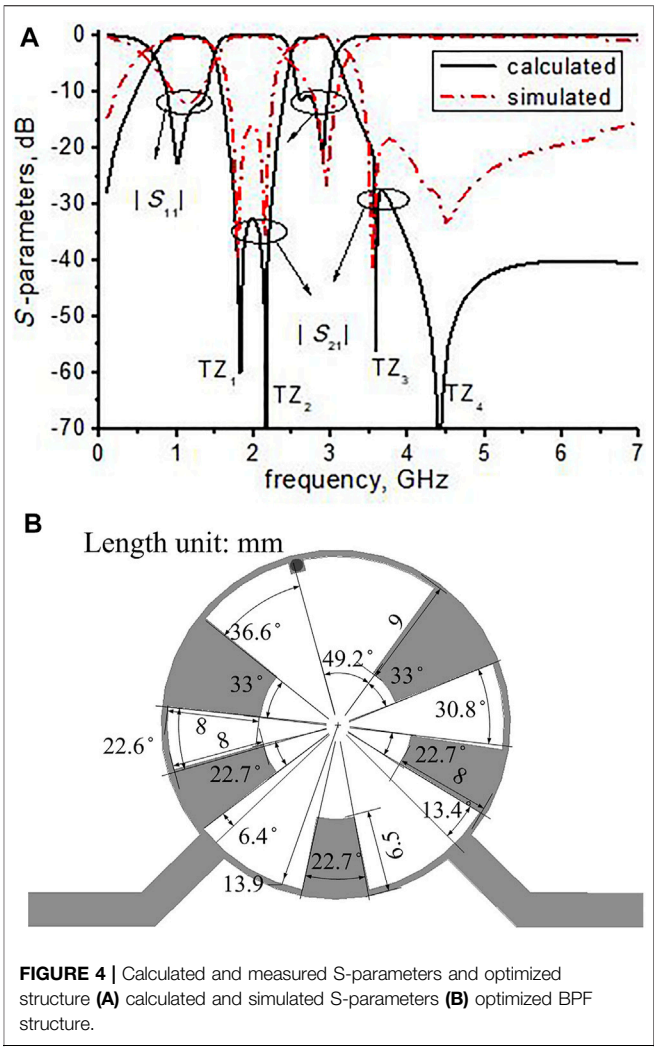

FIGURE 4 | Calculated and measured S-parameters and optimized structure **(A)** calculated and simulated S-parameters **(B)** optimized BPF structure.

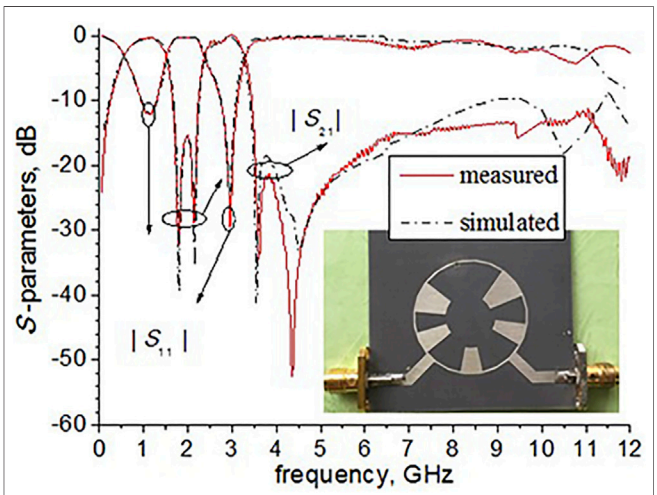

FIGURE 5 | Simulated and measured S-parameters with photograph inset.

TABLE 2 | Comparison of the proposed filter with previous designs.

Ref.	CF (GHz)/FBW (%)	IL (dB)	OBS	Controllable TZs	Size ($\lambda_g \times \lambda_g$)
[3]	1.5/12.7, 2.41/9.1	1.1, 0.9	2.4 f_{02}, >20 dB	--	0.12 × 0.09
Prototype 2 in [4]	0.68/94.9, 2.33/26.4	0.09, 0.83	--	3	0.5 × 0.75
[7]	0.72/16.7, 1/13	0.55, 0.6	--	3	0.27 × 0.39
[8]	0.7/--, 0.8/--	--	1.3 f_{02}, >20 dB	2	--
[12]	1.08/103.2, 3.05/48.5	0.2, 0.6	2.7 f_{02}, >15 dB	2	0.2 × 0.19
This work	1.03/91.3, 2.8/31	0.5, 0.8	4.3 f_{02}, >10 dB	4	0.15 × 0.15

tuned independently. Since the position of the last TP is near that of TZ_3, the upper stopband performance is effected by the move of TZ_3.

RESULTS

A dual-band BPF is designed and fabricated to demonstrate the design method. The CFs of dual passbands are 1 and 2.8 GHz, respectively. The stopbands are 1.75–2.2 GHz (<25 dB) and >3.55 GHz (<25 dB), respectively. Therefore, the TPs are preset as 1.8, 2.15, 3.6, and 4.4 GHz. The optimized L-C values are L_{a1} = 0.5922, L_{a2} = 2.5267, L_{a3} = 3.3803, L_0 = 3.0691, L_{b1} = 1.1153, L_{b2} = 2.4080, L_{b3} = 3.9501 (unit in nH), C_{a1} = 2.8256, C_{a2} = 3.2161, C_0 = 1.4321, C_{b1} = 2.8576, and C_{b2} = 3.6815 (unit in pF). The S-parameters calculated by the optimized L-C values are shown in **Figure 4A**. The roots of $P(s)$ are 0, 0, ±1.83j, ±2.16j, ±3.59j, and ±4.41j, which are calculated in unit GHz for facility. The positive imaginary roots of $P(s)$ represent the TZs. The L-C values of shunt admittance Y_{ins1} control TZ_2 and TZ_4, while the L-C values of shunt admittance Y_{ins2} control TZ_1 and TZ_3. The roots of $F(s)$ are 0, −0.05 ± 1.01j, 0.1 ± 1.37j, −0.07 ± 2.59j, 0.04 ± 2.9j, 0.03 ± 3.58j, −8.94, and 15.15. Since the roots 0.03 ± 3.58j of $F(s)$ are close to the roots ±3.59j of $P(s)$, the second passband has two TPs not three TPs [7].

The BPF is simulated and fabricated on a substrate with ε_r = 2.65, tanδ = 0.003, and h = 1 mm. Here, we choose the 117.8 Ω high-impedance line, which has the line-width of 0.5 mm. As shown in **Figure 4B**, the line width of the open stub which acts as the capacitor is tapered. The characteristic impedance is calculated by the waist width of the taper. Due to the discontinuity of the microstrip line and the minor coupling between the open stubs, the final dimension parameters are optimized by the full-wave electromagnetic simulation software HFSS. The optimized values of parameters are given in **Figure 4B**. The circuit size is about 0.15 λ_g × 0.15 λ_g, where λ_g is the guided wavelength at f_{01}. The simulated S-parameters agree well with the calculated ones, as shown in **Figure 4A**. **Figure 5** shows the simulated and measured S-parameters with the photograph inset. The measured results are in good agreement with the simulated ones. The discrepancies between the simulated results and the measured results may be due to the ignorance of transmission line discontinuity and fabrication tolerances. The measured CFs, fractional bandwidths (FBWs), insertion losses (ILs) at the CF, out-band suppressions (OBSs), the number of controllable TZs, and the size are listed in **Table 2**. As shown in **Table 2**, the proposed dual-band BPF with simple circuit topology has advantages such as relative low IL, wide FBW, wide upper stopband, and more controllable TZs.

CONCLUSION

A dual-band BPF with a controllable stopband bandwidth between the passbands is designed by the method of independently controlling TZs. By tuning the parameters of the two unsymmetrical shorted stubs, the introduced two TZs between adjacent passbands can be independently controlled. After optimizing the equivalent circuit lumped element values, the CFs, passband bandwidths, and stopband bandwidths can be tuned in a certain range. With a simple filter structure and good performance, the proposed method is attractive for application in high-selectivity filter designs.

DATA AVAILABILITY STATEMENT

The original contributions presented in the study are included in the article/Supplementary Material; further inquiries can be directed to the corresponding author.

AUTHOR CONTRIBUTIONS

All authors listed have made a substantial, direct, and intellectual contribution to the work and approved it for publication.

REFERENCES

1. He J, Chen C-m. A Dual-Band BPF with Controllable Center Frequencies and Bandwidths Using a Single SIW Cavity. In: Prceeding of the 2021 IEEE 4th International Conference on Electronics Technology (ICET); 7-10 May 2021; Chengdu, China. IEEE (2021). p. 489–92. doi:10.1109/ICET51757.2021.9451069
2. Lin W, Lee T-H, Wu K Dual-Band Bandpass SIW Resonator Filter with Flexible Frequency Ratio. In: Prceeding of the 2019 49th European Microwave Conference (EuMC); 1-3 Oct. 2019; Paris, France. IEEE (2019). p. 364–7. doi:10.23919/EuMC.2019.8910700

3. Lin L, Sun SJ, Wu B, Liang CH Dual-band Bandpass Filter with Wide Upper Stopband Using Quad-mode Stepped Impedance Stub-loaded Resonator. *Electron Lett* (2014) 50(16):1145–6. doi:10.1049/el.2014.2004
4. Sanchez-Soriano MA, Gomez-Garcia R Sharp-Rejection Wide-Band Dual-Band Bandpass Planar Filters with Broadly-Separated Passbands. *IEEE Microw Wireless Compon Lett* (2015) 25(2):97–9. doi:10.1109/LMWC.2014.2382669
5. Phani Kumar KV, Karthikeyan SS Compact, High Selectivity and Wideband Bandpass Filter with Multiple Transmission Zeros. *AEU - Int J Electronics Commun* (2018) 94:79–83. doi:10.1016/j.aeue.2018.06.047
6. Yogesh SS, Phani K, Karthikeyan SS Compact Dual-Wideband Bandpass Filter for Wireless Applications. *AEU - Int J Electronics Commun* (2018) 95: S1434841118304618. doi:10.1016/j.aeue.2018.08.007
7. Gomez-Garcia R, Guyette AC Reconfigurable Multi-Band Microwave Filters. *IEEE Trans Microwave Theor Techn.* (2015) 63(4):1294–307. doi:10.1109/TMTT.2015.2405066
8. Gómez-García R, Guyette AC, Psychogiou D, Naglich EJ, Peroulis D Quasi-Elliptic Multi-Band Filters with Center-Frequency and Bandwidth Tunability. *IEEE Microwave Wireless Components Lett* (2016) 26(3):192–4. doi:10.1109/LMWC.2016.2526026
9. Xu K-D, Li D, Liu Y High-Selectivity Wideband Bandpass Filter Using Simple Coupled Lines with Multiple Transmission Poles and Zeros. *IEEE Microw Wireless Compon Lett* (2019) 29(2):107–9. doi:10.1109/LMWC.2019.2891203
10. Xu KD, Zhang F, Liu Y, Nie W High Selectivity Seventh-order Wideband Bandpass Filter Using Coupled Lines and Open/shorted Stubs. *Electron Lett* (2018) 54(4):223–5. doi:10.1049/el.2017.4233
11. Tang S-C, Chu P-C, Kuo J-T, Wu L-K Dual-band Bandpass Filter Based on Frequency Transformations with Enhanced Inter-band Isolation. In: Prceeding of the 2020 IEEE Asia-Pacific Microwave Conference (APMC); 8-11 Dec. 2020; Hong Kong, Hong Kong. IEEE (2020). p. 758–60. doi:10.1109/APMC47863.2020.9331380
12. Yang Q, Jiao YC, Zhang Z Dual-wideband BPF with Wide Upper Stopband Using Shorted Stepped-impedance Stub-loaded Lowpass Filter. *Electron Lett* (2016) 52(19):1615–6. doi:10.1049/el.2016.2475
13. Xu J, Wu W, Miao C Compact and Sharp Skirts Microstrip Dual-Mode Dual-Band Bandpass Filter Using a Single Quadruple-Mode Resonator (QMR). *IEEE Trans Microwave Theor Techn.* (2013) 61(3):1104–13. doi:10.1109/tmtt.2013.2238949
14. Sun S-J, Su T, Deng K, Wu B, Liang C-H Compact Microstrip Dual-Band Bandpass Filter Using a Novel Stub-Loaded Quad-Mode Resonator. *IEEE Microw Wireless Compon Lett* (2013) 23(9):465–7. doi:10.1109/LMWC.2013.2274038
15. Peng Y, Zhang L, Fu J, Wang Y, Leng Y Compact Dual-Band Bandpass Filter Using Coupled Lines Multimode Resonator. *IEEE Microw Wireless Compon Lett* (2015) 25(4):235–7. doi:10.1109/LMWC.2015.2400936
16. Jin X, Wen W, Chen M Compact Microstrip Dual-/Tri-/Quad-Band Bandpass Filter Using Open Stubs Loaded Shorted Stepped-Impedance Resonator. *IEEE Trans Microwave Theor Tech* (2013) 61(9):3187–99. doi:10.1109/TMTT.2013.2273759
17. Kim CH, Chang K Independently Controllable Dual-Band Bandpass Filters Using Asymmetric Stepped-Impedance Resonators. *IEEE Trans Microwave Theor Techn.* (2011) 59(12):3037–47. doi:10.1109/TMTT.2011.2168973

Conflict of Interest: Authors NW and HW were employed by the State Grid Shaanxi Electric Power Research Institute. KG and XR were employed by the company State Grid Xi'an Electric Power Corporation. XC was employed by the State Grid Shaanxi Maintenance Company. QX was employed by the State Grid Weinan Electric Power Corporation.

The remaining authors declare that the research was conducted in the absence of any commercial or financial relationships that could be construed as a potential conflict of interest.

frontiers in Physics

ORIGINAL RESEARCH
published: 17 February 2022
doi: 10.3389/fphy.2022.860606

A Low-Profile Broadband Metasurface Antenna With Polarization Conversion Based on Characteristic Mode Analysis

*Jian Dong, Rigeng Wu and Yaxi Pan**

School of Computer Science and Engineering, Central South University, Changsha, China

In this paper, a low-profile, broadband metasurface antenna for polarization conversion is proposed based on characteristic mode analysis (CMA). A new type of metasurface unit with a partially chamfered symmetrical triangular structure is designed. The inherent physical characteristics of the antenna are analyzed based on CMA, and the expected characteristic modes are selected for excitation at a suitable position. Slot-coupled feeding via microstrip line realizes the performance of wide impedance bandwidth and axial ratio bandwidth (ARBW). The measured -10 dB impedance bandwidth of 36.3% (4.38–6.32 GHz) and the 3 dB ARBW of 20.1% (5.41–6.62 GHz) are achieved. The left-hand circular polarization (LHCP) is realized, and the measured highest gain in the working frequency band is 6.05 dBic. The overall size of the designed and fabricated metasurface antenna is 0.58 λ_0 × 0.58 λ_0 × 0.07 $\lambda_0$at 5 GHz. The proposed metasurface antenna can be well used in C-band satellite communications due to its low profile, broadband, and circular polarization.

Keywords: metasurface, characteristic mode analysis, polarization conversion, low-profile, broadband

OPEN ACCESS

Edited by:
Kai-Da Xu,
Xi'an Jiaotong University, China

Reviewed by:
Haofeng Dou,
China Academy of Space Technology, China
Rong Jin,
Huazhong University of Science and Technology, China

****Correspondence:***
Yaxi Pan
yaxipan@csu.edu.cn

Specialty section:
This article was submitted to Optics and Photonics, a section of the journal Frontiers in Physics

Received: *23 January 2022*
Accepted: *03 February 2022*
Published: *17 February 2022*

Citation:
Dong J, Wu R and Pan Y (2022) A Low-Profile Broadband Metasurface Antenna With Polarization Conversion Based on Characteristic Mode Analysis. Front. Phys. 10:860606. doi: 10.3389/fphy.2022.860606

INTRODUCTION

In recent years, with the continuous development of wireless communication technology, the antenna as an important part of the communication system has attracted more and more scholars to invest in related research. The polarization mode of the antenna includes linear polarization (LP), circular polarization (CP), and elliptical polarization. With the advancement of communication technology, LP has been difficult to meet the modern complex communication environment, so the demand for CP is increasing [1]. CP has the properties of reducing multipath interference, polarization mismatch, and overcoming the Faraday rotation effect [2], and is widely used in communication equipment.

Traditional microstrip patch antennas are used in many scenarios because of their low profile, simple structure, easy fabrication, and easy integration [3–5]. However, as the requirements for antennas become higher and higher, microstrip patch antennas are difficult to meet the needs of modern communications because of their narrow impedance bandwidth and low gain. Metasurface antenna is expected to overcome such drawbacks as the traditional microstrip patch antenna. In recent years, metasurface antennas have been applied to CP antenna design by more and more scholars to improve the impedance bandwidth, axial ratio bandwidth (ARBW), and the gain of the antenna [6, 7]. In [8], a metasurface unit for polarization conversion was proposed, where the unit consisted of a hexagonal ring enclosed within a rectangular ring and printed on both sides of the dielectric substrate. Although the high gain was achieved, the impedance bandwidth and ARBW

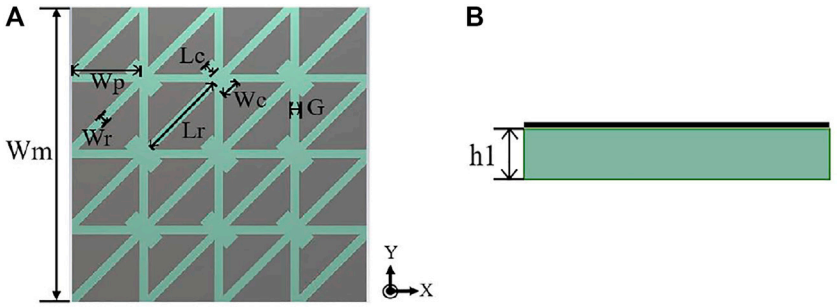

FIGURE 1 | The structure of the metasurface layer: **(A)** Front view; **(B)** Side view.

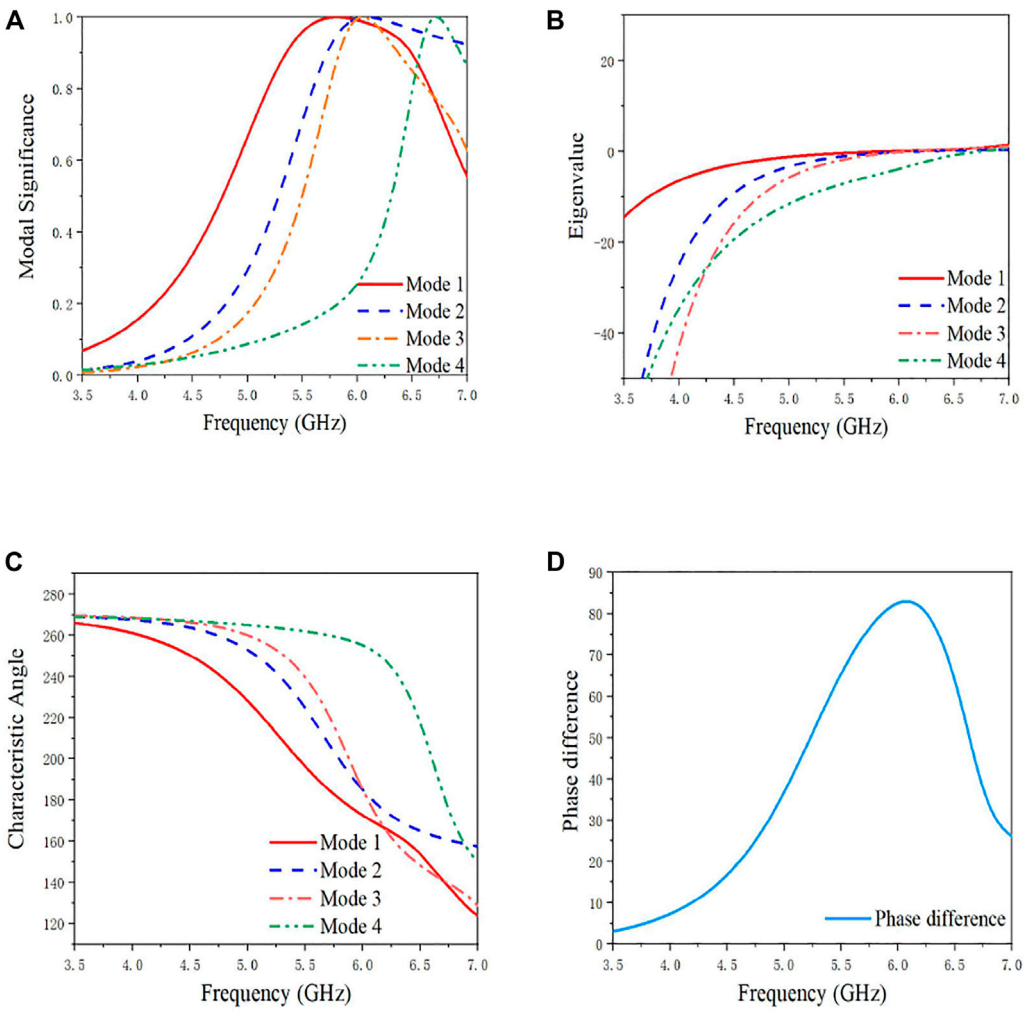

FIGURE 2 | MS, eigenvalue, and CA of the metasurface layer and the difference between the CA of Mode 1 and Mode 4: **(A)** MS; **(B)** Eigenvalue; **(C)** CA; **(D)** Difference of CA.

were both narrow. In [9], a metasurface antenna composed of square metal patch units was proposed, and four intersecting slots were used for slot coupling feed through the microstrip line. The antenna achieved the 3 dB ARBW of 14.5%, and the axial ratio beam bandwidth was more than 205°, but the impedance bandwidth of -10 dB was only 17%. In [10], a metasurface antenna with periodic elliptical patches rotated 45° to achieve polarization conversion was proposed. The antenna analyzed the

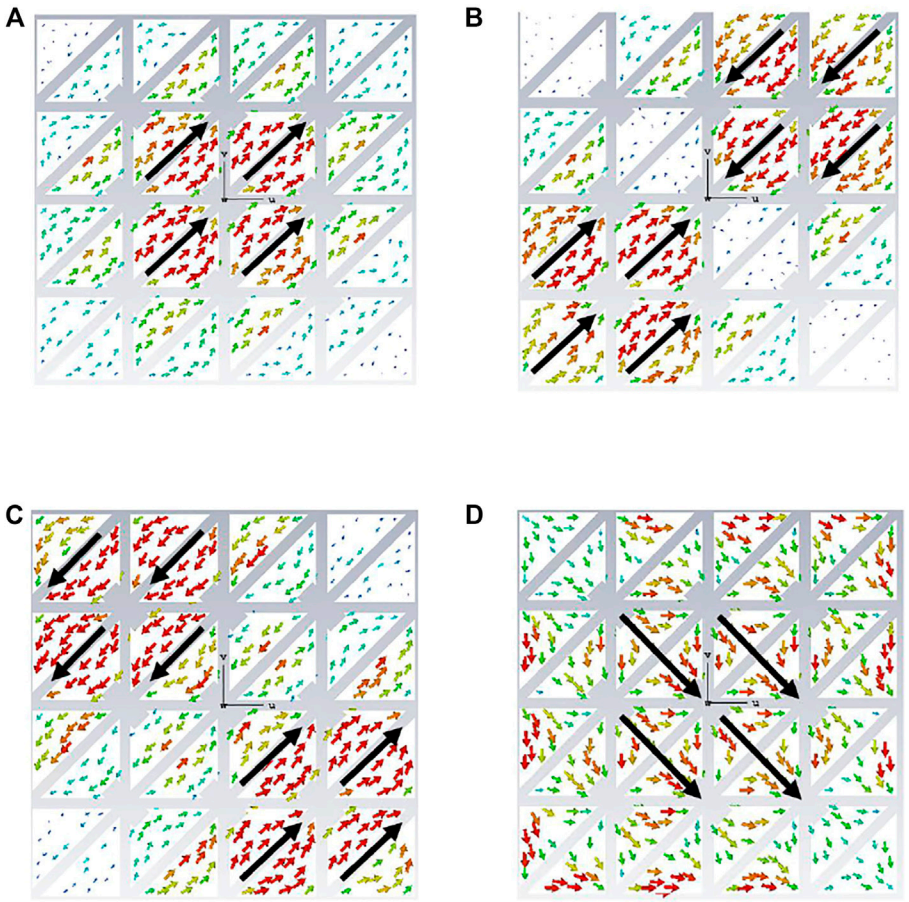

FIGURE 3 | Characteristic current of the metasurface at 5.8 GHz: **(A)** Mode 1; **(B)** Mode 2; **(C)** Mode 3; **(D)** Mode 4.

principle of CP on the metasurface by using the equivalent circuit method. The antenna achieved the 3 dB ARBW of 17.4% and the peak gain of 8 dBic. But the size of the antenna was large and the -10 dB impedance bandwidth was only 20.6%. In [11], the metasurface unit composed of a split ring resonator and microstrip line was proposed, and the rotation angle between two adjacent units differed by 90°. Although a low radar cross-section and high gain were achieved, it had a narrow ARBW and a complex feed network. In [12], a metasurface CP antenna for 5G indoor applications was proposed, which was analyzed using transmission line and equivalent circuit models. The 2D meta-resonator construction and sloping slot coupled feeding achieved CP radiation, but its impedance bandwidth and ARBW were narrow. For the above-mentioned papers, some of them do not have an in-depth analysis to explain the inherent physical properties.

In recent years, characteristic mode analysis (CMA) has been used to analyze the inherent physical characteristics of the designed antenna and to gain a deep understanding of its working principle [13, 14]. Using CMA to analyze metasurface can well analyze its resonance characteristics and radiation characteristics, and obtain the best antenna performance through the analysis of each mode [15]. In [16], an H-shaped metasurface unit was proposed and the feed was slot-coupled through the cross-shaped aperture on the ground. Although CMA was used for the analysis, the paper mentioned did not consider the effects caused by the slot structure and did not analyze the results of modal weighting coefficient (MWC). In [17], a windmill-shaped metasurface unit was proposed to realize a reconfigurable tri-polarized antenna, and the 3 dB ARBW of 15% was obtained. The proposed metasurface structure was analyzed by using the modal significance and characteristic currents in CMA, but the principle of achieving CP was not analyzed in depth. In [18], a novel stereo metasurface unit was proposed, which effectively reduced the size and increased the bandwidth of the antenna. Although the resonant characteristics of the patch antenna and the metasurface were analyzed by CMA, only the modal importance was used for the analysis. However, CMA has several parameters available for antenna analysis, and it is difficult to characterize the antenna with one or two alone, and MWC as an important parameter is rarely analyzed.

In this paper, a new low-profile broadband metasurface antenna consisting of 4 × 4 partially chamfered symmetrical triangular structure units with a slot coupling feeding structure is proposed for a wide impedance bandwidth and ARBW. Different from most CMA-based designs where only the metasurface layer is analyzed, this paper also analyzes the effect of introducing a

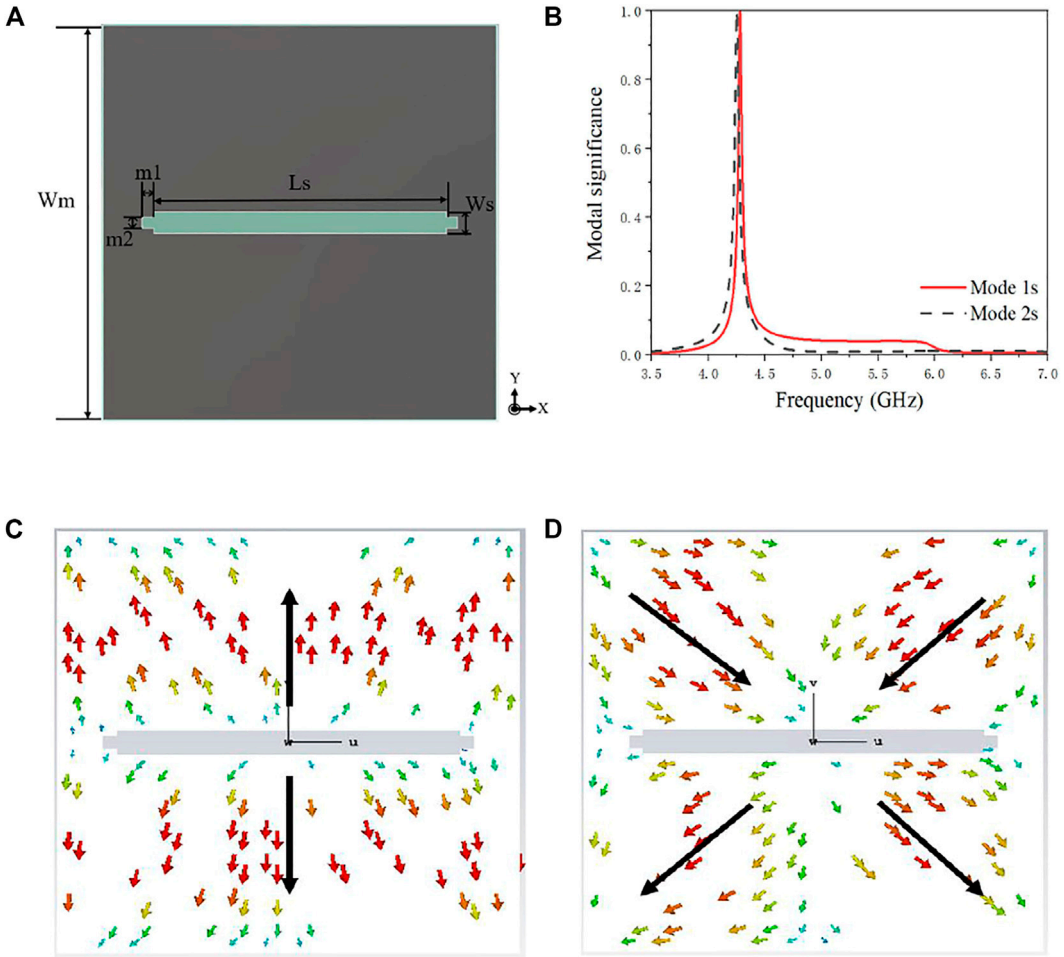

FIGURE 4 | The structure, MS, and characteristic current of the stepped slot patch antenna: **(A)** Antenna structure; **(B)** MS; **(C)** The characteristic current of Mode 1s; **(D)** The characteristic current of Mode 2s.

slot-coupled structure. In addition, the amplitude and phase of the MWC are analyzed to find the modes that are eventually excited and the modes that produce CP.

The rest of the paper is organized as follows. In *Design and Analysis of Polarization Conversion Antenna*, the metasurface antenna and the stepped slot patch antenna are introduced. At the same time, CMA is used to understand their resonance characteristics and radiation characteristics, and the final antenna design is given. In *Results and Discussion*, the designed metasurface antenna is fabricated, and its characteristics are measured and analyzed. In *Conclusion*, the conclusion of this paper is presented.

DESIGN AND ANALYSIS OF POLARIZATION CONVERSION ANTENNA

Analysis of Proposed Antenna Based on CMA

CMA is a method of analyzing antenna without adding excitation, which is determined by factors such as antenna structure and size. There are three important parameters in CMA: eigenvalue (λ_n), modal significance (MS), and characteristic angle (CA) [19]. When λ_n equals to zero, the associated mode is resonant and radiates the most efficiently. MS is used to characterize the potential ability of a certain mode to play a role in a certain frequency band [20]. The calculation formula for MS is $MS = |1/(1 + j\lambda_n)|$. If the MS is close to 1 at a certain frequency point, it means that this mode is important at this frequency. If appropriate excitation is added, this mode can become the main radiation mode. The calculation formula of the CA is $CA = 180° - \tan^{-1}\lambda_n$. When the CA is 180°, it indicates that the resonance state is reached at this frequency. If the difference between the CAs of the two characteristic modes reaches 90°, the two modes have the potential to achieve CP. In addition, the total current of the CMA can be expressed as a linear superposition of a series of mode currents and is defined as $J = \sum \alpha_n J_n$, where the coefficient α_n is used to indicate the degree to which each mode is excited and is also known as the MWC.

To explain the working mechanism of the proposed metasurface antenna with polarization conversion, the CMA of the proposed metasurface antenna structure is carried out in the

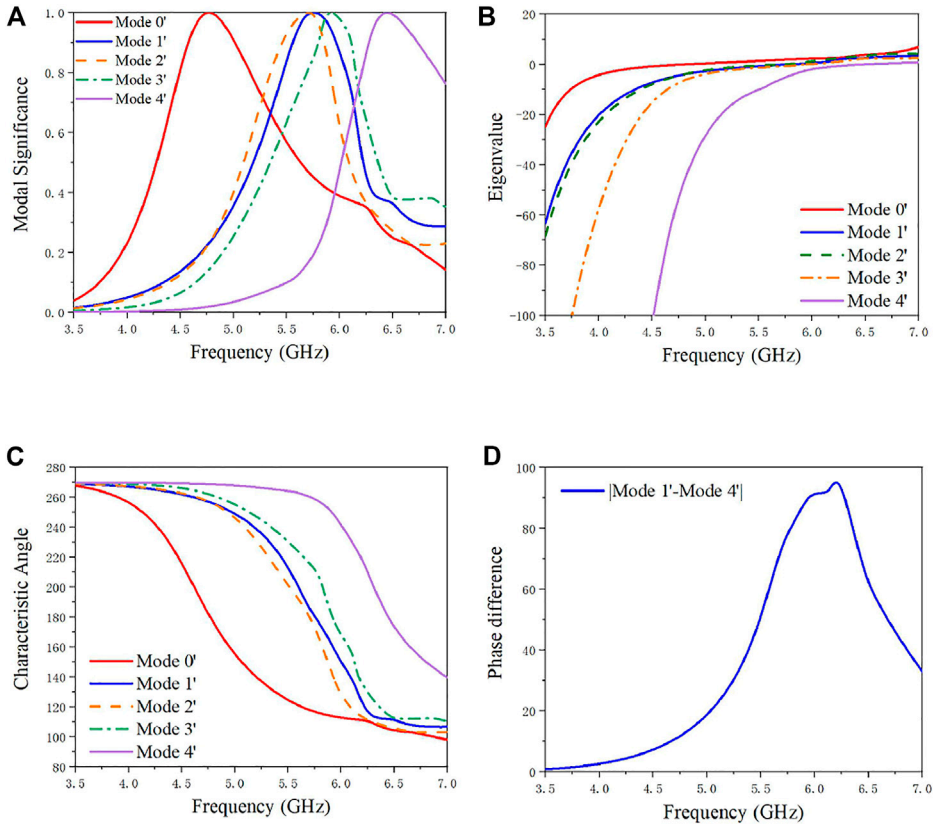

FIGURE 5 | CMA of the overall structure: **(A)** MS; **(B)** Eigenvalue; **(C)** CA; **(D)** CA difference.

commercial software CST MWS 2021 to study its working characteristics. First, the multi-layer solver is used to analyze the CMA of the metasurface antenna from 3.5 to 7 GHz. The metasurface layer is composed of the upper metasurface and the underlying dielectric substrate, as shown in **Figure 1**. The substrate and ground are considered to be infinite. The material of the metasurface is Perfect Electric Conductor (PEC), and the dielectric substrate uses FR4 (ε_r = 4.3) as the lossless material. The length of the dielectric substrate is W_m, and the height is h_1. The length of the patch is W_p, the gap between each unit is G in both x and y directions.

The first four characteristic modes of the antenna are used for CMA at 5.8 GHz. **Figure 2A** shows the MS of the first four characteristic modes. It can be seen from the figure that the first three characteristic modes are close to 1 at 5.8 GHz, and Mode 4 is close to 1 at 6.7 GHz. The eigenvalues of each mode at the respective resonant frequency are close to 0 as shown in **Figure 2B**. The CAs of the four modes are shown in **Figure 2C**, and the difference between the CA of Mode 1 and Mode 4 is close to 90° at 5.8 GHz as shown in **Figure 2D**. To study the radiation characteristics, the characteristic current is analyzed. The characteristic currents of the four modes at 5.8 GHz are shown in **Figure 3** and the arrow on the metasurface antenna represents the direction of the characteristic current. It can be seen from the figure that the current directions of Mode 1 and Mode 4 are orthogonal, and the maximum current distribution is concentrated at the center patch. The characteristic current direction of Mode 2 is mirror symmetry, and the characteristic current direction of Mode 3 is symmetric about the geometric center. Therefore, Mode 1 and Mode 4 are a pair of orthogonal modes due to the symmetry of the metasurface. It is possible to obtain CP by exciting with the same amplitude and a phase difference of 90°. If the excitation is added at the suitable location where the current is maximum, Mode 1 and Mode 4 can be excited at the same time to achieve CP.

CMA is performed on the stepped slot patch antenna, which structure is shown in **Figure 4A**. The first two characteristic modes of the stepped slot patch antenna are used for CMA. It can be seen from **Figure 4B** that the maximum values of the MS of the two modes are close to 1 at 4.25 GHz, and the potential bandwidth of the two modes greater than 0.707 is relatively narrow, which makes it difficult to achieve broadband. The characteristic currents of the two modes are shown in **Figures 4C,D**. Mode 1s is the main mode and its characteristic current is LP along the y-axis, while the characteristic current of Mode 2s has different directions so it is not representative and is ignored. Therefore, if the selected excitation location is appropriate, the stepped slot patch antenna can be excited to achieve LP along the y-axis.

CMA is used to analyze the overall structure of the antenna, and the results are shown in **Figure 5**. The first five most

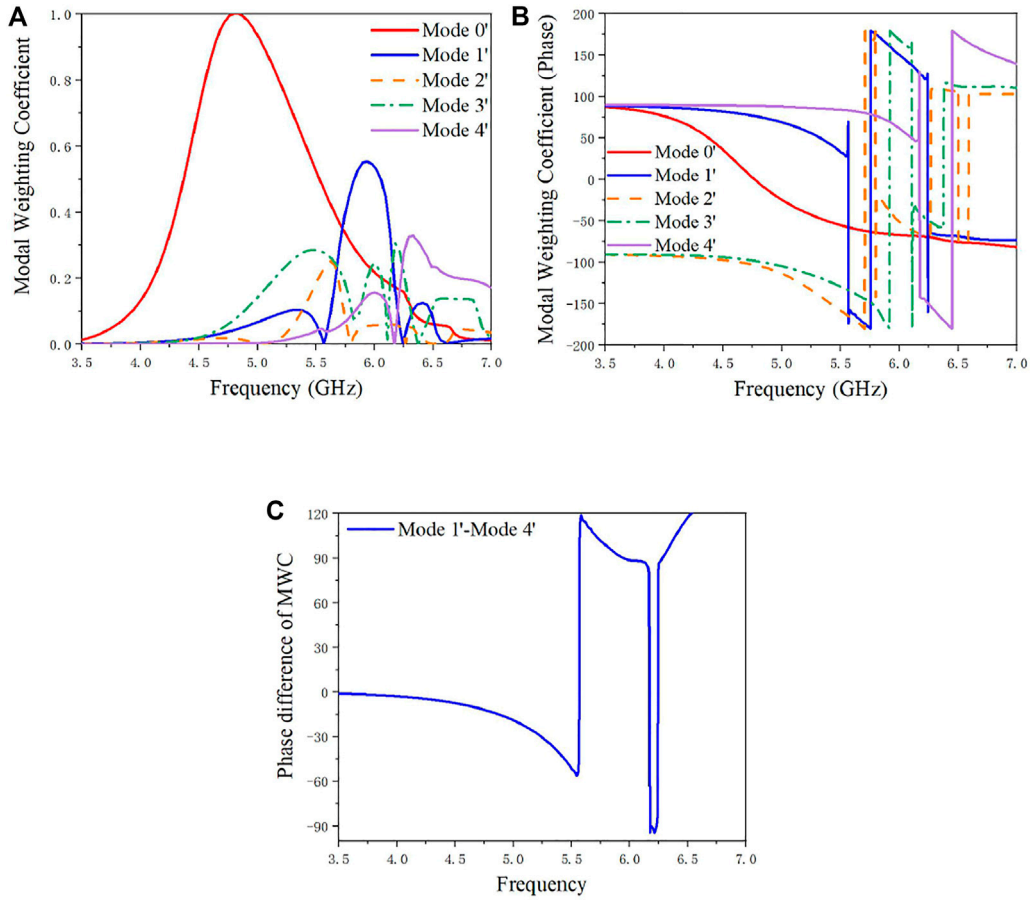

FIGURE 6 | The result of MWC: **(A)** Magnitude of MWC; **(B)** Phase of MWC; **(C)** Phase difference of MWC.

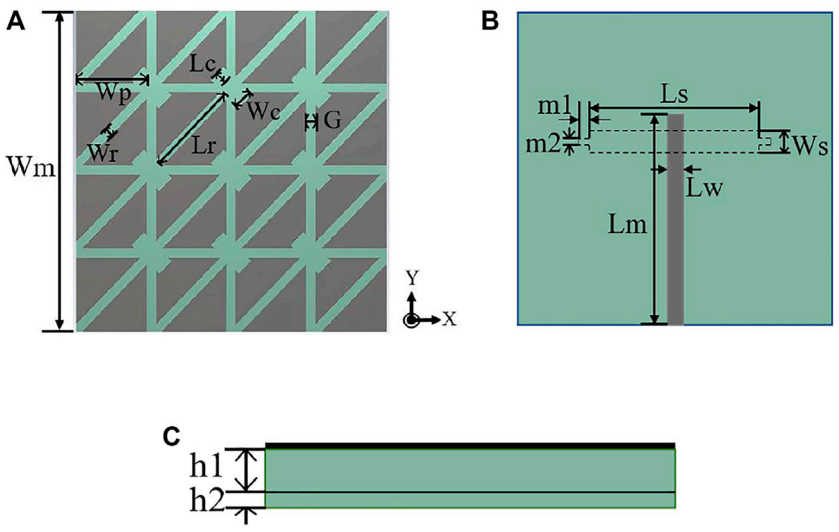

FIGURE 7 | The overall structure of the CP metasurface antenna: **(A)** Top view; **(B)** Back view; **(C)** Side view.

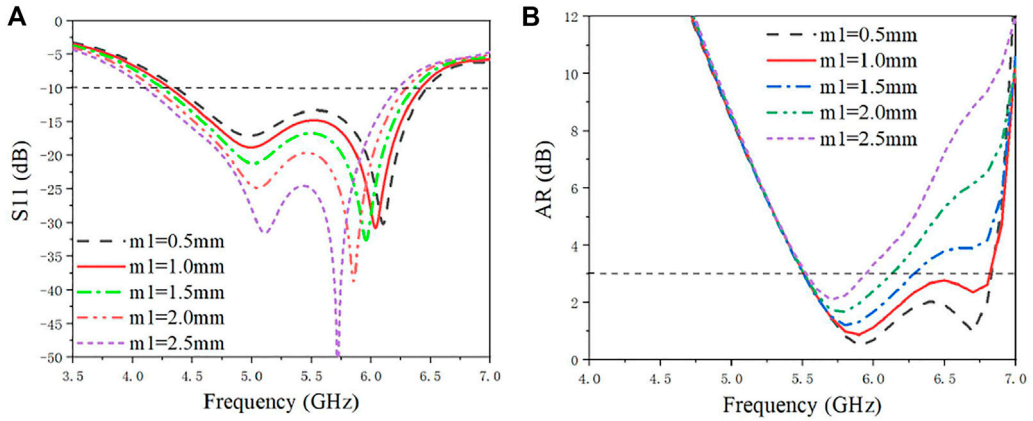

FIGURE 8 | S_{11} and ARBW when m_1 takes different values: **(A)** S_{11}; **(B)** ARBW.

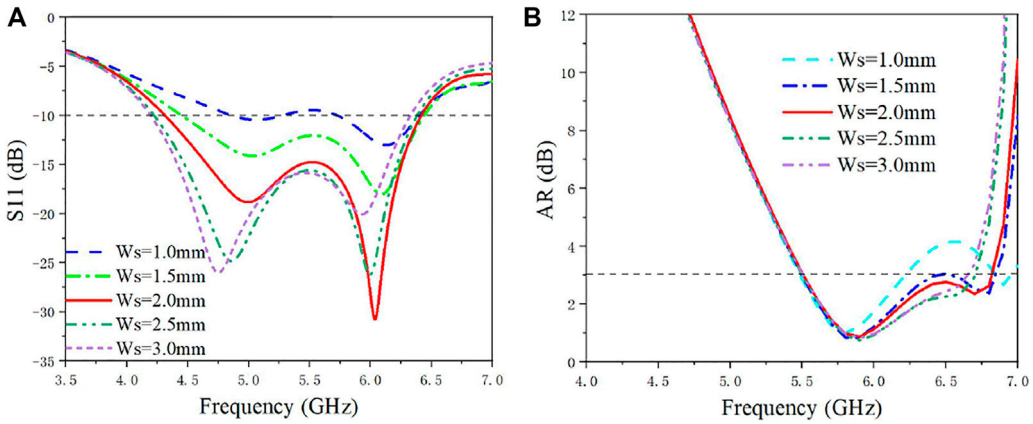

FIGURE 9 | S_{11} and ARBW when W_s takes different values: **(A)** S_{11}; **(B)** ARBW.

characteristic feature patterns are taken for analysis. From the MS in **Figure 5A**, it can be seen that Mode 0′ reaches 1 at 4.77 GHz, which satisfies the condition of resonance. The resonance frequency points of Mode 1′-Mode 3′ are all located at 5.5–6 GHz, and the resonance frequency point of Mode 4′ is 6.45 GHz. According to the results of the CMA performed on the slotted patch above, Mode 0′ is a characteristic mode introduced by the slotted patch, i.e., the slot mode, and the other four characteristic modes are the modes possessed by the metasurface. **Figure 5B** shows the eigenvalues corresponding to each characteristic mode and all of them reach 0 at their respective resonance points, satisfying the resonance condition. The CA of each characteristic mode is shown in **Figure 5C**, and the difference of CA between Mode 1′ and Mode 4′ is shown in **Figure 5D**. It can be seen that after the CMA of the overall structure of the antenna, the difference of the CA reaches 90°, and the structure has the condition to realize CP.

It is worth noting that the five modes are excited to some extent with the addition of the incentive structure. As can be seen in **Figure 6A**, the Mode 0′ is excited to a large extent, followed by the metasurface generated Mode 1′ and Mode 4'. Mode 2′ and Mode 3′ are also excited to some extent, but the degree of excitation is not high and the effect caused is small. The phases of the MWC of the

TABLE 1 | Parameters of the proposed antenna (in millimeters).

Parameter	Description	Value
W_m	Length of the substrate	35
h_1	Height of the upper substrate	3.5
h_2	Height of the lower substrate	0.5
W_p	Length of the patch unit	8
G	Width of the gap between units	1
L_r	Length of the truncated rectangle in the patch	11.3
W_r	Width of the truncated rectangle in the patch	1
L_c	Length of the clipped corner of the patch	1.5
W_c	Width of the clipped corner of the patch	2
L_s	Length of the rectangular gap on the floor	26
W_s	Width of the rectangular gap on the floor	2
m_1	Length of the mini-rectangular slot on the patch	1
m_2	Width of the mini-rectangular slot on the patch	1
L_m	Length of microstrip line	24
L_w	Width of microstrip line	1.5

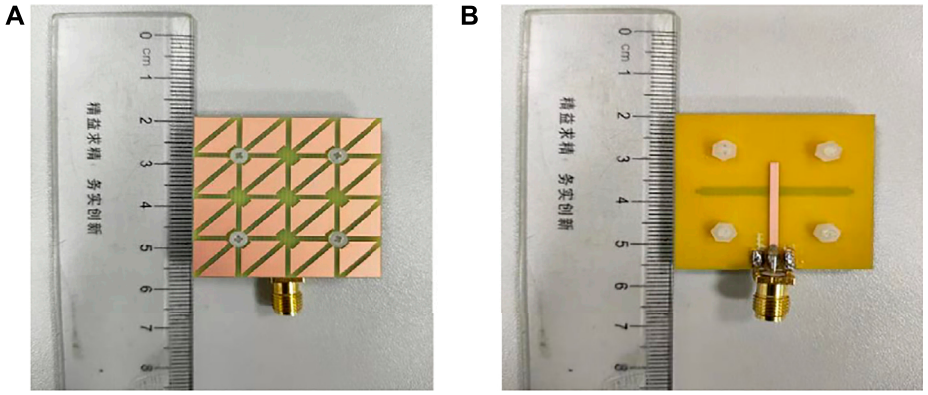

FIGURE 10 | Fabricated photos of metasurface antenna: **(A)** Top view; **(B)** Rear view.

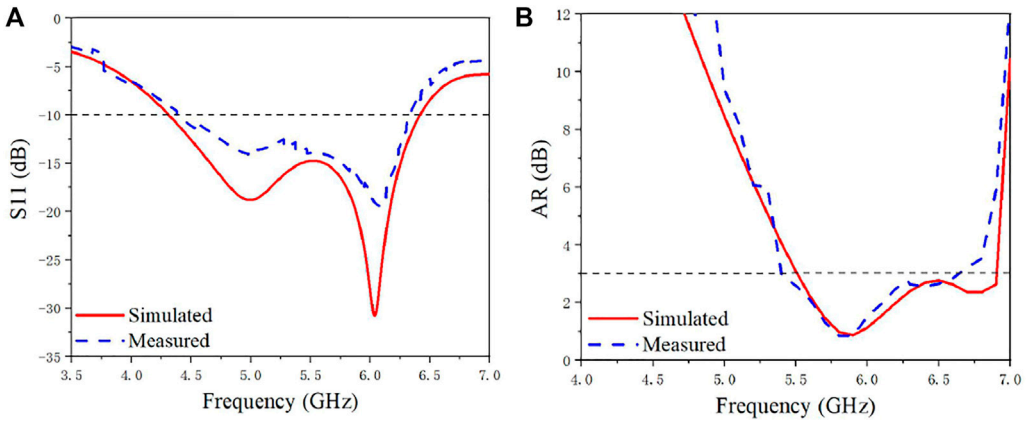

FIGURE 11 | Simulation and measurement of the S_{11} and ARBW of the proposed antenna: **(A)** S_{11}; **(B)** ARBW.

five modes are shown in **Figure 6B** and the phase difference between Mode 1′ and Mode 4′ is shown in **Figure 6C**, and the results show that the antenna structure has the condition to achieve CP.

Antenna Structure and Parameter Analysis

Through the above analysis of the inherent physical characteristics of the antenna using CMA, when the stepped slot patch antenna and the metasurface are excited at the same time, the conversion from LP to CP can theoretically be realized. The overall structure of the proposed metasurface antenna for converting LP to CP is shown in **Figure 7**. The geometry of the proposed antenna is composed of three metal layers and two substrate layers. The antenna consists of two layers of dielectric substrates with thicknesses of h_1 and h_2, respectively, and the material used is FR4 ($\varepsilon_r = 4.3$, $tan\delta = 0.02$). The metasurface layer composed of 4×4 units is located above the upper dielectric substrate and is used to convert polarized waves from LP to CP. The stepped slot ground is located between the two dielectric substrates, and the 50 Ω microstrip line is located below the lower dielectric substrate.

By opening a stepped slot on the ground, the impedance matching and the ARBW can be better adjusted. The length m_1 of the two steps on the ground will affect the impedance bandwidth and ARBW. As shown in **Figure 8**, when the other parameters remain unchanged, the parameter scan analysis is performed with m_1 from 0.5 to 2.5 mm at intervals of 0.5 mm. It can be seen from the figure that the influence of m_1 on the impedance bandwidth is not as great as the ARBW, and the impedance bandwidth is maintained at about 40%. However, for the ARBW, as the parameter m_1 increases, the ARBW gradually becomes narrow, which will cause the performance of CP to deteriorate. Through comparative analysis, the final value of m_1 is 1 mm. As shown in **Figure 9**, while keeping the other parameters unchanged, the interval of W_s from 1.0 to 3.0 mm is 0.5 mm for parameter scanning, and when W_s takes different values, the change of impedance bandwidth is greater than the impact on the ARBW. When the value of W_s is less than 2.0 mm, the impedance bandwidth and ARBW will become narrow, especially the impedance bandwidth. When W_s is 1.0 mm, the impedance bandwidth is only 19%, and the impedance bandwidth at this value is difficult to achieve broadband. At the same time, this value also narrows the ARBW, which makes it difficult to achieve the ideal CP effect. When the value of W_s is greater than 2.0mm, although the impedance bandwidth will be broadened, the ARBW will be affected. When the value of W_s is 3.0 mm, the ARBW is only 18%. Through comparative analysis, the final value of W_s is 2.0 mm.

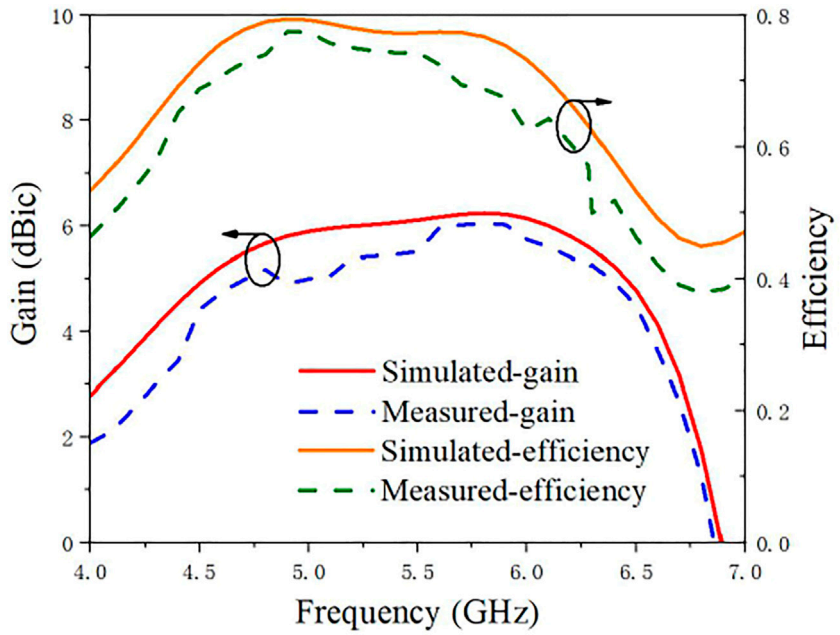

FIGURE 12 | Simulation and measurement of the gain and efficiency of the proposed antenna.

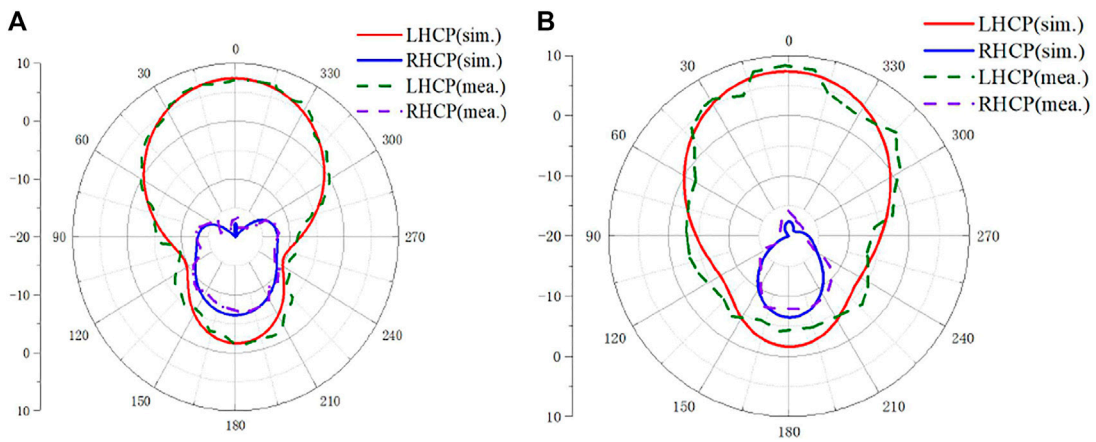

FIGURE 13 | Comparison of simulated and measured radiation patterns at 5.8 GHz: **(A)** xoz-plane. **(B)** yoz-plane.

Based on the above analysis and optimization, other parameters of the metasurface antenna are shown in **Table 1**. By using the commercial software CST MWS for simulation optimization, the simulated impedance bandwidth of -10 dB is 39.33% (4.31–6.42 GHz), the ARBW of 3 dB is 21.25% (5.51–6.82 GHz), and the maximum gain is 6.25 dBic. The overall size of the proposed metasurface antenna is $0.58\lambda_0 \times 0.58\lambda_0 \times 0.07\lambda_0$ at 5 GHz.

RESULTS AND DISCUSSION

In order to verify whether the performance of the designed antenna meets actual requirements, the designed antenna is fabricated and measured. The metasurface antenna is fabricated using a commonly used printed circuit board (PCB), as shown in **Figure 10**. **Figure 11** illustrates the impedance bandwidth and ARBW obtained under simulation and measurement. The simulated −10 dB impedance bandwidth and 3 dB ARBW of the proposed metasurface antenna is 39.33% from 4.31 to 6.42 GHz and 21.25% from 5.51 to 6.82 GHz, respectively. The −10 dB impedance bandwidth and 3 dB ARBW of the fabricated metasurface antenna are 36.3% from 4.38 to 6.32 GHz and 20.1% from 5.41 to 6.62 GHz, respectively. Both the simulation and measurement results show that after the excitation is added, the mode of the stepped slot patch and the mode of the metasurface is excited at the same time, and the impedance bandwidth of the

TABLE 2 | Comparison of the performance of recently reported CP metasurface antennas.

REF	f_0 (GHz)	Size (λ_0^3)	−10 dB S_{11} BW (%)	3 dB ARBW (%)	Gain (dBic)
Reference [8]	10.5	1.57 × 1.57×0.12	21.5	19.23	10
Reference [10]	5.8	0.79 × 0.79×0.067	20.6	17.4	8
Reference [11]	10	3.73 × 3.73×0.13	22.7	16	17.9
Reference [12]	3.55	0.29 × 0.29×0.04	14.1	2.3	5.4
Reference [17]	4	0.58 × 0.58×0.04	24.6	15	5.25
Reference [21]	5.525	0.76 × 0.76×0.065	19	11.4	8.2
Reference [22]	5.86	0.52 × 0.52×0.078	29.41	9.05	6.34
Reference [23]	5.7	0.86 × 0.86×0.038	18	12.8	6.9
Reference [24]	5.25	0.6 × 0.49×0.07	33.7	18.5	5.8
Reference [25]	7.45	1.87 × 1.87×0.6	6.87	6.87	12.31
Reference [26]	4	0.61 × 0.52×0.05	16	10	5.5
Reference [27]	5.6	0.86 × 0.67×0.13	22.6	14.3	4.8
Reference [28]	3.5	0.58 × 0.58×0.043	21	8.5	6.4
Proposed	5	0.58 × 0.58×0.07	36.3	20.1	6.05

antenna is broadened. **Figure 12** shows the gain and efficiency of the metasurface antenna under simulation and measurement. The maximum gain in the simulation and measurement are 6.25 dBic and 6.05 dBic, respectively, and the efficiencies in the simulation and measurement are 79.5 and 75.8%, respectively.

Figure 13 shows the radiation patterns of the xoy-plane and yoz-plane at 5.8 GHz of the metasurface antenna under simulation and measurement. It can be seen from the figure that the simulated and measured radiation patterns are basically the same. In the xoz-plane and the yoz-plane, the measured LHCP levels are approximately from -3 dBic to 7 dBic, and the measured RHCP levels are approximately from -7 dBic to -18 dBic. In both the xoz-plane and the yoz-plane, the measured LHCP level is higher than RHCP, which means that the proposed metasurface antenna is an LHCP antenna. The simulation and measurement results show that the LP generated by the stepped slot patch is converted into CP after adding the metasurface layer, thereby realizing the polarization conversion. Due to the influences and limitations of manufacturing accuracy and measurement environment, the simulation results and the measurement results are different.

Table 2 summarizes the comparison of the performance of recently reported CP metasurface antennas in terms of measurement results. As can be seen from the table, the proposed antenna has the widest impedance bandwidth and ARBW. Although some designs have higher antenna gain than our design, they have a larger size. Also, the design and fabrication of some antennas are more complicated because of the including of the feeding network.

CONCLUSION

In this paper, a novel low-profile broadband polarization conversion metasurface antenna using a partially chamfered symmetric triangular unit structure is proposed. The resonance characteristics and radiation characteristics of the metasurface antenna are analyzed by CMA, and the principle of polarization conversion is explained in depth. The slot-coupled feed through the microstrip line excites both the slot mode and the metasurface mode at the same time, which broadens the bandwidth of the antenna and realizes the polarization conversion. Simulated results show that the -10 dB impedance bandwidth and 3 dB ARBW of the proposed metasurface antenna are 39.33% (4.31–6.62 GHz) and 21.25% (5.51–6.82 GHz), respectively. By fabricating and measuring the antenna as verification, the measurement results show that the −10 dB impedance bandwidth of the proposed antenna is 36.3% (4.38–6.32 GHz), and the 3 dB ARBW is 20.1% (5.41–6.62 GHz). The measurement results and the simulation results are in good agreement. Moreover, the proposed antenna achieves a compact structure of only $0.58\lambda_0 \times 0.58\lambda_0 \times 0.07\lambda_0$ at 5 GHz, and has the characteristics of simple structure and easy processing, which is suitable for C-band satellite communications.

DATA AVAILABILITY STATEMENT

The original contributions presented in the study are included in the article/Supplementary Material, further inquiries can be directed to the corresponding author.

AUTHOR CONTRIBUTIONS

JD and RW designed the structure and fabricated the sample. RW and YP performed the experiments. JD and RW wrote the manuscript with contributions from all the other authors. All authors participated in the discussion of the results.

FUNDING

This research was funded in part by the National Natural Science Foundation of China, grant number 61801521 and 61971450, in part by the Natural Science Foundation of Hunan Province, grant number 2018JJ2533, and in part by the Fundamental Research Funds for the Central Universities, grant number 2018gczd014 and 20190038020050.

REFERENCES

1. Dong J, Ding C, Mo J. A Low-Profile Wideband Linear-To-Circular Polarization Conversion Slot Antenna Using Metasurface. *materials* (2020) 13:1164. doi:10.3390/ma13051164
2. Liu S, Yang D, Pan J. A Low-Profile Broadband Dual-Circularly-Polarized Metasurface Antenna. *Antennas Wirel Propag Lett* (2019) 18:1395–9. doi:10.1109/lawp.2019.2917758
3. Malekpoor H, Hamidkhani M. Bandwidth and Gain Improvement for Reduced Size of Stacked Microstrip Antenna Fed by Folded Triangular Patch with Half V-shaped Slot. *Int J RF Microwave Computer-Aided Eng* (2021) 31:e22649. doi:10.1002/mmce.22649
4. Wan W, Xue M, Cao L, Ye T, Wang Q. Low-profile Compact Metasurface-loaded Patch Antenna with Enhanced Bandwidth. *Microw Opt Technol Lett* (2021) 63:2656–61. doi:10.1002/mop.32961
5. Xu KD, Zhu J, Liao S, Xue Q. Wideband Patch Antenna Using Multiple Parasitic Patches and its Array Application with Mutual Coupling Reduction. *IEEE Access* (2018) 6:42497–506. doi:10.1109/access.2018.2860594
6. Gao G, Zhang R-F, Geng W-F, Meng H-J, Hu B. Characteristic Mode Analysis of a Nonuniform Metasurface Antenna for Wearable Applications. *Antennas Wirel Propag Lett* (2020) 19:1355–9. doi:10.1109/lawp.2020.3001049
7. Supreeyatitikul N, Torrungrueng D, Phongcharoenpanich C. Quadri-Cluster Broadband Circularly-Polarized Sequentially-Rotated Metasurface-Based Antenna Array for C-Band Satellite Communications. *IEEE Access* (2021) 9:67015–27. doi:10.1109/access.2021.3075994
8. Swain R, Chatterjee A, Nanda S, Mishra RK. A Linear-To-Circular Polarization Conversion Metasurface Based Wideband Aperture Coupled Antenna. *J Electr Eng Technol* (2020) 15:1293–9. doi:10.1007/s42835-020-00402-z
9. Liu S, Yang D, Pan J. A Low-Profile Circularly Polarized Metasurface Antenna with Wide Axial-Ratio Beamwidth. *Antennas Wirel Propag Lett* (2019) 18:1438–42. doi:10.1109/lawp.2019.2919533
10. Yuan L, Yu-Xuan H, Zhan-Wei L, Shu-Ting C, Xiao-Ming X, Jing G. Design of a Compact Wideband CP Metasurface Antenna. *Int J RF Microwave Computer-Aided Eng* (2020) 30:e22332. doi:10.1002/mmce.22332
11. Fan Y, Wang J, Li Y, Zhang J, Han Y, Qu S. Low-RCS and High-Gain Circularly Polarized Metasurface Antenna. *IEEE Trans Antennas Propagat* (2019) 67:7197–203. doi:10.1109/tap.2019.2920355
12. Wang Z, Liang T, Dong Y. Metamaterial-based , Compact, Wide Beam-width Circularly Polarized Antenna for 5G Indoor Application. *Microw Opt Technol Lett* (2021) 63:2171–8. doi:10.1002/mop.32866
13. Xu K-D, Luyen H, Behdad N. A Decoupling and Matching Network Design for Single- and Dual-Band Two-Element Antenna Arrays. *IEEE Trans Microwave Theor Techn.* (2020) 68:3986–99. doi:10.1109/tmtt.2020.2989120
14. Qas Elias BB, Soh PJ, Abdullah Al-Hadi A, Vandenbosch GAE. Design of a Compact, Wideband, and Flexible Rhombic Antenna Using CMA for WBAN/WLAN and 5G Applications. *Int J Numer Model Electron Networks, Devices Fields* (2021) 34:e2841. doi:10.1002/jnm.2841
15. Liang Z, Ouyang J, Yang F. Design and Characteristic Mode Analysis of a Low-Profile Wideband Patch Antenna Using Metasurface. *J Electromagn Waves Appl* (2018) 32:2304–13. doi:10.1080/09205071.2018.1507843
16. Zhao C, Wang C-F. Characteristic Mode Design of Wide Band Circularly Polarized Patch Antenna Consisting of H-Shaped Unit Cells. *IEEE access* (2018) 6:25292–9. doi:10.1109/access.2018.2828878
17. Huang H, Wen H. Miniaturized Reconfigurable Tri-polarization Metantenna Based on Characteristic Mode Analysis with High-aperture Efficiency. *Int J RF Microwave Computer-Aided Eng* (2021) 31:e22867. doi:10.1002/mmce.22867
18. Li X, Xi X, Yang X, Chen P, Wu R-X. Compact Patch Antenna Enabled by a Metasurface with Stereo Elements. *Opt Express* (2020) 28:38983–92. doi:10.1364/oe.412315
19. Mohanty A, Behera BR. CMA Assisted 4-port Compact MIMO Antenna with Dual-Polarization Characteristics. *AEU - Int J Elect Commun* (2021) 137:153794. doi:10.1016/j.aeue.2021.153794
20. Yan S, Vandenbosch GAE. Design of Wideband Button Antenna Based on Characteristic Mode Theory. *IEEE Trans Biomed Circuits Syst* (2018) 12:1383–91. doi:10.1109/tbcas.2018.2857466
21. Liu Y, Huang YX, Liu ZW, Cai ST, Xiong XM, Guo J. A New Broadband Circularly Polarized Antenna with a Single-layer Metasurface. *Int J RF Microwave Computer-Aided Eng* (2020) 30:e22226. doi:10.1002/mmce.22226
22. Rajanna PK, Rudramuni K, Kandasamy K. Characteristic Mode-Based Compact Circularly Polarized Metasurface Antenna for In-Band RCS Reduction. *Int J Microwave Wireless Tech* (2019) 12:1–7. doi:10.1017/s1759078719001119
23. Liang Z, Ouyang J, Yang F. Low-profile Wideband Circularly Polarised Single-layer Metasurface Antenna. *Electron Lett* (2018) 54:1362–4. doi:10.1049/el.2018.6790
24. Zhao W, Long L, Li Y, Xi C. Metasurface Superstrate Antenna with Wideband Circular Polarization for Satellite Communication Application. *IEEE Antennas Wireless Propagation Lett* (2016) 15:374–7.
25. Rajanna PKT, Rudramuni K, Kandasamy K. A High-Gain Circularly Polarized Antenna Using Zero-index Metamaterial. *Antennas Wirel Propag Lett* (2019) 18:1129–33. doi:10.1109/lawp.2019.2910805
26. Yue T, Jiang ZH, Werner DH. Compact, Wideband Antennas Enabled by Interdigitated Capacitor-Loaded Metasurfaces. *IEEE Trans Antennas Propagat* (2016) 64:1595–606. doi:10.1109/tap.2016.2535499
27. Hussain N, Naqvi SI, Awan WA, Le TT. A Metasurface-based Wideband Bidirectional Same-sense Circularly Polarized Antenna. *Int J RF Microwave Computer-Aided Eng* (2020) 30:e22262. doi:10.1002/mmce.22262
28. Juan Y, Yang W, Che W. Miniaturized Low-Profile Circularly Polarized Metasurface Antenna Using Capacitive Loading. *IEEE Trans Antennas Propagat* (2019) 67:3527–32. doi:10.1109/tap.2019.2902735

Conflict of Interest: The authors declare that the research was conducted in the absence of any commercial or financial relationships that could be construed as a potential conflict of interest.

frontiers in Physics

ORIGINAL RESEARCH
published: 17 February 2022
doi: 10.3389/fphy.2022.851121

Highly Efficient Dual-Beam Frequency Scanning Based on SSPPs With Parasitic Patch Array

Bai Cao Pan[1,2], *Ben Jian Guo*[1], *Ping Yu*[1], *Ben Geng Cai*[1], *Xi Wang Dai*[1] *and Guo Qing Luo*[1]*

[1]*Key Laboratory of RF Circuits and System Ministry of Education, School of Electronics and Information, Hangzhou Dianzi University, Hangzhou, China,* [2]*State Key Laboratory of Millimeter Waves, Southeast University, Nanjing, China*

A leaky-wave antenna (LWA) realizes radiation of travelling wave along guiding structures. Periodic modulation is an effective approach to turn non-radiating modes into radiating modes. A high-efficient LWA based on spoof surface plasmon polaritons (SSPPs) loaded with parasitic patch array is proposed. Sinusoidal modulation is used for the radiation of SSPPs, while parasitic array mitigates the open stopband (OSB) effect. A prototype is fabricated and measured. The measured and simulated results agree well with each other. Such design shows wide angle coverage of 83° from backward to forward and stable gain distribution of about 12 dB within the whole operating band.

Keywords: dual-beam, frequency scanning, SSPPs, highly efficient, parasitic patch array

OPEN ACCESS

Edited by:
Zhewang Ma,
Saitama University, Japan

Reviewed by:
Xi Gao,
Guangxi University of Science and Technology, China
Shen Xiaopeng,
China University of Mining and Technology, China

***Correspondence:**
Guo Qing Luo
luoguoqing@hdu.edu.cn

Specialty section:
This article was submitted to Optics and Photonics, a section of the journal Frontiers in Physics

Received: *09 January 2022*
Accepted: *24 January 2022*
Published: *17 February 2022*

Citation:
Pan BC, Guo BJ, Yu P, Cai BG, Dai XW and Luo GQ (2022) Highly Efficient Dual-Beam Frequency Scanning Based on SSPPs With Parasitic Patch Array. Front. Phys. 10:851121. doi: 10.3389/fphy.2022.851121

INTRODUCTION

Leaky-wave antennas (LWAs) was first introduced by Hansen in 1940, consisting of a slotted rectangular waveguide [1]. Since then, great improvements have been achieved in such field, taking advantages of low profile, wide frequency scanning coverage and ease of fabrication [2]. LWAs are popular in microwave designs because conical beam with good directivity related to frequency is achieved without complex feeding network. In recent years, they have been used in high-resolution radar systems, conformal antennas on aircraft, satellites, and guiding systems.

Spoof surface plasmon polaritons (SSPPs) are novel guiding modes excited on the surface of periodic metamaterial structures. Such modes mimic the dispersion property of surface plasmon polaritons (SPPs) that only exist in optical or near-infrared bands. SSPPs shows unique properties of low-pass, high field confinement, and shorter operating wavelength, which provides great reference to improve traditional microwave circuits and systems. In 2014, broadband excitement of SSPPs is reported, which makes great contributions to researches of SSPPs [3]. Since then, a series of passive and active functional devices based on SSPPs were reported [4–8].

However, the near electric field of SSPP modes locates around the metallic structure of the SSPP waveguides during propagation. It decays exponentially with the increasing distance away from the waveguide. Such distribution ensures low cross-talk between devices while increasing difficulties in designing radiation components. In order to turn the non-radiating mode into a radiating mode, periodical modulation and parasitic radiating patches are used. SSPP could work as excitation of certain patches to achieve effective radiation. Two rows of circular patch arrays were excited by SSPP transmission line with both perfect electric conductor (PEC) and artificial magnetic conductor (AMC) [9]. A single-beam scanning range of 40° is obtained. The circular patch array placed at only one side of the SSPP structures could also provide single-beam radiation [10]. In such circumstances, a lateral radiation with stable high gains is designed. Open-loop elements were also used as radiation

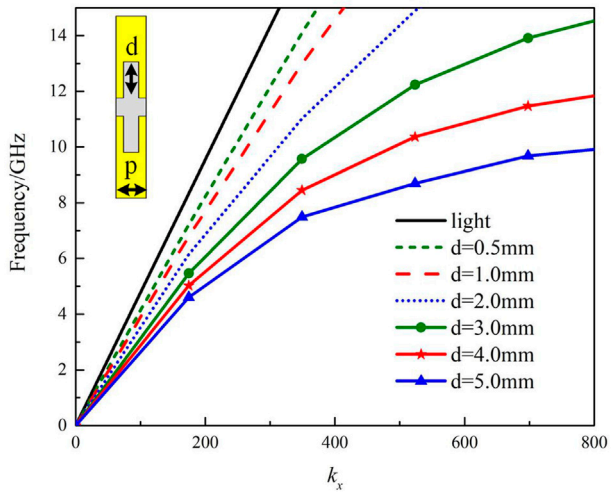

FIGURE 1 | The wavenumber k_x of SSPP unit under different dimensions. Inset: the structure of the complementary SSPP unit with dimensions labelled.

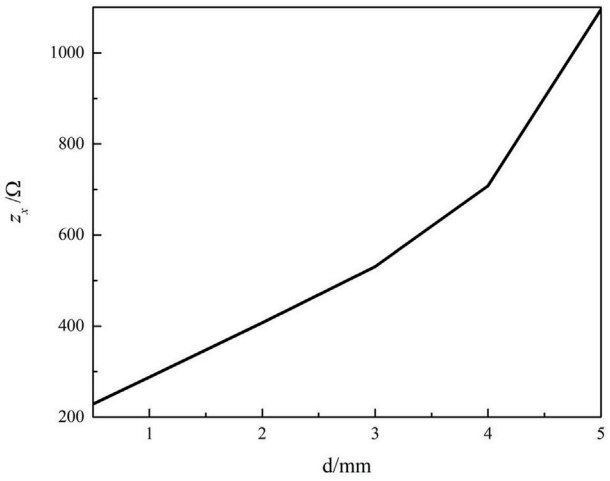

FIGURE 2 | Surface impedance of SSPP corresponding to different groove depth d.

elements to design two Ka-band LWA with frequency scanning in both E-plane and H-plane [11]. In 2021, a novel split-ring-shaped SSPP transmission line is proposed to excited two elliptical-shaped patch arrays [12]. The open stopband (OSB) effect is mitigated and a wide scanning range from −90° to 22° is demonstrated. Circular patches fed by symmetrical SSPP are able to form dual-linear polarization [13]. For different excitation of in-phase and out-phase on SSPP structures, horizontal and vertical polarizations are acquired. Despite of exciting patches as radiators, periodic modulation of SSPP units could also provide efficient radiation. A wide-scanning-angle LWA is proposed with shorting stubs loaded with metallic posts [14]. The scanning range reaches 80 ° with high realized gain. Periodic surface waveguide is cascaded between two SSPP transmission lines to form well-performed LWA [15]. Such antenna produces a single-side scanning beam of 8.7 dB gain with an overall efficiency of 75%. Backfire beam scanning is investigated based on the odd-mode SSPPs [16]. The main beam scans from backfire to broadside with high gain and radiation efficiency. Different order of space harmonics of periodic modulated SSPP is also used to provides extra radiation beam [17]. Both -1st and -2nd order space harmonics were proposed for forward and backward radiation respectively.

In this paper, a highly efficient LWA is proposed for wide beam scanning coverage from backward to forward. Periodically modulated grooves are used for the radiation of SSPP mode. And parasitic patch array is added inside the complementary SSPP line to improve radiation efficiency and mitigate the OSB effect.

Radiation of SSPPs

As a kind of TM surface modes, the surface impedance of SSPP mode could be obtained from its dispersion property according to the surface impedance theory. For SSPP mode, electric field decays exponentially with the distance away from the waveguide. The wavenumber along the direction perpendicular to the structure is imaginary. Thus, the wavenumber in transmission direction is real and it is larger than the that in free space. The surface impedance of SSPP could be expressed as:

$$Z = Z_0 \sqrt{1 - \left(\frac{k_x}{k_0}\right)^2} \tag{1}$$

where $Z_0 = \sqrt{\mu_0/\varepsilon_0}$ and k_0 are the wave impedance and wavenumber in free space, k_x is the wavenumber of SSPP along transmission direction.

The wavenumber of SSPP k_x could be calculated from its dispersion relationship. The dispersion relationship of traditional complementary SSPP grooves are shown in **Figure 1**. The structure of the unit is shown in the inset of **Figure 1**. The cycle of the unit p is 1 mm. The depth of the groove is d. And the widths of the center slot and groove are 2 and 0.5 mm, respectively. The cut-off frequencies of the units are directly controlled by the depths of the grooves. At a certain frequency, the deeper the groove is, the larger its wavenumber would be. From the figure we can also find that such mode located in slow wave area and it would not radiate. Hence, according to the LWA theory, periodic modulation is used. The dimensions of the grooves along transmission direction is designed under sinusoidal distribution. The surface impedance is expressed as

$$Z_x = jX_s\left[1 + M^{'}\cos\left(\frac{2\pi x}{P_n}\right)\right] \tag{2}$$

where X_s is the average surface impedance, $M^{'}$ is the modulation factor, P_n is the cycle of the composite modulated unit. Sinusoidal modulation could excite multiple space harmonics. The n-order space harmonic along transmission direction is

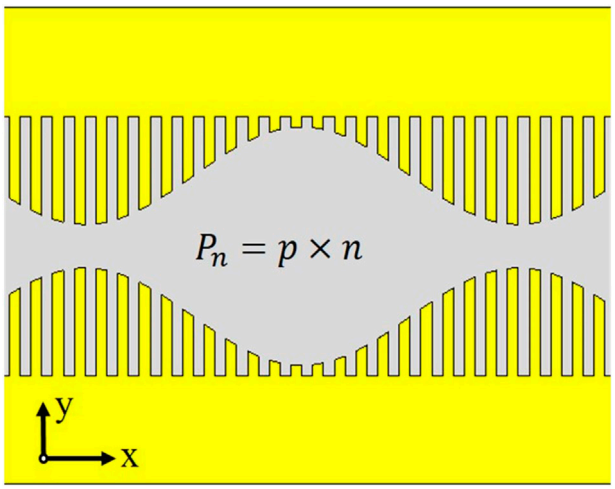

FIGURE 3 | The structure of the periodic modulated composite SSPP unit.

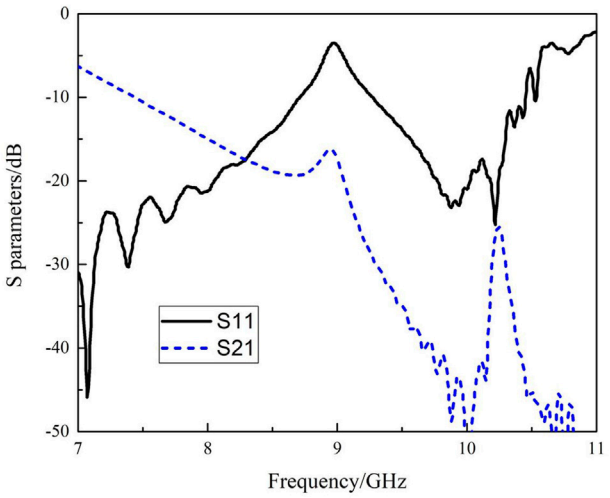

FIGURE 5 | The simulated S parameters of the LWA based on SSPP.

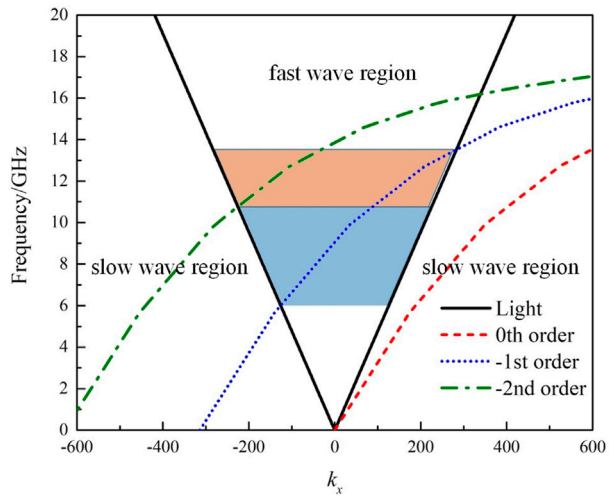

FIGURE 4 | The dispersion relationship of space harmonics.

$$k_{x,n} = k_{x,0} + \frac{2\pi n}{P_n} \tag{3}$$

According to the radiation theory of LWA, frequency scanning is valid as long as the condition of $|k_{x,-1}| \le k_0$ is met. And the radiation direction is calculated with

$$\theta_{-1} = \arcsin\left(\sqrt{1 + X'^2} - \frac{2\pi}{k_0 P_n}\right) \tag{4}$$

where $X' = X_s/Z_0$ is normalized surface impedance.

The center frequency of the proposed radiator is designed to be around 9 GHz. Since the wavenumber of SSPP is dispersive, the surface impedance under different groove depths at 9 GHz is collected and shown in **Figure 2**. Since the cut-off frequency would be below 9 GHz when depth exceeds 6 mm. The maximum of the depth used is 5 mm. And the minimum of the depth is 0.5 mm. The surface impedance changes from 229 Ω to 1,095 Ω. The average surface impedance X_s is chose to be 500 Ω when the depth is 2.8 mm. The normalized surface impedance $X' = 1.33$. Since the antenna shows broadside radiation at 9 GHz, the radiation direction $\theta_{-1} = 0°$. We got the modulated composite cycle $P_n = \lambda_0/\sqrt{1 + X'^2} = 20.032$ mm. The modulated number $n = 20$ is used. The structure of the modulated composite unit is shown in **Figure 3** with 20 sub-units of grooves per unit. The depth of each sub-unit follows the sinusoidal distribution. The maximum and minimum dimensions of grooves in the composite unit are 5 and 0.5 mm respectively.

The modulated n-order space harmonics of the average wavenumber is shown in **Figure 4**. Most harmonics locate outside the symmetrical light axis. Within band from 6 to 10.5 GHz (blue marked area), only the -first order harmonic locates in the fast wave area. Good frequency scanning could be realized. Within band from 10.5 to 14 GHz (orange marked area), both -first and -2nd order harmonics locates in the fast wave area. In such circumstance, radiation beam would split into two lobes in both backward and forward directions. The efficiency and radiation pattern would be affected. So the antenna is designed for band in which only -first order harmonic works.

Periodic extension of the composite unit forms a high-performance leaky-wave radiation. The S parameters of such 2-port device is shown in **Figure 5**. Backward and forward frequency scanning are achieved around 8 and 9.5 GHz. However, within the operating band, a clearly uplift around 9 GHz is observed due to the OSB effect. The reflection at 9 GHz reaches -3.5 dB, which means most of the energy is reflected back to input. The radiation efficiency is damaged.

Improved Performance With Parasitic Patch Array

In order to improve the broadside radiation efficiency, parasitic circular patch array is introduced. The patches are excited by the

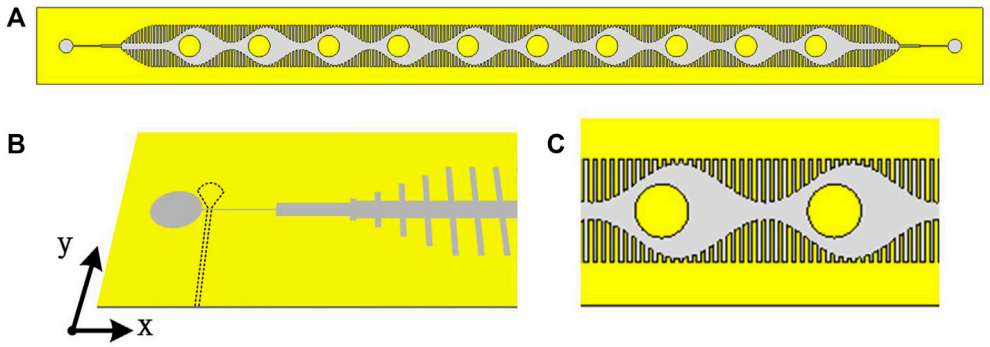

FIGURE 6 | Schematic structure of **(A)** the proposed device, **(B)** the feeding network and **(C)** the composite unit.

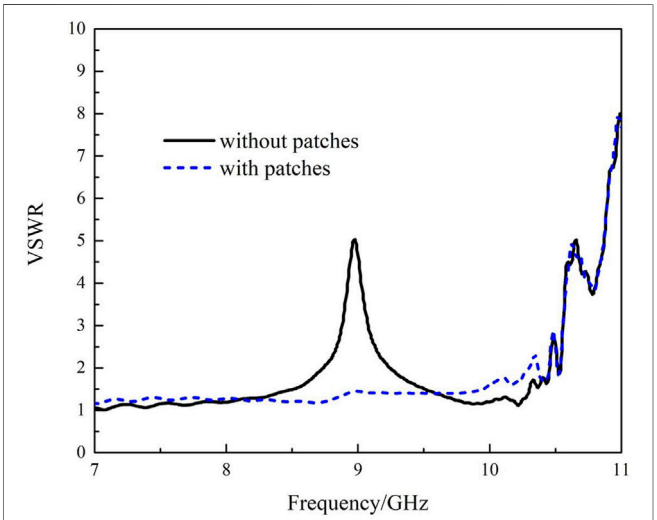

FIGURE 7 | VSWR of designs with and without parasitic patches.

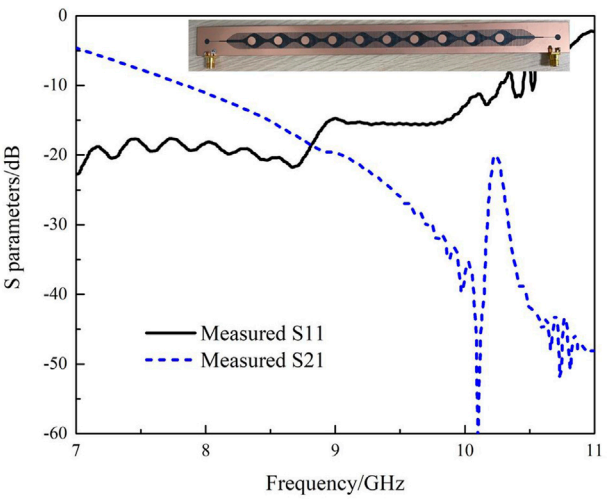

FIGURE 8 | Measured S parameters of the proposed design. Inset: Photo of the prototype.

SSPP mode inside the transmission structure and provide extra radiation. The operating wavelength of the SSPP transmission line can be obtained from the modulated average wavenumber as $\lambda_{8.8GHz} = 2\pi/k_x = 12.6$ mm. Thus, the radius of the circular patch is set to be 3.1 mm. As long as the patches locate in the same area, the phase different on the patches can be ignored and broadside radiation could be realized. On the other hand, limited by the space allocation, the cycle of the patch array is also 20 mm, larger than the operating wavelength. According to antenna theory of linear array in broadside design, grating lobe would occur. In addition, the patches are placed 2.2 mm to the left of the center of the composite unit. The center point of the composite unit is defined as the place where the minimum groove's depth appears. When the patches deviate from the center point, the symmetry of the composite unit is broken and the OSB effect can be mitigated. The schematic structure of the proposed design is shown in **Figure 6**. At both terminals, microstrip lines on the bottom layer is used for excitation and reception. Circular cavities are supposed to improve the coupling efficiency between the slot and microstrip lines. Six units of grooves with gradient depths are used for broadband excitation of SSPP mode. And ten-unit of the composite units are cascaded for leaky-wave radiation.

The voltage standing wave ratio (VSWR) of the design with and without parasitic patches are compared in **Figure 7**. Within the whole operating band, the design with parasitic patches keeps around 1.4, and the significant peak disappeared.

The prototype illustrated in the inset of **Figure 8** is fabricated on F4B substrate with whole dimensions of 270 mm × 20 mm. The thickness of the substrate is 0.5 mm and its relative dielectric constant is 2.65. The measured S parameters are shown in **Figure 8**. Both reflection and transmission are below -10 dB from 8 to 10 GHz, indicating a good radiation performance. OSB effect for broadside radiation around 9 GHz is clearly suppressed. And beam-scanning from backward to forward is realized. For band from 7 to 8 GHz, transmission is above -10dB. The total efficiency drops but the radiation pattern still shows high gain property, which would be discussed later.

The simulated and measured far-field radiation patterns are shown in **Figure 9**, corresponding to different frequencies. The

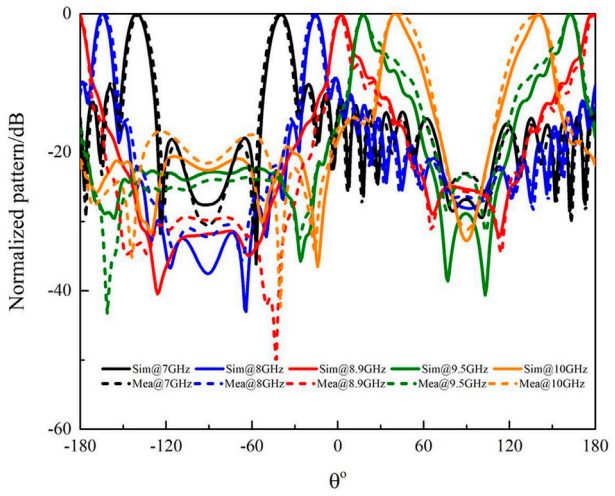

FIGURE 9 | Simulated and measured normalized pattern at different frequencies.

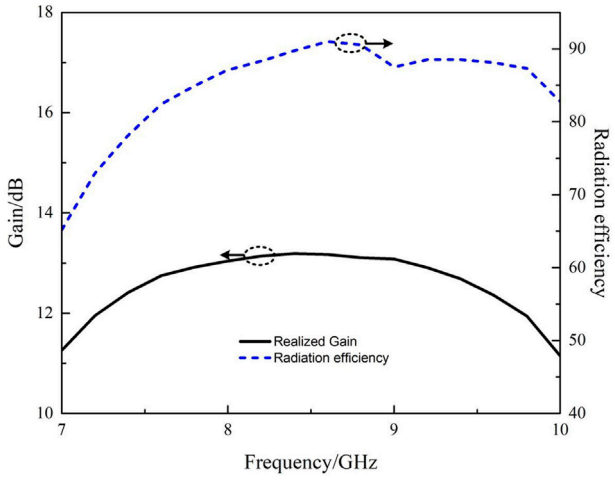

FIGURE 10 | Realized gain and radiation efficiency.

broadside radiation appears at 8.9 GHz. The measured results are in good agreement with the simulated results. Within band from 7 to 9 GHz, the design shows radiation of backward frequency scanning. And within band from 9 to 10 GHz, forward radiation is accomplished. the direction of the main lobe at 7 GHz, 8 GHz, 9.5 GHz and 10 GHz are -41°, -17°, 16° and 42°, respectively. The broadside radiation locates at 8.9 GHz with narrowest HPBW of 4.5 °. And it increases with the frequency increasing or decreasing. The HPBWs at 7 and 10 GHz are 6.4° and 8°, respectively. The measured HPBWs are about 1° smaller than the simulated ones. The simulated total efficiencies and measured gains are shown in **Figure 10**. The gain keep stable at around 12 dB within the whole operating band. And the maximum gain of 13.2 dB appears at 8.4 GHz.

CONCLUSION

In this letter, a high-efficient dual-beam LWA based on complementary SSPP modes has been proposed. Wide scanning coverage from backward radiation to forward radiation is achieved. Additional parasitic patch array is introduced in the modulated composite unit to improve the radiation efficiency and mitigates the OSB effect. The device shows stable gain distribution within the whole operating band, while scanning from −41 ° to 42 °. A prototype is fabricated and measured. The measured results agree with the simulated ones. Such design is available for conformal applications and other kinds of radiation systems.

DATA AVAILABILITY STATEMENT

The original contributions presented in the study are included in the article/Supplementary Material, further inquiries can be directed to the corresponding author.

AUTHOR CONTRIBUTIONS

All authors listed have made a substantial, direct, and intellectual contribution to the work and approved it for publication.

FUNDING

This work is supported by Open Research Program of State Key Laboratory of Millimeter Wave under contract K202221.

REFERENCES

1. Jackson DR, Caloz C, Itoh T. Leaky-Wave Antennas. *Proc IEEE* (2012) 100(7): 2194–206. doi:10.1109/jproc.2012.2187410
2. Caloz C, Jackson DR, Itoh T. *Leaky-wave Antennas, in Frontiers in AntennasNext Generation Design & Engineering*. New York: McGraw-Hill (2011).
3. Ma HF, Shen X, Cheng Q, Jiang WX, Cui TJ. Broadband and High-Efficiency Conversion from Guided Waves to Spoof Surface Plasmon Polaritons. *Laser Photon Rev* (2014) 8:146–51. doi:10.1002/lpor.201300118
4. Pan BC, Liao Z, Zhao J, Cui TJ. Controlling Rejections of Spoof Surface Plasmon Polaritons Using Metamaterial Particles. *Opt Express* (2014) 22: 13940. doi:10.1364/oe.22.013940
5. Gao X, Hui Shi J, Shen X, Feng Ma H, Xiang Jiang W, Li L, et al. Ultrathin Dual-Band Surface Plasmonic Polariton Waveguide and Frequency Splitter in Microwave Frequencies. *Appl Phys Lett* (2013) 102:151912. doi:10.1063/1.4802739
6. Panaretos AH, Werner DH. Spoof Plasmon Radiation Using Sinusoidally Modulated Corrugated Reactance Surfaces. *Opt Express* (2016) 24:2443. doi:10.1364/oe.24.002443

7. Xu Y, Gu C, Hou B, Lai Y, Li J, Chen H. Broadband Asymmetric Waveguiding of Light without Polarization Limitations. *Nat Commun* (2013) 4:2561. doi:10.1038/ncomms3561
8. Xu K-D, Lu S, Guo Y-J, Chen Q. High-order Mode of Spoof Surface Plasmon Polaritons and its Application in Bandpass Filters. *IEEE Trans Plasma Sci* (2021) 49(1):269–75. doi:10.1109/tps.2020.3043889
9. Zhang Q, Zhang Q, Chen Y. Spoof Surface Plasmon Polariton Leaky-Wave Antennas Using Periodically Loaded Patches above PEC and AMC Ground Planes. *Antennas Wirel Propag Lett* (2017) 16:3014–7. doi:10.1109/lawp.2017.2758368
10. Liu L, Chen M, Cai J, Yin X, Zhu L. Single-Beam Leaky-Wave Antenna with Lateral Continuous Scanning Functionality Based on Spoof Surface Plasmon Transmission Line. *IEEE Access* (2019) 7:25225–31. doi:10.1109/access.2019.2899824
11. Cao D, Li Y, Wang J. Spoof Surface Plasmon Polaritons Fed Frequency-Scanning Open-Loop Antenna Arrays. *IEEE Access* (2019) 7:179954–60. doi:10.1109/access.2019.2956999
12. Ye L, Yang Z, Zhuo J, Han F, Li W, Liu QH. A Back-Fire to Forward Wide-Angle Beam Steering Leaky-Wave Antenna Based on SSPPs. *in IEEE Trans Antennas Propagation* (2021) 1:1. doi:10.1109/TAP.2021.3137241
13. Yu HW, Jiao YC, Zhang C, Weng ZB. Dual-Linearly Polarized Leaky-Wave Patch Array with Low Cross-Polarization Levels Using Symmetrical Spoof Surface Plasmon Polariton Lines. *IEEE Trans Antennas Propagation* (2021) 69(3):1781–6.
14. Wei D, Li J, Yang J, Qi Y, Yang G. Wide-Scanning-Angle Leaky-Wave Array Antenna Based on Microstrip SSPPs-TL. *Antennas Wirel Propag Lett* (2018) 17(8):1566–70. doi:10.1109/lawp.2018.2855178
15. Ge S, Zhang Q, ChiuChiu CYY, Chen Y, Murch RD. Single-Side-Scanning Surface Waveguide Leaky-Wave Antenna Using Spoof Surface Plasmon Excitation. *IEEE Access* (2018) 6:66020–9. doi:10.1109/access.2018.2879086
16. Du X, Ren J, Li H, Zhang C, Liu Y, Yin Y. Design of a Leaky-Wave Antenna Featuring Beam Scanning from Backfire Utilizing Odd-Mode Spoof Surface Plasmon Polaritons. *IEEE Trans Antennas Propagat* (2021) 69(10):6971–6. doi:10.1109/tap.2021.3076166
17. Zhang C, Ren J, Du X, Yin Y. Dual-Beam Leaky-Wave Antenna Based on Dual-Mode Spoof Surface Plasmon Polaritons. *Antennas Wirel Propag Lett* (2021) 20(10):2008–12. doi:10.1109/lawp.2021.3102060

Conflict of Interest: The authors declare that the research was conducted in the absence of any commercial or financial relationships that could be construed as a potential conflict of interest.

frontiers in Physics

ORIGINAL RESEARCH
published: 17 February 2022
doi: 10.3389/fphy.2022.851150

Unequal Bandpass Filtering Power Divider Based on Hybrid HMSIW-SSPP Modes

Bai Cao Pan[1,2], *Ping Yu*[1], *Ben Jian Guo*[1], *Ya Hui Qian*[1] *and Guo Qing Luo*[1]*

[1]Key Laboratory of RF Circuits and System Ministry of Education, School of Electronics and Information, Hangzhou Dianzi University, Hangzhou, China, [2]State Key Laboratory of Millimeter Waves, Southeast University, Nanjing, China

This letter presents a novel unequal bandpass filtering power divider based on hybrid-mode of half mode substrate integrated waveguide (HMSIW) and spoof surface plasmon polaritons (SSPPs). Bandpass response is achieved by combining the transmission properties of HMSIW and SSPPs simultaneously. The operating bandwidth can be designed in a wide range by simply optimizing the dimensions of HMSIW and SSPPs. In addition, defected ground structures (DGSs) are etched on the bottom of the substrate to improve out-of-band suppression. The power division ratio of the proposed unequal power divider is finally optimized to 1:3. The measured results agree with the simulated one. Such design provides a stable power division within wide frequency range from 6.5 to 9.5 GHz.

Keywords: unequal power divider, bandpass filtering, SSPPs, HMSIW, wide band

OPEN ACCESS

Edited by:
Kai-Da Xu,
Xi'an Jiaotong University, China

Reviewed by:
Cheng Zhang,
Wuhan University of Technology, China
Jia-Yuan Yin,
Xidian University, China

***Correspondence:**
Guo Qing Luo
luoguoqing@hdu.edu.cn

Specialty section:
This article was submitted to Optics and Photonics, a section of the journal Frontiers in Physics

Received: *09 January 2022*
Accepted: *24 January 2022*
Published: *17 February 2022*

Citation:
Pan BC, Yu P, Guo BJ, Qian YH and Luo GQ (2022) Unequal Bandpass Filtering Power Divider Based on Hybrid HMSIW-SSPP Modes. Front. Phys. 10:851150. doi: 10.3389/fphy.2022.851150

INTRODUCTION

The rapid development of wireless communication systems proposes more and more requirements for functional devices. In order to meet the market demands, different kinds of well-performed functional devices have been widely studied. In the past decade, substrate integrated waveguide (SIW) has become one of the hotspots in researches [1]. Considering its perfect high-pass transmission with low-loss, high-efficient properties, functional devices such as filter [2], power divider [3–6] and coupler [7] have been proposed. Half-mode SIW (HMSIW) consists of only half of SIW structures, while keeping the same performance as SIW [8, 9]. Miniaturization can be realized. Spoof surface plasmon polaritons (SSPPs) are guiding surface modes along periodic metamaterial structures. Such modes have also received wide attention for its unique properties of perfect low-pass transmission and near-field confinement [10, 11]. SSPPs have been studies in field of different high-efficient designs such as bandpass filter [12, 13], power divider [14, 15], coupler [16], radiator [17].

Filters and power dividers are the most commonly-used functional devices in wireless communication systems. In certain applications, both kinds of devices are required to be integrated with each other to reduce the occupied space. And their performances are crucial for systems stability. In recent years, a series of filters and power dividers based SIW and SSPPs have been reported [18, 19]. In order to improve the integration and operating properties, parasitic structures like resonators [20], interdigital structures (ISs) [21], defected ground structures (DGSs) [22, 23] have also been studied. The combination of SIW and SSPP provides a new solution for the miniaturization designs, since the power dividers of SIW are usually narrow-band and those of SSPP have limits of bulky dimensions.

In this letter, we proposed a novel unequal bandpass filtering power divider based on the hybrid HMSIW-SSPP modes, which shows compact size and power division ratio of 1:3. The hybrid unit can

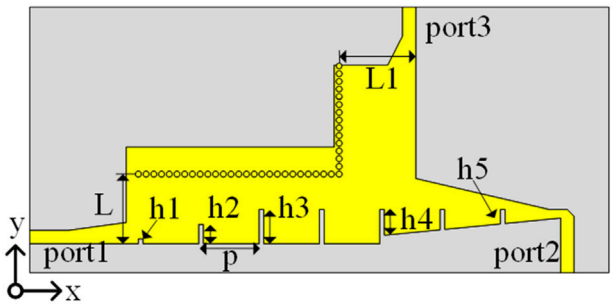

FIGURE 1 | Schematic of the proposed unequal filtering power divider.

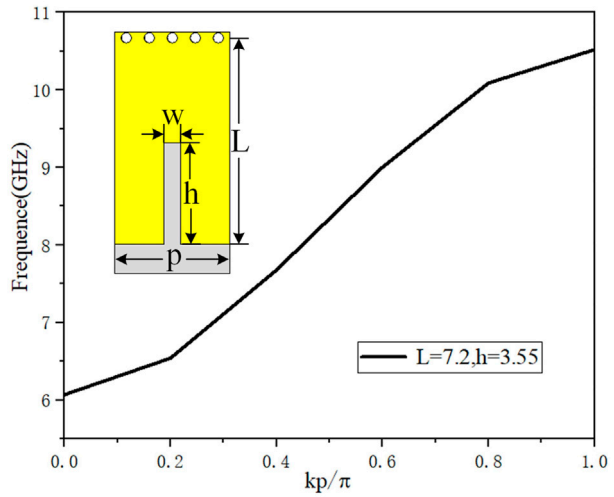

FIGURE 2 | The dispersion curves of the hybrid HMSIW-SSPP unit. Inset: the structure of the hybrid HMSIW-SSPP unit.

be compatible with the functional techniques of both HMSIW and SSPPs. The lower and upper edges of the passband can be controlled independently by changing the dimensions of HMSIW and SSPPs. Defected ground structure is also loaded aiming for improving out-of-band suppression.

Design of Unequal Power Divider

The schematic configuration of the proposed unequal filtering power divider is shown in **Figure 1** with dimensions labelled. As it can be seen in the figure, periodic corrugated slots are etched on the top layer of HMSIW. Two slots with gradient groove depths of h1 and h2 are used to achieve broadband excitation of SSPP modes. Optimizing grooves' depths can help to improvement of the transmission efficiency. Two uniformed grooves of SSPP with depth of h3 are set as the transmission part. They collaborate with the HMSIW structures to provide the hybrid HMSIW-SSPP modes with unique transmission properties. The periodic interval of the SSPP units is p. At the output terminals, a SSPP channel of three unit matching structures with gradient grooves' depths and tapered edges are designed for momentum matching of SSPP at port 2. Meanwhile, another HMSIW channel is paralleled connected between the hybrid unit and the SSPP channel. The widths of both HMSIW structures are L and L1, respectively.

Figure 2 show the dispersion curves of the hybrid HMSIW-SSPP unit. And its structure is shown in the inset of **Figure 2**. It can be observed from the figure that the cutoff frequency of HMSIW modes is lower than that of SSPP modes. Thus, bandpass response can be obtained. The hybrid unit provides bandpass property from 6.1 to 10.5 GHz. As is introduced in literatures, the cutoff frequencies of SIW and SSPP modes can be controlled by changing the width of SIW and the depth of SSPP grooves. For the proposed design, reduction of L or h leads to upper shifting of the lower or upper cutoff frequencies, respectively. Limited by the space allocation, SSPP grooves are always smaller than HMSIW. So the cutoff frequencies of SIW are always lower than those of SSPPs.

The dispersion properties of the hybrid HMSIW-SSPP unit under different parameters are compared in **Figure 3**. The unit with dimensions of h = 3.5 mm, L = 7 mm, w = 0.5 mm and p = 6 mm is used as reference and shown as the red dashed lines in the figure. Then each dimension is optimized and compared. In **Figure 3A**, the groove's depth in HMSIW unit is examined. When the depth h3 increases from 3 to 4 mm, the upper cutoff frequencies shift from 11.2 to 9.4 GHz, while the lower cutoff frequencies keep at 6.1 GHz. Similarly, from **Figure 3B** it can be seen that when width L increases from 6 to 8 mm, the lower cutoff frequencies of the hybrid unit reduce from 6.8 GH to 5.5 GHz. Meanwhile, small range fluctuation between 10.1 and 10.3 GHz of the upper cutoff frequencies is observed. The width of the groove w and its interval p can also be used for the modulation of operating band (shown in **Figures 3C,D**). The groove width w can change the upper cutoff frequencies in a small range. And the interval p has a significant impact on the upper cutoff frequencies. Since the increasing interval would lead to excessive length of the device, depth L is usually used in modulation of operating band.

The simulated transmissions at port 3 of the unequal filtering power divider are illustrated in **Figure 4** to testify the bandwidth modulation of the hybrid unit. As is compared in **Figures 4A,B**, upper cutoff frequencies or lower cutoff frequencies of S_{31} shift to lower frequency band independently without apparently mutual influence. Based on the above analysis, a high-efficient passband from 6.5 to 9.5 GHz of unequal filtering power divider can be designed. The simulated S parameters are shown in **Figure 5**. In the whole passband, the reflection coefficient S_{11} keeps below −10 dB, while the transmission coefficient S_{21} and S_{31} are around −2.2 dB and −7 dB.

OPTIMIZATION AND MEASUREMENT

The DGS can disturb the current distribution on the metallic ground and introduce an extra transmission zero. In the optimized model, a two-element array of inverted T-shaped

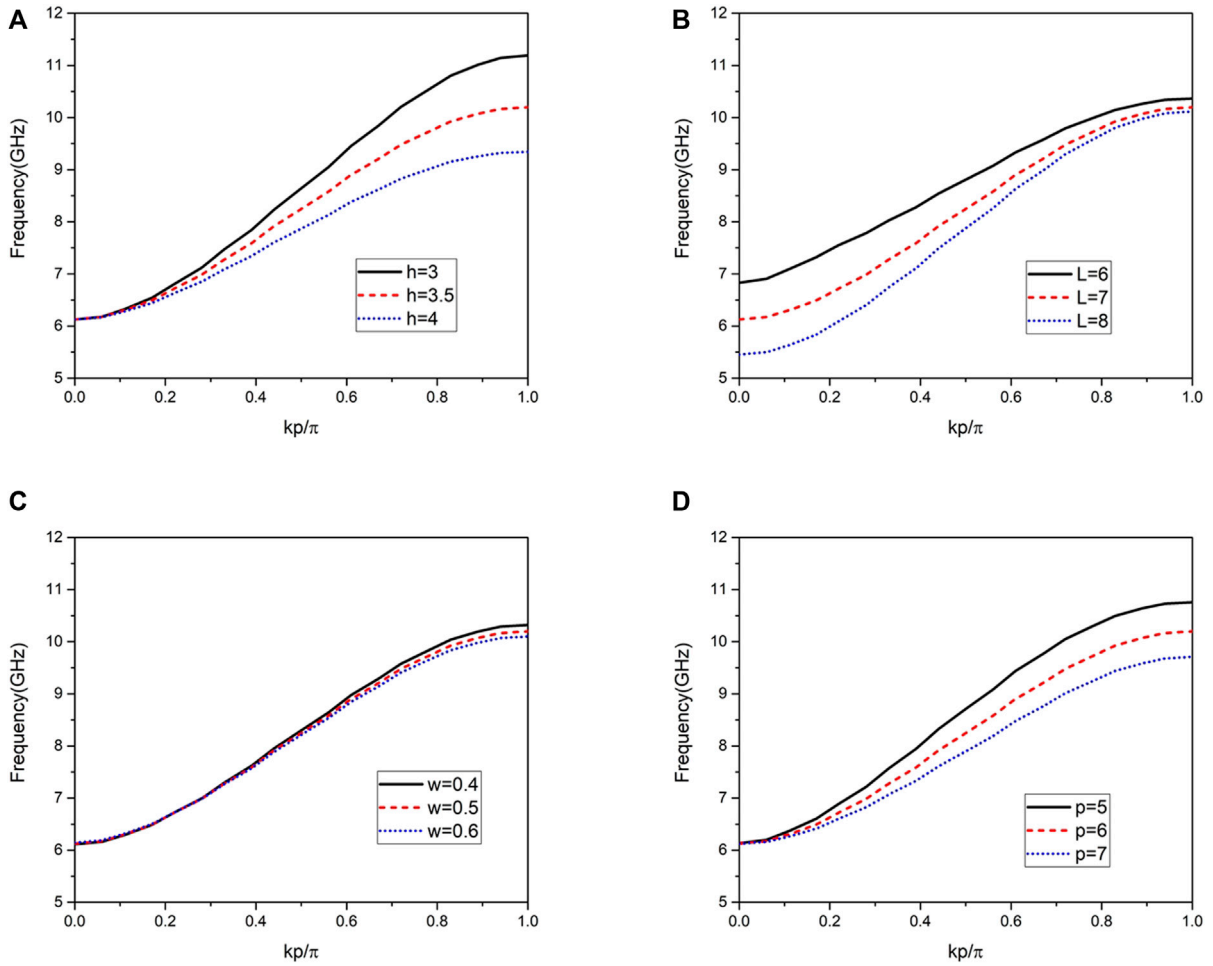

FIGURE 3 | The dispersion properties of the hybrid unit under different parameters of **(A)** depth of SSPP grooves h, **(B)** width of HMSIW L, **(C)** width of SSPP grooves w, and **(D)** interval of SSPPs p.

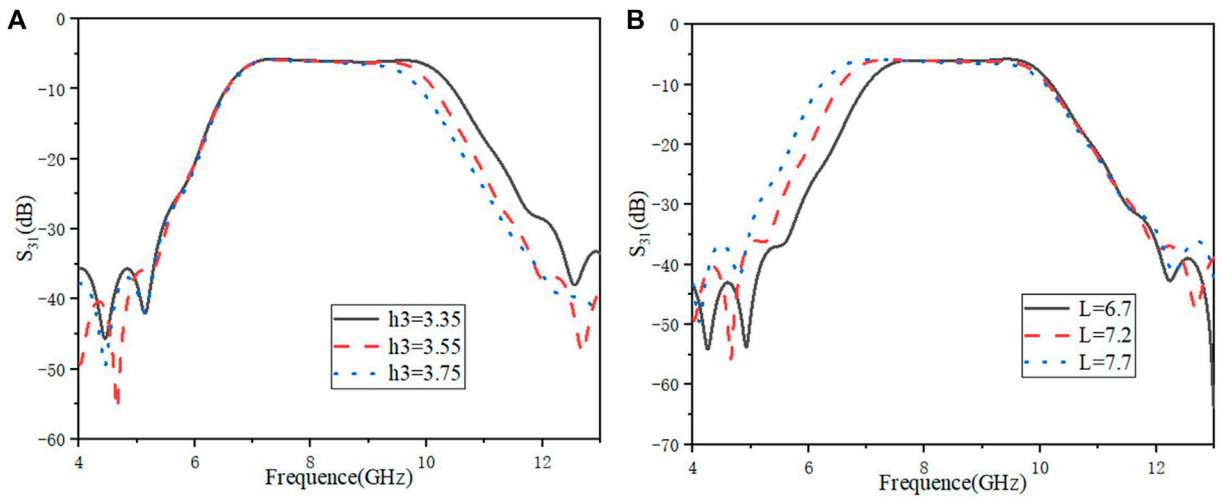

FIGURE 4 | Simulated transmission coefficients (S_{31}) with different dimensions of **(A)** h3 and **(B)** L.

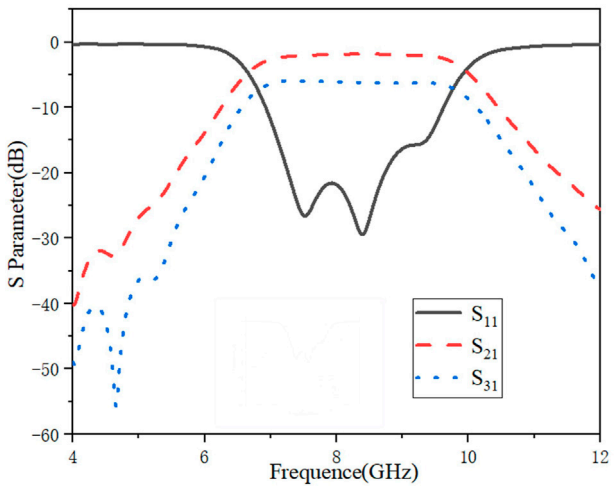

FIGURE 5 | Simulated S parameters of unequal filtering power divider.

DGSs is introduced. The DGSs are loaded on the bottom layer of the hybrid HMSIW-SSPP units to improve the upper stopband rejection. The structure of the DGS unit is shown in the inset of **Figure 6A**, in which the red line represents the contour of the grooves on the top layer. The DGS is etched on the bottom layer and it is in the middle of two adjacent grooves. The dimensions of the DGS decide the frequency of its transmission zero. And the optimized dimensions are a1 = 1.9 mm, a2 = 4.4 mm, a3 = 3.8 m, t = 0.6 mm, s = 0.45 mm, g = 0.25 mm. The comparison of S_{21} of the design with and without the DGSs is shown in **Figure 6A**. The transmission with two-element array of DGSs provides an extra transmission zero, providing better out-of-band suppression. The cut-off efficiency of transmission zero of DGS at 10 GHz can be improved by increasing the number of DGSs used in the model. A small shift of the cutoff frequency of SSPPs is observed due to the coupling between DGSs and SSPPs. The transmission of the proposed design loaded with DGSs are shown in **Figure 6B**. An unequal power divider with bandpass filtering effect is observed within band from 6.5 to 9.5 GHz. The simulated S_{11}

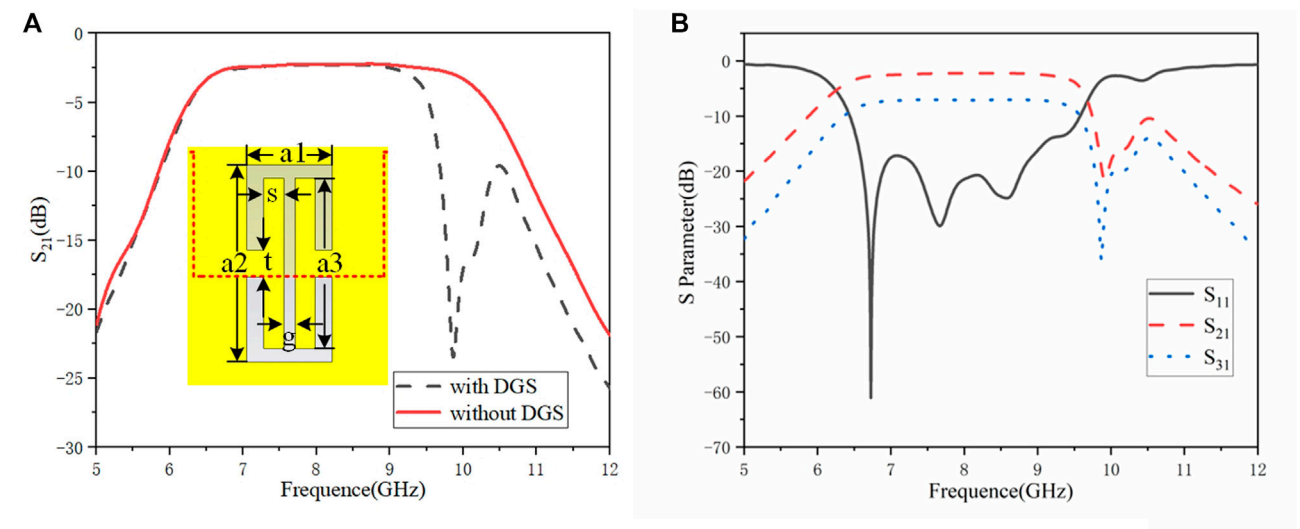

FIGURE 6 | (A) the comparison of S_{21} of the designs with and without DGSs. **(B)** Simulated S-parameters of the design with DGS.

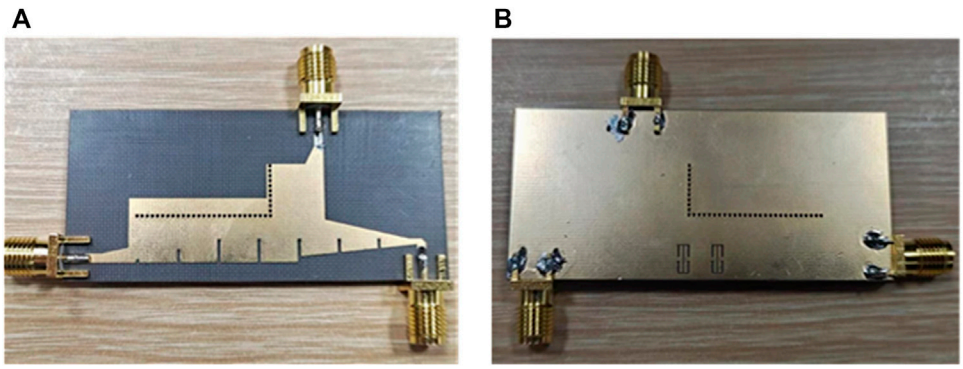

FIGURE 7 | (A) Top view and **(B)** back view of the prototype.

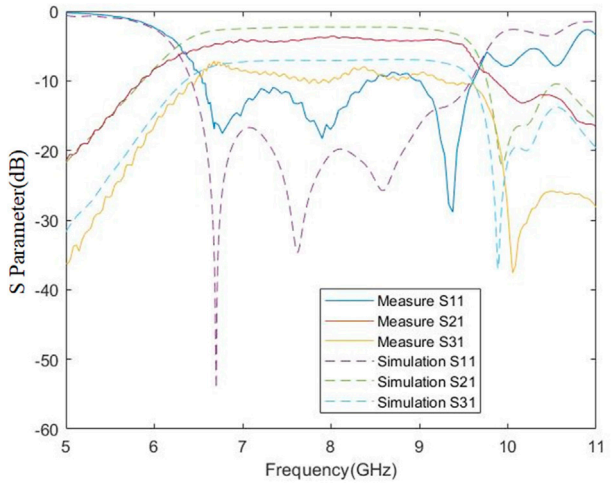

FIGURE 8 | Comparison of simulated and measured S-parameters.

is lower than −20 dB in the passband. S_{21} and S_{31} are −2.2 dB and −7 dB, respectively. Within the whole operating band, S21 undulates between −2.6 dB and −2.3 dB, and S31 undulates between −7.4 dB and −7 dB. The simulations indicate a stable power division. The power division ratio of port 2 and port 3 is 3:1.

A prototype of the proposed unequal filtering power divider is fabricated and measured. The substrate is F4B board with relative permittivity of 2.65 and thickness of 1 mm. Photographs of the prototype are shown in **Figure 7**. The total dimensions of the proposed design are 45 mm × 25 mm × 1 mm. **Figure 8** shows the compared of the simulated and measured S-parameters. The measured transmissions are about 1 dB lower than the simulated ones, because of the machining accuracy of the sample and the unskilled welding of SMA connectors in the experiments. The operating bandwidth and power division effect keeps steady.

CONCLUSION

In this paper, an unequal filtering power divider based on hybrid HMSIW-SSPP mode is proposed. The passband can be controlled independently by changing the dimensions of HMSIW and SSPPs. DGSs are introduced on the bottom layer of the device to improve the out-of-band suppression. A prototype working from 6.5 to 9.5 GHz is designed and fabricated. And power division ratio of 1:3 is obtained. Such design provides solutions for miniaturized multi-functional devices, and could be used in wireless communication systems.

DATA AVAILABILITY STATEMENT

The original contributions presented in the study are included in the article/Supplementary Material, further inquiries can be directed to the corresponding author.

AUTHOR CONTRIBUTIONS

All authors listed have made a substantial, direct, and intellectual contribution to the work and approved it for publication.

FUNDING

This work is supported partly by Open Research Program of State Key Laboratory of Millimeter Wave under contract K202221, partly by Zhejiang Provincial Natural Science Foundation of China under contract LQ19F010010, and partly by National Natural Science Foundation of China under contract 61901143.

REFERENCES

1. Deslandes D, Wu K. Integrated Microstrip and Rectangular Waveguide in Planar Form. *IEEE Microw Wireless Compon Lett* (2001) 11(2):68–70. doi:10.1109/7260.914305
2. Nedelchev M, Stosić B, Iliev I, Ilieva A, Dončov N. "Wave-based Digital Model of Substrate-IntegratedWaveguide (SIW) Filters for K Band," In 2020 43rd International Conference on Telecommunications and Signal Processing (TSP); Milan, Italy (2020). p. 325–8. doi:10.1109/TSP49548.2020.9163541
3. Shreyus GS, Khatwani H, Shambavi K. "Power Divider with Substrate Integrated Waveguide and CSRR for C Band Application," In 2017 Innovations in Power and Advanced Computing Technologies (i-PACT); Vellore, India (2017). p. 1–5. doi:10.1109/IPACT.2017.8245019
4. Xu H-X, Wang G-M, Zhang C-X, Yu Z-W, Chen X. Composite Right/left-Handed Transmission Line Based on Complementary Single-Split Ring Resonator Pair and Compact Power Dividers Application Using Fractal Geometry. *IET Microw Antennas Propag* (2012) 6(9):1017–25. doi:10.1049/iet-map.2011.0427
5. Moznebi A-R, Afrooz K. Compact Power Divider Based on Half Mode Substrate Integrated Waveguide (HMSIW) with Arbitrary Power Dividing Ratio. *Int J Microw Wireless Technol* (2017) 9(3):515–21. doi:10.1017/S1759078716000544
6. Xu H-X, Liang J-G, Wang G-M, Wu F-T, Zhang C-X. Modelling of Composite Right/left-Handed Transmission Line Based on Fractal Geometry with Application to Power Divider. *Microwaves, Antennas & Propagation, IET* (2012) 6:1415–21. doi:10.1049/iet-map.2012.0137
7. Pezhman M, Heidari A. Design of Compact SIW-Based Multi-Aperture Coupler for Ku-Band Applications. 2019 27th Iranian Conference on Electrical Engineering (ICEE). 30 April-2 May 2019, Yazd, Iran (IEEE) 1338–41. (2019). doi:10.1109/iraniancee.2019.8786463
8. Hong W, Liu B, Wang Y, Lai Q, Tang H, Yin XX, et al. "Half Mode Substrate Integrated Waveguide: A New Guided Wave Structure for Microwave and Millimeter Wave Application," In 2006 Joint 31st International Conference on Infrared Millimeter Waves and 14th International Conference on Teraherz Electronics; Shanghai, China (2006). p. 219. doi:10.1109/ICIMW.2006.368427
9. Cui Y, Xu K-D, Guo Y-J, Chen Q. Half-mode Substrate Integrated Plasmonic Waveguide for Filter and Diplexer Designs. *J Phys D: Appl Phys* (2022) 55:125104. doi:10.1088/1361-6463/ac44bf
10. Ma HF, Shen X, Cheng Q, Jiang WX, Cui TJ. Broadband and High-Efficiency Conversion from Guided Waves to Spoof Surface Plasmon Polaritons. *Laser Photon Rev* (2014) 8(1):146–51. doi:10.1002/lpor.201300118
11. Garcia-Vidal FJ, Martín-Moreno L, Pendry JB. Surfaces with Holes in Them: New Plasmonic Metamaterials. *J Opt A: Pure Appl Opt* (2005) 7(2):S97–S101. doi:10.1088/1464-4258/7/2/013

12. Jaiswal RK, Pandit N, Pathak NP. Spoof Surface Plasmon Polaritons Based Reconfigurable Band-Pass Filter. *IEEE Photon Technol Lett* (2019) 31(3): 218–21. doi:10.1109/LPT.2018.288900710.1109/lpt.2018.2889007
13. Xu K-D, Lu S, Guo Y-J, Chen Q. High-order Mode of Spoof Surface Plasmon Polaritons and its Application in Bandpass Filters. *IEEE Trans Plasma Sci* (2021) 49(1):269–75. doi:10.1109/tps.2020.3043889
14. Wu Y, Li M, Yan G, Deng L, Liu Y, Ghassemlooy Z. Single-conductor Co-planar Quasi-Symmetry Unequal Power Divider Based on Spoof Surface Plasmon Polaritons of bow-tie Cells. *AIP Adv* (2016) 6(10):105110. doi:10.1063/1.4966051
15. Gao X, Zhou L, Yu XY, Cao WP, Li HO, Ma HF, et al. Ultra-wideband Surface Plasmonic Y-Splitter. *Opt Express* (2015) 23(18):23270. doi:10.1364/OE.23.023270
16. Gao X, Zhang HC, He PH, Wang ZX, Lu J, Yan RT, et al. Crosstalk Suppression Based on Mode Mismatch between Spoof SPP Transmission Line and Microstrip. *IEEE Trans Compon., Packag Manufact Technol* (2019) 9(11): 2267–75. doi:10.1109/TCPMT10.1109/tcpmt.2019.2931373
17. Tang X, Zhang Q, Hu S, Chen Y. "Spoof Surface Plasmon Polaritons (SSPP) for Endfire Radiation,," In 2018 IEEE Asia-Pacific Conference on Antennas and Propagation (APCAP); Auckland, New Zealand (2018). p. 414–5. doi:10.1109/APCAP.2018.8538201
18. Zhang Q, Zhang HC, Wu H, Cui TJ. A Hybrid Circuit for Spoof Surface Plasmons and Spatial Waveguide Modes to Reach Controllable Band-Pass Filters. *Sci Rep* (2015) 5:16531. doi:10.1038/srep16531
19. Guan D-F, You P, Zhang Q, Xiao K Hybrid Spoof Surface Plasmon Polariton and Substrate Integrated Waveguide Transmission Line and its Application in Filter. *IEEE Trans Microwave Theor Techn.* (2017) 65(12):4925–32. doi:10.1109/tmtt.2017.2727486
20. Li T, Wang G-M, Lu K, Xu H-X, Liao Z-H, Zong B. Novel Bandpass Filter Based on Csrr Using Koch Fractal CurveIn *PIER Lett* (2012) 28:121–8. doi:10.2528/PIERL11082903
21. Pan BC, Luo GQ, Liao Z, Cai JL, Cai BG. Wideband Miniaturized Design of Complementary Spoof Surface Plasmon Polaritons Waveguide Based on Interdigital Structures. *Sci Rep* (2020) 10:3258. doi:10.1038/s41598-020-60244-7
22. Pan BC, Yu P, Liao Z, Zhu F, Luo GQ. A Compact Filtering Power Divider Based on Spoof Surface Plasmon Polaritons and Substrate Integrated Waveguide. *IEEE Microw Wireless Compon Lett* (2021) 1–4. doi:10.1109/lmwc.2021.3116169
23. Han Y, Liu Z, Zhang C, Mei C, Chen Q, Hu K, et al. . A Flexible Microstrip Low-Pass Filter Design Using Asymmetric Pi-Shaped DGS. *Ieee Access* (2019) 7:49999–50006. doi:10.1109/access.2019.2910350

Conflict of Interest: The authors declare that the research was conducted in the absence of any commercial or financial relationships that could be construed as a potential conflict of interest.

Publisher's Note: All claims expressed in this article are solely those of the authors and do not necessarily represent those of their affiliated organizations, or those of the publisher, the editors and the reviewers. Any product that may be evaluated in this article, or claim that may be made by its manufacturer, is not guaranteed or endorsed by the publisher.

frontiers in Physics

ORIGINAL RESEARCH
published: 25 February 2022
doi: 10.3389/fphy.2022.857960

A Broadband Low-RCS Circularly Polarized Meta-Antenna

Hongkun Zhou, Yuchao Wang, Chengguo Liu and Cheng Zhang**

Hubei Engineering Research Center of RF-Microwave Technology and Application, School of Science, Wuhan University of Technology, Wuhan, China

A low-profile circularly polarized (CP) meta-antenna with a broadband low-RCS feature is proposed in this article. Our design is the combination of a CP antenna with a chessboard polarization conversion metasurface (CPCM) for balancing the radiation property and stealth feature. To relieve the adverse effect of the CPCM on the entire radiation performance, several redundant meta-atoms with the opposite phase state were removed to enhance the realized gain within the operation bandwidth (8.0–9.0 GHz). The proposed meta-antenna showed excellent radiation performance: −10 dB impedance relative bandwidth was 26.48% (6.78–8.85 GHz), and 3-dB axial ratio relative bandwidth was 22.03% (7.27–9.07 GHz). In addition, RCS reduction over 5 dB was achieved *via* our design from 8.5 to 21.5 GHz (86.67%) with the help of the deliberately designed CPCM. The final measured results demonstrate great consistency with the simulated ones.

Keywords: low profile, circularly polarized, broadband, radar cross-section reduction, meta-antenna

OPEN ACCESS

Edited by:
Zhen Liao,
Hangzhou Dianzi University, China

Reviewed by:
Hai Lin,
Central China Normal University, China
Qiye Wen,
University of Electronic Science and Technology of China, China

****Correspondence:***
Chengguo Liu
liucg@whut.edu.cn
Cheng Zhang
czhang2020@whut.edu.cn

Specialty section:
This article was submitted to Optics and Photonics, a section of the journal Frontiers in Physics

Received: *19 January 2022*
Accepted: *27 January 2022*
Published: *25 February 2022*

Citation:
Zhou H, Wang Y, Liu C and Zhang C (2022) A Broadband Low-RCS Circularly Polarized Meta-Antenna. Front. Phys. 10:857960. doi: 10.3389/fphy.2022.857960

INTRODUCTION

In recent years, antennas with a wideband low radar cross section (RCS) have drawn significant attention in the low-observable needed platforms, such as military aircraft and missiles. Traditional strategies to reduce the RCS of the antennas are shape design or adding absorbers such as metamaterial absorbers [1, 2], frequency-selective surfaces/absorbers (FSS/FSA) [3–5], and electromagnetic bandgap structures [6] onto the antennas. Through these methods, the backward RCS can be confined to certain extent, while the radiation performances, including the working bandwidth and realized gain, are difficult to be maintained. For instance, in Ref. [5], an FSA was adopted in a 4 × 4-array antenna to restrain the normal reflection from the whole structure by an average of 11 dB (from 4.41 to 5.43 GHz) by absorbing the incident electromagnetic waves. But the antenna could only work at the same bandwidth. To further improve the stealth performance, a low-RCS Fabry–Perot (FP) antenna was proposed in Ref. [7], in which a partially reflecting surface was utilized to achieve low RCS (over 4 dB from 6 to 14 GHz). However, the operation bandwidth of the antenna further shrunk. From the previous discussions, it is easy to find that obtaining a good radiation feature and broadband stealth performance at the same time is challenging.

Nowadays, the prompt development of metasurfaces [8–10] provides an alternative and potential strategy to address the aforementioned problem. Compared to the traditional methods, the polarization conversion metasurface (PCM) has been widely used to design low-RCS devices [11, 12], of which through optimizing the polarization conversion (PC) bandwidth and the polarization conversion ratio of the corresponding meta-atoms, the operation bandwidth for RCS reduction can be flexibly controlled as desired. Therefore, several attempts have been taken to design a low-RCS meta-antenna while not affecting its radiation performance. In Ref. [11], a chessboard polarization conversion metasurface (CPCM) was used in a slot array antenna, and its RCS reduction over 5 dB was achieved from 6 to 18 GHz. In the meantime, a dumbbell CPCM

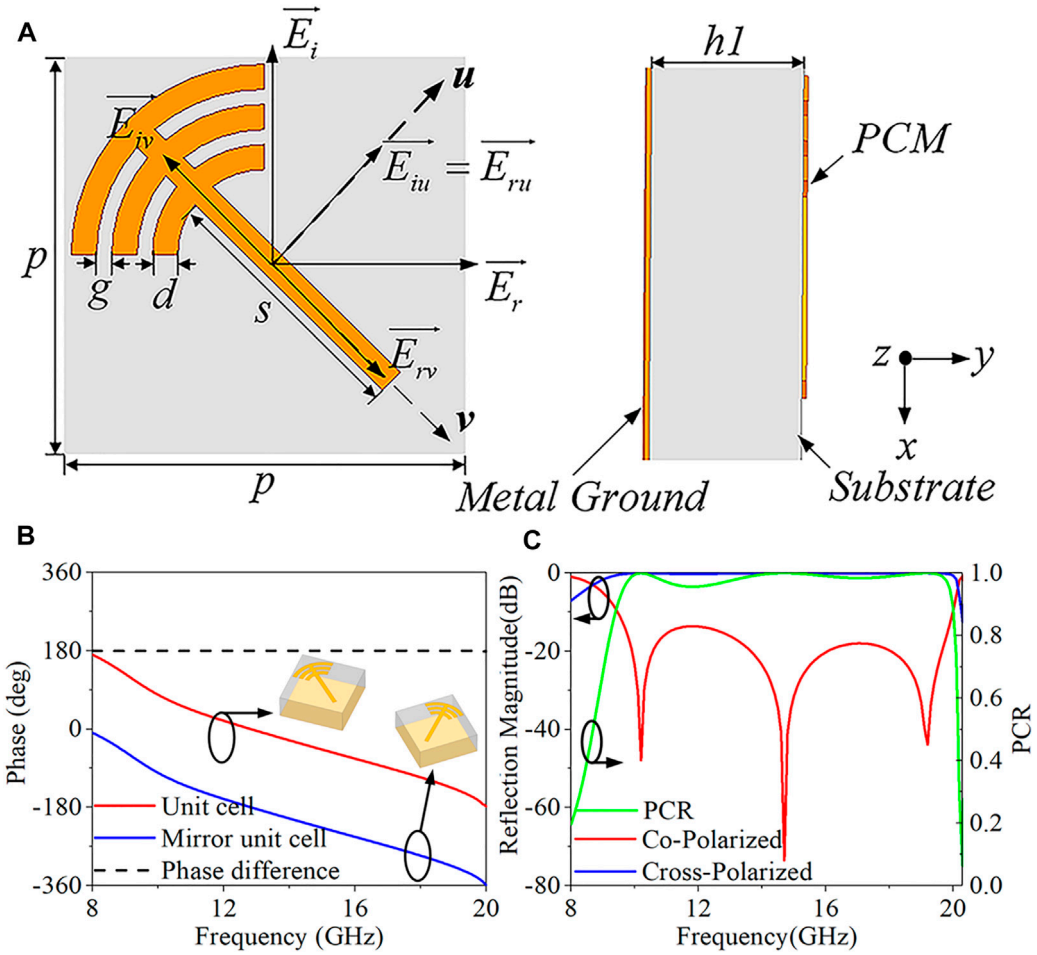

FIGURE 1 | (A) Top view and side view of a typical unit cell. **(B)** The reflection phase of the unit cell and its mirror. **(C)** Co- and cross-polarized reflection coefficients and PCR of the proposed meta-atom.

applied to an FP antenna was proposed in Ref. [12], which achieved an RCS reduction bandwidth of 8–26 GHz and an antenna operating bandwidth of 8.41–12.11 GHz. In addition, most of the reported low-RCS antennas just can interact with the linearly polarized waves [12, 13], but only a few circularly polarized (CP) antennas have been investigated. More attention should be paid to low-RCS CP antennas due to their widespread applications such as radar, communication, and sensor systems. Several attempts have been made to solve this problem. For example, in Ref. [14], a gain of 3.5 dB and impedance bandwidth of 500 MHz were achieved *via* placing a CPCM onto a patch antenna; however, the RCS reduction bandwidth only covered a frequency range of 9–13 GHz. In Ref. [15], RCS reduction over 6 dB was achieved at 4.95–15.73 GHz as the CP patch antenna was loaded with a CPCM, but the reflection coefficient increased from −30 dB to −20 dB compared to the reference antenna without a CPCM. Hence, there is still a need for a plentiful effort to be made for developing a CP antenna with a good stealth feature and excellent radiation performance.

In this article, a low-profile CP circular patch meta-antenna is proposed. With the help of the elaborately designed CPCM, our design can achieve good RCS reduction performance within an ultra-wideband frequency range. CP performance of the proposed meta-antenna was achieved by a feed network consisting of a Wilkinson power divider and a 90° broadband phase shifter. Meanwhile, slots were cut in the patch to increase the axial bandwidth. It is worthy to note that the radiation performance of the antenna was still maintained even after loading the CPCM.

DESIGN AND ANALYSIS OF THE CPCM

The schematic diagram of the proposed meta-atom is illustrated in **Figure 1A**. The unit cell comprises a top metallic pattern and a bottom metallic ground plane with a dielectric substrate between them. The top layer is the PC structure that consists of a quarter of three adjacent rings and a rectangular strip. The dielectric layer adopts an F4B substrate (a relative dielectric constant of 2.2) with

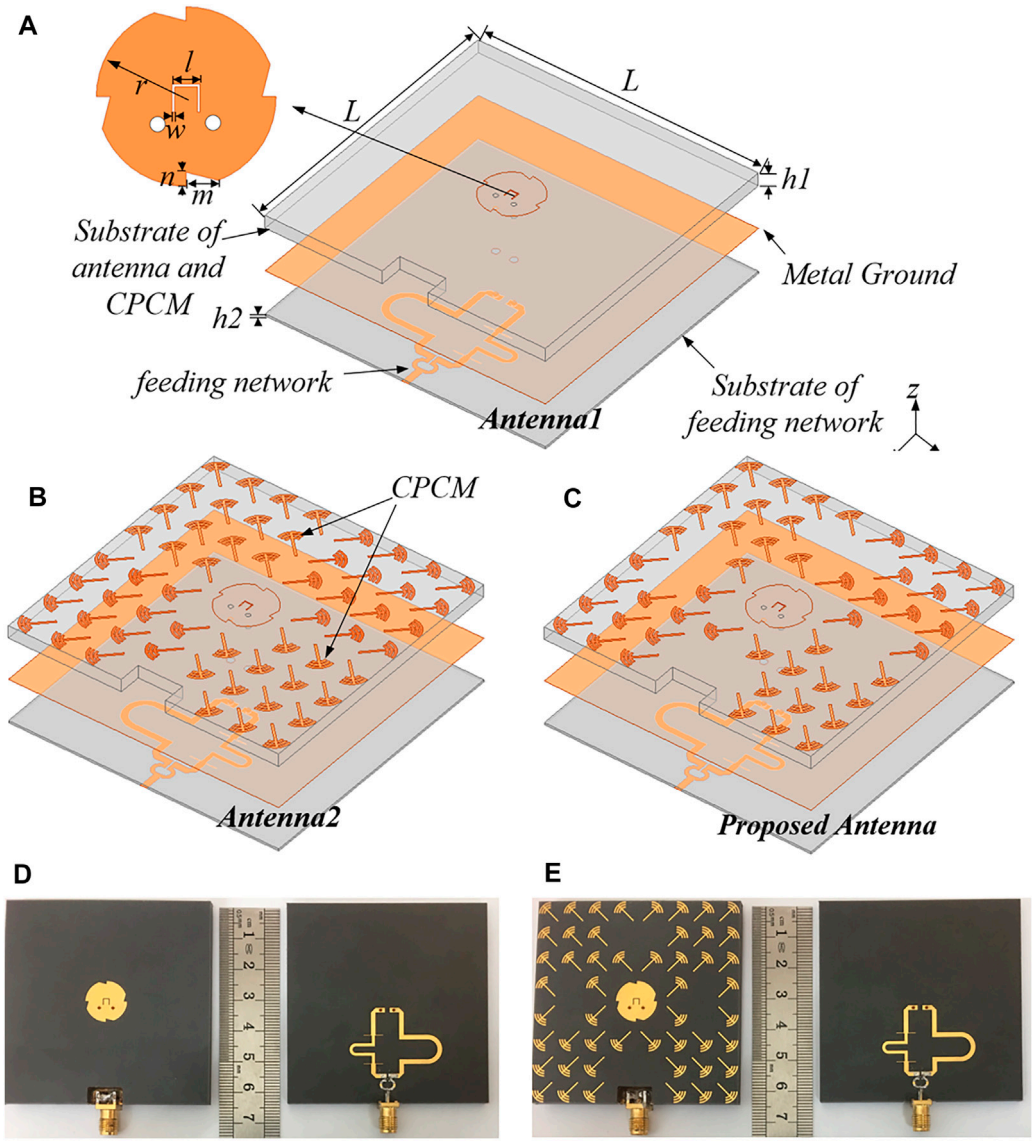

FIGURE 2 | Design process of the proposed meta-antenna: **(A)** antenna1 and dimensional parameters of the antenna patch and substrate, **(B)** antenna2, and **(C)** the proposed meta-antenna. The corresponding photograph of the samples: **(D)** antenna1 and **(E)** the proposed meta-antenna.

a thickness of 3 mm. The typical geometrical parameters of the unit cell are as follows: $s = 8.5$ mm, $d = 0.3$ mm, $p = 8$ mm, and $g = 0.2$ mm. Electromagnetic simulation software HFSS was used to calculate the performance of the unit cell by using Mater/Slaver boundary conditions.

In **Figure 1A**, to investigate the PC response of the proposed unit cell, the electric field $\vec{E_i}$ of the x-polarized incident wave was decomposed into two components $\vec{E_{iu}}$ and $\vec{E_{iv}}$. When the electric fields were along the u- and v-axis (135° and 225° from x-axis), the magnitudes of the two reflected fields $\vec{E_{ru}}$ and $\vec{E_{rv}}$ were almost the same. Therefore, the total reflected electric field $\vec{E_r}$ is vertical to the x-axis with the same magnitude as $\vec{E_i}$. For the chessboard arrangement, the mirror unit cell also has a reflected electric field of the same magnitude, and the reflection phase difference between the unit cell and its mirror was nearly 180°, as shown in **Figure 1B**. Under the illumination of electromagnetic waves, the scattering pattern of the CPCM can be determined by the superposition of far fields from the unit cells by using the following formula [16, 17]:

$$f(\theta,\varphi) = f_e(\theta,\varphi)\sum_{m=1}^{M}\sum_{n=1}^{N}\exp\left\{-i\left\{\varphi(m,n)+k_0 p\sin\theta\left[(m-1/2)\cos\varphi+(n-1/2)\sin\varphi\right]\right\}\right\}, \quad (1)$$

where m and n are the row and column numbers in the CPCM, respectively. p is the element periodicity. θ, φ, and k_0 are the

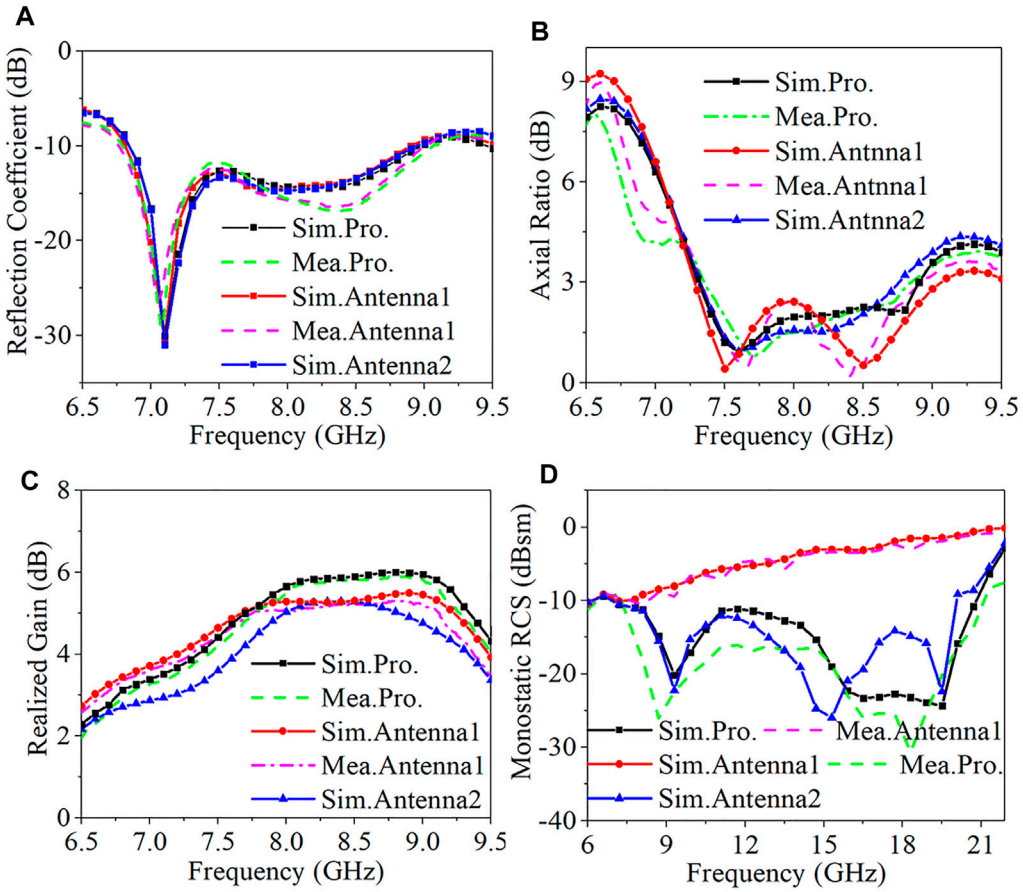

FIGURE 3 | Simulated and measured reflection coefficients **(A)**, axial ratio **(B)**, realized gain **(C)**, and monostatic RCS for the *x*-polarized incidence **(D)**.

elevation angle, azimuth angle, and wavenumber of the free space, respectively. $\varphi(m,n)$ is the reflection phase of the lattice (m,n), and $f_e(\theta,\varphi)$ is the pattern function of a single unit. Indeed, the scattering beam can be adjusted by inverting the unit cell phase by iterating a fast Fourier transform. Therefore, phase cancellation of the reflected electric field and reduction of RCS can be achieved by the CPCM.

Co-polarized and cross-polarized reflection coefficients with *x*-polarized incident waves are illustrated in **Figure 1C**. It can be seen that the operating band (where the co-polarization reflection coefficient is less than −10 dB) of the meta-atom is from 9.46 to 20.01 GHz. The polarization conversion ratio (PCR) is used to describe electromagnetic polarization rotation and is defined as the ability to convert *x*- or *y*-polarized waves into cross-polarized waves that can be expressed as

$$PCR = |R_{cross}|^2 / \left(|R_{cross}|^2 + |R_{co}|^2\right), \tag{2}$$

where R_{co} and R_{cross} represent the reflection coefficient of co- and cross-polarization, respectively. The operating band was from 9.46 to 20.01 GHz as the value of the PCR was greater than 90%, which illustrates that more than 90% of the linearly polarized incident power can be converted into cross-polarized power.

META-ANTENNA DESIGN

Figure 2 shows the geometry and design process of the CP patch meta-antenna. The entire size of the meta-antenna is 64 mm × 64 mm × 3.5 mm. As depicted in **Figure 2A**, the antenna is designed with double dielectric plates (F4B). The antenna is composed of a patch, ground, and the feeding network. The top patch and the bottom feeding network are connected *via* two holes. Below the metal ground, the feeding network consisting of a Wilkinson power divider and a 90° broadband phase shifter was mounted on the bottom substrate with a thickness of h_1. The Wilkinson power divider can achieve equal power division and impedance by transforming between input and output ports. After the original input signal splits into two ways, they pass through the two paths of the 90° phase shifter to obtain a stable phase shifting. In this design, a pair of 8/λ open and short lines was deployed to smooth the phase variation, where λ is the wavelength of the center frequency (8 GHz) on the substrate. All ports of the divider were matched to 50 Ω. The isolation between the two outputs was determined by a 100-Ω chip resister. Therefore, the CP radiation was achieved by generating two output signals with equal amplitude and 90°

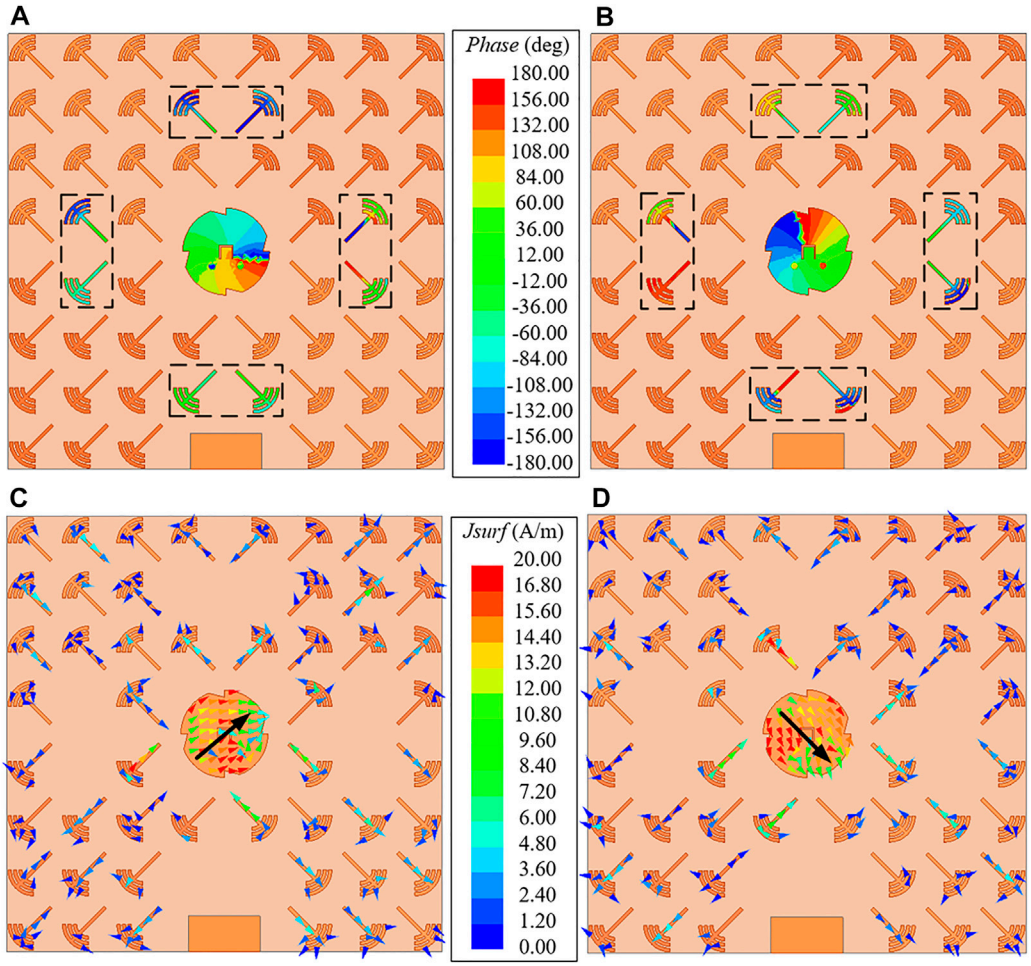

FIGURE 4 | Phase distribution of antenna2 at 7.5 GHz **(A)** and 8 GHz **(B)**. Surface current vector distribution of the proposed meta-antenna in the radiation case at 8 GHz: **(C)** phase = 0° and **(D)** phase = 90°.

phase difference of the feeding network. In addition, a U-shaped slot and four triangular slots were cut on the circular patch. The function of the U-slot is to introduce a capacitance that can suppress the inductance induced *via* the holes and to enhance the impedance and axial-ratio bandwidths. Four triangular slots were embedded to further reduce the size of the antenna. The CP slotted patch antenna was simulated by the electromagnetic simulation software HFSS and measured in the microwave anechoic chamber. The dimensional parameters of the antenna patch and the substrate are as follows: L = 64 mm, r = 6.8 mm, l = 2 mm, w = 0.2 mm, m = 4 mm, n = 1 mm, h_1 = 3 mm, and h_2 = 0.5 mm.

The design process of the low-RCS meta-antenna is shown in **Figures 2A–C**. First, a CP slotted patch antenna was designed as the basic model shown in **Figure 2A**. The PC meta-atoms and their mirrors were arranged around the original antenna in a chessboard pattern to reduce the RCS of the whole structure, as shown in **Figure 2B**. In order to improve the radiation performance, some unit cells on the aperture were removed to relieve the coupling between the CPCM and the patch (**Figure 2C**). To demonstrate the performance of the proposed meta-antenna, the simulated and measured results were compared with those of the reference antenna without the CPCM. The antenna1 and the proposed meta-antenna were fabricated as shown in **Figure 2** and **Figure 2E**, respectively. It should be emphasized that considering the good contact between the SMA connector and the metal ground, a 10 mm × 5 mm × 3 mm slot was cut at the edge of the substrate with a thickness of h_2, which had a little effect on the radiation performance.

The simulated and measured reflection coefficients and axial ratios of antennas are shown in **Figures 3A,B**. The relative operation bandwidth of proposed meta-antenna and antenna1 were 26.48% (6.78–8.85 GHz) and 27.05% (6.84–8.98 GHz), respectively. The 3-dB axial ratio bandwidth of our design and antenna1 were 22.03% (7.27–9.07 GHz) and 19.39% (7.31–8.88 GHz). The realized gain is shown in **Figure 3C**, and the peak realized gain was 6.01 dB at 8.8 GHz. Furthermore, at 8.0–9.0 GHz, the realized gain of the proposed antenna increased by 1dB compared with that of the

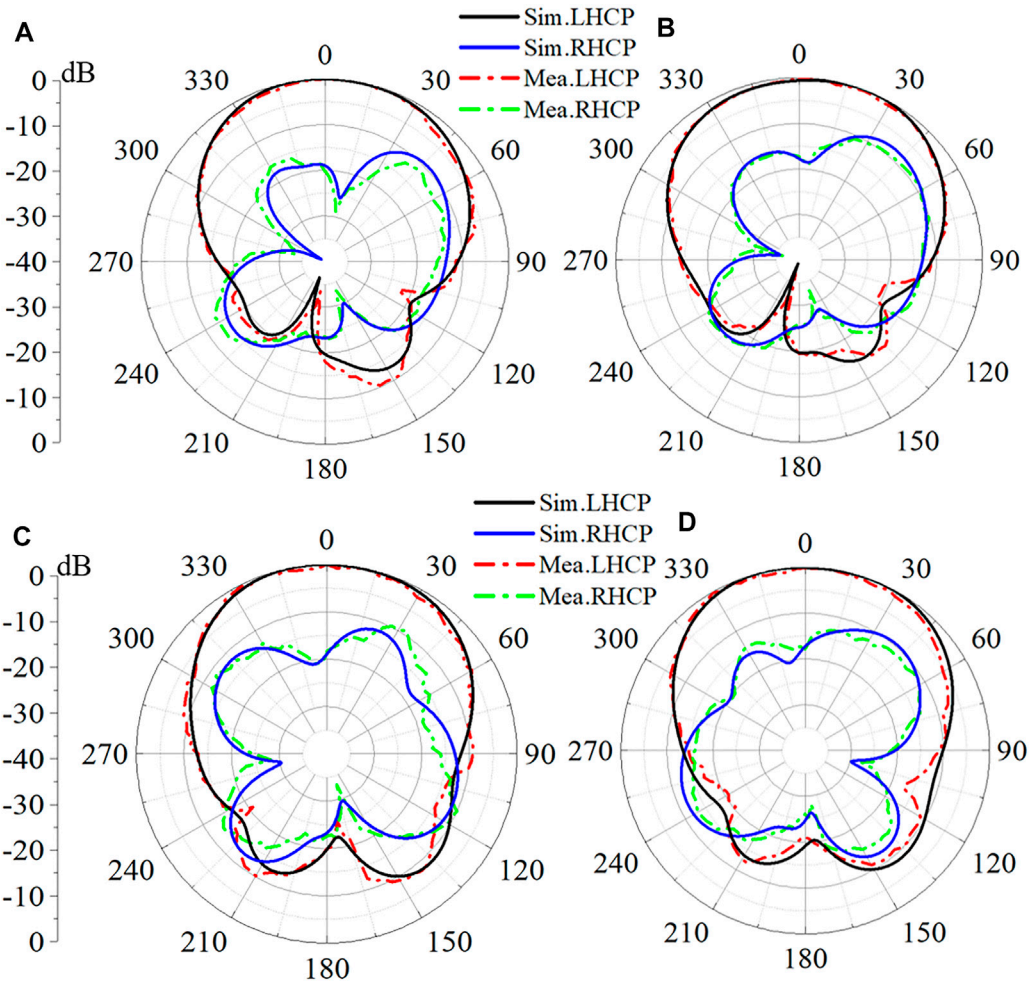

FIGURE 5 | Simulated and measured 2D radiation patterns of the proposed meta-antenna at 8 GHz (**(A)** for *xoz*-plane; **(C)** for *yoz*-plane) and antenna1 (**(B)** for *xoz*-plane; **(D)** for *yoz*-plane).

antenna1. The simulated and measured monostatic RCS are shown in **Figure 3D**. Compared with the reference antenna1, the proposed meta-antenna can achieve RCS reduction over 5 dB ranging from 8.5 to 21.5 GHz, which covers the working bandwidth of the proposed antenna. The peak RCS reduction at 19.4 GHz was 34.3 dB.

Referring to the results of antenna2 in **Figures 3A–D**, it is shown that placing a complete CPCM around an antenna has little influence on the return loss and axial ratio, but the gain of the antenna decreases by 1 dB at 7–7.75 GHz and 8.85–9.15 GHz without a CPCM because an inverting electric field is excited by several meta-atoms. The phase distribution of antenna2 at 7.5 and 8 GHz is shown in **Figure 4A** and **Figure 4B**, respectively. Therefore, to improve the realized gain of the meta-antenna, eight unit cells that are located at 0.5λ away from the center of our design have been removed since they are oppositely phased with the surrounding counterparts. In addition, compared with antenna2, the RCS of the proposed meta-antenna has improved by about 4.1 dB on an average from 11.1 to 15.8 GHz by following the aforementioned procedure. In the meantime, the current distribution of antenna1 and the proposed meta-antenna at 8.0 GHz is shown in **Figure 4C** and **Figure 4D**, respectively. The proposed meta-atoms act as parasitical radiators due to the coupling between the patch and CPCM in the radiation case. Two orthogonal modes with 90° phase difference were excited to obtain left-hand circularly polarized (LHCP) radiation. Hence, the improvement of the radiation aperture, namely, redistributing the meta-atoms, proves to be a vital function for the gain enhancement.

The LHCP and right-hand circularly polarized (RHCP) radiation patterns of the proposed meta-antenna and the reference antenna at 8 GHz are shown in **Figure 5**. It can be seen that the main polarization is LHCP, which is consistent with the current vector distribution in **Figure 4**. The measured cross-polarization levels in both *xoz*-plane and *yoz*-plane were about 20 dB lower than co-polarizations. Moreover, the front-to-back ratios remained better than 20 dB at 8 GHz.

In comparison, the performance of the proposed meta-antenna approached that of the antenna1, and the measured

data are in good agreement with the simulation results. Some little differences are mainly due to the following reasons: I) machining and fabrication errors, II) interference of measurement environment and instrument settings, and III) the SMA and cable loss. In summary, the comparison of the above results shows that the CPCM causes little degradation in antenna radiation performance.

CONCLUSION

A CP slotted patch meta-antenna is presented in this article for reducing the backward RCS with the help of the predesigned CPCM. The measured results show that the proposed meta-antenna has an operating bandwidth of 6.79–9.06 GHz and 3-dB axial ratio bandwidth of 7.35–8.85 GHz, and the measured RCS reduction of more than 9 dB was achieved from 8.3 to 21.1 GHz without disturbing the radiation performance. Our design reached a good balance between the radiation feature and broadband stealth performance, and shows great prospects in practical applications.

DATA AVAILABILITY STATEMENT

The original contributions presented in the study are included in the article/Supplementary Material, further inquiries can be directed to the corresponding authors.

AUTHOR CONTRIBUTIONS

All authors listed have made a substantial, direct, and intellectual contribution to the work and approved it for publication.

FUNDING

This work was supported by the National Natural Science Foundation of China (Nos 62101394, 61722106, 62001338, and 61731010), the Fundamental Research Funds for the Central Universities (WUT: 2021IVA064 and 2021IVB029), and the Foundation from the Guangxi Key Laboratory of Optoelectronic Information Processing (GD21203).

REFERENCES

1. Liu T, Cao X, Gao J, Zheng Q, Li W, Yang H. RCS Reduction of Waveguide Slot Antenna with Metamaterial Absorber. *IEEE Trans Antennas Propagat* (2013) 61(3):1479–84. doi:10.1109/TAP.2012.2231922
2. Liu Y, Zhao X. Perfect Absorber Metamaterial for Designing Low-RCS Patch Antenna. *Antennas Wirel Propag Lett* (2014) 13:1473–6. doi:10.1109/LAWP.2014.2341299
3. Wang W-T, Gong S-X, Wang X, Yuan H-W, Ling J, Wan T-T. RCS Reduction of Array Antenna by Using Bandstop FSS Reflector. *J Electromagn Waves Appl* (2009) 23(11):1505–14. doi:10.1163/156939309789476473
4. Genovesi S, Costa F, Monorchio A. Low-Profile Array with Reduced Radar Cross Section by Using Hybrid Frequency Selective Surfaces. *IEEE Trans Antennas Propagat* (2012) 60(5):2327–35. doi:10.1109/TAP.2012.2189701
5. Han Y, Zhu L, Bo Y, Che W, Li B. Novel Low-RCS Circularly Polarized Antenna Arrays via Frequency-Selective Absorber. *IEEE Trans Antennas Propagat* (2020) 68(1):287–96. doi:10.1109/TAP.2019.2939845
6. You-Quan Li Y, Hui Zhang H, Yun-Qi Fu Y, Nai-Chang Yuan N. RCS Reduction of Ridged Waveguide Slot Antenna Array Using EBG Radar Absorbing Material. *Antennas Wirel Propag Lett* (2008) 7:473–6. doi:10.1109/LAWP.2008.2001548
7. Pan W, Huang C, Chen P, Ma X, Hu C, Luo X. A Low-RCS and High-Gain Partially Reflecting Surface Antenna. *IEEE Trans Antennas Propagat* (2014) 62(2):945–9. doi:10.1109/TAP.2013.2291008
8. Zhang C, Long C, Yin S, Song RG, Zhang BH, Zhang JW, et al. Graphene-Based Anisotropic Polarization Meta-Filter. *Mater Des* (2021) 206:109768. doi:10.1016/j.matdes.2021.109768
9. Zhang C, Yin S, Long C, Dong BW, He D, Cheng Q. Hybrid Metamaterial Absorber for Ultra-low and Dual-Broadband Absorption. *Opt Express* (2021) 29(9):14078–86. doi:10.1364/OE.423245
10. Zhang C, Cheng Q, Yang J, Zhao J, Cui TJ. Broadband Metamaterial for Optical Transparency and Microwave Absorption. *Appl Phys Lett* (2017) 110(14):143511. doi:10.1063/1.4979543
11. Liu Y, Li K, Jia Y, Hao Y, Gong S, Guo YJ. Wideband RCS Reduction of a Slot Array Antenna Using Polarization Conversion Metasurfaces. *IEEE Trans Antennas Propagat* (2016) 64(1):326–31. doi:10.1109/TAP.2015.2497352
12. Liu Z, Liu S, Bornemann J, Zhao X, Kong X, Huang Z, et al. A Low-RCS, High-GBP Fabry-Perot Antenna with Embedded Chessboard Polarization Conversion Metasurface. *IEEE Access* (2020) 8:80183–94. doi:10.1109/ACCESS.2020.2990602
13. Pandit S, Mohan A, Ray P. Low-RCS Low-Profile Four-Element MIMO Antenna Using Polarization Conversion Metasurface. *Antennas Wirel Propag Lett* (2020) 19(2):2102–6. doi:10.1109/LAWP.2020.3023454
14. Li K, Liu Y, Jia Y, Guo YJ. A Circularly Polarized High-Gain Antenna with Low RCS over a Wideband Using Chessboard Polarization Conversion Metasurfaces. *IEEE Trans Antennas Propagat* (2017) 65(8):4288–92. doi:10.1109/TAP.2017.2710231
15. Zhang W, Liu Y, Jia Y. Circularly Polarized Antenna Array with Low RCS Using Metasurface-Inspired Antenna Units. *Antennas Wirel Propag Lett* (2019) 18(7):1453–7. doi:10.1109/LAWP.2019.2919716
16. Xie B, Tang K, Cheng H, Liu Z, Chen S, Tian J. Coding Acoustic Metasurfaces. *Adv Mater* (2017) 29(6):1603507. doi:10.1002/adma.201603507
17. Cui TJ, Qi MQ, Wan X, Zhao J, Cheng Q. Coding Metamaterials, Digital Metamaterials and Programmable Metamaterials. *Light Sci Appl* (2014) 3(10):e218. doi:10.1038/lsa.2014.99

Conflict of Interest: The authors declare that the research was conducted in the absence of any commercial or financial relationships that could be construed as a potential conflict of interest.

Publisher's Note: All claims expressed in this article are solely those of the authors and do not necessarily represent those of their affiliated organizations, or those of the publisher, the editors, and the reviewers. Any product that may be evaluated in this article, or claim that may be made by its manufacturer, is not guaranteed or endorsed by the publisher.

frontiers in Physics

ORIGINAL RESEARCH
published: 28 February 2022
doi: 10.3389/fphy.2022.866656

A High-Efficiency and Reconfigurable Rectenna Array for Dynamic Output DC Power Control

Yuchao Wang, Yangkun Song, Bohan Zhang, Shaonan Chen, Qiang Chen and Cheng Zhang**

Hubei Engineering Research Center of RF-Microwave Technology and Application, School of Science, Wuhan University of Technology, Wuhan, China

In this paper, an output power reconfigurable rectenna array is proposed for the first time to harvest RF energy. The proposed rectenna array can be used to capture abundant RF energy with high conversion efficiency in a wide range of input power levels and load impedance at 1.88, 2.35, 3.5, and 4.9 GHz simultaneously. The output DC power of the proposed rectenna array can be changed exponentially by altering the on-off state of the switches located between the antenna and the rectifier. The measured result shows that the output power is linearly related to the number of opened switches. Therefore, the proposed rectenna array can be flexibly applied to battery-free or low-power-requiring devices according to their different power needs.

Keywords: four-band rectifier, high gain antenna, reconfigurabale rectifier array, RF energy harvesting, output DC power control

OPEN ACCESS

Edited by:
Zhen Liao,
Hangzhou Dianzi University, China

Reviewed by:
Ye Ming Qing,
Southeast University, China
Yan Xi,
Xidian University, China

****Correspondence:***
Qiang Chen
qiangchen@whut.edu.cn
Cheng Zhang
czhang2020@whut.edu.cn

Specialty section:
This article was submitted to Optics and Photonics, a section of the journal Frontiers in Physics

Received: *31 January 2022*
Accepted: *14 February 2022*
Published: *28 February 2022*

Citation:
Wang Y, Song Y, Zhang B, Chen S, Chen Q and Zhang C (2022) A High-Efficiency and Reconfigurable Rectenna Array for Dynamic Output DC Power Control. Front. Phys. 10:866656. doi: 10.3389/fphy.2022.866656

INTRODUCTION

To realize the interconnection of all things, wireless sensing networks are widely applied in our daily lives. Conventional batteries to power basic sensors are very inconvenient, and improper disposal of batteries can pollute the environment [1, 2]. The prompt development of wireless communication technology paves a new way to address these problems by utilizing a contactless charge strategy [3–5]. As the RF energy around us increases sharply, which is an abundant power source for electronic devices, the rectenna rises in response to this condition to gather RF energy.

Rectennas, as one of the key devices for harvesting RF energy, have experienced long-term development, and much effort has been made to enhance the overall RF-DC conversion efficiency and output DC power. Considering the above two aims, many rectennas with the characteristics of high efficiency [6, 7], broadband [8–10], multiband [11–13], or multiport [14, 15] have been extensively investigated by researchers in recent decades, driving the improvement of wireless energy usage. For example, a high-efficiency rectenna was proposed in Ref. [16] by directly matching the receiving antenna conjugately with a rectifier, and the efficiency could achieve 83% at 2.45 GHz when the input power level was 0 dBm. Furthermore, a compact and low-profile rectenna was proposed in Ref. [17], which strategically combines 12 single Vivaldi slot rectenna elements. The measured output DC power of the rectenna array could reach 65 μW in a real ambient environment outdoors.

From the abovementioned discussion, it is evident that with the development of energy harvesting technology, existing rectennas can meet the requirements of most daily applications, but once fabricated, their performance is fixed. Thus, without considering the discrepancy of the ambient power density, traditional rectennas lacking reconfigurability can supply specific devices, confining their practical application. Because the rated power and voltage of different devices are distinct, how

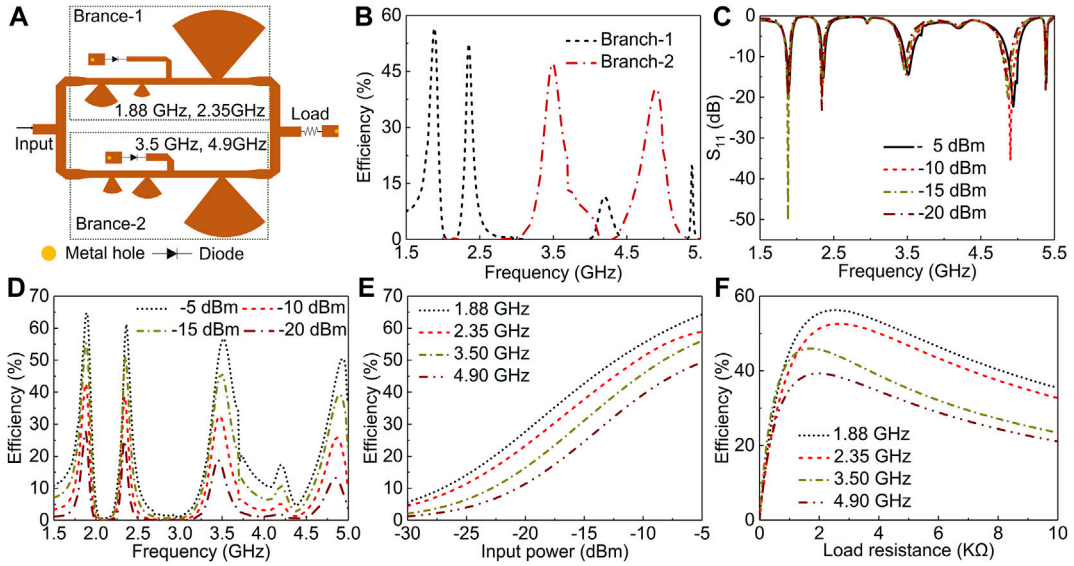

FIGURE 1 | (A) The topology of the proposed rectifier. **(B)** Simulated RF-DC conversion efficiency of the three branches at the input power level of −10 dBm. **(C,D)** Simulated reflection coefficient and RF-DC conversion efficiency of the proposed rectifier at different input power levels for a load resistance of 2000 Ω. **(E)** Simulated RF-DC conversion efficiency of the proposed rectifier versus input power level for a load resistance of 2000 Ω. **(F)** Simulated RF-DC conversion efficiency of the proposed rectifier versus load resistance at an input power of −10 dBm.

to achieve the dynamic control of the output DC power according to the demands of the electrics must be solved.

To address the above problems, in this paper, a DC power reconfigurable 4 × 4 rectenna array is proposed by controlling the operating status of a single rectenna with the help of RF switches that are located between the antennas and rectifiers. The rectifier array is designed to operate at four frequency bands to harvest abundant RF energy, and the conversion efficiency of the proposed rectifier can achieve 53, 52, 49, and 45% at 1.88, 2.35, 3.5, and 4.9 GHz, respectively, when the input power level is −10 dBm. The receiving antenna is composed of four monopole antennas and an AMC structure to increase the gain of the antenna. To our knowledge, the proposed rectenna array is the first design to reconfigure the output power as desired and provides a new strategy for dynamic power supplements of different applications.

RECTIFIER ARRAY DESIGN

A rectifier array composed of four single shunt diode rectifiers is proposed in this section to realize high efficiency at four different working bands. We first designed a four-band rectifier and then arrayed it (four rectifiers) to harvest more RF energy and flexibly control the output power levels. The detailed design process is described as follows.

The topological structure of the proposed four-band rectifier is shown in **Figure 1A**. It consists of two single shunt diode rectifier branches in parallel to obtain four operating bands. Each rectifier branch comprises a diode, DC-pass filter, and matching network. To improve the RF-DC conversion at a low input level, the Schokkty diode SMS7630 is chosen as the rectifier diode due to its low-loss property within a broad power range (from −20 to 0 dBm).

In addition, the DC-pass filter is designed by connecting a transmission line and a radius branch in series to prevent RF energy from passing through the load. To develop a four-band rectifier, each rectifier branch is designed to operate at two frequency bands by mainly designing the matching network and the DC-pass filter. A *Π*-type matching network is optimized to match the single shunt diode rectifier to 50 Ω. The ultimate structure of the proposed four-band rectifier is shown in **Figure 1A**. Furthermore, to study the contribution of the two branches, the simulated RF-DC conversion efficiency of the two branches at an input power level of −10 dBm is presented in **Figure 1B**. It is easy to find that branch-1 can rectify the RF energy at 1.88 and 2.35 GHz, and the other branch (branch-2) is able to operate at 3.5 and 4.9 GHz. Moreover, almost the entire RF power can be converted to DC power by the corresponding rectifier branches.

The simulated S_{11} and conversion efficiency of the proposed rectifier versus frequency are also shown in **Figures 1C,D** at four different input power levels (−5, −10, −15, and −20 dBm). The rectifier maintains robust efficiency as the input power level changes. In addition, the four designed operating frequencies hardly change with different input power levels. Because the input impedance of the diode changes with the input power level, the effect of the input power level on the conversion efficiency was studied, as shown in **Figure 1E**. The efficiency increases as the input power increases from −30 to −5 dBm, making our design suitable for a wide range of environmental power levels. Next, the effect of the load resistance on the

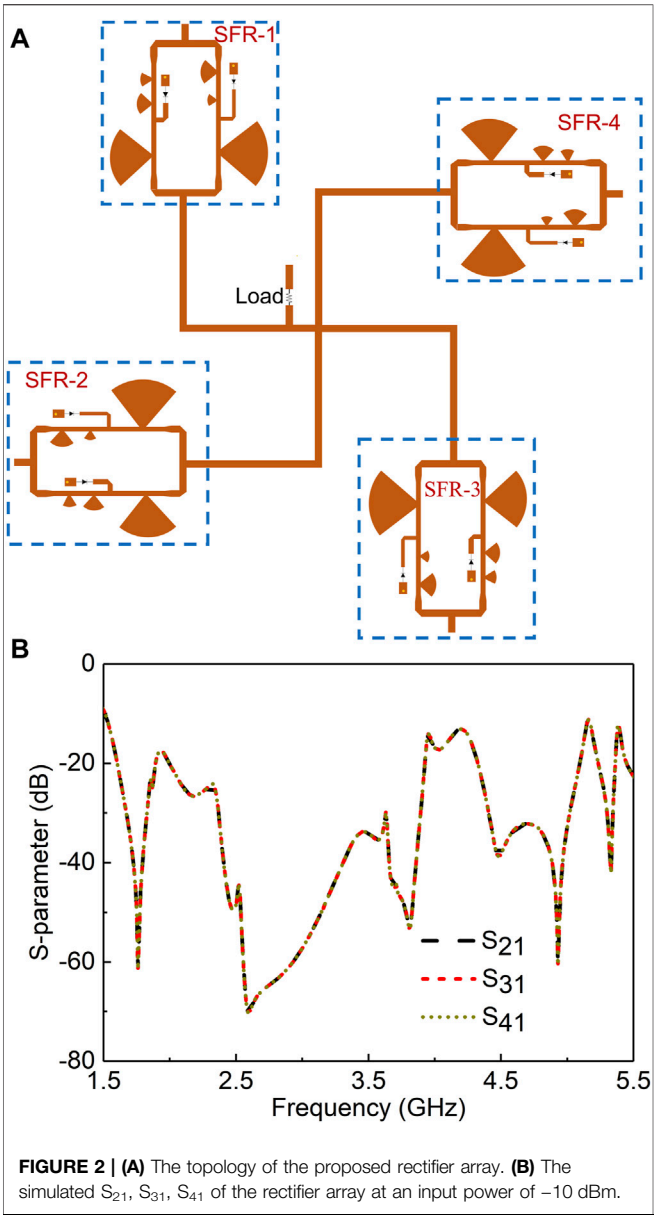

FIGURE 2 | (A) The topology of the proposed rectifier array. **(B)** The simulated S_{21}, S_{31}, S_{41} of the rectifier array at an input power of −10 dBm.

efficiency was also studied when the input power was −10 dBm (**Figure 1F**), and the optimal load resistance of approximately 2000 Ω was determined by comprehensively considering the efficiency of the four working bands. In addition, our design is insensitive to the load resistance, and stable efficiency can be maintained even when the load resistance dramatically changes (1,000 Ω–10,000 Ω).

To date, a single four-band rectifier (SFR) has been achieved by adopting a dual-branch circuit. In the following, the four uniform SFRs are connected in parallel to form a rectifier array, as shown in **Figure 2A**. To study the isolation between different input ports, S_{21}, S_{31}, and S_{41} are shown in **Figure 2B**. It is obvious that port 1 has great isolation with port 2, port 3, and port 4 since the other three SFRs hardly affect SFR-1 due to the elaborate matching network and DC-pass filter. Of course, the isolation performance of any two ports is the same as above since the four ports are symmetrical.

To verify our design, a prototype size of 196 mm × 196 mm was printed on a low-cost F4B substrate with a relative permittivity of 2.2, loss tangent of 0.0011, and thickness of 0.787 mm (**Figure 3A**). The reflection coefficient of the rectifier was measured with a vector network analyzer (VNA, Agilent E5072A). The measured S_{11} at four different input power levels is shown in **Figure 3A**. Although a slight discrepancy can be observed for S11, the measured results (**Figure 3A**) are still consistent with the simulated results (**Figure 1C**), including the four predesigned frequency bands. Next, the conversion efficiency was measured as a function of the input power level at four operating frequency bands, as shown in **Figure 3B**. The measured result shows that the conversion efficiency achieved 47.8, 44.6, 45.2, and 38.1% at 1.88, 2.35, 3.5, and 4.9 GHz, respectively, when the input power was −10 dBm. Consistent with the simulation results, the conversion efficiency improved as the input power level increased due to diode losses increasing more slowly than the input power. However, the measured efficiency was lower than the simulated efficiency due to the unknown parasitic behavior of the diode. In addition, the S_{21}, S_{31}, and S_{41} of the rectifier array were also measured to study the isolation of the different ports. The rectifier array has great isolation at the four operating frequency bands. Although there are some deviations between the measured and simulated results, the measured results also verify the excellent performance of the designed rectifier at low input power levels.

BROADBAND HIGH GAIN ANTENNA ARRAY DESIGN

A broadband monopole antenna array integrated with an artificial magnetic conductor (AMC) is proposed as the receiving antenna of the rectenna array due to its high gain characteristic. In addition, the reflecting ground plane can be integrated with the rectifier array to decrease the size of the rectenna array. The proposed broadband high gain antenna array was made on an F4b substrate with a relative permittivity of 2.2. The substrate thickness of the monopole antenna array was 0.787 mm and that of the AMC array was 0.508 mm. The distance between the antenna and the AMC was designed as 5 mm by comprehensively considering the profile and the effect of the AMC on the input impedance of the antenna. To extend the operating band (where the reflection phase ranges from −90° to +90°) of the AMC, the distance between the AMC and reflecting ground plane was designed as 20 mm.

The receiving antenna consists of four independent high gain antennas (HGA). Each HGA was designed by combining the monopole antenna with AMC to achieve high gain and broadband performance. The size of the monopole antenna is dependent on the operating frequency. To reduce the omnidirectional radiation of the monopole, an AMC was

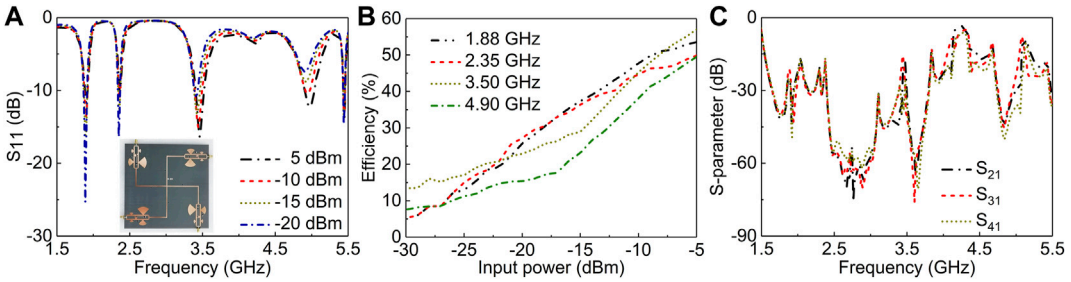

FIGURE 3 | (A) Measured reflection coefficient of the proposed rectifier at different input power levels for a load resistance of 2000 Ω. **(B)** Measured RF-DC conversion efficiency of the proposed rectifier versus input power level a for a load resistance of 2000 Ω. **(C)** Measured S_{21}, S_{31}, S_{41} of the rectifier array at an input power of −10 dBm.

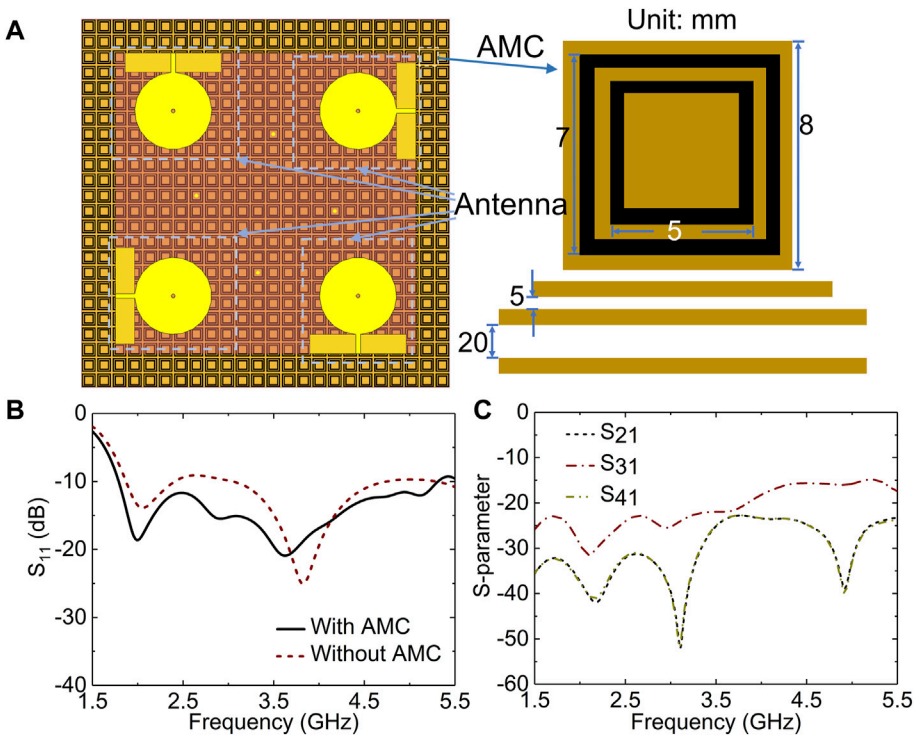

FIGURE 4 | (A) Geometry of the proposed antenna array. **(B)** Simulated reflection coefficient of the antenna with and without AMC structure. **(C)** Simulated S_{21}, S_{31}, S_{41} of the antenna array.

placed under the monopole antenna to increase the gain of the receiving antenna. The AMC is consisted of 24 × 24 square ring cells, and the dimension of the AMC cells is shown in **Figure 4A**. This design improves the radiation performance (S_{11}), and the corresponding impedance bandwidth can be extended to 1.79~5.31 GHz as shown in **Figure 4B**. Next, similar to the rectifier array design, the isolation feature of the antenna array was also studied, as shown in **Figure 4C**. It is obvious that the isolation performance between port 1 and port 2 (port 4) is excellent since the polarization of the two antennas is vertical. In addition, S_{31}, denoting the isolation between port 1 and port 3, is also less than −15 dB at the operating band, showing little cross-talk between ports. Similar characteristics of other ports can be drawn since the locations of the four monopoles are rotationally symmetric.

For evaluation, the proposed optimal antenna array was printed on a 0.787-mm-thick F4B substrate, as shown in **Figure 5B**, and the measured S_{11}, S_{21}, S_{31}, and S_{41} of the fabricated antenna array are illustrated in **Figure 5A**. The measured relative impedance bandwidth ($|S_{11}|$<−10 dB) of the antenna was 101.1% (1.74–5.3 GHz), and the center frequency was approximately 3.52 GHz. The measured S_{21}, S_{31}, and S_{41} show that the four antennas have great isolation. The simulated and measured realized gains of the antenna are also shown in

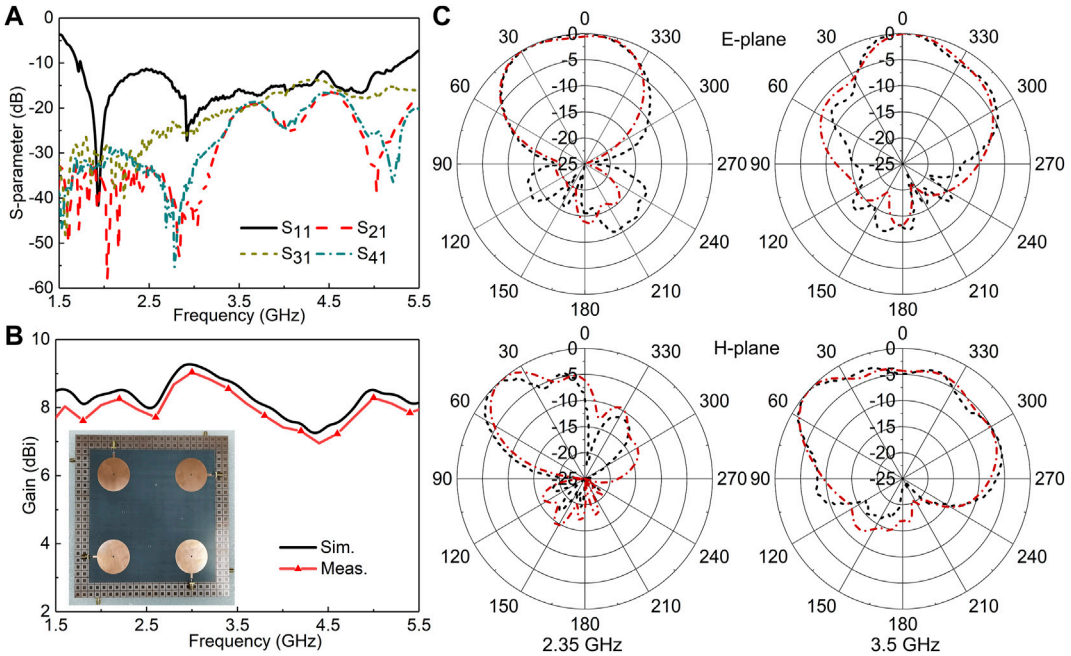

FIGURE 5 | Measured S-parameter **(A)**, gain **(B)** and radiation pattern **(C)**.

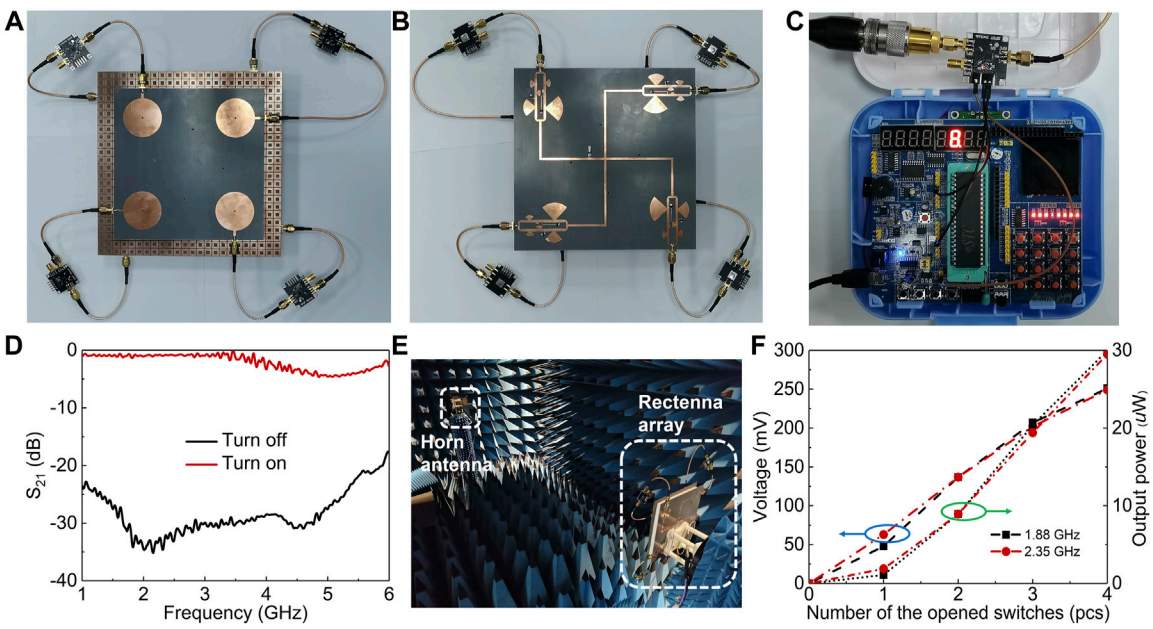

FIGURE 6 | (A,B) Photograph of the rectenna array. **(C)** The photograph of the single chip microcomputer and RF switch. **(D)** The measured S21 of the switch. **(E)** Measurement setup inside an anechoic chamber. **(F)** Measured voltage and out power of the rectenna array versus the number of the opened switches.

Figure 5B. The measured gain was approximately 7~9.5 dBi over the entire operating band. The simulated and measured 2-D radiation patterns of the proposed antenna array at 2.35 and 3.5 GHz are given in **Figure 5C**. The measured results agree well with the simulated results.

OUTPUT POWER RECONFIGURABLE RECTENNA ARRAY

Ultimately, the rectifier array is located under the AMC, and the ground plane of the rectifier array was designed as the reflecting

plane of the AMC to reduce the overall size. A photograph of the proposed power-reconfigurable rectenna array is shown in **Figures 6A,B**. Each HGA is connected to SFR by an RF switch to compose the dynamic rectenna array. The on-off state of the RF switch can be tuned by adding a 5 V bias voltage or not, which is provided by a single chip microcomputer, as shown in **Figure 6C**. The measured S_{21} of the RF switch is also shown in **Figure 6D**. The status of the RF switch can effectively affect the transmissive energy level, and therefore, the input energy to the rectifier is decided by changing the number of opened switches, resulting in the dynamic control of the output DC power.

To verify our design, the power reconfigurable rectenna array is measured in a microwave anechoic chamber, where the horn antenna connected with an RF signal generator is used as a transmitting antenna, and our design is adopted to receive RF energy, as shown in **Figure 6E**. The distance between the horn antenna and rectenna was taken as 2.7 m. Next, the output voltage and DC power across the load resistance were measured at 1.88 and 2.35 GHz with the number of opened switches, as shown in **Figure 6F**. The output voltage and output power increase with an increasing number of opened switches at two frequency bands. That is, in practice, different numbers of RF switches can be turned on according to the power required by the load.

CONCLUSION

In this paper, a reconfigurable rectenna array was proposed to realize the dynamic manipulation of the output DC power. The rectifier array and antenna array prototypes were constructed and measured to demonstrate the performance. The measured result shows that when the input RF energy is fixed, the output DC power can be successfully divided into four different levels by controlling the on-off state of the external RF switches. Our design shows great potential in driving low-power electronics since it can adjust its output voltage or output power according to the needs of applications.

DATA AVAILABILITY STATEMENT

The original contributions presented in the study are included in the article/Supplementary Material, further inquiries can be directed to the corresponding authors.

AUTHOR CONTRIBUTIONS

All authors listed have made a substantial, direct, and intellectual contribution to the work and approved it for publication.

FUNDING

This work was supported by the National Natural Science Foundation of China (62101394, 61722106, 62001338, and 61731010), the Fundamental Research Funds for the Central Universities (WUT: 2021IVA064, and 2021IVB029), and the Foundation from the Guangxi Key Laboratory of Optoelectronic Information Processing (GD21203).

REFERENCES

1. Song C, Huang Y, Zhou J, Carter P, Yuan S, Xu Q, et al. Matching Network Elimination in Broadband Rectennas for High-Efficiency Wireless Power Transfer and Energy Harvesting. *IEEE Trans Ind Electron* (2017) 64(5): 3950–61. doi:10.1109/tie.2016.2645505
2. Varasteh M, Rassouli B, Clerckx B. On Capacity-Achieving Distributions for Complex AWGN Channels under Nonlinear Power Constraints and Their Applications to SWIPT. *IEEE Trans Inform Theor* (2020) 66(10):6488–508. doi:10.1109/tit.2020.2998464
3. Zhang C, Long C, Yin S, Song RG, Zhang BH, Zhang JW, et al. Graphene-based Anisotropic Polarization Meta-Filter. *Mater Des* (2021) 206:109768. doi:10.1016/j.matdes.2021.109768
4. Zhang C, Yin S, Long C, Dong BW, He D, Cheng Q. Hybrid Metamaterial Absorber for Ultra-low and Dual-Broadband Absorption. *Opt Express* (2021) 29(9):14078–86. doi:10.1364/OE.423245
5. Zhang C, Cheng Q, Yang J, Zhao J, Cui TJ. Broadband Metamaterial for Optical Transparency and Microwave Absorption. *Appl Phys Lett* (2017) 110(14):143511. doi:10.1063/1.4979543
6. Nie M-J, Yang X-X, Tan G-N, Han B. A Compact 2.45-GHz Broadband Rectenna Using Grounded Coplanar Waveguide. *Antennas Wirel Propag Lett* (2015) 14:986–9. doi:10.1109/lawp.2015.2388789
7. Li X, Yang L, Huang L. Novel Design of 2.45-GHz Rectenna Element and Array for Wireless Power Transmission. *IEEE Access* (2019) 7:28356–62. doi:10.1109/access.2019.2900329
8. Mansour MM, Kanaya H. High-Efficient Broadband CPW RF Rectifier for Wireless Energy Harvesting. *IEEE Microw Wireless Compon Lett* (2019) 29(4): 288–90. doi:10.1109/lmwc.2019.2902461
9. Liu W, Huang K, Wang T, Zhang Z, Hou J. A Broadband High-Efficiency RF Rectifier for Ambient RF Energy Harvesting. *IEEE Microw Wireless Compon Lett* (2020) 30(12):1185–8. doi:10.1109/lmwc.2020.3028607
10. He Z, Liu C. A Compact High-Efficiency Broadband Rectifier with a Wide Dynamic Range of Input Power for Energy Harvesting. *IEEE Microw Wireless Compon Lett* (2020) 30(4):433–6. doi:10.1109/lmwc.2020.2979711
11. Singh N, Kanaujia BK, Tariq Beg M, Mainuddin S, Kumar S. A Triple Band Circularly Polarized Rectenna for RF Energy Harvesting. *Electromagnetics* (2019) 39(7):481–90. doi:10.1080/02726343.2019.1658164
12. Keshavarz R, Shariati N. Highly Sensitive and Compact Quad-Band Ambient RF Energy Harvester. *IEEE Trans Ind Electron* (2022) 69:3609–21. doi:10.1109/tie.2021.3075888
13. Song C, Huang Y, Carter P, Zhou J, Yuan S, Xu Q, et al. A Novel Six-Band Dual CP Rectenna Using Improved Impedance Matching Technique for Ambient RF Energy Harvesting. *IEEE Trans Antennas Propagat* (2016) 64(7):3160–71. doi:10.1109/tap.2016.2565697
14. Shen S, Chiu C-Y, Murch RD. A Dual-Port Triple-Band L-Probe Microstrip Patch Rectenna for Ambient RF Energy Harvesting. *Antennas Wirel Propag Lett* (2017) 16:3071–4. doi:10.1109/lawp.2017.2761397
15. Shen S, Zhang Y, Chiu C-Y, Murch R. An Ambient RF Energy Harvesting System where the Number of Antenna Ports Is Dependent on Frequency. *IEEE Trans Microwave Theor Techn.* (2019) 67(9):3821–32. doi:10.1109/tmtt.2019.2906598
16. Sun H, Guo Y, He M, Zhong Z. Design of a High-Efficiency 2.45-GHz Rectenna for Low-Input-Power Energy Harvesting. *Antennas Wirel Propag Lett* (2012) 11:929–32. doi:10.1109/lawp.2012.2212232

17. Song C, Lu P, Shen S. Highly Efficient Omnidirectional Integrated Multiband Wireless Energy Harvesters for Compact Sensor Nodes of Internet-Of-Things. *IEEE Trans Ind Electron* (2021) 68(9):8128–40. doi:10.1109/tie.2020.3009586

Conflict of Interest: The authors declare that the research was conducted in the absence of any commercial or financial relationships that could be construed as a potential conflict of interest.

Publisher's Note: All claims expressed in this article are solely those of the authors and do not necessarily represent those of their affiliated organizations, or those of the publisher, the editors and the reviewers. Any product that may be evaluated in this article, or claim that may be made by its manufacturer, is not guaranteed or endorsed by the publisher.

frontiers in Physics

ORIGINAL RESEARCH
published: 14 March 2022
doi: 10.3389/fphy.2022.872992

Liquid Metal-Embedded Layered-PDMS Antenna for Flexible and Conformal Applications

*Meng Wang, Zhifu Liu and Jian Dong**

School of Computer Science and Engineering, Central South University, Changsha, China

This article proposes a dual-band slot IFA antenna using a combined technique of liquid metal (LM) filling and polydimethylsiloxane substrate. The antenna working at 2.4 and 5.8 GHz consists of three liquid metal layers—radiation patch, short circuit stub, and ground plane and can be bent to different radiuses for flexible, conformal, and wearable applications. The vacuum filling method enables realization of a monolithic-integrated substrate. The applicability of this antenna for a wearable wristband is validated through simulation.

Keywords: liquid metal, flexible antennas, microfluidic channel, PDMS, wearable application

OPEN ACCESS

Edited by:
Zhewang Ma,
Saitama University, Japan

Reviewed by:
Lei Xing,
Nanjing University of Aeronautics and Astronautics, China
Jun Xiao,
Jimei University, China

****Correspondence:***
Jian Dong
dongjian@csu.edu.cn

Specialty section:
This article was submitted to Optics and Photonics, a section of the journal Frontiers in Physics

Received: *10 February 2022*
Accepted: *21 February 2022*
Published: *14 March 2022*

Citation:
Wang M, Liu Z and Dong J (2022) Liquid Metal-Embedded Layered-PDMS Antenna for Flexible and Conformal Applications. Front. Phys. 10:872992. doi: 10.3389/fphy.2022.872992

INTRODUCTION

The demand for compact, multiband, and flexible microwave components and antennas is increasing due to the prosperity of the Internet of Things (IoT) [1, 2]. Typical IoT systems are found in a lot of emerging and conventional scenarios, such as smart industry or wireless body area network (WBAN), where various sensors are required for industrial information collecting or human healthcare monitoring, among which conformal or flexible antennas are critical to transit the collected data. Such antennas for wearable applications (clothes, shoes, bracelets, and glasses) utilize flexible substrate, including paper, textiles or polymer composites, and conductive materials, such as electro-textiles and nanowire, instead of conventional rigid substrates or metal in cases they can be bent or twisted when worn on the human body [3–6]. Furthermore, in order to maximize the connectivity, the antenna for body communications usually operates at multiple bands for on- and off-body communications [7–9].

Eutectic liquid metal (LM) with low toxicity and high conductivity at room temperature is potential for creating antennas with flexibility and high conformity [10]. Particularly, the LM fluidity is critical for maintaining conductive continuity during deformation. When capsulated within soft materials, such as polydimethylsiloxane (PDMS), the LM-enabling technology enables creation of flexible antennas. The bendable microstrip patch and dipole antennas are constructed by injecting LM into microfluidic channels molded by PDMS [11, 12]. A flexible antenna based on liquid metal and additive printing technologies is given in [13], in which the microfluidic branch is printed in flexible NinjaFlex plastic. These antennas can be bent or curved to different radiuses, and at the same time the antenna radiation properties maintain stability during the deformation. Most of these LM channels or cavities are constructed along one-dimensional axis or on two-dimensional surfaces with only two layers, while the three-dimensional volume has not been fully exploited. Stretchable sensors using 3D-printed LM demonstrate stable conductivity of the liquid metal paste circuit interconnects among [14]. The combined technique of liquid metal filling and PDMS material as a substrate has great potential in flexible antenna applications. Based on the authors' knowledge, there has not been much investigation into the LM antennas for wearable applications.

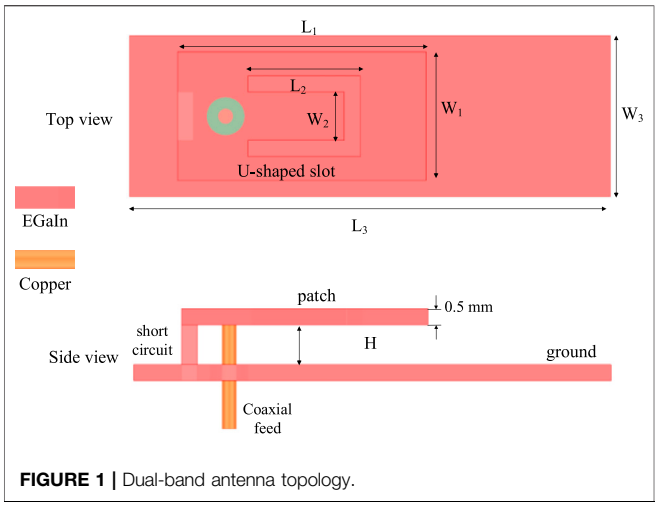

FIGURE 1 | Dual-band antenna topology.

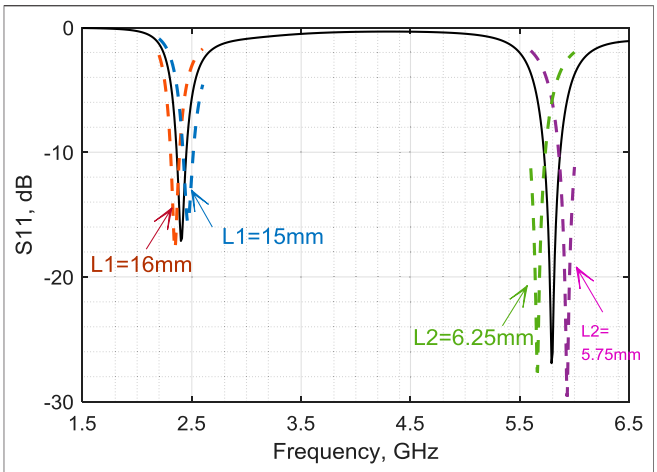

FIGURE 2 | Reflection coefficient of the dual-band IFA.

This article proposes the design and implementation of a LM dual-band antenna for wrist-worn applications. The antenna, with dimensions of 30 × 12 × 4.5 mm^3, operating at two WLAN frequency bands—2.4 and 5.8 GHz, comprises radiating cavities formed by LM filling within a PDMS substrate. In order to fabricate the proposed antenna, a layered-bonding method to fabricate the PDMS wristband structure and a vacuum compression method to inject LM into the microfluidic channels are implemented.

ANTENNA DESIGN AND FABRICATION

Antenna Design

The structure of the LM antenna adopts the structure of inverted-F antenna (IFA) with three parts—the radiation patch of width W_1 and length L_1 on the top layer, a U-slot of width W_2 and length L_2 is etched on the radiation patch for generating the band at 5.8 GHz while the IFA resonates at 2.4 GHz, the ground plane of width W_3 and length L_3 on the bottom layer, and the rectangular short circuit of width SW and height H in between as shown in **Figure 1**. The distance from the short circuit to the left side of the grounding plane is optimized to be 2 mm for impedance matching. The two resonances can be roughly determined from the following equations (15),

$$f_1 = \frac{c}{4(H + L_1 + W_1)}, f_2 = \frac{c}{4(H + L_2 + W_2)}$$

Dimensions of the patch, the slot, and the short circuit are optimized to resonate the antenna at the aforementioned two bands and listed as follows: W_1 = 8 mm, L_1 = 15.5 mm, W_2 = 3 mm, L_2 = 7 mm, W_3 = 10 mm, L_3 = 30 mm, and H = 2.5 mm. The proposed antenna operates at dual-bands—2.4 GHz covering 100 MHz and 5.8 GHz covering 150 MHz with a well-matched reflection coefficient below −10dB. Different to conventional copper cladding on PCB technology, LM-based devices use post-filled LM to construct a conductive path. Based on our experimental experience, the whole cavity volume can be filled

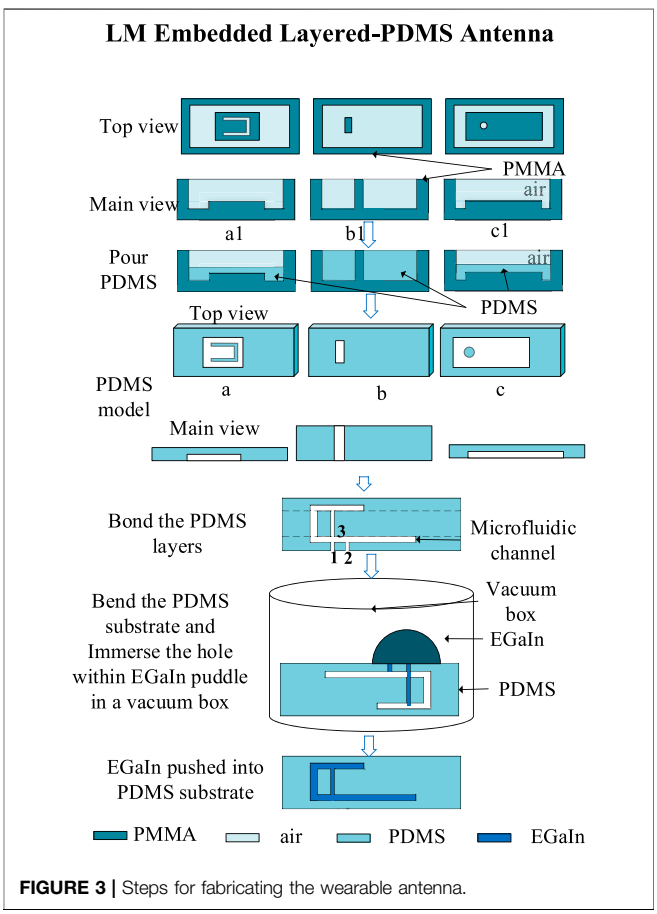

FIGURE 3 | Steps for fabricating the wearable antenna.

with LM through visual checking. But, still minor possibility of unfilled cavity corners might exit. Therefore, it is reasonable to briefly evaluate the sensitivity of the antenna resonances to the change of the aforementioned dimensions. Parametric simulations show that the resonance shifts less than 5% when

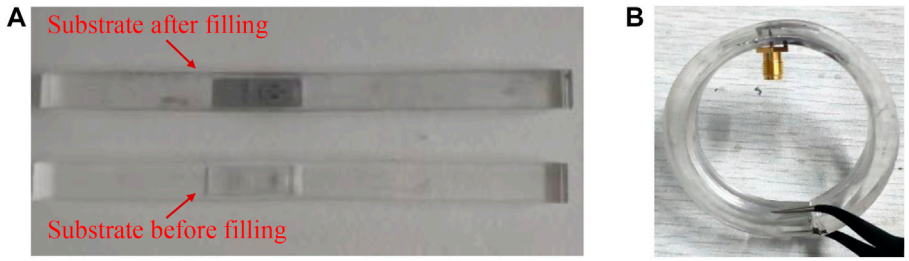

FIGURE 4 | Photographs of the fabricated wearable antenna. **(A)** Flat wristband before and after filling LM and **(B)** curved wristband filled with LM.

L_1 and L_2 vary between 0.5 and 0.25 mm shown in **Figure 2**, respectively. This ensures that when corners of the microfluidic channels and cavities are occasionally hollow due to partially filled LM, the frequencies still locate within the desired bands and maintain the desired frequencies.

To achieve flexibility and mitigate the user discomfort of the antenna wristband, PDMS (Sylgard 184 kit, Dow Corning) with a dielectric constant of 2.68 and loss tangent of 0.0375 is chosen as the substrate material for its high elasticity and low surface tension. Meanwhile, PDMS is human skin-safe and widely used in various consumer and cosmetic products. PDMS is composed of two solvents—polymer and crosslinker with a mass ratio 10:1. PDMS can be cured by placing it in an oven at 80°C for 2 h and therefore is routinely used for preparing microfluidic channels. A layered bonding process technology is implemented to assemble the different PDMS layers. Due to the liquid nature of LM, channels are reserved within the PDMS substrate for latterly injecting LM into the channel.

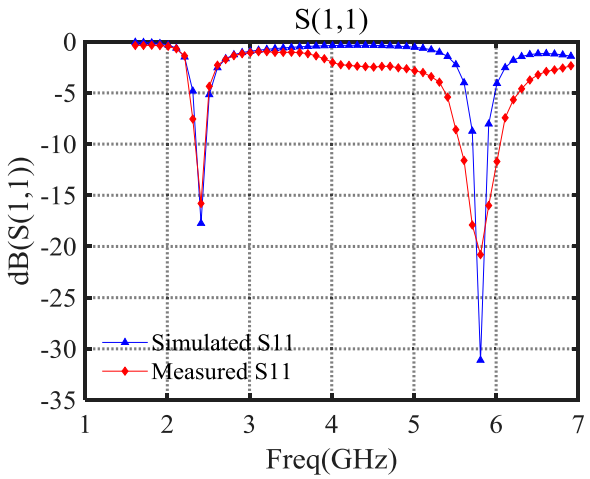

FIGURE 5 | Reflection coefficient of the wearable antenna.

Antenna Fabrication

The schematic view of the manufacturing process is presented in **Figure 3**. The fabrication process of the wearable antenna includes mainly molding the PDMS wristband and metalizing the wristband [16]. The three layers of wristband are made, respectively, which are made of PMMA material and processed using a high-precision computerized numerical control (CNC) machine. To ensure that LM is completely wrapped, the heights of the molds are not consistent. The prepared PDMS solution is poured into three molds, respectively, and then put them into a vacuum oven to cure at 80°C for 2 h. Since the PMMA material is easy to demold, the cured PDMS can be peeled out of the mold to obtain three substrate layers. These layers are bonded after cleansed using a plasma cleaning machine. A total of three holes with a diameter of 0.9 mm are drilled in the model, and then LM is pneumatically pushed into the cavity by the vacuum compression method [17]. In order to inject EGaIn into the PDMS wristband model, the wristband model is inverted and placed in the vacuum oven after putting the LM on top of the circular holes 1 and 2. After evacuating the air in the vacuum box and the microfluidic channel, EGaIn will all be pushed into the microfluidic channel once the vacuum box is opened.

The prototype of the wearable antenna is fabricated as shown in **Figure 4**. The three PDMS layers are molded, respectively, and then bonded together by plasma treatment. Then, LM is pushed into the microfluidic channels through vacuum filling after assembling the three layers. The vacuum-filling method ensures that the least air bubbles are generated during this process so that the three-dimensional conductive path is well established. Superglue is attached between SMA connectors and the PDMS substrate to fix the connection in case the LM leaks and the frequency bands shift. Based on our knowledge, this is the first demonstration of multilayer PDMS-embedded liquid metal antenna for wearable applications. Compared to the liquid metal antenna printed on a planar surface with only two layers, although can be curved to different radiuses, this prototype antenna realizes a three-dimensional-layered LM structure that utilizes the vertical space of the flexible substrate. Although the antenna topology in this article is an inverted-F antenna commonly used for wireless communication, the proposed process technology can be extended to manufacturing of more complicated antenna structures, therefore exploiting the three-dimensional space and maximizing the design degree.

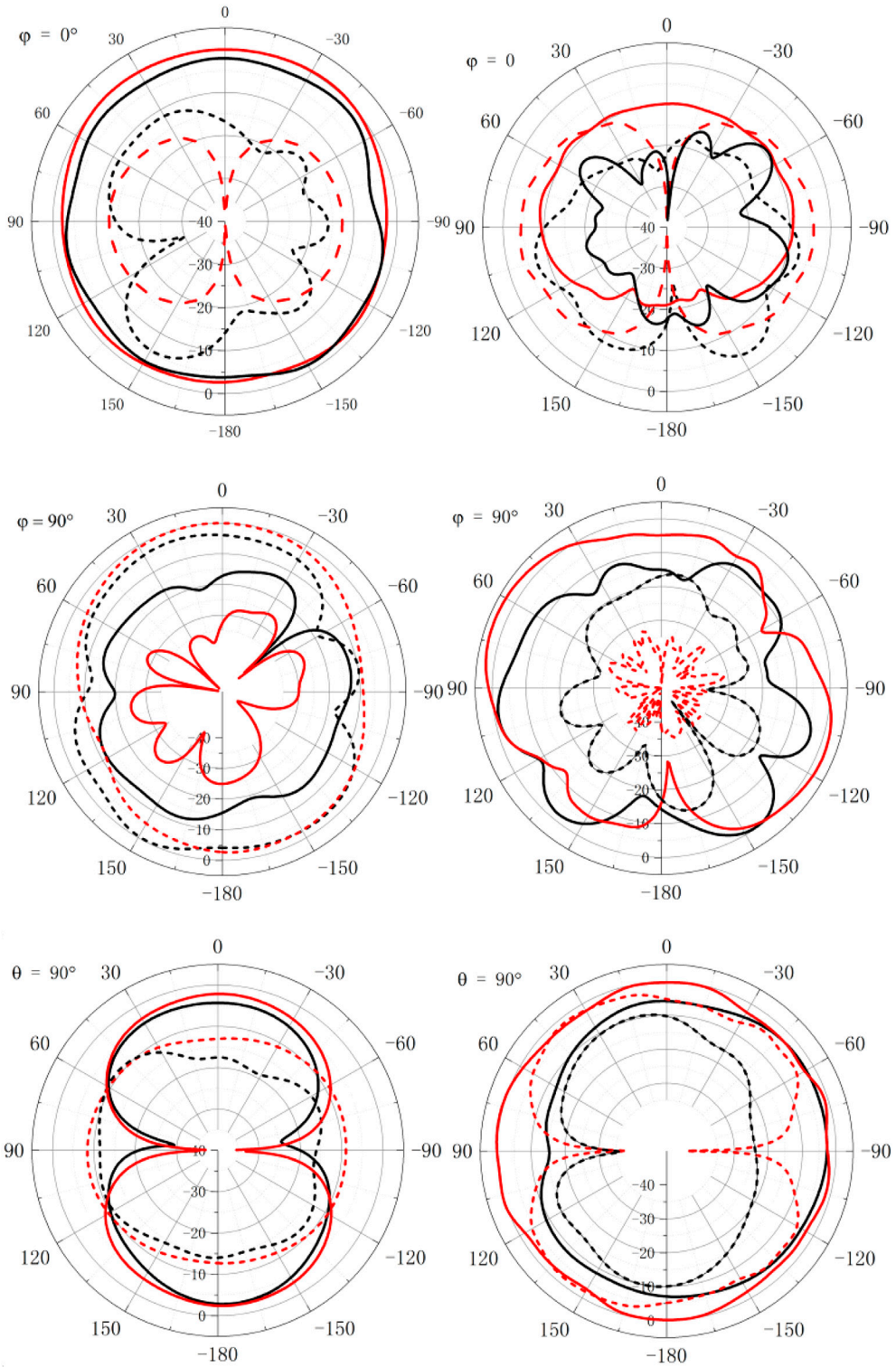

FIGURE 6 | Measured and simulated radiation patterns of the wearable antenna for the x-z, y-z, and x-y planes at 2.4 GHz (left) and 5.8 GHz (right). Solid lines indicate the E_{φ} component and dashed lines for E_{θ} component. Red lines indicate the simulated patterns and black lines for measured patterns.

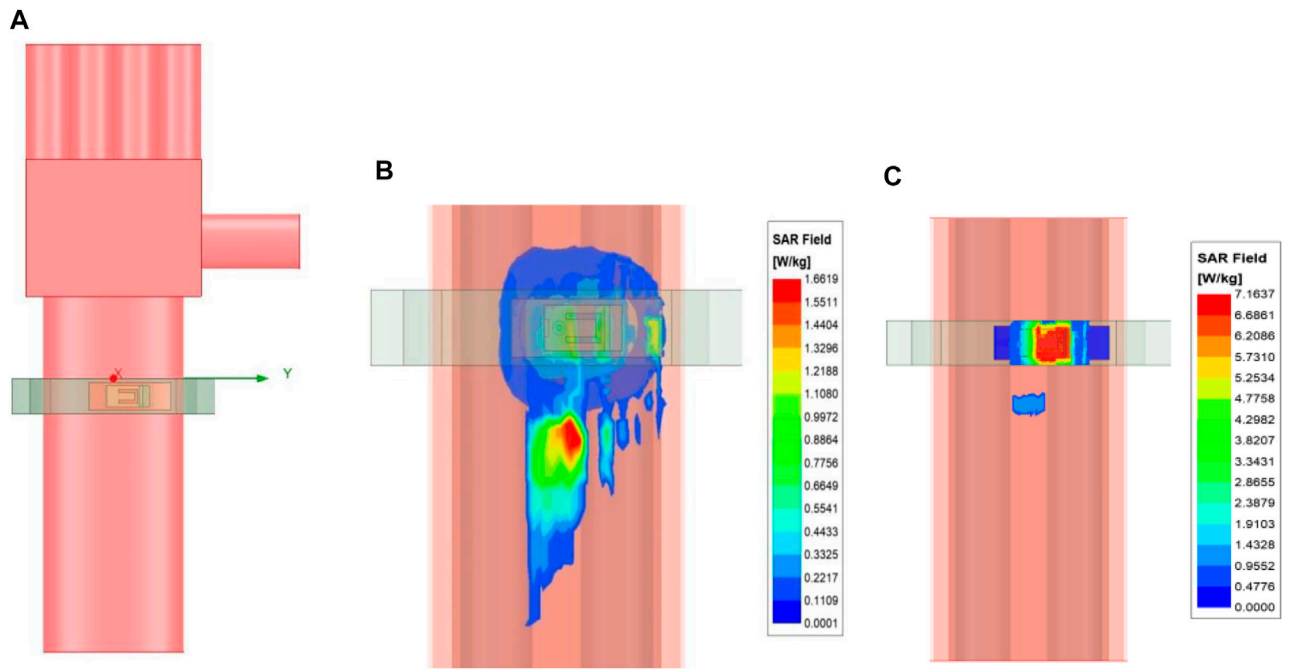

FIGURE 7 | Average SAR values of the human wrist wearing the LM antenna. **(A)** Antenna worn on the human wrist, **(B)** average SAR values of the human wrist at 2.4 GHz, and **(C)** average SAR values of the human wrist at 5.8 GHz.

ANTENNA RESULTS AND DISCUSSION

To assess the radiation properties of the proposed flexible antenna, the prototype antenna in **Figure 4** is built and measured. The experimental data are compared to the simulation results obtained from a full-wave simulator. The antenna impedance matching behavior over the frequency range of 1–7 GHz is shown in **Figure 5**. Due to the flexibility of the PDMS substrate and the fluidity of LM, this wearable antenna can be bent to curvatures of different radiuses.

The radiation patterns of the flexible antenna on a flat platform (in the x-y, x-z, and y-z planes) are simulated and measured as shown in **Figure 6**. The plots show the graphs of the E_φ and E_θ components, and it is seen that the patterns are nearly omnidirectional at several conditions of the two frequencies. The discrepancies between the simulated and measured radiation patterns are more prominent at higher frequencies possibly due to uneven filling of LM within cavities or unstable connection of LM to an SMA connector during rotation of measurements. The measured gain and efficiency of the flexible antenna are 1.55 dBi and 34.6% at 2.4 GHz, 1.66 dBi and 28.74% at 5.8 GHz, respectively. Compared to antenna structures copper plated on commercial substrates (Rogers or FR4 boards), this antenna has a low efficiency mainly due to the lossy PDMS substrates. Customizable PDMS made of different proportions of materials can be implemented to mitigate the negative effects brought by the PDMS substrates [16].

Since this flexible antenna can be bent to different radiuses, it could be used as a wearable antenna. Such as when worn on the human wrist, the antenna mainly works in areas close to the human body; the nonuniform human body will mutually affect the antenna performance due to its electrical complexity. **Figure 7** shows a human wrist model consisting of skin, muscle, fat, and bone, exhibiting various electromagnetic properties over the bands of interest [18]. Our full-wave analysis indicates that when the wearable antenna is 5 mm away from the surface of the human body, the antenna operates with the same bands within free space. Meanwhile, the human body absorbs and dissipates part of the antenna electromagnetic radiation due to its lossy intrinsic, usually quantified by the specific absorption rate (SAR). SAR is usually limited to a standard of 2 W/kg per 10 g of human tissue [19]. **Figure 5** shows the SAR values at the bands of 2.4 and 5.8 GHz. The local SAR peaks are 1.66 W/kg and 7.16 W/kg when the input power is on the scale of mW, which, however, is higher than the regulated SAR standards. For this particular scenario, the ground plane of the antenna is narrower than a typical IFA antenna, and the antenna structure has not been optimized for a reduced SAR. Enlarging the ground plane of the antenna and adapting the antenna topology are methods to reduce the SAR values to the regulated levels in our future research.

CONCLUSION

This article introduces a dual-band flexible antenna for conformal or wearable applications. The combined technique of using liquid metal as the radiating patch and PDMS as the substrate enables creation of such flexible antenna structures. At the same time, a layered bonding processing technology and vacuum compression technology facilitate the monolithic integration. The radiation

properties of the two bands at 2.4 and 5.8 GHz are evaluated. As a demonstration, the LM-embedded layered-PDMS antenna is implemented on a human wrist for validating its applicability. This article concludes that the LM–PDMS combined technique can be extended to more complex scenarios, such as flexible and conformal reconfigurable antenna arrays for sensing and communicating.

DATA AVAILABILITY STATEMENT

The original contributions presented in the study are included in the article/Supplementary Material, further inquiries can be directed to the corresponding author.

AUTHOR CONTRIBUTIONS

MW contributed to the conceptual design and simulation; ZL performed the simulation and wrote the first version of this manuscript; JD contributes to the conceptual design and implementation. All authors contributed to manuscript revision, and read and approved the submitted version.

FUNDING

This work was supported in part by the National Natural Science Foundation of China under Grant No. 61801521 and 61971450, in part by the Natural Science Foundation of Hunan Province under Grant No. 2018JJ2533.

REFERENCES

1. Xu K-D, Luyen H, Behdad N. A Decoupling and Matching Network Design for Single- and Dual-Band Two-Element Antenna Arrays. *IEEE Trans Microwave Theor Techn.* (2020) 68(9):3986–99. doi:10.1109/tmtt.2020.2989120
2. Xu K-D, Xia S, Jiang Y, Guo Y-J, Liu Y, Wu R, et al. Compact Millimeter-Wave On-Chip Dual-Band Bandpass Filter in 0.15-μm GaAs Technology. *IEEE J Electron Devices Soc* (2022) 10:152–6. doi:10.1109/jeds.2022.3143999
3. Chen SJ, Kaufmann T, Ranasinghe DC, Fumeaux C. A Modular Textile Antenna Design Using Snap-On Buttons for Wearable Applications. *IEEE Trans Antennas Propagat* (2016) 64(3):894–903. doi:10.1109/tap.2016.2517673
4. Ullah M, Islam M, Alam T, Ashraf F. Paper-Based Flexible Antenna for Wearable Telemedicine Applications at 2.4 GHz ISM Band. *Sensors* (2018) 18(12):4214. doi:10.3390/s18124214
5. Kim S, Ren Y-J, Lee H, Rida A, Nikolaou S, Tentzeris MM. Monopole Antenna with Inkjet-Printed EBG Array on Paper Substrate for Wearable Applications. *Antennas Wirel Propag Lett* (2012) 11:663–6. doi:10.1109/lawp.2012.2203291
6. Kim BS, Shin K-Y, Pyo JB, Lee J, Son JG, Lee S-S, et al. Reversibly Stretchable, Optically Transparent Radio-Frequency Antennas Based on Wavy Ag Nanowire Networks. *ACS Appl Mater Inter* (2016) 8(4):2582–90. doi:10.1021/acsami.5b10317
7. Sanz-Izquierdo B, Miller JA, Batchelor JC, Sobhy MI. Dual-band Wearable Metallic Button Antennas and Transmission in Body Area Networks. *IET Microw Antennas Propag* (2010) 4(2):182–90. doi:10.1049/iet-map.2009.0010
8. Zhang XY, Wong H, Mo T, Cao YF. Dual-Band Dual-Mode Button Antenna for On-Body and Off-Body Communications. *IEEE Trans Biomed Circuits Syst* (2017) 11(4):933–41. doi:10.1109/tbcas.2017.2679048
9. Xu KD, Li D, Liu Y, Liu QH. Printed Quasi-Yagi Antennas Using Double Dipoles and Stub-Loaded Technique for Multi-Band and Broadband Applications. *IEEE Access* (2018) 6:31695–702. doi:10.1109/access.2018.2838328
10. Khan MR, Eaker CB, Bowden EF, Dickey MD. Giant and Switchable Surface Activity of Liquid Metal via Surface Oxidation. *Proc Natl Acad Sci USA* (2014) 111(39):14047–51. doi:10.1073/pnas.1412227111
11. Hayes GJ, Ju-Hee So JH, Qusba A, Dickey MD, Lazzi G. Flexible Liquid Metal Alloy (EGaIn) Microstrip Patch Antenna. *IEEE Trans Antennas Propagat* (2012) 60(5):2151–6. doi:10.1109/tap.2012.2189698
12. Morishita AM, Kitamura CKY, Ohta AT, Shiroma WA. A Liquid-Metal Monopole Array with Tunable Frequency, Gain, and Beam Steering. *Antennas Wirel Propag Lett* (2013) 12:1388–91. doi:10.1109/lawp.2013.2286544
13. Cosker M, Lizzi L, Ferrero F, Staraj R, Ribero J-M. Realization of 3-D Flexible Antennas Using Liquid Metal and Additive Printing Technologies. *Antennas Wirel Propag Lett* (2017) 16:971–4. doi:10.1109/lawp.2016.2615568
14. Votzke C, Daalkhaijav U, Menguc Y, Johnston ML. 3D-Printed Liquid Metal Interconnects for Stretchable Electronics. *IEEE Sensors J* (2019) 19(10):3832–40. doi:10.1109/jsen.2019.2894405
15. Salonen P, Keskilammi M, Kivikoski M. "Dual-band and Wide-Band PIFA with U- and Meanderline-Shaped Slots." in Proceedings of the IEEE Antennas and Propagation Society International Symposium 2001 Digest Held in conjunction with: USNC/URSI National Radio Science Meeting (Cat No01CH37229); 8-13 July 2001; Boston, MA, USA (2001).
16. Trajkovikj J, Zurcher J-F, Skrivervik AK. PDMS, A Robust Casing for Flexible W-BAN Antennas [EurAAP Corner]. *IEEE Antennas Propag Mag* (2013) 55(5):287–97. doi:10.1109/map.2013.6735538
17. Bharambe V, Parekh DP, Ladd C, Moussa K, Dickey MD, Adams JJ. Liquid-Metal-Filled 3-D Antenna Array Structure with an Integrated Feeding Network. *Antennas Wirel Propag Lett* (2018) 17(5):739–42. doi:10.1109/lawp.2018.2813309
18. Jun SY, Elibiary A, Sanz-Izquierdo B, Winchester L, Bird D, McCleland A. 3-D Printing of Conformal Antennas for Diversity Wrist Worn Applications. *IEEE Trans Compon., Packag Manufact Technol* (2018) 8(12):2227–35. doi:10.1109/tcpmt.2018.2874424
19. Xiaomu H, Yan S, Vandenbosch GAE. Wearable Button Antenna for Dual-Band WLAN Applications with Combined on and Off-Body Radiation Patterns. *IEEE Trans Antennas Propagat* (2017) 65(3):1384–7. doi:10.1109/tap.2017.2653768

Conflict of Interest: The authors declare that the research was conducted in the absence of any commercial or financial relationships that could be construed as a potential conflict of interest.

Publisher's Note: All claims expressed in this article are solely those of the authors and do not necessarily represent those of their affiliated organizations, or those of the publisher, the editors, and the reviewers. Any product that may be evaluated in this article, or claim that may be made by its manufacturer, is not guaranteed or endorsed by the publisher.

frontiers in Physics

ORIGINAL RESEARCH
published: 22 March 2022
doi: 10.3389/fphy.2022.850186

Mixed-Resolution High-Q Sensor Based on Hybridized Spoof Localized Surface Plasmons

Jiangpeng Wang[1,2], *Jingjing Zhang*[1,2], *Hao Gao*[3,4], *Xiaojian Fu*[1,2], *Di Bao*[1,2]* and *Tie Jun Cui*[1,2]*

[1]Institute of Electromagnetic Space, Southeast University, Nanjing, China, [2]State Key Laboratory of Millimeter Waves, Southeast University, Nanjing, China, [3]Silicon Austria Labs, Linz, Austria, [4]Electrical Engineering Department, Eindhoven University of Technology, Netherlands

Spoof localized surface plasmons (LSPs) have proven significant advantages in sensing and detection. In this work, we propose a high-*Q*-factor and high-sensitivity hybridized spoof LSP sensor and a mixed-resolution algorithm. The sensor consists of two concentric inner and outer LSP structures with corrugated rings coupled to each other. The achieved *Q*-factor is up to 178, and the sensing figure of merit (*FoM*) is up to 30. Moreover, a mixed-resolution algorithm, combined with multiple resonant peaks, is proposed to enhance the *Q*-factor and sensing *FoM*. This algorithm doubles the *Q*-factor and sensing *FoM* effectively. This mixed-resolution sensor has a wide range of application prospects in the field of high-frequency on-chip resonators and sensors.

Keywords: spoof localized surface plasmons, sensor, hybridization, mixed-resolution, spoof surface plasmons

OPEN ACCESS

Edited by:
Kai-Da Xu,
Xi'an Jiaotong University, China

Reviewed by:
Zhen Liao,
Hangzhou Dianzi University, China
Dibakar Roy Chowdhury,
Mahindra École Centrale College of Engineering, India

***Correspondence:**
Di Bao
dibao@seu.edu.cn
Tie Jun Cui
tjcui@seu.edu.cn

Specialty section:
This article was submitted to Optics and Photonics, a section of the journal Frontiers in Physics

Received: *07 January 2022*
Accepted: *11 February 2022*
Published: *22 March 2022*

Citation:
Wang J, Zhang J, Gao H, Fu X, Bao D and Cui TJ (2022) Mixed-Resolution High-Q Sensor Based on Hybridized Spoof Localized Surface Plasmons. Front. Phys. 10:850186. doi: 10.3389/fphy.2022.850186

INTRODUCTION

Spoof localized surface plasmons (LSPs) in corrugated metal cylinders were proposed by Pendry et al. [1] in 2012, and magnetic spoof LSPs with long curved corrugated grooves were proposed and experimentally demonstrated by Cui et al. [2]. In 2014, Cui et al. realized the design and verification of ultrathin LSPs for the first time [3]. Following that, many different structures of spoof LSPs such as ultrathin corrugated metal–insulator–metal ring resonator [4], compact spoof LSPs [5], spoof LSP hybridization [6], spiral spoof LSPs [7], and meander line structure [8] were investigated and proposed. Spoof LSPs have been proven to be valuable in the design of resonators [9–11], filters [12, 13], sensors [14], biomedical applications [15], etc. Due to the strong confinement of the electromagnetic field [16], the spoof LSP resonance has a high-*Q*-factor [17] and is sensitive to the surrounding environment. Therefore, spoof LSP structures became popular and widely used in microwave and millimeter wave sensor research.

A metallic ring with corrugated gratings is the elementary structure of spoof LSPs. There have been several reports on spoof LSP sensors, such as quarter-mode spoof LSP microfluidic chemical sensor [18, 19], flexible and printed microwave plasmonic sensor [20], single hybrid plasmonic resonator [21], and effective LSP sensor [22]. Those spoof LSP structures could improve *Q*-factor and sensitivity significantly, compared to conventional resonator structures [21, 23]. Asymmetric metamaterials [24] or symmetry-broken in toroidal plasmonic resonator [25] can exhibit sharp Fano-resonances or a high-*Q* trapped mode, which shows excellent performance in resonator and sensor fields. In previous research, hybridization of spoof LSP structures can produce enormous field enhancement and improve the *Q*-factor [26]. The hybridized spoof LSPs can enhance resonance while preserving the structure area, which is beneficial to on-chip integration design [6].

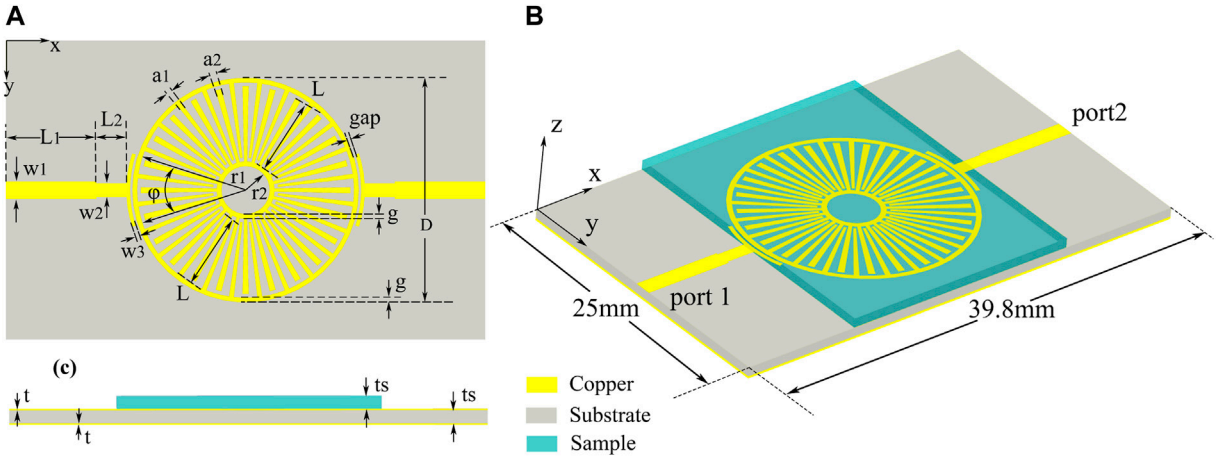

FIGURE 1 | Proposed spoof LSP sensor structure. **(A)** The detail and geometric parameters of the top view. **(B)** The 3D perspective view of the spoof LSP sensor. **(C)** The side view of the schematic diagram.

In addition to simple physical sensors, other dimensions of sensing enhancing methods such as multifactor sensing [27], chemical sensing with the addition of black phosphorus and graphene [28], and index sensors with multimode interference [29] have been carried out. Nevertheless, those methods are limited to the structural level, resulting in high operation difficulty and cost. It would be cheap, convenient, fast, and easy to implement *Q*-factor and sensing *FoM* enhancement through back-end data processing.

In this study, we designed a multimode and high-sensitivity sensor in the microwave region, and this sensor is based on hybridized spoof localized surface plasmons and proposes a mixed-resolution algorithm to enhance the *Q*-factor further. The hybridized spoof LSP sensor is a coupling structure with inner and outer corrugated rings. The sensor exhibits a high-*Q*-factor and high sensing *FoM* with samples of different permittivity values on the top of the spoof LSP structure. Measurements and simulations match well, which confirm the theory. It also demonstrated that spoof LSPs could be excited and functional as a microwave sensor with a high-*Q*-factor and sensing *FoM*. The proposed mixed-resolution algorithm combines two or more resonant peaks to form one resonant peak with almost doubled *Q*-factor and sensing *FoM* than raw data. The mixed-resolution spoof LSP sensor can be extended to the terahertz band and has a wide range of applications in on-chip high-frequency resonators and sensors.

HIGH-*Q* HYBRIDIZED SPOOF LOCALIZED SURFACE PLASMON RESONATOR

The proposed high-*Q* concentric corrugated ring-coupled resonator is excited by microstrip lines (MSs), as demonstrated in **Figure 1**. Both the inner and outer LSP structures contain 24 grooves. The inner radius, the groove height, the groove width, and the strip width of the inner and the outer corrugated rings are $r_1 = 9mm$, $r_2 = 2mm$, $L = 6.3mm$, $a_1 = 0.4mm$, $a_2 = 0.4mm$, and $g = 0.4mm$, respectively. The length and width of the 50Ω microstrip line and the impedance matching strip are $L_1 = 7.5mm$, $L_2 = 2.5mm$, $w_1 = 1.45mm$, and $w_2 = 1.15mm$. The angle φ and the width w_3 of the circular arc of the coupling feed structure are 36° and $0.3mm$, respectively. The width of the gap (gap) between the coupling feeding structure and the LSPs is $0.2mm$. The LSP resonator and MS coupling structures are etched on a 0.508-mm-thick Rogers RT5880 substrate with 0.018-mm copper. To enhance the resonances of this LSP structure and define the microstrip line's ground plane, the whole back of the substrate is covered with copper, as shown in **Figure 1C**. The sample for characterization is placed on the top of this structure, as demonstrated in **Figure 1B**. Rogers' plates with very small loss and different permittivities were selected as the samples.

The simulated transmission coefficients of the spoof localized surface plasmon resonator are obtained using the commercial software CST. The experimental results are measured using a vector network analyzer (Agilent N5230C). Both simulated and measured results are plotted in **Figure 2A**. It shows that the simulated results are in good agreement with the measured results. This structure is designed with 7 resonance peaks, marked as *m1* to *m7* from the range of 0 to 8 GHz. Those resonance frequencies are located at 2.03, 3.72, 4.29, 4.91, 5.69, 6.46, and 7.82 GHz. In the measurement, the measured frequency responses confirmed those 7 resonance peaks. And those frequency points are located at 2.037, 3.736, 4.27, 4.94, 5.73, 6.43 and 7.77 GHz, respectively, which matches the design. The quality factor of resonator represents the ratio of stored energy to the consumed energy of the resonant circuit, respectively, which can be expressed as follows:

$$Q = \frac{f_0}{\Delta f_{3dB}}, \tag{1}$$

where f_0 is the resonance frequency and Δf_{3dB} represents the 3dB bandwidth of the resonance peak. In **Figure 2A**, the

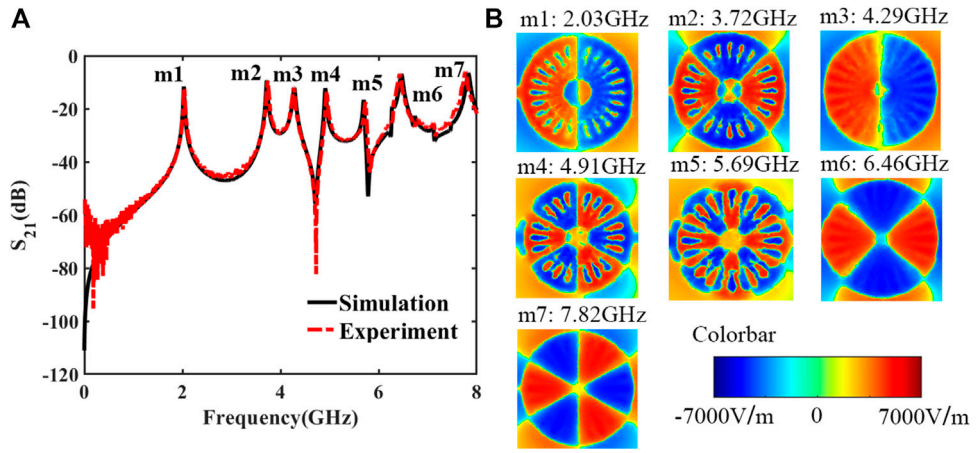

FIGURE 2 | (A) Simulated and measured transmission coefficients of the spoof LSP resonator. **(B)** The simulated 2D near electric field distributions at the resonance frequencies on the plane 1 mm above the resonator.

Q-factors of simulated modes *m*1 to *m*7 are 122, 147.6, 98, 186.8, 245, 103, and 122. The *Q*-factors of measured results are 108, 118, 97.3, 178.4, 160.3, 93.2, and 121.3 at each resonance peak, which is also close to the simulated data. The measured highest *Q*-factor is 178.4 at 4.94 GHz.

To further study the mechanism of this high-*Q*-factor resonance of the spoof LSP structure, a 2D near-field electric distribution at the resonance modes *m*1 to *m*7 on the plane 1 mm above the resonator is illustrated in **Figure 2B**. The *m*1, *m*2, *m*4, and *m*5 modes in **Figure 2B** are the odd dipole, quadrupole, hexapole, and octupole, respectively. The inner and outer spoof LSP resonators are resonant in opposite phases in these odd modes. The modes *m*3, *m*6, and *m*7 can be seen as resonator's even modes, with the inner and outer rings resonating in phases. And the *Q*-factors of odd modes are higher than even modes. And the Q-factors of odd modes are higher than even modes. As can be seen in **Figure 2B**, the embedded electric field in the odd modes is more complicated than the even modes, so they have different equivalent circuits with fewer losses from the even mode and achieve higher Q-factors.

Previous studies have shown that the Q-factor of outer corrugated spoof LSP resonator is higher than that of inner LSP resonator [5, 30], so only the outer corrugated spoof LSPs are analyzed here. The transmission coefficients of the hybridized spoof LSP resonator and outer corrugated spoof LSP resonators covered with tested samples are compared and analyzed to verify the superiority of the hybridized structure in the sensing test. In this part, only odd modes *m*1, *m*2, and *m*5 are analyzed. The curves in **Figure 3** show the measured transmission coefficients, which are tested by hybridized spoof LSPs, as shown in **Figure 1B**, and the outer corrugated spoof LSP structure, as shown in **Figure 3**. The tested samples are 0.508-mm-thick Rogers RT5880 plates, with a permittivity of 2.2. The black line describes the transmission coefficient of the hybridized spoof LSPs, and the *Q*-factors of *m*1 to *m*4 modes are 103.2, 124.6, 71.4, and 141.6. The red dotted line depicts the transmission coefficient of the outer corrugated spoof LSPs, where the *Q*-factor of the corresponding *M*1 and *M*2 is 77.2 and 71.2, respectively. The hybridized structure consists of an inner spoof LSPs and an embedded outer corrugated spoof LSPs. By coupling the inner LSPs, outer LSPs, and the metal ground, the electromagnetic field in the hybridized structure is highly concentrated, which reduces the radiation loss and reflection loss, thus improving the resonant Q-factor noticeably. In addition, the complex coupling structure of the hybridized spoof LSPs increases the electromagnetic field transmission path, which reduces the resonant frequencies compared to the outer spoof LSPs. Therefore, the hybridized spoof LSPs show superior advantages over the single outer spoof LSPs in resonance strength and dimension.

HIGH-*FOM* SPOOF LOCALIZED SURFACE PLASMON SENSOR

The hybridized spoof LSP structure-based resonator with a high-*Q*-factor is a primary condition for the resonance sensor as the sensitivity requirement. In order to verify the sensing performance, a prototype of this LSP sensor and several samples with different permittivities are fabricated and characterized for demonstration. A spoof LSP sensor and excitation microstrip lines are printed on the substrate of Rogers RT5880, with a relative permittivity of 2.2, as shown in **Figure 4**. Three Rogers materials, namely, RT5880, RO3003, and RO4003, are applied in the test samples. Those samples are 0.508 mm thickness, and their relative permittivity is 2.2, 3, and 3.55, respectively. The samples are kept in the same size, while their permittivities are different. Those sizes are 20 mm × 25 mm×0.508 mm, and they can be laid on the spoof LSP sensor.

Sensing *FoM* is an important parameter to characterize the sensor's sensitivity [31], which synthetically indicates the overall

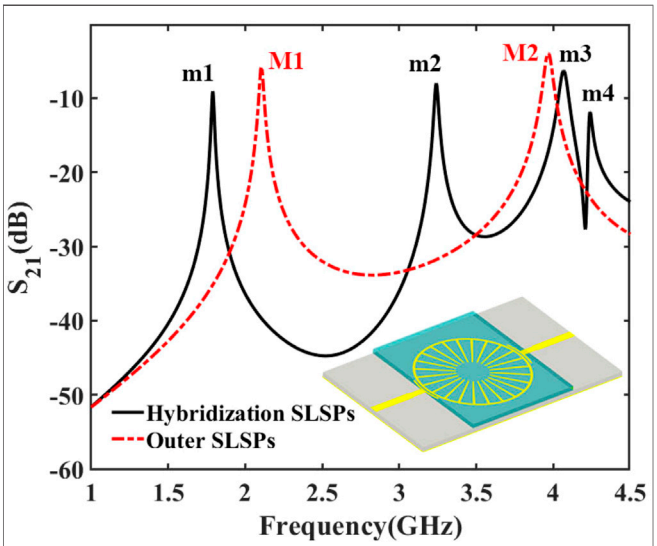

FIGURE 3 | Transmission coefficients of the hybridization spoof LSP resonator and outer corrugated spoof LSP resonator. The inset shows the outer corrugated spoof LSP structure.

interaction effect with the environment. The sensing *FoM* is defined as follows [32]:

$$Sensing\ FoM = \frac{Sensitivity}{\Delta f_{3dB}}, \tag{2}$$

where sensitivity is the frequency offset Δf when the corresponding refractive index Δn changes by unit and can be defined as follows [33]:

$$Sensitivity = \frac{\Delta f}{\Delta n}, \tag{3}$$

where the refractive index n means the square root of the relative permittivity ε of the tested sample, and it can be calculated by $n = \sqrt{\varepsilon}$. From the aforementioned analysis, when the permittivity changes at the same level, the larger the frequency offset and the smaller the 3dB bandwidth, the larger the sensing *FoM*.

The sample under test is placed directly above the spoof LSP structure in the measurement. The sample and the sensor are fixed together with two identical small iron clips to secure the position and distance, as illustrated in **Figure 5A**. The spoof LSPs have strong confinement of electromagnetic field, and the field intensity outside of spoof LSPs is weak. Therefore, the small iron clip has little impact on the sensor's performance, which is also verified in the measurement process. The sensor's simulated and measured transmission coefficients are plotted in **Figure 5A**. **Figures 5B,C** show the detail of the $m5$'s resonant mode in simulation and in the measurement.

The simulated odd dipole modes locate at 1.6176, 1.6896, and 1.792 GHz with *Q*-factors of 95.2, 94.5, and 102 when the sample relative permittivity changes from 3.55, 3, to 2.2. The odd quadrupole modes are located at 2.912, 3.0496, and 3.2544 GHz with *Q*-factors of 112, 116.8, and 124.6 when the sample relative permittivity changes from 3.55, 3, to 2.2. Meanwhile, the odd octupole mode $m5$ is located at 4.38, 4.61, and 4.93 GHz with *Q*-factors of 103, 179.8, and 200. When the permittivity ε changes

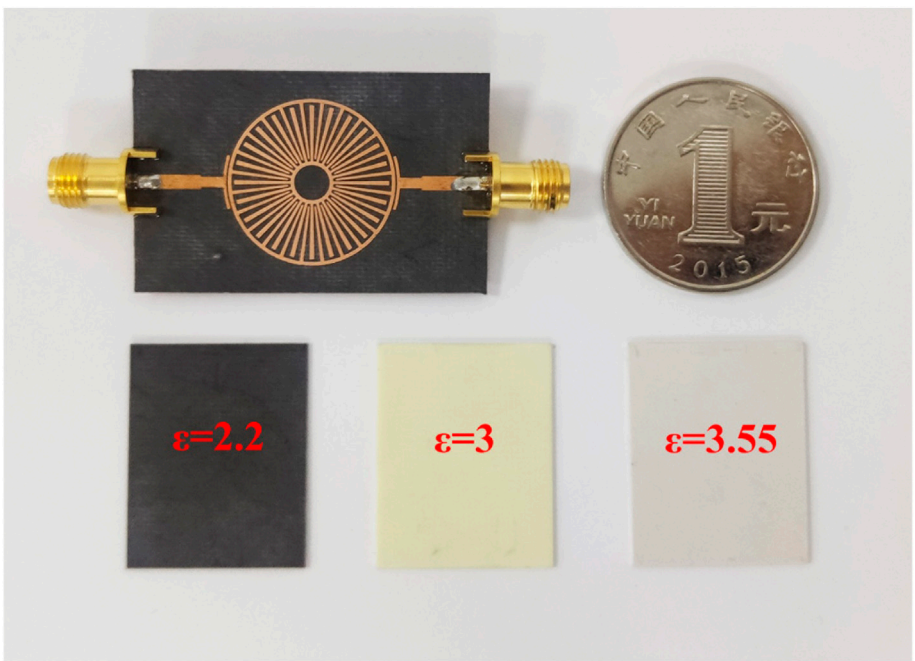

FIGURE 4 | Photo of the fabricated prototype. The three small squares at the bottom of the picture are the three samples under assessment with different permittivities for sensor detection.

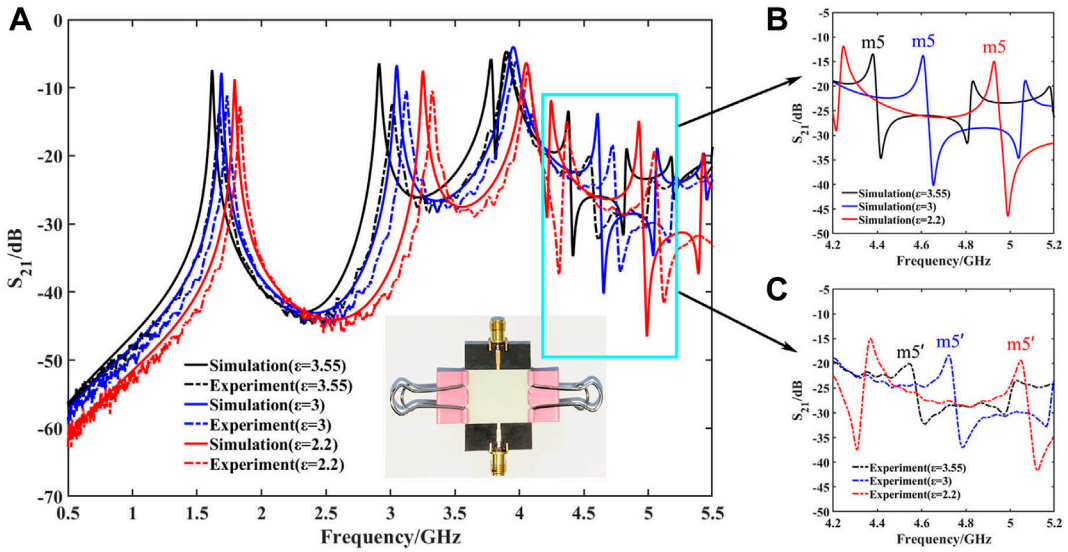

FIGURE 5 | (A) Simulated and measured transmission coefficients of the spoof LSP sensor. The inset is a photograph of the sensor under experiment. **(B)** Details of simulated transmission coefficients of resonant mode *m*5. **(C)** Details of the measured transmission coefficients of resonant mode *m*5′.

from 3.55 to 3, the offsets of the dipole mode, quadrupole mode, and octupole mode are 0.072, 0.1344, and 0.2272 GHz, respectively. The corresponding sensitivities are 0.475 GHz · RIU^{-1}, 0.905 GHz · RIU^{-1}, and 1.494 GHz · RIU^{-1}, respectively, while sensing *FoM*s are 27.05 RIU^{-1}, 34.33 RIU^{-1}, and 51.43 RIU^{-1}, respectively. When the permittivity ε changes from 3 to 2.2, the offsets of dipole mode, quadrupole mode, and octupole mode are 0.1024, 0.2032, and 0.3232 GHz, respectively. The corresponding sensitivities are 0.42 GHz · RIU^{-1}, 0.817 GHz · RIU^{-1}, and 1.299 GHz · RIU^{-1}, respectively, while sensing *FoM*s are 26.45 RIU^{-1}, 31.6 RIU^{-1}, and 54.53 RIU^{-1}, respectively. Both the Q-factor and sensitivity of this LSP sensor are beyond the state of art in the passive design [21].

The measured results are presented in **Figures 5A,C** as the dotted line. The measured odd dipole modes locate at 1.6738, 1.724, and 1.835 GHz with *Q*-factors of 59.8, 76.7, and 81.6 when the sample relative permittivity changes from 3.55 to 3 to 2.2. The odd quadrupole modes locate at 3.015, 3.113, and 3.325 GHz with *Q*-factors of 70.8, 94.1, and 106.3, while the odd octupole mode locates at 4.546, 4.711, and 5.049 GHz with *Q*-factors of 44.6, 103, and 111. When the permittivity ε changes from 3.55 to 3, the offset of the dipole mode, quadrupole mode, and octupole mode are 0.05, 0.098, and 0.165 GHz. The corresponding sensitivities are 0.333 GHz · RIU^{-1}, 0.45 GHz · RIU^{-1}, and 1.082 GHz · RIU^{-1}, while sensing *FoM*s are 15.5 RIU^{-1}, 17.16 RIU^{-1}, and 14.25 RIU^{-1}. When the permittivity ε changes from 3 to 2.2, the offset of dipole mode, quadrupole mode, and octuple mode are 0.111, 0.212, and 0.338 GHz. The corresponding sensitivities are 0.446 GHz · RIU^{-1}, 0.852 GHz · RIU^{-1}, and 1.36 GHz · RIU^{-1}, while sensing *FoM*s are 19.8 RIU^{-1}, 26.46 RIU^{-1}, and 30.72 RIU^{-1}.

Comparing the simulated results with measured results, it can conclude that the frequencies of the resonant modes are blue-shifted, and both the *Q*-factor and sensing *FoM* have been reduced, especially in the odd octuple mode. This shift could be caused by the unavoidable air gap between the samples and the sensor. Also, from the simulation and experiment, it is not difficult to find that the lower the permittivity of the sample, the higher the resonant frequency. The air gap causes the effective permittivity above the sensor to be less than the relative permittivity of the samples, resulting in this blue shift. The odd octuple mode is a resonant mode which is similar to Fano resonance produced by coupling internal and

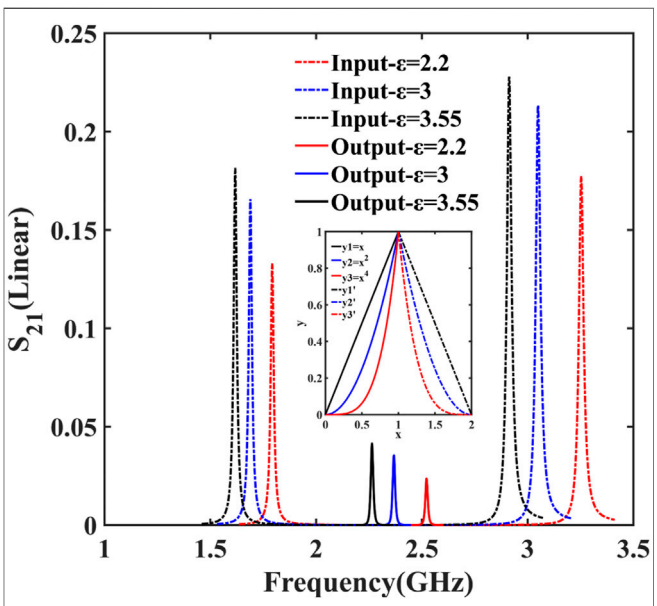

FIGURE 6 | Input and output linear transmission coefficients of the mixed-resolution algorithm.

TABLE 1 | Comparison of input and output Q-factor and sensing *FoM*. All of the data in the table are calculated automatically using the mixed-resolution algorithm.

Comparison		Dipole mode			Quadrupole mode		
		$\varepsilon = 3.55$	$\varepsilon = 3$	$\varepsilon = 2.2$	$\varepsilon = 3.55$	$\varepsilon = 3$	$\varepsilon = 2.2$
Input	Q factor	92	96	101.8	113.8	112.1	127.1
	Sensing *FoM* (RIU^{-1})	23.38	30.94		26.89	34.27	
		$\varepsilon = 3.55$		$\varepsilon = 3$		$\varepsilon = 2.2$	
Output	Q factor	157.3		185.1		197.1	
	Sensing *FoM* (RIU^{-1})	50.7			47.9		

external resonators, requiring higher environment configuration. Manufacturing, material, and measurement errors affect the measured resonant frequency, resonant intensity, and sensitivity.

The proposed hybridized spoof LSP sensor shows excellent performance in simulation and measurement, with *Q*-factors up to 178.4 and sensing *FoM* up to 30.72 RIU^{-1}. The electrical size of the sensor is very small as the path length of the surface current is compressed, significantly smaller than the size of the spoof LSP sensor. The size of the resonant structure is about one-tenth of the working wavelength. The spoof LSPs of the resonator improve the ability to confine electromagnetic fields and the sensitivity to the surrounding environment. Moreover, the sensor detection can be realized with low cost and simple operation by replacing the sample, which dramatically improves its practical engineering value.

OPTIMIZATION ALGORITHM

Although the proposed hybridized sensor achieved a very high-*Q*-factor and sensing *FoM*, they are expected to be even higher by data processing. Therefore, a mixed-resolution optimization algorithm is proposed to enhance the *Q*-factor and sensing *FoM* based on the multi-resonance property. The algorithm is based on the resulting linear data and combines several resonant modes later to form a new resonant mode. The new resonant mode achieves narrower 3dB bandwidth, improving the *Q*-factor and sensing *FoM*.

To precisely describe the algorithm for increasing the resonant *Q*-factor and sensing *FoM*, a schematic diagram is inserted in **Figure 6**. Suppose there is a resonant peak, which consists of a curve y_1 with slope 1 and a curve $y_1^{'}$ with slope -1. Then, the 3dB bandwidth here is 1, which can be obtained by calculating the bandwidth when the ordinate is half of the peak value, and the corresponding *Q*-factor is 1. If there are two such resonant peaks, the linear values of the curves are multiplied to the left of the two peaks, which results in a curve of $y_2 = x^2$, and the same process is repeated to the right to get the curve of $y_2^{'}$ as blue curves shown in the illustration. The 3dB bandwidth and *Q*-factor here can be calculated as 0.586 and 1.71. Compared with curves y_1 and $y_1^{'}$, the 3dB bandwidth is reduced by 41.4%, and the *Q*-factor is increased by 71%. Furthermore, the multiplication of two curves composed of y_2 and $y_2^{'}$ gives the curves y_3 and $y_3^{'}$ illustrated in red lines, whose 3dB bandwidth and *Q*-factor become 0.32 and 3.14, respectively. The 3dB bandwidth is reduced by 1.83 times, and the *Q*-factor increases by 1.83 times. It can be seen that when the slopes on both sides of the original resonant peaks are larger, the bandwidth of the composite peak is narrower, and the *Q*-factor is higher. Also, from **Eq. 2**, the sensing *FoM* of the sensor will increase when the 3dB bandwidth is reduced. In the electromagnetic field, the resonant peak cannot reach 1, and there are larger slopes on both sides of the peaks, which further improves the performance of the proposed mix-resolution algorithm.

First, to apply this mixed-resolution algorithm to sensor data processing, 100 linear sampling points at higher frequency and 100 at lower frequency around the dipole and quadrupole resonant frequencies were taken, respectively. The sampling points with different permittivities are shown as the input dotted curves in **Figure 6**. Then, these three groups of data are processed using the described mixed-resolution algorithm, respectively, and it generated three new groups of resonant peaks, as shown in the

solid line in **Figure 6**. The frequency of the output resonant peak is half the sum of the corresponding frequencies of the dipole and quadrupole. Finally, according to **Eqs 1–3**, an algorithm for automatically calculating resonant *Q*-factors and sensing *FoM* is developed. The calculated input and output *Q*-factor and sensing *FoM* are listed in **Table 1**. As compared in **Table 1**, the mixed-resolution algorithm increases the *Q*-factor from 96 by 1.93 times to 185.1, and the sensing *FoM* increases by 2.17 times, from 23.38 to 50.7. The algorithm can almost double the *Q*-factor and sensing *FoM* without changing the sensor structure, which is an important breakthrough in the microwave sensor field [34–37]. With this mixed-resolution algorithm, sensors are expected to achieve multimode enhanced sensing in the future. Also, it can detect more subtle environmental changes to a great extent.

DISCUSSION AND CONCLUSION

In this work, a hybridized spoof LSP sensor is proposed, implemented, and measured with high environmental sensitivity. A mixed-resolution algorithm was also proposed to further improve the *Q*-factor and sensing *FoM* by combining multimode resonant peaks. A prototype was designed, fabricated, and measured for demonstration. High-*Q*-factor and high sensing *FoM* are achieved by applying the algorithm. Meanwhile, the mixed-resolution can further double them. The hybridized spoof LSP sensor and the mixed-resolution algorithm have great potential in the field of high-frequency on-chip resonators and sensors.

DATA AVAILABILITY STATEMENT

The original contributions presented in the study are included in the article/Supplementary Material, further inquiries can be directed to the corresponding authors.

AUTHOR CONTRIBUTIONS

JW conducted the numerical simulations and experiment, and wrote the manuscript. DB and TC conceived the idea, suggested the designs, and supervised the work. All the authors conducted the analytical modeling and discussed the results. XF provided some assistance in the experimental process.

FUNDING

This work was supported in part from the National Key Research and Development Program of China (Grant Nos. 2017YFA0700201, 2017YFA0700202, and 2017YFA0700203), the National Natural Science Foundation of China (Grant No. 61735010), and the 111 Project (Grant No. 111-2-05).

REFERENCES

1. Pors A, Moreno E, Martin-Moreno L, Pendry JB, Garcia-Vidal FJ. Localized Spoof Plasmons Arise while Texturing Closed Surfaces. *Phys Rev Lett* (2012) 108(22):223905. doi:10.1103/physrevlett.108.223905
2. Huidobro PA, Shen X, Cuerda J, Moreno E, Martin-Moreno L, Garcia-Vidal FJ, et al.Magnetic Localized Surface Plasmons. *Phys Rev X* (2014) 4:101103. doi:10.1103/physrevx.4.021003
3. Shen X, Cui TJ. Ultrathin Plasmonic Metamaterial for Spoof Localized Surface Plasmons. *Laser Photon Rev* (2014) 8(1):137–45. doi:10.1002/lpor.201300144
4. Zhou YJ, Xiao QX, Jia Yang B. Spoof Localized Surface Plasmons on Ultrathin Textured MIM Ring Resonator with Enhanced Resonances. *Sci Rep* (2015) 5: 14819. doi:10.1038/srep14819
5. Bao D, Rajab KZ, Jiang WX, Cheng Q, Liao Z, Cui TJ. Experimental Demonstration of Compact Spoof Localized Surface Plasmons. *Opt Lett* (2016) 41(23):5418–21. doi:10.1364/ol.41.005418
6. Bao D, Cheng Q, Jiang WX, Zhang JJ, Liao Z, Wu JW, et al.Concentric Designer Plasmon Hybridization in Deep Subwavelength Metamaterial Resonator. *Appl Phys Lett* (2019) 115. 1063.doi:10.1063/1.5116776
7. Gao Z, Gao F, Zhang Y, Zhang B. Complementary Structure for Designer Localized Surface Plasmons. *Appl Phys Lett* (2015) 107:191103. doi:10.1063/1.4935360
8. Zhao P-C, Zong Z-Y, Wu W, Li B, Fang D-G. An FSS Structure with Geometrically Separable Meander-Line Inductors and Parallel-Plate Capacitors. *IEEE Trans Antennas Propagat* (2017) 1:1. doi:10.1109/tap.2017.2729158
9. Yang BJ, Zhou YJ, Xiao QX. Spoof Localized Surface Plasmons in Corrugated Ring Structures Excited by Microstrip Line. *Opt Express* (2015) 23(16): 21434–42. doi:10.1364/oe.23.021434
10. Zhang X, Cui TJ. Single-Particle Dichroism Using Orbital Angular Momentum in a Microwave Plasmonic Resonator. *ACS Photon* (2020) 7(12):3291–7. doi:10.1021/acsphotonics.0c01139
11. Li Z, Liu L, Gu C, Ning P, Xu B, Niu Z, et al.Multi-band Localized Spoof Plasmons with Texturing Closed Surfaces. *Appl Phys Lett* (2014) 104:101063. doi:10.1063/1.4868126
12. Shen Y, Chen N, Dong G, Hu S. Manipulating Multipole Resonances in Spoof Localized Surface Plasmons for Wideband Filtering. *Opt Lett* (2021) 46:1364. doi:10.1364/ol.417004
13. Yang Z-B, Guan D-F, Huang X, Zhang HC, You P, Xu S-D, et al.Compact and Wideband Octuple-Mode Filter Based on Hybrid Substrate Integrated Waveguide and Spoof Localized Surface Plasmon Structure. *IEEE Trans Circuits Syst* (2020) 67(11):2377–81. doi:10.1109/tcsii.2020.2971235
14. Zhao HZ, Zhou YJ, Cai J, Li QY, Li Z, Xiao ZY. Ultra-high Resolution Sensing of Glucose Concentration Based on Amplified Half-Integer Localized Surface Plasmons Mode. *J Phys D: Appl Phys* (2020) 53:1088. doi:10.1088/1361-6463/ab5b4f
15. Anker JN, Hall WP, Lyandres O, Shah NC, Zhao J, Van Duyne RP. Biosensing with Plasmonic Nanosensors. *Nat Mater* (2008) 7(6):442–53. doi:10.1038/nmat2162
16. Shen X, Cui TJ, Martin-Cano D, Garcia-Vidal FJ. Conformal Surface Plasmons Propagating on Ultrathin and Flexible Films. *Proc Natl Acad Sci* (2013) 110(1): 40–5. doi:10.1073/pnas.1210417110
17. Chen L, Xu N, Singh L, Cui T, Singh R, Zhu Y, et al.Defect-Induced Fano Resonances in Corrugated Plasmonic Metamaterials. *Adv Opt Mater* (2017) 5: 1600960. doi:10.1002/adom.201600960
18. Shao RL, Zhou YJ, Yang L. Quarter-mode Spoof Plasmonic Resonator for a Microfluidic Chemical Sensor. *Appl Opt* (2018) 57(28):8472–7. doi:10.1364/ao.57.008472
19. Gholamian M, Shabanpour J, Cheldavi A. Highly Sensitive Quarter-Mode Spoof Localized Plasmonic Resonator for Dual-Detection RF Microfluidic Chemical Sensor. *J Phys D-Applied Phys* (2020) 53:145401. doi:10.1088/1361-6463/ab667
20. Dai LH, Zhao HZ, Zhao X, Zhou YJ. Flexible and Printed Microwave Plasmonic Sensor for Noninvasive Measurement. *IEEE Access* (2020) 1:1. doi:10.1109/access.2020.3020268

21. Zhang X, Yan RT, Cui TJ. High-FoM Resonance in Single Hybrid Plasmonic Resonator via Electromagnetic Modal Interference. *IEEE Trans Antennas Propagat* (2020) 68(8):6447–51. doi:10.1109/tap.2020.2970037
22. Jiang Q, Yu Y, Zhao Y, Zhang Y, Liu L, Li Z. Ultra-Compact Effective Localized Surface Plasmonic Sensor for Permittivity Measurement of Aqueous Ethanol Solution with High Sensitivity. *IEEE Trans Instrumentation Meas* (2021) 70: 1109. doi:10.1109/tim.2021.3092783
23. Xiao QX, Yang BJ, Zhou YJ. Spoof Localized Surface Plasmons and Fano Resonances Excited by Flared Slot Line. *J Appl Phys* (2015) 118:1063. doi:10.1063/1.4938153
24. Wu C, Khanikaev AB, Adato R, Arju N, Yanik AA, Altug H, et al.Fano-resonant Asymmetric Metamaterials for Ultrasensitive Spectroscopy and Identification of Molecular Monolayers. *Nat Mater* (2011) 11(1):69–75. doi:10.1038/nmat3161
25. Zhang X, Cui TJ. Deep-Subwavelength and High-Q Trapped Deep-Subwavelength and High-Q Trapped Mode Induced by Symmetry-Broken in Toroidal Plasmonic Resonator. *IEEE Trans Antennas Propagat* (2021) 69(4): 2122–9. doi:10.1109/tap.2020.3026480
26. Zhang J, Liao Z, Luo Y, Shen X, Maier SA, Cui TJ. Spoof Plasmon Hybridization. *Laser Photon Rev* (2017) 11:1003. doi:10.1002/lpor.201600191
27. Sun X, Du H, Dong X, Hu Y, Duan Ja. Simultaneous Curvature and Temperature Sensing Based on a Novel Mach-Zehnder Interferometer. *Photonic Sens* (2019) 10(2):171–80. doi:10.1007/s13320-019-0551-z
28. Singh Y, Paswan MK, Raghuwanshi SK. Sensitivity Enhancement of SPR Sensor with the Black Phosphorus and Graphene with Bi-layer of Gold for Chemical Sensing. *Plasmonics* (2021) 10:11468. doi:10.1007/s11468-020-01315-3
29. Taue S, Daitoh H, Fukano H. Sensitivity Enhancement of Fiber-Optic Refractive index Sensor Based on Multimode Interference with Gold Nanoparticles. *Jpn J Appl Phys* (2015) 54:04DL07. doi:10.7567/jjap.54.04dl07
30. Zhou YJ, Dai LH, Li QY, Xiao ZY. Two-Way Fano Resonance Switch in Plasmonic Metamaterials. *Front Phys* (2020) 8:3389. doi:10.3389/fphy.2020.576419
31. Zhang X, Cui WY, Lei Y, Zheng X, Zhang J, Cui TJ. Spoof Localized Surface Plasmons for Sensing Applications. *Adv Mater Tech* (2021) 6.
32. Offermans P, Schaafsma MC, Rodriguez SRK, Zhang Y, Crego-Calama M, Brongersma SH, et al.Universal Scaling of the Figure of Merit of Plasmonic Sensors. *Acs Nano* (2011) 5(6):5151–7. doi:10.1021/nn201227b
33. Homola J, Yee SS, Gauglitz G. Surface Plasmon Resonance Sensors: Review. *Sensors and Actuators B-Chemical* (1999) 54(1-2):3–15. doi:10.1016/s0925-4005(98)00321-9
34. Monzón-Hernández D, Martínez-Ríos A, Salceda-Delgado G, Villatoro J. Compact Sensors Based on Cascaded Single-Mode–Multimode–Single-Mode Fiber Structures. *Appl Phys Express* (2013) 6.
35. Rota-Rodrigo S, Gonzalez-Herraez M, Lopez-Amo M. Compound Lasing Fiber Optic Ring Resonators for Sensor Sensitivity Enhancement. *J Lightwave Technol* (2015) 33(12):2690–6. doi:10.1109/jlt.2014.2387428
36. Chen Z, Yang J, Zhang X, Bai J, Feng T, Tang J, et al.*Mathematical Model and Reference Frequency Optimization for Digital Dual-Band Pulsewidth Modulation. In 2020 IEEE MTT-S International Wireless Symposium (IWS)* (2020). p. 1–3.
37. Ali MM, Memon SF, Lewis E, Lim KS, Ahmad H., *Modal Sensitivity Enhancement of Few-Mode Fiber Bragg Gratings for Refractive Index Measurement. 2016 International Conference for Students on Applied Engineering (Icsae)* 2016, 308–11., doi:10.1109/icsae.2016.7810208

Conflict of Interest: HG was employed by the company Silicon Austria Labs GmbH.

The remaining authors declare that the research was conducted in the absence of any commercial or financial relationships that could be construed as a potential conflict of interest.

frontiers in Physics

ORIGINAL RESEARCH
published: 23 March 2022
doi: 10.3389/fphy.2022.869333

A Wideband Controllable Bandpass Filter Based on Spoof Surface Plasmon Polaritons

Xi Chen[1,2], *Chonghu Cheng*[1] *and Leilei Liu*[1]*

[1]College of Electronic and Optical Engineering, Nanjing University of Posts and Telecommunications, Nanjing, China, [2]School of Information Technology, Jiangsu Open University, Nanjing, China

A wideband controllable band-pass filter is proposed, which is based on the spoof surface plasmon polaritons (SSPP) and slip ring resonators (SRR). The design concept of the bandpass filter is using the SSPP and SRR to control the high cut-off frequency and filter the low-frequency wave, respectively. The bandpass filter is used diode reconfigurable technology to tunable the bandwidth. The filter has a passband range of 5–9 GHz, an out-band rejection of −20 dB for the lower sideband, and an out-band rejection of −50 dB for the upper sideband. The simulated and measured results are in good agreement over the operating band. Benefit from its low-profile and low-cost, the proposed bandpass filter has a great potential for development in plasmonic functional devices at microwave frequencies.

Keywords: bandpass filter, split ring resonators, spoof surface plasmon polaritons, reconfigurable technology, wideband

OPEN ACCESS

Edited by:
Zhewang Ma,
Saitama University, Japan

Reviewed by:
Yingjiang Guo,
University of Electronic Science and Technology of China, China
Zhen Liao,
Hangzhou Dianzi University, China

***Correspondence:**
Leilei Liu
liull@njupt.edu.cn

Specialty section:
This article was submitted to Optics and Photonics, a section of the journal Frontiers in Physics

Received: *04 February 2022*
Accepted: *28 February 2022*
Published: *23 March 2022*

Citation:
Chen X, Cheng C and Liu L (2022) A Wideband Controllable Bandpass Filter Based on Spoof Surface Plasmon Polaritons. Front. Phys. 10:869333. doi: 10.3389/fphy.2022.869333

INTRODUCTION

Due to the congestion in the lower frequency ranges, more occupancy of these regimes may cause interference, crosstalk and mutual coupling problem [1]. Meanwhile, compact integrated circuits with efficient energy, low loss and low crosstalk need to be investigated to satisfy the continuous development of wireless communication. Band pass filters (BPF) are one of the essential components of the wireless transceiver, thus designing a broadband BPF is important for RF circuit designers. Several structures have been reported in this regard [2, 3]. In literature [2], the BPF structures generated dual passband notches with the help of multiple stubs attached to patch. In literature [3], the BPF structures with multiple transmission zeros enable frequency response. However, most of the reported structures were of large circuit area and complex construction due to the use of vias or fabrication limitation. Therefore, a band pass filter based on the spoof surface plasmon polariton (SSPP) may be a good candidate for future microwave communications.

Surface plasmon polariton (SPP) is a class of special surface electromagnetic wave mode, which was used only in the optical region for a long time [4]. Pendry et al. [5]and Hibbins et al. [6]proposed that the metal embedding with periodic sub wavelength structures could also support SPP-like mode in lower frequencies, which is known as spoof SPP(SSPP). The SSPP has several advantages over conventional microwave devices, including limiting the microwave field in a sub-wavelength scale, rejecting electromagnetic (EM) interference, and having a wide bandwidth. In 2013, Shen and Cui [7] proposed a planar structure that could realize SSPP. After that, many planar SSPP structures employing printed circuit board (PCB) technology were presented in microwave region from C to K bands [8, 9]. Since then, some SSPP structures have been realized by modulating periodic holes or grooves on the metal surface in [10–16]. Meanwhile, some works on GaAs–based BPFs have been reported in

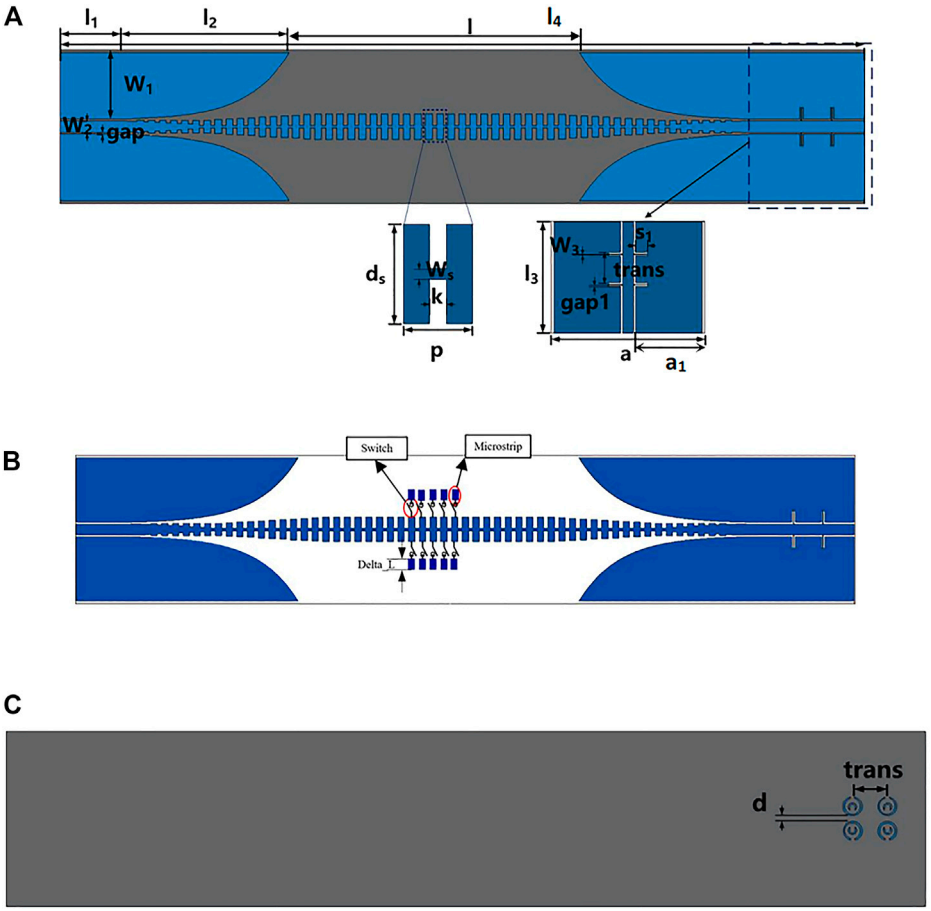

FIGURE 1 | (A) the front view of the spoof surface plasmon filter, **(B)** the front view of the spoof surface plasmon filter using diode reconfigurable technology, and **(C)** the back view of the spoof surface plasmon filter.

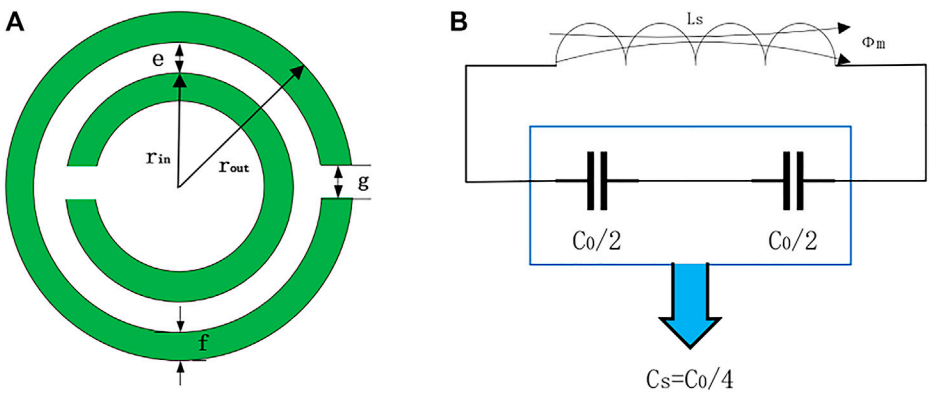

FIGURE 2 | (A) The structure of SRR, **(B)** the equivalent circuit diagram of the SRR structure.

recent years [17–19]. In [18], a bandpass filter with a notched band has good transmission performance was constructed. In [19], a new GaAs-based wideband SSPP waveguide with super compact size was presented.

Recently, several SSPP-based bandpass filters have been proposed [20–26]. Substrate integrated waveguides (SIWs) were used to achieve high-efficiency SSPP propagation with controlled lower cut-off frequencies, allowing for more tuning freedom [20–23].

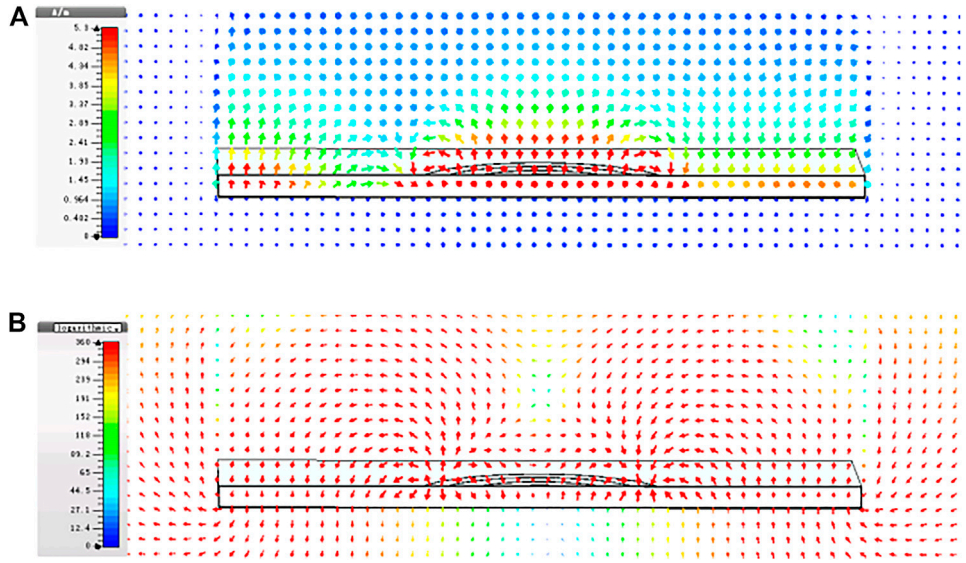

FIGURE 3 | (A) Simulation of electric field distribution of SRR at f = 4.75 GHz. **(B)** Simulation of magnetic field distribution of SRR at f = 4.75 GHz.

TABLE 1 | Parameter values of the SRR (unit: mm).

Parameter values of SRR (unit: mm)	
r_{out}	6
r_{in}	1
g	3
f	1
e	1.22

The SIW waveguide was directly coupled to the SSPP structure in literature [20], resulting in an extremely long physical length. In SIW, embedded SSPP units [21–23] were used to minimize the physical size. HMSIW was used to minimize the overall size of the filter in [24–26]. Using slotted HMSIW, a unit cell capable of supporting SSPP was proposed. The dispersion diagram, which is distinct from that of standard SSPP, may forecast both higher and lower cut-off frequencies in the passband. However, these designs were electronically adjustable, and changing the bandwidth is challenging. As a result, it is theoretically challenging to develop a planar mechanically controlled bandpass filter with separate controllability of low and high cut-off frequencies and low cost. Therefore, SSPP-based structures were a good choice for managing high cut-off frequency because of their advantages of having a high cut-off frequency that can be readily controlled by optimizing geometrical parameters [27–31]. Furthermore, some CPW- or microstrip-based coupling structures [32, 33]could be a promising candidate for controlling the low cut-off frequency following modification.

In this work, a wideband controllable bandpass filter is proposed, which is based on the SRR high-pass filter cascaded SSPP transmission line. The transmission characteristics own both the features of SRR and SSPP. The low-pass cut-off frequency can be controlled by SSPP structure, while the high-pass cut-off frequency can be controlled by SRR structure. The bandwidth can be tuned by diode reconfigurable technology. The filter has an operating passband over 5–9 GHz, an out-band rejection of −20 dB for the lower sideband, and an out-band rejection of −50 dB for the upper

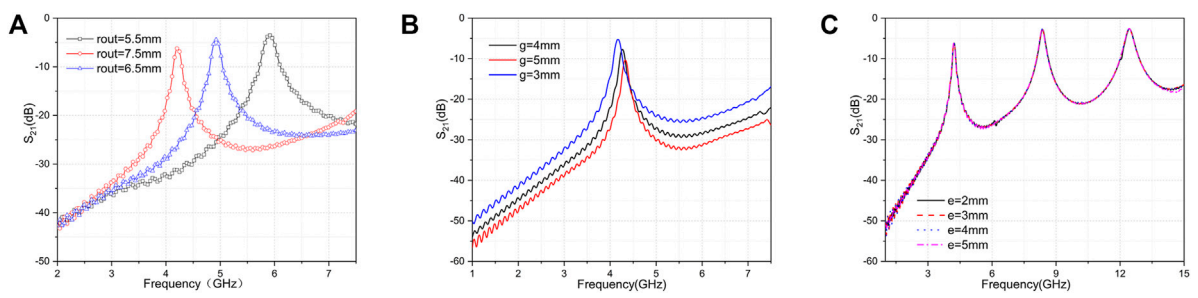

FIGURE 4 | (A) Analysis of the radius parameter r_{out} of the SRR outer ring. **(B)** Parameter analysis of the SRR ring opening spacing g. **(C)** Parameter analysis of the SRR ring opening spacing e.

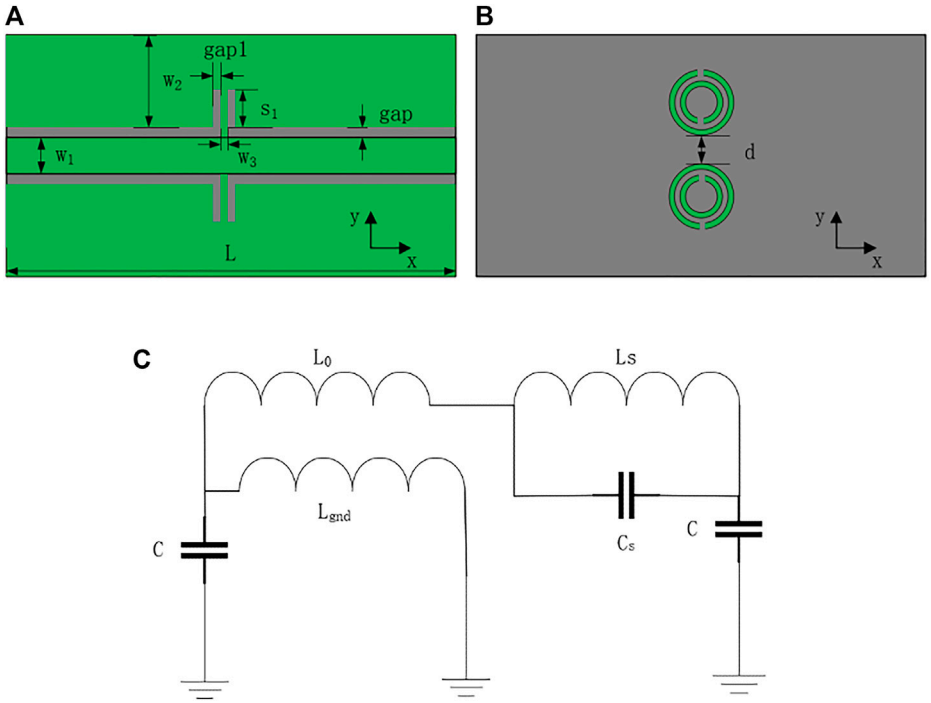

FIGURE 5 | Schematic diagram of bandpass filter based on SRR CPW structure. **(A)** The front side view **(B)** The back side view **(C)** Equivalent circuit of the SRR CPW structure.

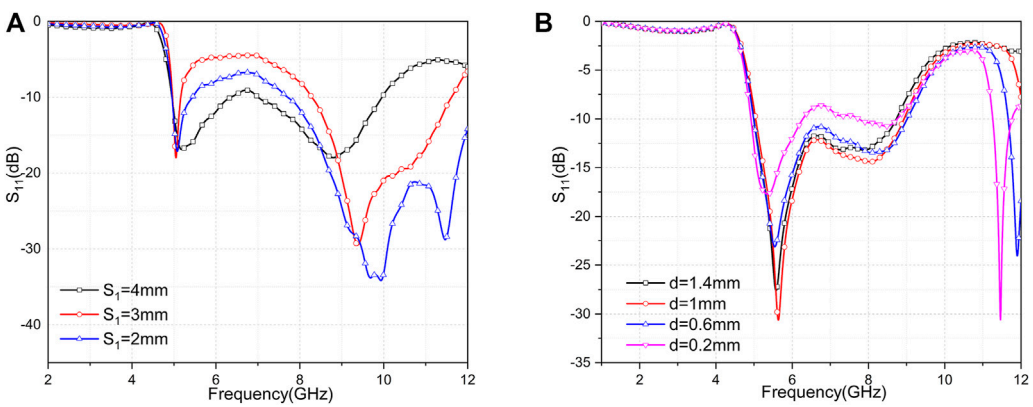

FIGURE 6 | (A) Performing sweep analysis on filter parameter S_1 **(B)** Performing sweep analysis on filter parameter *d*.

TABLE 2 | Parameter values of the bandpass filter with CPW structure based on SRR (unit: mm).

Parameter values of bandpass filter with CPW structure based on SRR (unit: mm)					
W_1	4	L	40	f	0.6
W_2	8.7	W_g	0.2	g	3
W_3	0.3	S_1	4.5	r_{in}	1.5
gap	0.3	d	1	r_{out}	3.2
gap_1	0.2	e	0.9	—	—

sideband. The physical processing is performed and verified, and the measured results agree well with the simulated results.

CONFIGURATION AND ANALYSIS

The bandpass filter is illustrated in **Figures 1A–C**. It can be considered as a combination of the SRR and SSPP units. The SSPP shown in **Figure 1A** controls the high cut-off frequency by changing the unit cell depth, while the SRR shown in **Figure 1C**

TABLE 3 | Parameters of bandpass filter with CPW structure based on SRR (unit: mm) (optimized).

Parameter values of bandpass filter with CPW structure based on SRR (unit: mm)					
W_1	4	L	43	f	0.62
W_2	32.7	W_g	0.7	g	1.454
W_3	0.3	S_1	4.5	r_{in}	1.28
gap	0.3	d	0.2	r_{out}	3.2
gap_1	0.2	e	1.92	—	—

TABLE 4 | Parameter values of SSPP filter.

Parameter values of SSPP filter (unit: mm)					
W_1	24	l_3	40	f	0.52
W_2	4	d_s	9.2	g	1.4
W_3	0.3	s_1	5	r_{in}	1.27
gap	0.7	d	1.83	r_{out}	3
gap_1	0.5	e	1.47	w_s	1
trans	11	p	6.4	k	1.6
l	290	a	53.4	l_2	44
l_1	10	l_4	182	a_1	24.7

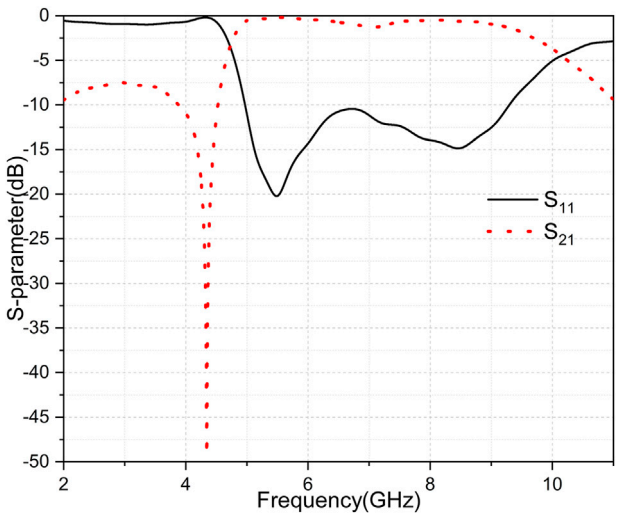

FIGURE 7 | Bandpass filter simulation results of SRR-based coplanar waveguide structure.

based coupling structure controls the low cut-off frequency by changing the width of grooves. In addition, the RF diodes in **Figure 1B** controlled by a DC power are added in the SSPP to regulate the bandwidth of passband.

The structure is printed on the 1 mm thick Taconic RF-35 substrate (relative permittivity $\varepsilon_r = 3.5$, loss tangent $\tan\delta = 0.001$). The SSPP is composed of a 50-Ω CPW transmission line using matched conversion. The width and length of SSPP uints are denoted by d_s and p, and the depth and width of grooves are denoted by w_s and k, respectively. The total width and length of the SSPP filter are marked as a and l, the access part is marked as l_1, CPW feeding part is marked as l_2, and the SRR part is marked as l_3. The gap width is marked as w_1, and the width of ground of CPW is marked as w_2. The length and width of the slotted slit are marked as s_1 and w_3, respectively. The slotted spacing is denoted by gap_1. Likewise, the distances between two SRR stages are denoted by *trans*, and the distances between two SRRs are denoted by d.

Configuration of Slip Ring Resonators

For the sake of clarity, the design of the bandpass filter starts with the basic bandpass filter, which consists of a CPW coupled with slip ring resonators (SRR). The structure of SRR is shown in **Figure 2A**. The coloring part is covered with a metal part, and its shape is the common center of two open rings spliced together. The currents will be induced in SRR when an external electromagnetic action received. The ring currents act as magnetic pole moments, which leads to the negative magnetic permeability. The coloring part of the figure is the copper-clad part, where r_{out} is the outer ring radius, e is the ring distance, f is the ring width, and r_0 is the average radius of the ring. These parameters are related to the main performance of the SRR. In a certain frequency range, this structure can be equivalent to the assembled element circuit diagram as shown in **Figure 2B**. C_0 is the equivalent capacitance between the whole ring and C_s is the series capacitance composed of the upper half and the lower half capacitances, which can be obtained from the series capacitance formula: $C_s = C_0/4$. L_s is the equivalent inductance of the SRR. The resonant frequency of the whole resonant circuit is given by

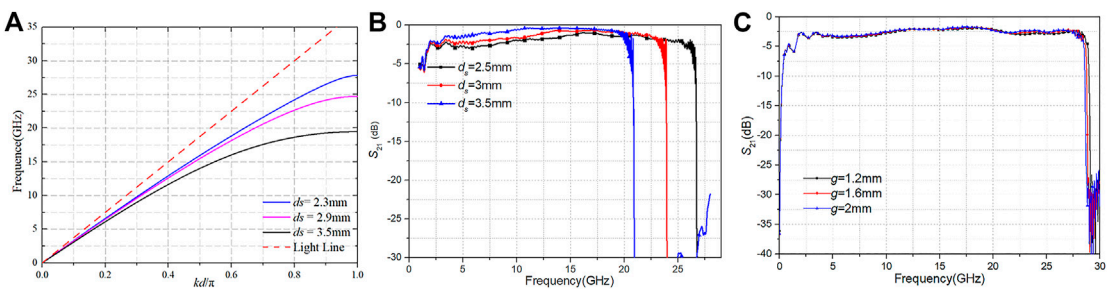

FIGURE 8 | (A) Dispersion performance of the SSPP-TL with different d_s. **(B)** S_{21} of the SSPP-TL with different d_s. **(C)** S_{21} of the SSPP-TL with different g.

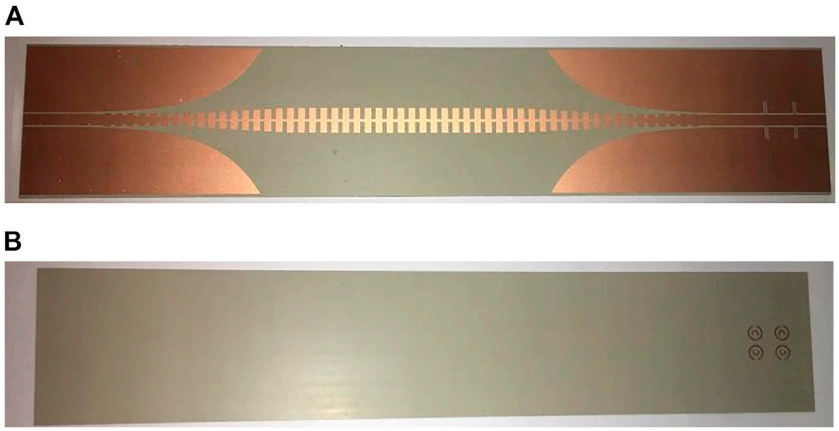

FIGURE 9 | The SSPP filter **(A)** front side **(B)** reverse side.

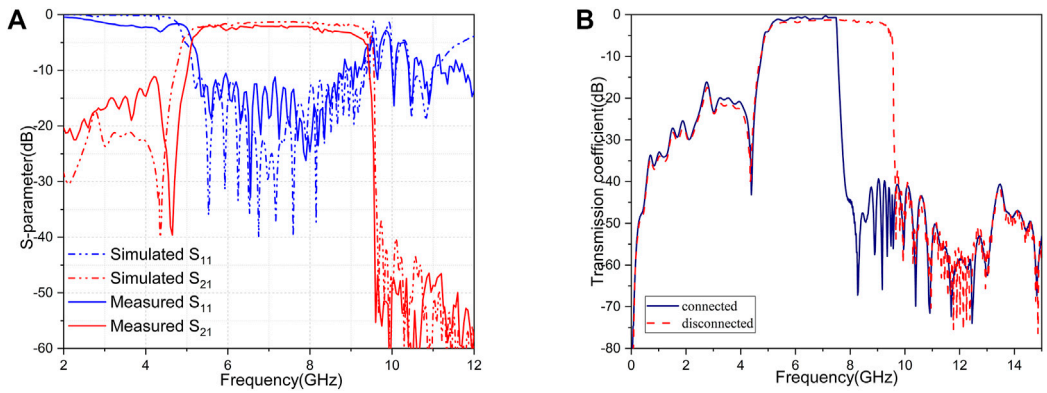

FIGURE 10 | (A) The *S*-parameters simulated and measured results of SSPP filter. **(B)** The transmission coefficient results of SSPP diode reconfigurable filter in **Figure 1B**.

TABLE 5 | Comparative study of the SSPP bandpass structure.

Ref.	BW/ GHz	Out-of-band rejection at low frequency	Out-of-band rejection at high frequency	Controllability of passband range
[9]	7.3–11.2	–30 dB	–40 dB	No
[15]	3–4.8	–30 dB	–30 dB	No
[19] A	3.6–7.1	–20 dB	–20 dB	No
[20]	0.6–1.5	–30 dB	–20 dB	No
[31]	7.3–10.5	–30 dB	–20 dB	No
This work	5–9.5	–40 dB	–50 dB	Yes

$$f = \frac{1}{2\pi\sqrt{L_s C_s}} \quad (1)$$

By structuring the SRR on the top of the dielectric substrate, the distributions of the electric field and the magnetic field are shown in **Figures 3A,B**, respectively. It can be observed that the electric- and magnetic-field distributions on the SRR symmetry surface are consistent.

From **Eq. 1**, the resonant frequency of the SRR is related to the ring radius. Because the inductance and the length are proportional, the length of the ring equivalent and the equivalent inductance L_s both increase with the raise of the ring radius. The dielectric substrate is Rogers RO4003C with the dielectric constant ε_r = 3.38, tanδ = 0.001, and thickness h = 1 mm. The Parameter values of the SRR is shown in **Table 1**.

The results simulated by the model *via* changing only the radius r_{out} of the outer ring of the SRR are shown in the **Figure 4**.

The resonant frequency is 4.23, 4.75, and 5.75 GHz for the SRR outer ring radius r_{out} = 7.5, 6.5, and 5.5 mm, respectively. It can be seen that the resonant frequency of the SRR decreases with the increase of the outer ring radius. When the SRR ring opening spacing g increases, the equivalent length increases and L_s decreases, thus the resonant frequency increases. Keeping the outer radius of the SRR ring as a constant of r_{out} = 7.5 mm, the simulation results are obtained for different SRR ring opening spacing g. From the above simulation curve sshown in **Figure 4B**, the resonant frequencies of SRR are 4.2, 4.25, and 4.3 GHz for the opening pitch gap of 3, 4, and 5 mm, respectively. The resonant frequency of SRR is shifted to the high

frequency direction with the increase of the ring opening pitch. If only the ring spacing e is changed without changing other parameters (g and r_{out}), the performance curves are obtained from the simulation shown in **Figure 4C**. From the analysis above, the effect of ring spacing e on the SRR is relatively small.

To complete the transition and achieve tight coupling, the coplanar waveguide (CPW) structure is placed on the front, the SRR resonant ring is symmetrically placed on the back, as shown in **Figures 5A,B**. This structure could produce a negative permeability effect near the resonant frequency to prevent the transmission of electromagnetic waves. The dimensions of the above structure are listed in **Table 2**. The equivalent circuit is shown in **Figure 5C**, where L_0 and C are the equivalent inductance and capacitance generated after the action of the SRR with CPW structure, respectively. L_s and C_s are the equivalent inductance and capacitance of the SRR after resonance generated in the structure, respectively. L_{gnd} represents the equivalent value of the grounding inductance. The series branch will change from inductive impedance to capacitive impedance. The port impedance is 50 Ω, which could matched to the SRR with CPW structure.

Keep the other parameters unchanged to perform simulations on parameters S_1 and d, the results in **Figure 6** could be obtained.

As shown in **Figure 6**, the passband bandwidth of the filter decreases when S_1 increases. This is mainly due to the increase of the ground inductance, which leads to the increase of the local resonant frequency. Simulations of parameter d show that the transmission characteristics in the passband gradually become better as d increases (the transmission coefficient S_{21} can be inferred from S_{11}). However, its transmission bandwidth remains basically unchanged, so we conclude that the passband bandwidth can be controlled by adjusting parameters S_1 and d to regulate the impedance matching in the passband. Finally, the dimensions of the above structure are derived by optimization, as shown in **Table 3**.

The scattering parameter (*S*-parameter) of the bandpass filter based on the SRR with CPW structure is shown in **Figure 7**. The *S*-parameter is obtained by simulating the model created by CST, and it produces good passband characteristics from 5 to 9 GHz as shown in **Figure 7**.

Configuration of Spoof Surface Plasmon Polaritons

The high frequency characteristics of the filter is based on the SSPP transmission line (TL). The SSPP unit dispersion curves are displayed in **Figure 8A**. These curves remain in the slow wave region, which are similar to the natural SPP material. The cutoff frequency decreases when the length of the slot increases. The wave number of the SSPP-TL unit is larger than that of the microstrip line, which suggests that the SSPP-TL unit has better electromagnetic constrain, lower coupling, and lower signal crosstalk than the microstrip line. In order to investigate the transmission loss performance of the SSPP-TL, the numerical simulation is performed, as shown in **Figure 8B**. The depth d_s of the trench determines the cutoff frequency of the SSPP-TL. As the cutoff frequency decreases, the transmission loss decreases due to the stronger electromagnetic field binding.

As shown in **Figure 8C**, the slot width g has almost no effect on the transmission properties. Therefore, the deeper the slot, the lower the cutoff frequency and the stronger its binding.

IMPLEMENTATION AND MEASUREMENT

Based on the theoretical analysis above, a bandpass filter with SSPP is designed. As shown in **Figure 9**, the SSPP based filter is cascaded by the SSPP transmission line and the SRR with CPW section. In the SRR with CPW section, the two-section SRR structure is used, which can effectively increase the low frequency rejection effect. The cutoff frequency of the SSPP TL is at 9.5 GHz. By adding a first-order ground inductor and SRR series structure, low-frequency stopband rejection can be achieved, and the optimized dimensions are listed in **Table 4**.

As shown in **Figure 10A**, the proposed SSPP filter has a good window characteristics. The passband range is 5~9.5GHz, the out-of-band rejection at 4 GHz is −20dB, and the out-of-band rejection at 10 GHz is −50dB for the bandpass filter. The measurement results and simulation results are basically consistent. Using reconfigurable technology, the passband range can be changed from 9.5 to 7.5 GHz by diode switching based on **Figure 10B**. A comparative study of the SSPP bandpass structures reported in recent literatures is presented in **Table 5**. The proposed filter features out-of-band rejection and passband range control.

CONCLUSION

In this paper, a wideband pandpass SSPP filter is proposed, which structured based on a SRR CPW section and a SSPP transmission line. The passband can be controlled by the RF diodes. The passband of proposed filter is range from 5 to 9.5 GHz, out-of-band rejection of -20 dB at 4 GHz, and out-of-band rejection of −50 dB at 10 GHz. The measurement results and simulation results are in agreement. Finally, a passband controllable filter using diode reconfigurable technology is proposed, and the simulation analysis is given to provide a new scheme for future filter design.

DATA AVAILABILITY STATEMENT

The original contributions presented in the study are included in the article/Supplementary Material, further inquiries can be directed to the corresponding author.

AUTHOR CONTRIBUTIONS

XC and LL contributed to this work equally. All authors listed have made a substantial, direct, and intellectual contribution to the work and approved it for publication.

FUNDING

This work was supported by the Natural Science Foundation of China under Grant 62001250.

REFERENCES

1. Otsuji T, Shur M. Terahertz Plasmonics: Good Results and Great Expectations. *IEEE Microwave* (2014) 15(7):43–50. doi:10.1109/MMM.2014.2355712
2. Ghazali AN, Sazid M, Pal S. A Compact Broadside Coupled Dual Notched Band UWB-BPF with Extended Stopband. *AEU - Int J Electron Commun* (2017) 82: 502–7. doi:10.1016/j.aeue.2017.10.021
3. Ghazali AN, Sazid M, Pal S. Multiple Passband Transmission Zeros Embedded Compact UWB Filter Based on Microstrip/CPW Transition. *AEU - Int J Electron Commun* (2021) 129(1):153549. doi:10.1016/j.aeue.2020.153549
4. Barnes WL, Dereux A, Ebbesen TW. Surface Plasmon Subwavelength Optics. *Nature* (2003) 424(6950):824–30. doi:10.1038/nature01937
5. Pendry JB, Marti´n-Moreno L, Garcia-Vidal FJ. Mimicking Surface Plasmons with Structured Surfaces. *Science* (2004) 305(5685):847–8. doi:10.1126/science.1098999
6. Hibbins AP, Evans BR, Sambles JR. Experimental Verification of Designer Surface Plasmons. *Science* (2005) 308(5722):670–2. doi:10.1126/science.1109043
7. Shen X, Jun Cui T. Planar Plasmonic Metamaterial on a Thin Film with Nearly Zero Thickness. *Appl Phys Lett* (2013) 102(21):211909. doi:10.1063/1.4808350
8. Lei W, Che W, Deng K, Dong S. Narrow-Slot Bandpass Filter Based on Folded Substrate-Integrated Waveguide with Wide Out-Of-Band Rejection. *Microw Opt Technol Lett* (2008) 50:1155–9. doi:10.1002/mop.23327
9. Yang T, Chi P-L, Xu R, Lin W. Folded Substrate Integrated Waveguide Based Composite Right/Left-Handed Transmission Line and its Application to Partial H-Plane Filters. *IEEE Trans Microwave Theor Techn.* (2013) 61(2):789–99. doi:10.1109/TMTT.2012.2231431
10. Yu L-Z, Yuan C-W, He J-T, Zhang Q. Beam Steerable Array Antenna Based on Rectangular Waveguide for High-Power Microwave Applications. *IEEE Trans Plasma Sci* (2019) 47(1):535–41. doi:10.1109/TPS.2018.2884290
11. Feng W, Ma X, Shi Y, Shi S, Che W. High-Selectivity Narrow- and Wide-Band Input-Reflectionless Bandpass Filters with Intercoupled Dual-Behavior Resonators. *IEEE Trans Plasma Sci* (2020) 48(2):446–54. doi:10.1109/TPS.2020.2968481
12. Zhuang Z, Wu Y, Yang Q, Kong M, Wang W. Broadband Power Amplifier Based on a Generalized Step-Impedance Quasi-Chebyshev Lowpass Matching Approach. *IEEE Trans Plasma Sci* (2020) 48(1):311–8. doi:10.1109/TPS.2019.2954494
13. Kong M, Wu Y, Zhuang Z, Wang W, Wang C. Ultraminiaturized Wideband Quasi-Chebyshev/-Elliptic Impedance-Transforming Power Divider Based on Integrated Passive Device Technology. *IEEE Trans Plasma Sci* (2020) 48(4): 858–66. doi:10.1109/TPS.2020.2980029
14. Zhou K, Zhou C-X, Wu W. Substrate-Integrated Waveguide Dual-Mode Dual-Band Bandpass Filters with Widely Controllable Bandwidth Ratios. *IEEE Trans Microwave Theor Techn.* (2017) 65(10):3801–12. doi:10.1109/TMTT.2017.2694827
15. Liu L, Jiang Y, Hu Y, Jiang D, Zhu L. Wideband Millimeter-Wave Endfire Antenna Based on Symmetrical Spoof Surface Plasmon Polaritons. *IEEE Trans Antennas Propagat* (2021) 69(11):7386–93. doi:10.1109/TAP.2021.3076199
16. Jiang Y, Liu L, Hu Y, Jiang D. Wideband Small Aperture Endfire Antenna Based on Spoof Surface Plasmon Polaritons. *IEEE Trans Antennas Propagat* (2021) 69(8): 5026–31. doi:10.1109/TAP.2021.3060141
17. Guo Y-J, Xu K-D, Deng X, Cheng X, Chen Q. Millimeter-Wave On-Chip Bandpass Filter Based on Spoof Surface Plasmon Polaritons. *IEEE Electron Device Lett* (2020) 41(8):1165–8. doi:10.1109/LED.2020.3003804
18. Xu K-D, Lu S, Guo Y-J, Chen Q. High-Order Mode of Spoof Surface Plasmon Polaritons and its Application in Bandpass Filters. *IEEE Trans Plasma Sci* (2021) 49(1):269–75. doi:10.1109/TPS.2020.3043889
19. Xu K-D, Guo Y-J, Yang Q, Zhang Y-L, Deng X, Zhang A, et al. On-Chip GaAs-Based Spoof Surface Plasmon Polaritons at Millimeter-Wave Regime. *IEEE Photon Technol Lett* (2021) 33(5):255–8. doi:10.1109/LPT.2021.3054962
20. Guan D-F, You P, Zhang Q, Xiao K, Yong S-W. Hybrid Spoof Surface Plasmon Polariton and Substrate Integrated Waveguide Transmission Line and its Application in Filter. *IEEE Trans Microwave Theor Techn.* (2017) 65(12): 4925–32. doi:10.1109/TMTT.2017.2727486
21. Chen P, Li L, Yang K, Chen Q. Hybrid Spoof Surface Plasmon Polariton and Substrate Integrated Waveguide Broadband Bandpass Filter with Wide Out-Of-Band Rejection. *IEEE Microw Wireless Compon Lett* (2018) 28(11):984–6. doi:10.1109/LMWC.2018.2869290
22. Ye L, Chen Y, Xu KD, Li W, Liu QH, Zhang Y. Substrate Integrated Plasmonic Waveguide for Microwave Bandpass Filter Applications. *IEEE Access* (2019) 7: 75957–64. doi:10.1109/ACCESS.2019.2920925
23. Zhang D, Zhang K, Wu Q, Jiang T. Efficient Propagation of Spoof Surface Plasmon Polaritons Supported by Substrate Integrated Waveguide with Bandpass Features. *J Phys D: Appl Phys* (2020) 53(42):425104. doi:10.1088/1361-6463/ab9f6a
24. Cui Y, Xu K-D, Guo Y-J, Chen Q. Half-Mode Substrate Integrated Plasmonic Waveguide for Filter and Diplexer Designs. *J Phys D: Appl Phys* (2022) 55(12): 125104. doi:10.1088/1361-6463/ac44bf
25. Zhang D, Zhang K, Wu Q, Jiang T. A Compact Wideband Filter Based on Spoof Surface Plasmon Polaritons with a Wide Upper Rejection Band. *IEEE Photon Technol Lett* (2020) 32(24):1511–4. doi:10.1109/LPT.2020.3029290
26. Guo Y-J, Xu K-D, Deng X, Cheng X, Chen Q. Millimeter-Wave On-Chip Bandpass Filter Based on Spoof Surface Plasmon Polaritons. *IEEE Electron Device Lett* (2020) 41(8):1165–8. doi:10.1109/LED.2020.3003804
27. Zhang HC, He PH, Gao X, Tang WX, Cui TJ. Pass-Band Reconfigurable Spoof Surface Plasmon Polaritons. *J Phys Condens Matter* (2018) 30(13):134004. doi:10.1088/1361-648X/aaab85
28. Zhou YJ, Yang BJ. Planar Spoof Plasmonic Ultra-Wideband Filter Based on Low-Loss and Compact Terahertz Waveguide Corrugated with Dumbbell Grooves. *Appl Opt* (2015) 54(14):4529–33. doi:10.1364/AO.54.004529
29. Ma HF, Shen X, Cheng Q, Jiang WX, Cui TJ. Broadband and High-Efficiency Conversion from Guided Waves to Spoof Surface Plasmon Polaritons. *Laser Photon Rev* (2014) 8(1):146–51. doi:10.1002/lpor.201300118
30. Zhao L, Zhang X, Wang J, Yu W, Li J, Su H, et al. A Novel Broadband Band-Pass Filter Based on Spoof Surface Plasmon Polaritons. *Sci Rep* (2016) 6(1): 36069. doi:10.1038/srep36069
31. Zhang W, Zhu G, Sun L, Lin F. Trapping of Surface Plasmon Wave through Gradient Corrugated Strip with Underlayer Ground and Manipulating its Propagation. *Appl Phys Lett* (2015) 106:021104. doi:10.1063/1.4905675
32. Abbosh A, Ibrahim S, Karim M. Ultra-Wideband Crossover Using Microstrip-To-Coplanar Waveguide Transitions. *IEEE Microw Wireless Compon Lett* (2012) 22(10):500–2. doi:10.1109/LMWC.2012.2218586
33. Wang J, Zhao L, Hao Z-C. A Band-Pass Filter Based on the Spoof Surface Plasmon Polaritons and CPW-Based Coupling Structure. *IEEE Access* (2019) 7:35089–96. doi:10.1109/ACCESS.2019.2903147

Conflict of Interest: The authors declare that the research was conducted in the absence of any commercial or financial relationships that could be construed as a potential conflict of interest.

frontiers in Physics

ORIGINAL RESEARCH
published: 25 March 2022
doi: 10.3389/fphy.2022.872204

A Tunable low Pass Filter Based on Transmission Lines With Tunable Input/Output Impedance

*Zhonghai Zhang[1], Yuekai Zhao[1], Lin Chen[2], Zhihua Fang[1], Aiting Wu[1] and Pengquan Zhang[1]**

[1]Institute of Antenna and Microwave, Hangzhou Dianzi University, Hangzhou, China, [2]National Key Laboratory of Science and Blind Signal Processing, Chengdu, China

A tunable low pass filter (TLPF) based on the tuning of input/output impedance was presented in this letter. The TLPF mainly consisted of improved quarter-wavelength stubs. The input/output impedance of the improved quarter-wavelength stubs can be tuned in a certain range. The design procedure of this TLPF was derived from the filters based on the quarter-wavelength transmission stubs. Through the tuning of the input/output impedance of the transmission lines, the cut-off frequency of the TLPF can be adjusted in a certain range. The TLPF has relatively good designability and can be easily changed to meet other performance levels. Finally, a TLPF was designed, fabricated, and measured. The measured results verify the effectiveness of the design method.

Keywords: tunable filter, tunable impedance, cut off frequency, characteristic impedance, input/output impedance

OPEN ACCESS

Edited by:
Kai-Da Xu,
Xi'an Jiaotong University, China

Reviewed by:
Feng Wei,
Xidian University, China
Ji Laiyun,
Tianjin Hi-Tech Superconducting Electronic Technology, China

****Correspondence:***
Pengquan Zhang
zhpq1999@163.com

Specialty section:
This article was submitted to Optics and Photonics, a section of the journal Frontiers in Physics

Received: *09 February 2022*
Accepted: *18 February 2022*
Published: *25 March 2022*

Citation:
Zhang Z, Zhao Y, Chen L, Fang Z, Wu A and Zhang P (2022) A Tunable low Pass Filter Based on Transmission Lines With Tunable Input/Output Impedance. Front. Phys. 10:872204. doi: 10.3389/fphy.2022.872204

INTRODUCTION

As a key component in wireless communication systems, the filter can suppress the interference signal at the outband. A tunable filter can be applied to reconfigurable communication systems and has been widely studied [1–13]. The cut-off frequency of the tunable low pass filter (TLPF) can be adjusted according to the actual application which can be applied in a variety of communication systems with different parameters and has been studied widely [6–13]. The design methods of the TLPF can be summarized into three types. Firstly, some resonators with a special structure can realize a TLPF [6–9]. In this method, due to the particularity of the resonator structure, it was difficult to realize a TLPF to meet other requirements. Secondly, through the tuning of parameters, such as dielectric constant and permeability of the substrate, can also realize a tunable low pass filter [10, 11]. But in this method, the tuning range was relatively small. Thirdly, the improvement of the low pass prototype can also realize a TLPF [12, 13]. In this method, the change of the cut-off frequency can be achieved through the tuning of the capacitors or inductors in the LPF. It is difficult to achieve a tunable inductor in an LPF. Therefore, it is difficult to realize a wide tuning range for the cut-off frequency. Therefore, there are few studies on TLPFs with a larger cut-off frequency tuning range and better designability simultaneously.

Starting from the low pass filter equivalent circuit based on quarter-wavelength stubs, this letter attempts to achieve a TLPF based on the tuning of the input/output impedance of the transmission line in the equivalent circuit model. At the same time, the cut-off frequency tuning range of the TLPF can also be expanded. The resonators of the TLPF mainly consisted of step impedance lines loaded with tunable reactance at the connections of the high and low impedance lines and the open ends. The improved quarter-wavelength line between the resonators was mainly achieved with the transmission lines parallel to tunable reactances. Through the tuning of the tunable reactances loaded in the improved quarter-wavelength lines, the cut-off frequency of the TLPF can also be tuned in a certain range. Compared with

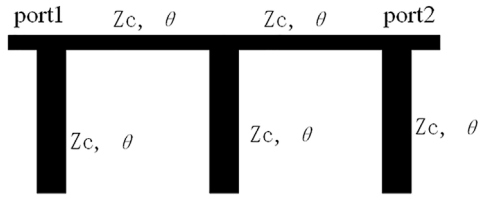

FIGURE 1 | The equivalent circuit of the TLPF.

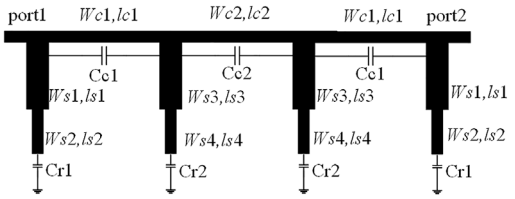

FIGURE 3 | The schematic of the designed TLPF.

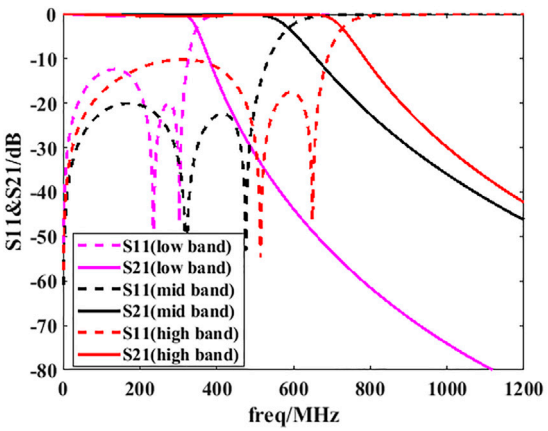

FIGURE 2 | The tuning of the low pass filter.

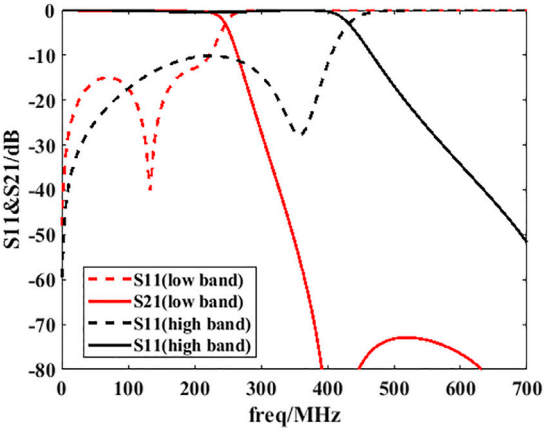

FIGURE 4 | The curve of transmission performance with Cc.

the traditional TLPF that achieves frequency tuning by adjusting the electrical length of the resonators [11–13], by inserting the step impedance lines and the transmission lines parallel to tunable reactances, the tuning range of the TLPF can be further expanded.

Analysis of the Equivalent Circuit of the TLPF

The equivalent circuit of the TLPF is shown in **Figure 1**.

In **Figure 1**, the open end stubs represent capacitance. The transmission lines between open end stubs represent inductance. The tuning of the electronic length θ can achieve the tuning of the cut-off frequency. But it was difficult to achieve the tuning of the electronic length θ for the transmission lines between open end stubs.

According to the design method of low pass filters based on quarter-wavelength transmission lines, in addition to the electrical length tuning, the cut-off frequency of the low pass filter can also be tuned in a certain range through the adjusting of the characteristic impedance Z of the transmission lines. The simulated results are shown in **Figure 2**.

In **Figure 2**, only through the tuning of the characteristic impedance can the cut-off frequency of the low pass filter be tuned from 430 to 670 MHz. The relative bandwidth of tuning was 43.6%. Beyond this range, the ripple and return loss performance in the passband of the low pass filter will deteriorate sharply.

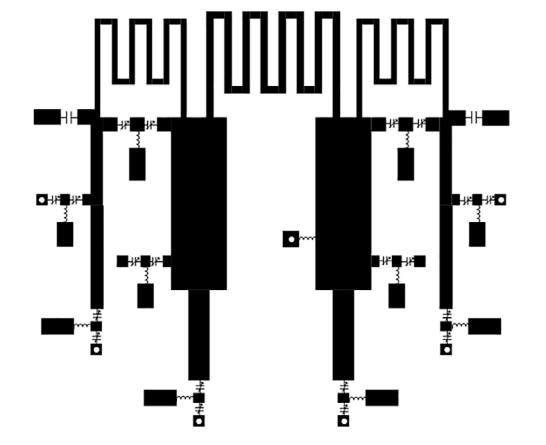

FIGURE 5 | The layout of the TLPF.

Obviously, the combination of the characteristic impedance tuning and electronic length θ tuning of the transmission lines can achieve a wider cut-off frequency tuning range.

Design of TLPF Based on Tunable Input/Output Impedance

For a transmission line, it was very difficult to adjust the characteristic impedance. But the tuning of the input/output

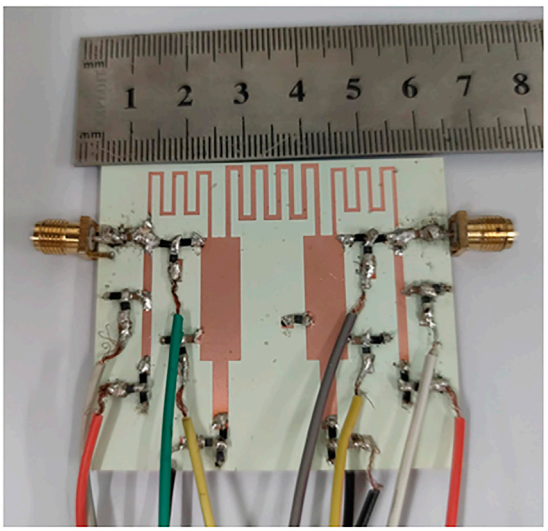

FIGURE 6 | The fabricated TLPF. The measured performance is shown in **Figure 7**.

impedance can be realized through inserting a tunable reactance parallel to the transmission lines. The feature of the input/output impedance tuning was similar to the tuning of the characteristic impedance. Therefore, the tuning of the input/output impedance of the transmission lines can be adopted to achieve a TLPF.

The schematic of the designed TLPF is shown in **Figure 3**.

In **Figure 3**, the transfer matrix can be derived as follows.

$$[T] = \begin{bmatrix} 1 & 0 \\ \frac{1}{Z_1} & 1 \end{bmatrix} \begin{bmatrix} 1 & Z_2 \\ 0 & 1 \end{bmatrix} \begin{bmatrix} 1 & 0 \\ \frac{1}{Z_3} & 1 \end{bmatrix} \begin{bmatrix} 1 & Z_4 \\ 0 & 1 \end{bmatrix} \begin{bmatrix} 1 & 0 \\ \frac{1}{Z_3} & 1 \end{bmatrix} \times \begin{bmatrix} 1 & Z_2 \\ 0 & 1 \end{bmatrix} \begin{bmatrix} 1 & 0 \\ \frac{1}{Z_1} & 1 \end{bmatrix} \quad (1)$$

In **Eq. 1**, Z1 and Z3 are the port impedances of the stepped impedance line loaded with tunable capacitors at the open ends of the first/fourth and second/third sections, respectively. Z2 and Z4 are the total input impedance of the quarter-wavelength transmission line parallel to the tunable capacitors Cc1 and Cc2, respectively. The expression of Z2 was as follows:

$$Z_2 = \frac{1}{Y + jwc} = \frac{Y}{Y^2 - w^2c^2} - j\frac{wc}{Y^2 - w^2c^2} \quad (2)$$

Substituting **Eq. 2** into **Eq. 1**, the transmission matrix of the entire TLPF can be obtained and T_{21} was the transmission characteristic of the filter. The calculation method of Z4 was similar to that of Z2.

Through the tuning of the capacitors Cc1 and Cc2, the tuning of the input/output impedance can be realized. The size of the schematic in **Figure 3** was optimized ($ws1$ = 1.6 mm, $ls1$ = 10.7 mm, $ws2$ = 1.5 mm, $ls2$ = 13 mm, $ws3$ = 6.8 mm, $ls3$ = 21 mm, $ws4$ = 3 mm, $ls4$ = 11 mm, $wc1$ = 0.7 mm, $lc1$ = 63 mm, $wc2$ = 0.8 mm, $lc2$ = 94 mm). With the tuning of Cc1 and Cc2, the simulated transmission performance of the TLPF is shown in **Figure 4**.

From **Figure 4**, the cut-off frequency of the tunable LPF can be tuned from 220 to 404 MHz providing Cc tuning from 1 pf to 8 pf.

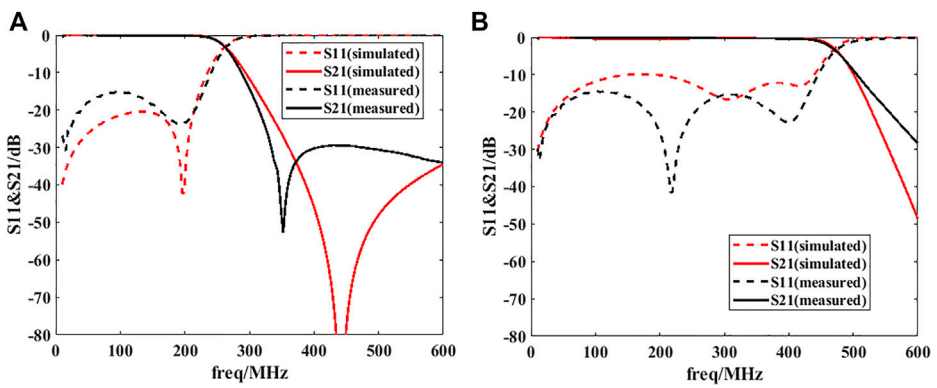

FIGURE 7 | (A) The measured performance of the TLPF (220 MHz). **(B)** The measured performance of the TLPF (440 MHz).

TABLE 1 | Comparison between the proposed TLPF and the references.

	Frequency tuning range (%)	Insertion loss (dB)	Circuit size (normalized to the highest frequency)	Designability
This work	66.7	0.5	0.14λ*0.14λ	Easy
[6]	65	0.7	0.6λ*0.42λ	Difficult
[7]	91.3	0.8	0.09λ*0.07λ	Difficult
[13]	46	0.8	0.2λ*0.09λ	Medium

The return loss of the passband was less than −10 dB. Beyond this frequency tuning range, the return loss of the tunable filter in the passband will deteriorate sharply.

Fabrication and Measurement of TLPF Based on Tunable Input/Output Impedance

To verify the effectiveness of the design method described in this letter, a TLPF with seven resonators was designed, fabricated, and measured. The Logers 4350b substrate was selected to realize this TLPF. The dielectric constant of this substrate was 3.48 and thickness was 40 mm. In order to expand the tuning range of the filter further, tunable capacitors were introduced at the connection of the high and low impedance lines. In order to obtain a larger tuning range, the size of the TLPF in this letter has been optimized. The layout of the TLPF is shown in **Figure 5**. The dimensions of the TLPF were the same as the ones in **Figure 3**. The fabricated TLPF is shown in **Figure 6**.

Due to the insertion of capacitors at the connections and open ends of the high and low impedance lines, the cut-off frequency tuning range of the TLPF was expanded compared to the situation with only input and output impedance tuning. As seen in **Figure 7**, the cut-off frequency of the TLPF can be tuned from 220 to 440 MHz, the relative bandwidth tuning range was 66.7%. The return loss of the TLPF was better than 10 dB. The insertion loss was better than 0.5 dB.

The TLPF proposed in this article has good designability and can be designed into a TLPF that meets other performance requirements easily the comparison between the proposed TLPF and the references (**Table 1**).

CONCLUSION

A tunable low pass filter adopting tunable input/output impedance technology was presented. Through the tuning of input/output impedance of the quarter-wavelength resonator, the cut-off frequency of the TLPF can be tuned in a certain range. The design of the TLPF based on variable input/output impedance can be generalized to other types of filters and filter designs with other properties.

DATA AVAILABILITY STATEMENT

The original contributions presented in the study are included in the article/supplementary material, further inquiries can be directed to the corresponding author.

AUTHOR CONTRIBUTIONS

All authors listed have made a substantial, direct, and intellectual contribution to the work and approved it for publication.

REFERENCES

1. Ouyang ZA, Qiu LL, Zhu L. Coplanar Waveguide Serially Connected Coplanar Strip Dual Stub Structure for Wideband Bandpass Filters. *Int J RF Microw Comput Aided Eng* (2021) 31(4):225–9. doi:10.1002/mmce.22571
2. Guan XH, Huang W, Ren BP. High Isolation Tunable Diplexer Based on Mixed Electromagnetic Coupling. *Int J RF Microw Comput Aided Eng* (2018) 2863(23):1–7. doi:10.1002/mmce.21199
3. Huang ZW, Cheng Y. Cross-coupled Dielectric Waveguide Filter. *Int J RF Microw Comput Aided Eng* (2021) 63(3):8–14. doi:10.1002/mmce.22585
4. Vkumar K, Mukherjee B. Compact Dual Bandpass Filter for Terrestrial Radio and GSM Applications. *Int J RF Microw Comput Aided Eng* (2017) 27(8):1–8. doi:10.1002/mmce.21131
5. Iqbal A, Smida A, Waly MI, Mallat NK. Highly-tunable and Wide Stopband Microstrip Bandpass Filters. *Int J RF Microw Comput Aided Eng* (2021) 31:1–6. Early Access. doi:10.1002/mmce.22610
6. Huang CC, Chen NW, Tsai HJ, Chen JY. A Coplanar Waveguide Bandwidth-Tunable Lowpass Filter with Broadband Rejection. *IEEE Microw Wireless Compon Lett* (2013) 23(3):134–6. doi:10.1109/lmwc.2013.2242323
7. Cai C, Wang J, Zhang G. Tunable Microstrip Lowpass Filter with Compact Size and Ultra-wide Stopband[J]. *Electron Lett* (2015) 51(19):1514–6. doi:10.1049/el.2015.0829
8. Kumar L, Parihar MS. A Compact Reconfigurable Low-Pass Filter with Wide-Stopband Rejection Bandwidth. *IEEE Microw Wireless Compon Lett* (2018) 28(5):401–3. doi:10.1109/lmwc.2018.2823001
9. Kumar N, Singh YK. Compact Tunable Low-pass to CFBW Bandpass Switchable Filter Using Concentric Resonators. *IET Microwaves, Antennas & Propagation* (2018) 12(14):2225–33. doi:10.1049/iet-map.2018.5345
10. Yang G-M, Wu J, Lou J, Liu M, Sun NX. Low-Loss Magnetically Tunable Bandpass Filters with YIG Films. *IEEE Trans Magn* (2013) 49(9):5063–8. doi:10.1109/tmag.2013.2253114
11. Yun Zhu Y, Gang Qiu G, Chi KH, Wang BBT, Tsai CS. A Tunable X-Band Band-Pass Filter Module Using YIG/GGG Layer on RT/Duroid Substrate. *IEEE Trans Magn* (2009) 45(10):4195–8. doi:10.1109/tmag.2009.2022642
12. Zhang R, Mansour RR. Novel Digital and Analogue Tunable Lowpass Filters. *IET Microw Antennas Propag* (2007) 1(3):549–55. doi:10.1049/iet-map:20060263
13. Jia N, Hong JS. Compact Continuously Tunable Microstrip Low Pass Filter[J]. *Ieee Transactions Microwave Theory Techniques* (2013) 61(5):1793–800. doi:10.1109/TMTT.2013.2252919

Conflict of Interest: The authors declare that the research was conducted in the absence of any commercial or financial relationships that could be construed as a potential conflict of interest.

frontiers | Frontiers in Physics

ORIGINAL RESEARCH
published: 06 April 2022
doi: 10.3389/fphy.2022.883686

60-GHz Double-Layer Transmitarray Antenna Using Complementary Structure

Wenxing An[1], *Xiaochi Zhang*[1], *Yu Luo*[1]*, *Jian Wang*[1]* *and Lin Xiong*[2]

[1]*The Tianjin Key Laboratory of Imaging and Sensing Microelectronic Technology, School of Microelectronics, Tianjin University, Tianjin, China,* [2]*The Department of Electronic Engineering, Tsinghua University, Beijing, China*

Abstract—A novel double-layer transmitarray element is presented at 60 GHz with linearly- and circularly-polarized characteristics. A planar frequency-selective structure using the complementary design is adopted to augment the element performance for millimeter-wave applications. By integrating two different types of structure, i.e. cross and slot type, the compensation phase range is extended effectively with a satisfactory transmission magnitude. A transmitarray prototype is fabricated and tested to verify this double-layer complementary design. The measured gain at 60.5 GHz is 33.1 dBi with an aperture efficiency of 42.15%. Low side-lobe and cross-polarization levels are obtained. The proposed double-layer complementary design can reduce the structure complexity effectively and offer a high aperture efficiency at a low cost, which can be a potential candidate for the millimeter-wave transmitarray.

Keywords: high gain, double-layer, transmitarray, antenna, millimeter (MM) wave

OPEN ACCESS

Edited by:
Kai-Da Xu,
Xi'an Jiaotong University, China

Reviewed by:
Huanhuan Yang,
Air Force Engineering University, China
Zihao Chen,
Harbin Institute of Technology, China

***Correspondence:**
Yu Luo
yluo@tju.edu.cn
Jian Wang
wangjian16@tju.edu.cn

Specialty section:
This article was submitted to Optics and Photonics, a section of the journal Frontiers in Physics

Received: *25 February 2022*
Accepted: *18 March 2022*
Published: *06 April 2022*

Citation:
An W, Zhang X, Luo Y, Wang J and Xiong L (2022) 60-GHz Double-Layer Transmitarray Antenna Using Complementary Structure. Front. Phys. 10:883686. doi: 10.3389/fphy.2022.883686

1 INTRODUCTION

Recently, transmitarray antenna has become a popular research item. Compared with the traditional lens antenna, the transmitarray aperture can be a planar frequency-selective surface, which makes it easy integration, visual invisibility, and economical fabrication with PCB technology. Many transmitarray antennas have been investigated with diverse performances such as wideband [1], multiple bands [2], low profile [3], multiple beams [4], and beam scanning [5].

Many devices have been reported for the millimeter-wave band near 60 GHz [6–8]. A three-layer linearly polarized transmitarray antenna was presented in [9] for millimeter-wave applications. Employing a slot-coupling method, a triple-layer linearly polarized transmitarray was proposed in [10]. Although satisfactory performances have been realized, these designs have at least three metallic layers that make the structure relatively complicated. A dual-layer transmitarray was proposed for the 77-GHz automotive radar applications [11]. However, the proposed element can only provide 0° and 180° phase differences, which would result in a relatively large phase error and lower aperture efficiency. A dual linearly polarized transmitarray was presented at D-band with a peak gain of 32 dBi and aperture efficiency of 32% at 150 GHz [12]. It is discussed in [13] that at least three metallic layers are required to achieve a compensation phase range of nearly 360°and -1-dB magnitude simultaneously. To reduce the structural complexity, the double-layer element has been investigated and reported. A double-layer transmitarray element with metallic vias was proposed [14, 15]. It was further investigated in [16–18] with improved performance. A two-layer linearly-polarized metal-only TA was presented in [19].

For the 60-GHz millimeter-wave and even higher frequency band, transmitarrays with a simple structure are desired for easy fabrication and low cost. Then, some double-layer designs without vias

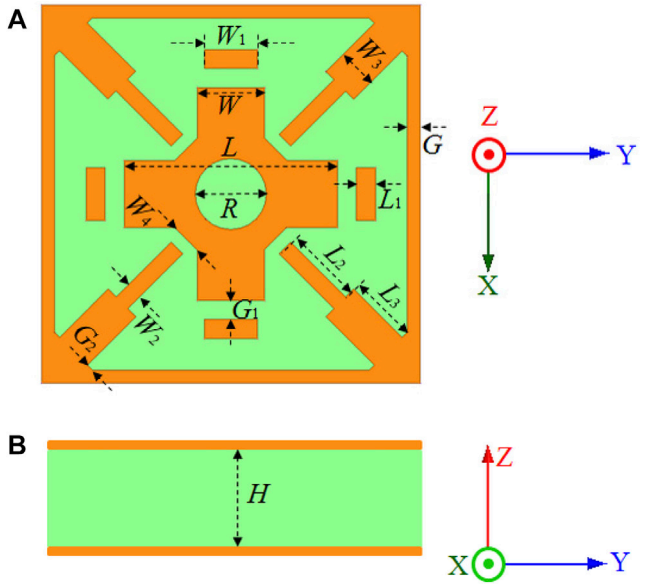

FIGURE 1 | Structure of the double-layer element. **(A)** Top view, **(B)** Side view.

are investigated. A double-layer planar lens antenna was presented in [20] using a gradient metasurface structure with a measured aperture efficiency of 24.6%. A double-layer design from [21] can achieve a high aperture efficiency of 60.2% using a circular polarization conversion approach for circular polarization. Recently, a conformal transmitarray was developed in [22] using a dual-layer Huygens element with single linear polarization. It has a measured gain of 20.6 dBi with an aperture efficiency of 47%. Although the above designs have achieved satisfactory performance, it is still difficult to accommodate both linear and circular polarizations simultaneously to meet the application requirements of different occasions. Recently, a planar transmitarray element based on a complementary frequency-selective structure was reported in [23] with an extended compensation phase range. It can be adapted potentially for millimeter-wave applications.

A complementary double-layer transmitarray element is presented for the millimeter-wave band in this letter. The element performance is improved effectively based on the hybrid design combining cross and slot-type structures with linear and circular polarization characteristics. Then, a transmitarray antenna is fabricated for verification. Satisfactory radiation performance has been achieved with a measured gain of 33.1 dBi. The measured aperture efficiency is 42.15% with low side-lobe and cross-polarization levels.

2 PROPOSED DOUBLE-LAYER COMPLEMENTARY ELEMENT

The double-layer complementary element is shown in **Figure 1**. The element size is 2.98 mm in the X- and Y-directions. Two identical metallic structures are printed on the top and bottom of the Rogers-5880 substrate with a thickness of 20 mil. The detailed parameters are in **Table 1**.

TABLE 1 | Antenna element parameters (mm).

Para	*L*1	*W*	*W*1	*W*2	*W*2	*W*3	*W*4
Value	0.15	0.53	0.42	0.13	0.13	0.31	0.25
Para	*G*	*G*1	*G*2				
Value	0.1	0.15	0.057				

The metallic structure consists of modified cross, slot, and parasitic structures. The slot-type structure has four stubs at the corners with lengths L_2, L_3, and widths W_2, W_3. The cross has the length L and width W with a circular slot carved at the center. Four parasitic rectangular patches with the sizes of L_1 and W_1 are distributed around the cross with a gap of G_1. All metallic structures are distributed symmetrically. The central symmetry structure makes it suitable for both linear and circular polarizations.

Using structural design freedom, two complementary elements with different stub and cross sizes are utilized to extend the compensation phase range, as shown in **Figure 2**. For element 1, the stub is relatively short with L_2 = 0.37 mm and L_3 = 0.05 mm, respectively. The diameter of the central slot is with the equation $D = -1.75L_2+4.52L-2.17$. The phase range is obtained by changing the cross length L from 0.9 to 1.67 mm. For element 2, the stub lengths L_2 and L_3 are 0.61 and 0.54 mm, respectively. D is with the equation of D=(1.96 mm–L)×2. The L varies between 1.68 and 1.9 mm. The element performances with a normal incidence at 60 GHz are plotted in **Figure 2**. The phase range of element 1 is from −59° to −141° with a transmission magnitude better than −1.5 dB. For element 2, the −1.5-dB phase range is from 40° to 133°. The phase range between −180° and 180° can be covered with a maximum phase error of 55° based on these two elements. So a double-layer complementary element with an

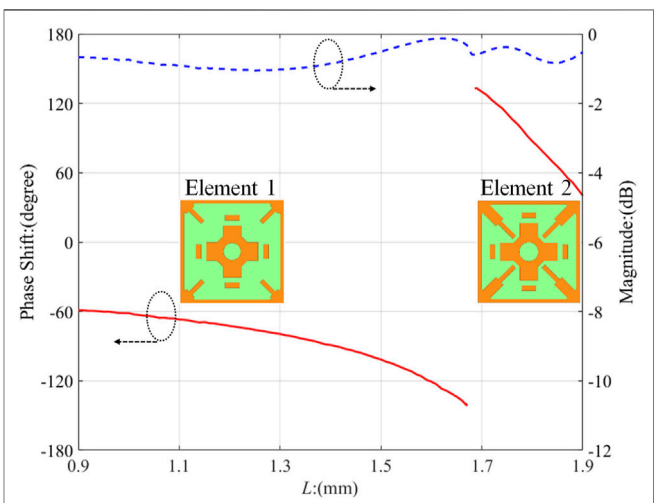

FIGURE 2 | Phase and magnitude performance of the complementary element at 60 GHz with normal incidence.

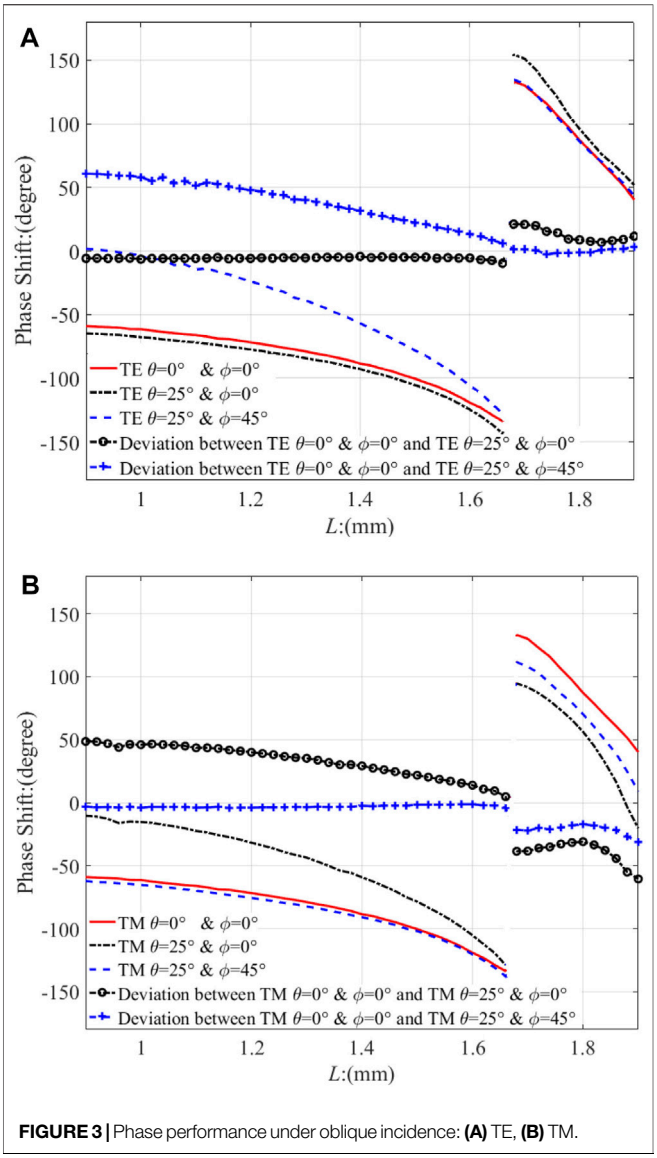

FIGURE 3 | Phase performance under oblique incidence: **(A)** TE, **(B)** TM.

extended phase range is realized for the 60-GHz millimeter-wave band.

3 ANTENNA ANALYSIS

The element performances under oblique incidence are simulated with the TE and TM sources. The phase and magnitude performances are plotted in **Figure 3** and. 4. It is observed in **Figure 3A** that the maximum phase error for TE source is 61° between the normal and oblique incidence with θ = 25° and φ = 45°. For the TM source in **Figure 3B**, the maximum phase error is 49° between the normal and oblique incidence with θ = 25° and φ = 0°. In **Figure 4**, the maximum magnitude error for TE source is −1.18 dB between the normal and oblique incidence with θ = 25° and φ = 45° while the maximum magnitude error for TM source is −2.5 dB between the normal and oblique incidence with θ = 25° and φ = 0°.

As elements 1 and 2 can cover the phase ranges from −180° to 0° and from 0° to 180° respectively, the effective current distributions are plotted for analysis, which is depicted in **Figure 5** with the cross length L = 1.68 mm.

For element 1, it is observed in **Figure 5A** that most currents distribute on the cross while there are few currents on the slot-type structure due to a relatively small stub length. The slot-type structure has little effect on the element performance when the stub length is electrically small, so the slot-type structure has limited influence on element 1.

In **Figure 5B**, the currents are on cross and slot-type structures of element 2. The slot-type structure affects the element performance when the stub length is comparable to the wavelength. The instantaneous current distributions are in **Figure 6**. The cross is excited at the reference time point of t in **Figure 6A**. The slot-type structure is excited at the time point

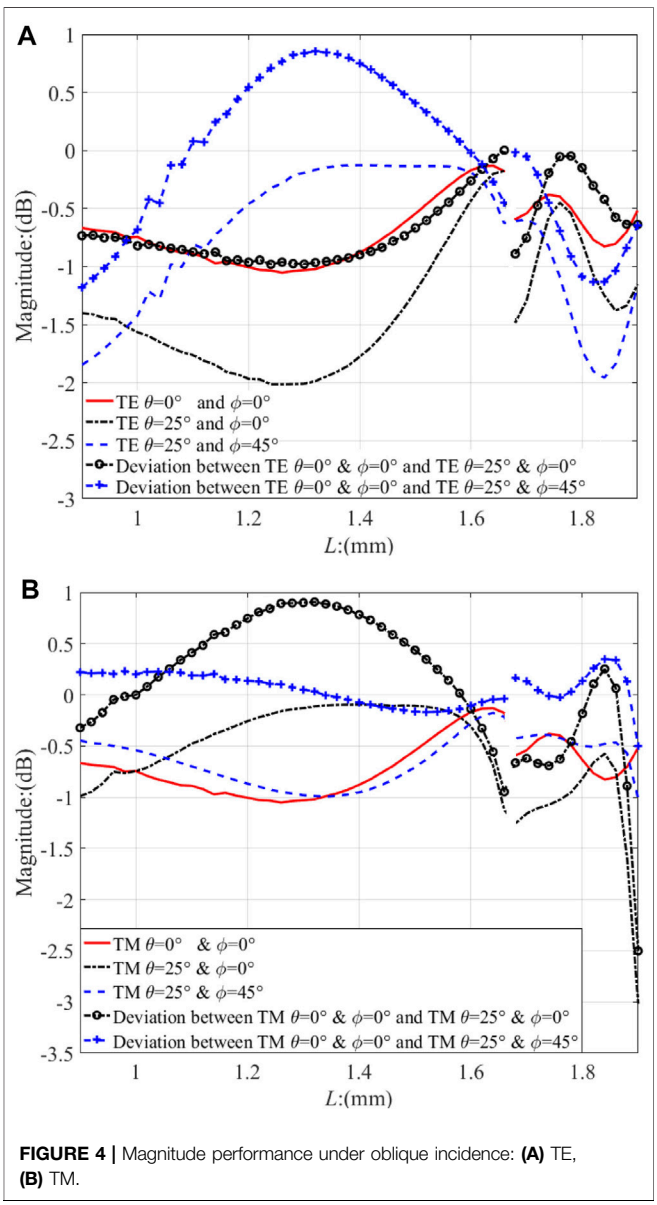

FIGURE 4 | Magnitude performance under oblique incidence: **(A)** TE, **(B)** TM.

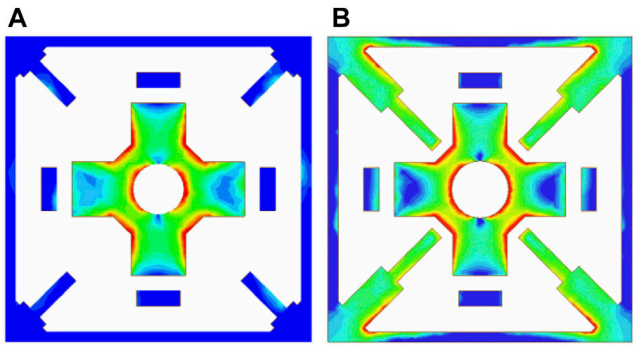

FIGURE 5 | Effective current distributions with L = 1.68 mm: **(A)** Element 1, **(B)** Element 2.

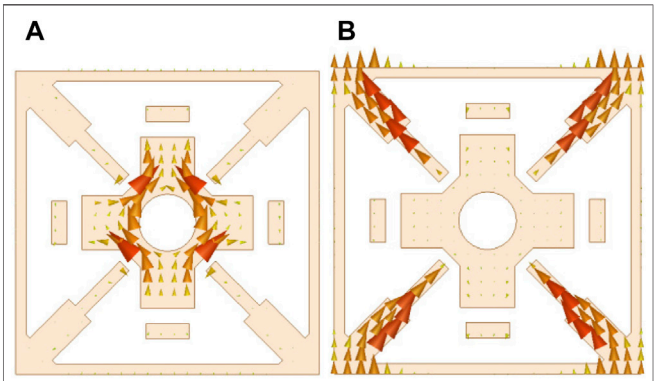

FIGURE 6 | Instantaneous current distributions of element 2 with L = 1.68 mm at different time points: **(A)** t, **(B)** t+T/6.

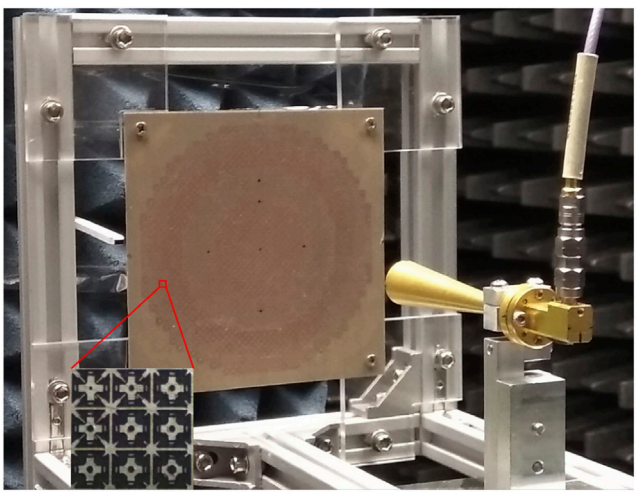

FIGURE 7 | Antenna prototype based on the proposed double-layer complementary element.

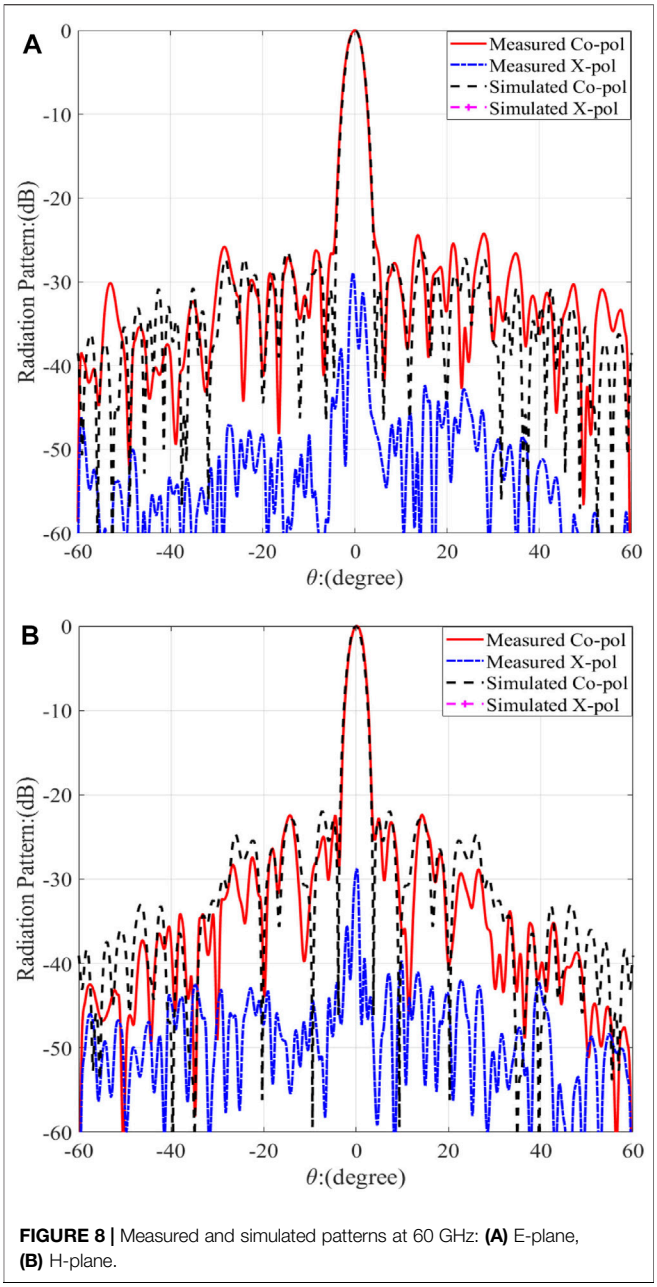

FIGURE 8 | Measured and simulated patterns at 60 GHz: **(A)** E-plane, **(B)** H-plane.

of t + T/6 in **Figure 6B** where T represents one cycle. It is noticed that the slot-type and cross structures are not excited simultaneously but with a time interval of T/6. The introduced slot-type structure can offer an extra phase shift compared with element 1, so the transmission phase is shifted from the negative range to the positive range, as shown in **Figure 2**. It can be concluded that the cross is responsible for the performance of element 1. Both the cross and slot-type structures affect the performance of element 2. They are stimulated successively within half cycle.

TABLE 2 | Comparison of the proposed antenna with existing designs.

References	Freq. (GHz)	No. of layers	Polariza-tion	Gain (dBi)	Aperture effi. (%)	3-dB-gain Bandwidth
[9]	61.5	3	Linear	32.5	42.7	21%
[10]	61	3	Linear	33.4	48	15.4%
[11]	76.5	2	Linear	24.1	19.3	N. A
[12]	150	3	Linear & Circular	32	32	19.8
This work	60.5	2	Linear & Circular	33.1	42.15	5.9%

4 EXPERIMENTAL VERIFICATION

To verify the proposed double-layer frequency-selective structure, a transmitarray antenna with a diameter of 113 mm is designed and fabricated, as shown in **Figure 7**. It includes 1,060 elements with a cross length varying between 0.9 and 1.89 mm. A linearly-polarized horn antenna with a gain of 18.25 dBi at 60 GHz is employed to illuminate the antenna aperture in the normal direction. The height is optimized to be 140 mm. Based on the element and feed characteristics, the compensation phase of each element is calculated [24]. A full-wave simulation is conducted using CST software. The calculated radiation patterns are plotted in **Figure 8**. In **Figure 9**, the antenna gain at 60 GHz is calculated to be 33.16 dBi with the simulated aperture efficiency of 43.7% [25].

An LPKF ProtoLaser system is employed for the aperture fabrication while the antenna prototype is assembled and tested in an anechoic chamber. The measured radiation patterns and gain are plotted in **Figures 8**, **9**, respectively. The measured gain at 60 GHz is 31.95 dBi with an aperture efficiency of 34.5% while the maximum gain is 33.1 dB at 60.5 GHz with an aperture efficiency of 42.15%. The 3-dB-gain bandwidth is from 58.4 to 61.9 GHz with a relative bandwidth of 5.9%. It is observed in **Figure 8** that the measured main beam almost overlaps with the simulation result. The measured side-lobe levels are below −24.2 dB at E-plane and −22.3 dB at H-plane while the maximum cross-polarization level is -29.1 dB. It is observed that the measured gain is 1.2 dB lower than the simulated one at 60 GHz while the simulated and measured gains are almost equal at 60.5 GHz.

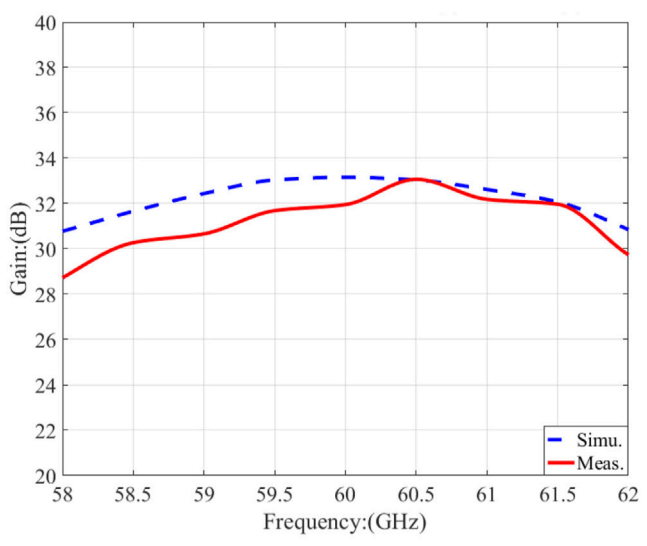

FIGURE 9 | Measured and simulated gains.

There are certain discrepancies between the simulation and measurement results. Firstly, certain elements are not etched precisely. It would introduce additional phase and magnitude errors. Secondly, the tramsmitarray prototype is assembled manually, the assembly errors with the radiation aperture and feeding horn are inevitable. Finally, the antenna is supported by a metallic frame. It would introduce more reflections and refractions, resulting in certain influences on the radiation patterns.

The proposed transmitarray is compared with some existing millimeter-wave designs in **Table 2**. Based on the traditional three-layer frequency-selective structure [9, 10], aperture efficiency of more than 42% has been realized with 3-dB-gain bandwidths of more than 15%. However, they are only suitable for linear-polarized applications with a relatively complex structure. A linearly-polarized dual-layer transmitarray was proposed [11] at 77 GHz with a relatively lower aperture efficiency of 19.3%. A triple-layer transmitarray antenna has been presented at D-band with both linear and circular polarization characteristics [12]. The measured gain is 32 dBi with an aperture efficiency of 32%. To improve the aperture efficiency and to reduce the structural complexity, a double-layer complementary frequency-selective structure is designed in this work. The measured aperture efficiency is improved to be 42.15%, which is close to the triple-layer designs of [9, 10]. Furthermore, the proposed element is suitable for linear and circular polarizations. It can fulfill various requirements and extend its application scenarios.

5 CONCLUSION

A double-layer complementary transmitarray structure is studied at 60 GHz for linear and circular polarizations. Combining the cross and slot-type structure, a double-layer frequency-selective element has been designed with good transmission phase and magnitude performances. The working principle of this complementary structure has been investigated and a prototype has been fabricated for verification. The measured antenna gain is 33.1 dB at 60.5 GHz with an aperture efficiency of 42.15%. The antenna structural complexity and cost have been reduced effectively. With these favorable advantages, this double-layer transmitarray antenna should have broad application prospects in the future.

DATA AVAILABILITY STATEMENT

The raw data supporting the conclusion of this article will be made available by the authors, without undue reservation.

AUTHOR CONTRIBUTIONS

WA prepared the idea and the original manuscript. XZ conducted the simulation and measurement, YL provided the instruction. LX provided and optimized. JW provided the fabrication and final manuscript.

FUNDING

This work was supported in part by National Natural Science Foundation of China (Grant no. 61701339), in part by National Natural Science Foundation of China for Key Project Grant no. 61831017).

REFERENCES

1. Abdelrahman AH, Nayeri P, Elsherbeni AZ, Yang F. Bandwidth Improvement Methods of Transmitarray Antennas. *IEEE Trans Antennas Propagat* (2015) 63(7): 2946–54. doi:10.1109/tap.2015.2423706
2. Aziz A, Yang F, Xu S, Li M. An Efficient Dual-Band Orthogonally Polarized Transmitarray Design Using Three-Dipole Elements. *IEEE Antennas Wireless Propag Lett* (2018) 17(2):1452–7. doi:10.1109/lawp.2017.2788412
3. Rahmati B, Hassani HR. Low-profile Slot Transmitarray Antenna. *IEEE Trans Antennas Propag* (2015) 63(1):178–80. doi:10.1109/tap.2014.2368576
4. Hou Y, Chang L, Li Y, Zhang Z, Feng Z. Linear Multibeam Transmitarray Based on the Sliding Aperture Technique. *IEEE Trans Antennas Propagat* (2018) 66(8): 3948–58. doi:10.1109/tap.2018.2835506
5. Nicholls JG, Hum SV. Full-space Electronic Beam-Steering Transmitarray with Integrated Leaky-Wave Feed. *IEEE Trans Antennas Propag* (2016) 64(4):3410–22. doi:10.1109/tap.2016.2576502
6. Xu K-D, Weng X, Li J, Guo Y-J, Wu R, Cui J, et al. 60-GHz Third-Order On-Chip Bandpass Filter Using GaAs pHEMT Technology. *Semicond Sci Technol* (2022) 2022. doi:10.1088/1361-6641/ac5bf8
7. Xu K-D, Guo Y-J, Liu Y, Deng X, Chen Q, Ma Z. 60-GHz Compact Dual-Mode On-Chip Bandpass Filter Using GaAs Technology. *IEEE Electron Device Lett* (2021) 42(8):1120–3. doi:10.1109/led.2021.3091277
8. Xu K-D, Xia S, Jiang Y, Guo Y-J, Liu Y, Wu R, et al. Compact Millimeter-Wave On-Chip Dual-Band Bandpass Filter in 0.15-μm GaAs Technology. *IEEE J Electron Devices Soc* (2022) 10:152–6. doi:10.1109/jeds.2022.3143999
9. Jouanlanne C, Clemente A, Huchard M, Keignart J, Barbier C, Le Nadan T, et al. Wideband Linearly-Polarized Transmitarray Antenna for 60 GHz Backhauling. *IEEE Trans Antennas Propag* (2017) 65(3):1440–5. doi:10.1109/TAP.2017.2655018
10. Dussopt L, Moknache A, Säily J, Lamminen A, Kaunisto M, Aurinsalo J, et al. A V-Band Switched-Beam Linearly Polarized Transmit-Array Antenna for Wireless Backhaul Applications. *IEEE Trans Antennas Propagat* (2017) 65(12):6788–93. doi:10.1109/tap.2017.2723921
11. Yeap SB, Qing X, Chen ZN. 77-GHz Dual-Layer Transmit-Array for Automotive Radar Applications. *IEEE Trans Antennas Propagat* (2015) 63(6):2833–7. doi:10.1109/tap.2015.2419691
12. Saleh W, Letestu Y, Sauleau R, Cruz EM. Design and Measurements of a High-Performance Wideband Transmitarray Antenna for D-Band Communications. *Antennas Wirel Propag Lett* (2021) 20(9):1765–9. doi:10.1109/lawp.2021.3096743
13. Abdelrahman AH, Elsherbeni AZ, Yang F. Transmission Phase Limit of Multilayer Frequency-Selective Surfaces for Transmitarray Designs. *IEEE Trans Antennas Propagat* (2014) 62(2):690–7. doi:10.1109/tap.2013.2289313
14. An W, Xu S, Yang F, Li M. A Double-Layer Transmitarray Antenna Using Malta Crosses with Vias. *IEEE Trans Antennas Propag* (2016) 64(3): 1120–5. doi:10.1109/TAP.2015.2513427
15. Yang F, An W, Xu S, Li M. Double-layer Planar Phase Modulation Device. U.S. patent no. US10193232B2 (2019).
16. Yi X, Su T, Li X, Wu B, Yang L. A Double-Layer Wideband Transmitarray Antenna Using Two Degrees of freedom Elements Around 20 GHz. *IEEE Trans Antennas Propagat* (2019) 67(4):2798–802. doi:10.1109/tap.2019.2893265
17. Cai M-B, Yan Z-H, Fan F-F, Yang S-Y, Li X. Double-Layer 45° Linearly Polarized Wideband and Highly Efficient Transmitarray Antenna. *IEEE Open J Antennas Propag* (2021) 2:104–9. doi:10.1109/ojap.2020.3046474
18. Yang S, Yan Z, Cai M, Fan F, Zhang T. A High-Efficiency Double-Layer Transmitarray Antenna Using Low-Loss Dual-Linearly Polarized Elements. *Antennas Wirel Propag Lett* (2020) 19(12):2378–82. doi:10.1109/lawp.2020.3033460
19. Hu W, Dong J, Luo Q, Cai Y, Liu X, Wen L, et al. A Wideband Metal-Only Transmitarray with Two-Layer Configuration. *Antennas Wirel Propag Lett* (2021) 20(7):1347–51. doi:10.1109/lawp.2021.3081445
20. Li H, Wang G, Liang J, Gao X, Hou H, Jia X. Single-layer Focusing Gradient Metasurface for Ultrathin Planar Lens Antenna Application. *IEEE Trans Antennas Propag* (2017) 65(3):1452–7. doi:10.1109/TAP.2016.2642832
21. Zhang X, Yang F, Xu S, Aziz A, Li M. Dual-layer Transmitarray Antenna with High Transmission Efficiency. *IEEE Trans Antennas Propagat* (2020) 68(8):6003–12. doi:10.1109/tap.2020.2989555
22. Song L-Z, Qin P-Y, Guo YJ. A High-Efficiency Conformal Transmitarray Antenna Employing Dual-Layer Ultrathin Huygens Element. *IEEE Trans Antennas Propagat* (2021) 69(2):848–58. doi:10.1109/tap.2020.3016157
23. An W, Hong L, Li S. A Double-Layer Transmitarray Element Based on Complementary FSS Structure. In: Proceedings of the 2018 Cross Strait Quad-Regional Radio Science and Wireless Technology Conference; September 2018; Xuzhou, China (2018). p. 1–2.
24. Nayeri P, Elsherbeni AZ, Yang F. Radiation Analysis Approaches for Reflectarray Antennas [Antenna Designer's Notebook]. *IEEE Antennas Propag Mag* (2013) 55(1):127–34. doi:10.1109/map.2013.6474499
25. Yu A, Yang F, Elsherbeni AZ, Huang J, Rahmat-Samii Y. Aperture Efficiency Analysis of Reflectarray Antennas. *Microw Opt Technol Lett* (2010) 52(2):364–72. doi:10.1002/mop.24949

Conflict of Interest: The authors declare that the research was conducted in the absence of any commercial or financial relationships that could be construed as a potential conflict of interest.

Publisher's Note: All claims expressed in this article are solely those of the authors and do not necessarily represent those of their affiliated organizations, or those of the publisher, the editors and the reviewers. Any product that may be evaluated in this article, or claim that may be made by its manufacturer, is not guaranteed or endorsed by the publisher.

frontiers | Frontiers in Physics

ORIGINAL RESEARCH
published: 05 April 2022
doi: 10.3389/fphy.2022.880606

A Dual-Polarized Horn Antenna Covering Full *Ka*-Band Using Turnstile OMT

Jun Xiao[1], *Geer Teni*[2], *Hongmei Li*[3]*, *Tongyu Ding*[1] *and Qiubo Ye*[1]*

[1]School of Ocean Information Engineering, JiMei University, Xiamen, China, [2]Beijing Xibao Electronic Technology Co. Ltd., Beijing, China, [3]Harbin Institute of Technology, Harbin, China

This article presents a dual-polarized corrugated horn antenna incorporated a turnstile orthomode transducer (OMT) covering the full *K*a-band (26.5–40 GHz). A three-stepped cylindrical tuning stub scattering element is designed in the turnstile junction to combine/split the two linearly polarized waves with high isolation. The proposed turnstile OMT shows a good simulated return loss better than 20 dB and a high isolation higher than 57 dB within the whole *K*a-band. Then, a corrugated horn antenna with five-stage choke rings is designed. Finally, the proposed horn antenna incorporated in the turnstile OMT is fabricated and measured. The measured impedance bandwidth for $|S_{11/22}| \leq -15$ dB is 50.7% from 25 to 42 GHz. The measured peak gain is 11.9 dBi. The proposed antenna system is a promising candidate for the 5G millimeter-wave applications.

Keywords: dual-polarized antenna, corrugated horn antenna, orthomode transducer (OMT), turnstile junction, Ka-band

OPEN ACCESS

Edited by:
Kai-Da Xu,
Xi'an Jiaotong University, China

Reviewed by:
Jianjia Yi,
Xi'an Jiaotong University, China
Zihang Qi,
Beijing University of Posts and Telecommunications (BUPT), China

***Correspondence:**
Hongmei Li
lihongmei@hit.edu.cn
Qiubo Ye
qbye@jmu.edu.cn

Specialty section:
This article was submitted to Optics and Photonics, a section of the journal Frontiers in Physics

Received: *21 February 2022*
Accepted: *10 March 2022*
Published: *05 April 2022*

Citation:
Xiao J, Teni G, Li H, Ding T and Ye Q (2022) A Dual-Polarized Horn Antenna Covering Full Ka-Band Using Turnstile OMT. Front. Phys. 10:880606. doi: 10.3389/fphy.2022.880606

INTRODUCTION

Recently, millimeter-wave (MMW) devices such as antennas [1], filters [2], etc., have attracted much attention from researchers. Reflector antennas have been widely utilized in many fields such as radar, radio astronomy, satellite communications due to the advantages of high gain. As a kind of feed source of the MMW reflector antennas, MMW horn antennas have been widely studied [3–5]. Corrugated horn antennas are one of the most popular feed antennas due to their advantages such as low cross-polarization, symmetrical radiation patterns in two orthogonal planes, and low sidelobe level [6–10]. On the other hand, we are faced with challenges in channel capacity limitations in communication systems. Orbital angular momentum (OAM) [11, 12] and dual-polarization [13] technologies have been proposed to increase the communication capacity. To realize dual-polarized horn antennas, dual-polarized quad-ridged horn antennas or linearly polarized horn antennas integrated with an orthomode transducer (OMT) have been reported. However, the quad-ridged horn antennas have the disadvantages such as high cross-polarization levels and unsymmetrical radiation patterns [14–16]. The OMT can combine or split the waves with two orthogonal polarizations simultaneously. In general, a three-port OMT is made up of a common port and two independent ports with high isolation between each other. Boifot OMT [17–20] and turnstile junction OMT [21–25] are the two kinds of widely used OMTs with wideband characteristics. Compared with the Boifot OMTs, the turnstile junction OMTs can achieve wide impedance bandwidth without pins or septums.

In this article, a dual-polarized corrugated horn antenna using turnstile OMT operating within 24–42 GHz is presented. The turnstile OMT can realize dual-linear polarization and provide high isolation. A corrugated horn antenna with five-stage choke rings is designed as the radiator. The

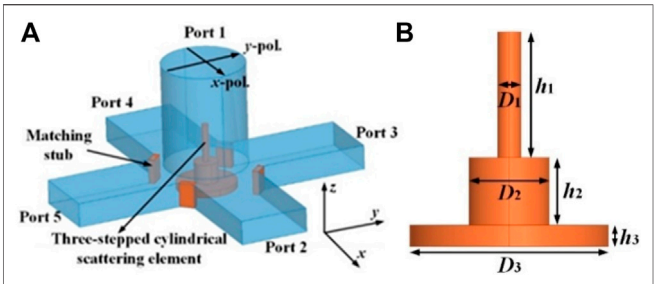

FIGURE 1 | Geometry of turnstile junction. **(A)** Internal view. **(B)** Three-stepped cylindrical scattering element.

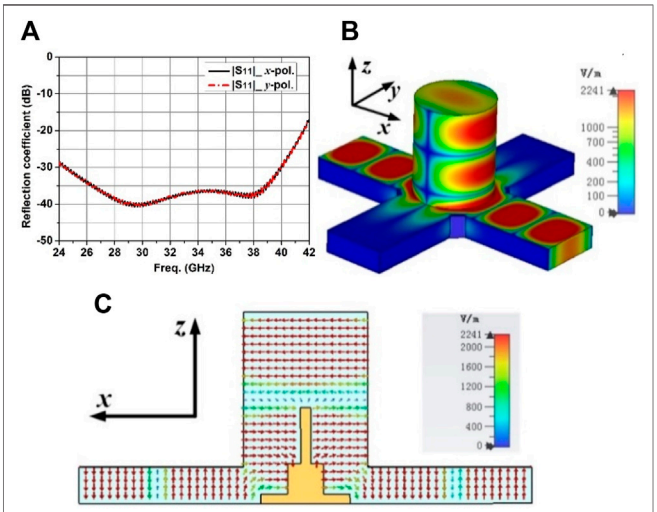

FIGURE 2 | Simulated results of the proposed turnstile junction. **(A)** Reflection coefficient. **(B)** *E*-field distribution in the turnstile junction at 35 GHz. **(C)** Section view of the *E*-field distribution (35 GHz) inside the turnstile junction.

fabricated horn antenna incorporated a turnstile OMT exhibits a 50.7% measured −15 dB impedance bandwidth and an 11.9 dBi measured maximum gain. The measured isolations between the two orthogonal polarizations are lower than -40 dB within the bandwidth.

ANTENNA DESIGN

Orthomode Transducer Design

As a key component of the turnstile OMT, the turnstile junction is designed first. The internal view of the proposed turnstile junction is shown in **Figure 1**. The turnstile junction is made up of a circular waveguide (port 1), a three-stepped cylindrical tuning stub, and four rectangular waveguide outputs (ports 2–5). The input waves with two orthogonal polarization directions from port 1 can be separated into two linearly polarized waves. The design of the scattering element is critical to the overall performance of the turnstile junction. A four-stepped cylindrical tuning stub has been designed in a turnstile junction achieving 40% bandwidth (10–15 GHz) [21]. According to [21], the impedance bandwidth

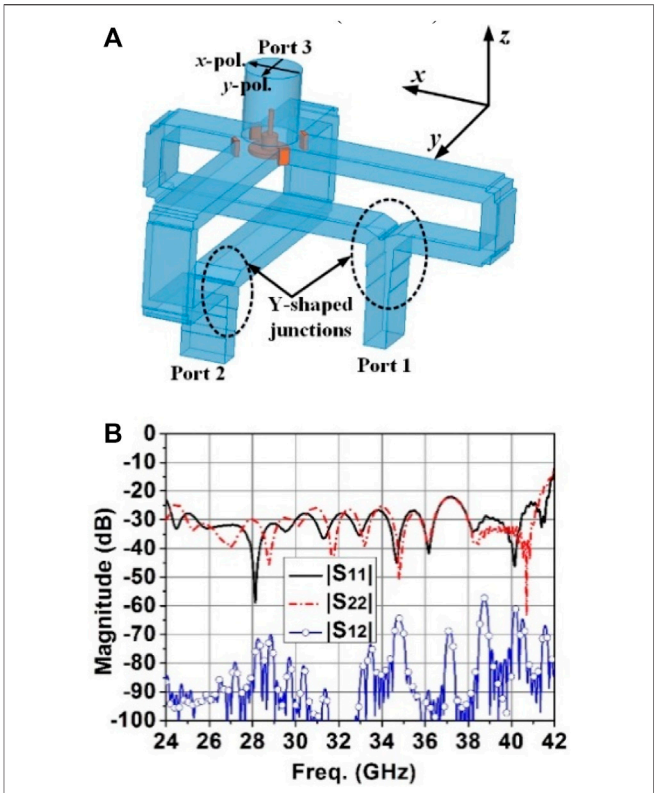

FIGURE 3 | (A) Internal view of the turnstile OMT. **(B)** Simulated results of the turnstile OMT.

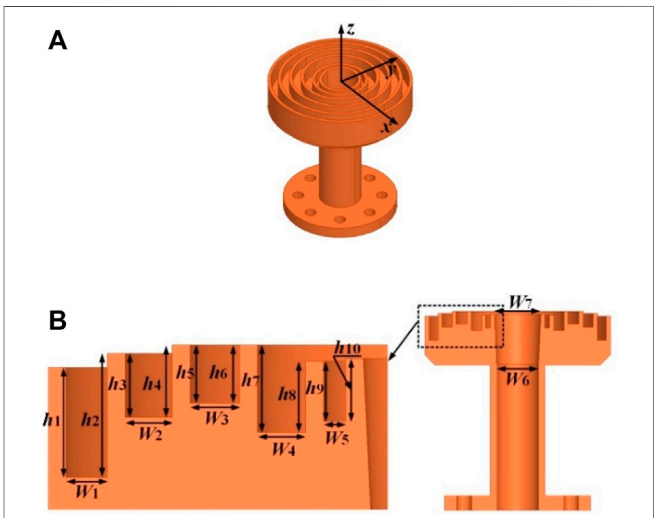

FIGURE 4 | Simulation model of the proposed corrugated horn antenna. **(A)** 3-D view. **(B)** Section view.

of a turnstile junction can be increased by increasing the number of steps of the multi-stepped cylindrical scattering element. However, the larger the number of steps, the larger the volume of the turnstile OMT. Moreover, the top metallic cylinder tends to be thinner

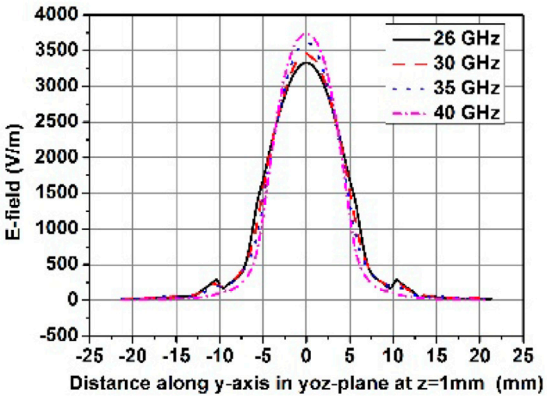

FIGURE 5 | Simulated electric field distributions in *yoz*-plane at $z = 1$ mm for different frequencies.

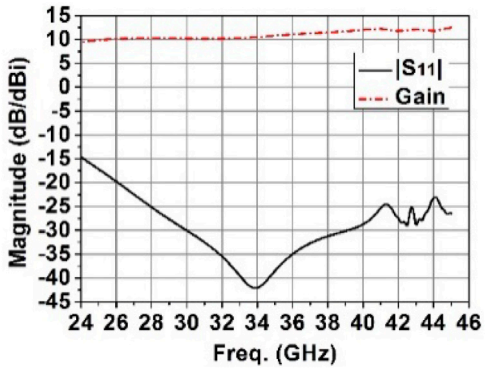

FIGURE 6 | Simulated results of the proposed corrugated horn antenna.

when the number of steps increases, which may cause larger mechanical errors, especially at millimeter-wave frequency bands. Then, a tradeoff is made between the impedance bandwidth and the number of the steps: a three-stepped cylindrical tuning stub is adopted as the scattering element. Four rectangular stubs are placed in the four corners to improve impedance matching. The detailed dimensions of the three-stepped cylindrical tuning stub are as follows (in mm): D_1 = 0.73, D_2 = 2.5, D_3 = 6.2, h_1 = 3.9, h_2 = 2.1, h_3 = 0.65.

The simulated results of the turnstile junction are shown in **Figure 2**. The two $|S_{11}|$ curves related to two orthogonal polarization directions are almost the same with each other. They are both almost lower than −20 dB within the bandwidth from 24 to 42 GHz. As shown in **Figure 2B**, the *E*-field distributions simulated results indicate that good isolation has been achieved between two input waves with two orthogonal directions, respectively. **Figure 2C** shows how the TE_{11} mode input wave in the circular waveguide is converted to two ways of TE_{10} mode wave.

Based on the above design, a turnstile OMT is designed, as shown in **Figure 3**. The proposed turnstile OMT includes a turnstile junction, two *Y*-shaped junctions, a common circular waveguide port (port 3), and two rectangular waveguide ports (port 1 and port 2, respectively). Thanks to the scattering element of turnstile junction, or the three-stepped cylindrical tuning stub, the wave from port 3 with two orthogonal polarization directions can be separated into two linearly polarized waves, which are sent to port 1 and port 2, respectively. Waves separated by the turnstile junction will be routed through 180° *E*-plane two-stepped bends. Then, power combinations will be carried out through the *Y*-shaped junctions. The simulated results of the proposed OMT are shown in **Figure 3B**. The simulated $|S_{11}|$ and $|S_{22}|$ are both lower than −20 dB within the bandwidth from 24 to 41.6 GHz.

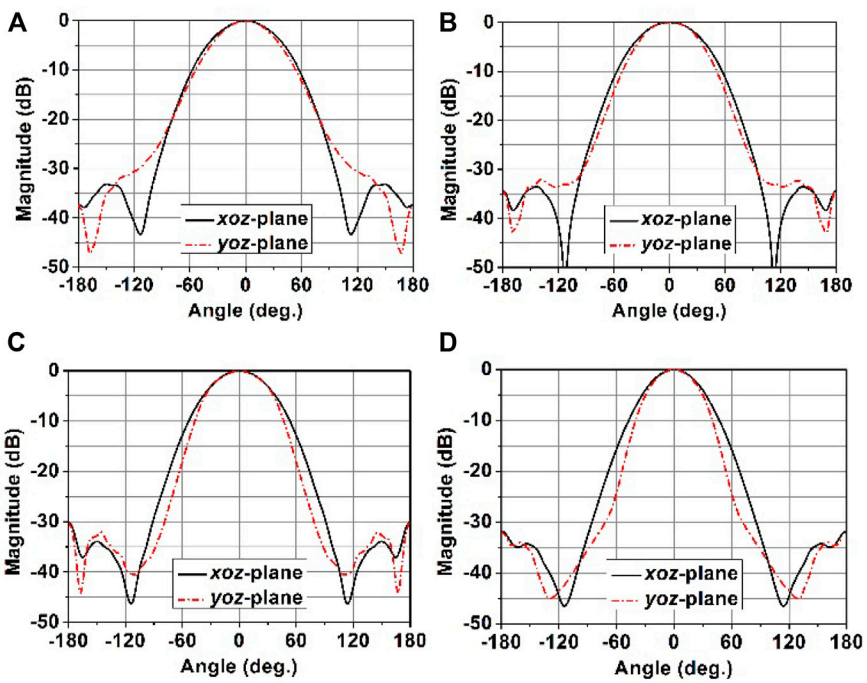

FIGURE 7 | Simulated radiation patterns of the proposed corrugated horn antenna element at **(A)** 26 GHz. **(B)** 30 GHz. **(C)** 35 GHz. **(D)** 40 GHz.

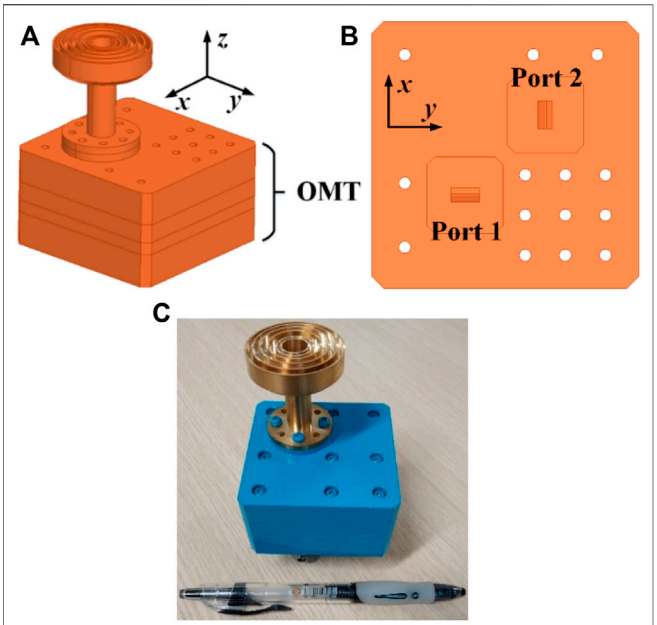

FIGURE 8 | Photographs of **(A)** Co-simulation model of the OMT and horn antenna. **(B)** Bottom view of the OMT. **(C)** Fabricated dual polarized horn antenna with OMT.

The proposed design shows high isolation between ports 1 and 2. The simulated $|S_{21}|$ is lower than −57 dB within the bandwidth from 24 to 42 GHz.

Corrugated Horn Design

The proposed choke ring horn antenna is shown in **Figure 4**. The five-stage choke rings are fed by a circular waveguide which is excited by dominant TE_{11} mode waves. According to the waveguide theory, TE_{mn} and TM_{mn} mode waves will be excited in the choke rings. The depth of each choke should be λ/4 to λ/2 to get equal beam widths, low cross-polarization levels, and low back radiation. To attain broadband impedance and radiation pattern bandwidths covering 26–40 GHz, the five chokes are designed and optimized as different depths. The detailed dimensions of the choke ring horn antenna are as follows (in mm): $h_1 = 4.97$, $h_2 = 5.59$, $h_3 = 2.87$, $h_4 = 3.26$, $h_5 = 2.61$, $h_6 = 2.61$, $h_7 = 3.95$, $h_8 = 3.2$, $h_9 = 2.71$, $h_{10} = 2.84$. $W_1 = 1.87$, $W_2 = 2.14$, $W_3 = 2.26$, $W_4 = 2.18$, $W_5 = 1$, $W_6 = 8.6$, $W_7 = 9.6$.

Under these conditions, the electric fields over the radiation aperture will decay along the radius axial direction. The simulated electric field distributions in *yoz*-plane at $z = 1$ mm for different frequencies are shown in **Figure 5**. It is observed that the *E*-fields are similar to Gaussian distribution which leads to rotationally symmetric radiation patterns. The simulated results of the proposed choke ring horn antenna are shown in **Figures 6**, **7**. The $|S_{11}|$ is less than −15 dB in 26–40 GHz frequency band. The maximum gain is 12.5 dBi. Good rotationally symmetric radiation patterns have been observed within the bandwidth.

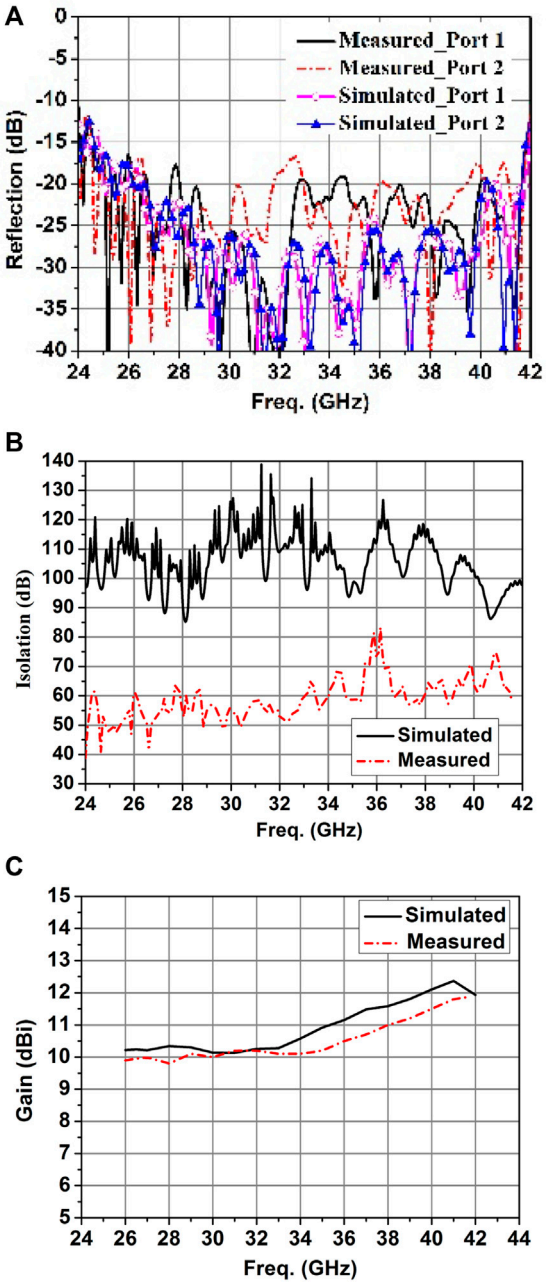

FIGURE 9 | Simulated and measured results of the dual-polarized corrugated horn antenna with OMT. **(A)** Reflection coefficient. **(B)** Isolation. **(C)** Gain.

EXPERIMENTAL VALIDATION AND DISCUSSION

Based on the designs presented above, the co-simulations of the OMT and choke ring horn antenna are carried out. The simulated model is shown in **Figure 8A**. Then, an OMT and a horn antenna are fabricated separately. The OMT is incorporated into a box-type flange. The fabricated dual-polarized antenna system after assembly is shown in

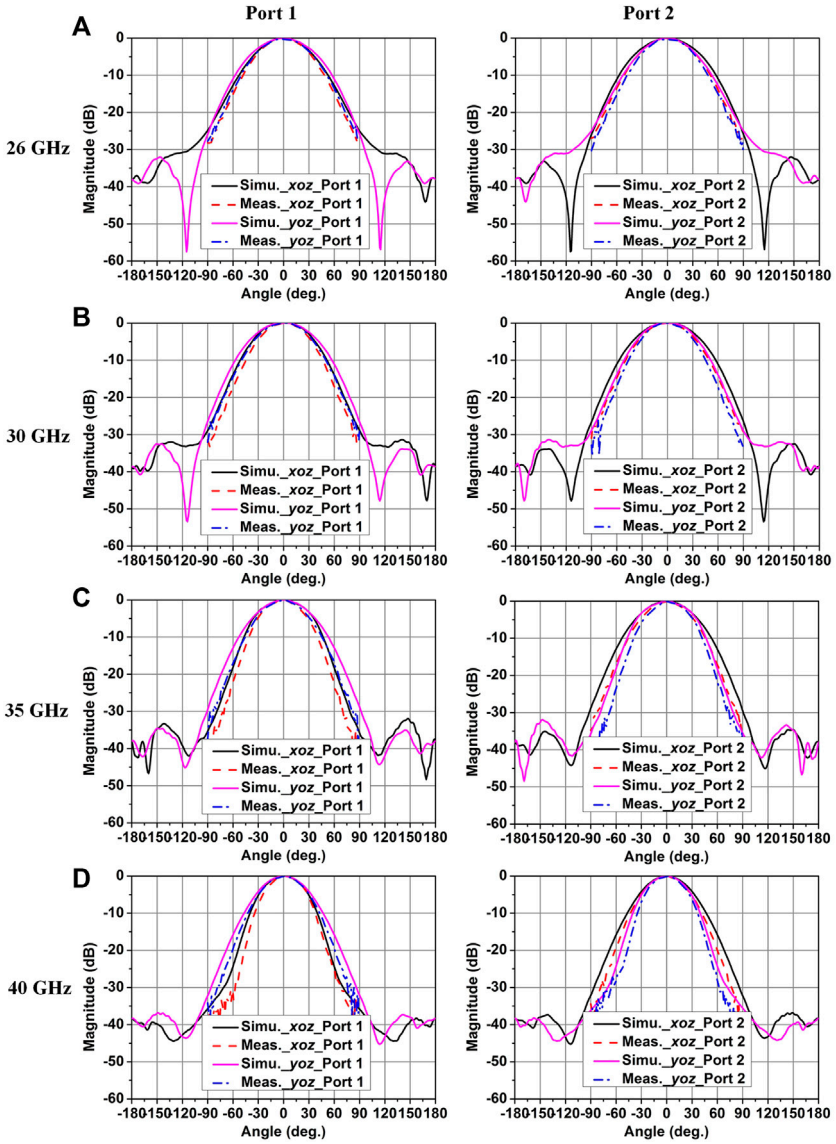

FIGURE 10 | Simulated and measured radiation patterns of the dual-polarized horn antenna with OMT at **(A)** 26 GHz. **(B)** 30 GHz. **(C)** 35 GHz. **(D)** 40 GHz.

Figure 8C. The measured results of port matching and port isolation are shown in **Figure 9**. The measured −15 dB impedance bandwidths ($|S_{11/22}| \leq -15$ dB) are both 50.7% covering from 25 to 42 GHz at two ports, respectively. The simulated and measured isolations between two ports are larger than 85 and 40 dB within the bandwidth of 25–42 GHz, respectively. The measured maximum gain is 11.9 dBi at 42 GHz while the simulated one is 12.4 dBi at 41 GHz. The measured gains are all larger than 9.9 dBi within the bandwidth. The measured radiation efficiency can be calculated by comparing the simulated directivity and the measured gain. Then the measured radiation efficiency of the horn antenna (with OMT) is 90.2% at 36 GHz. The measured aperture efficiency is 78.6% at 36 GHz. The simulated and measured radiation patterns for port 1 at frequencies of 26, 30, 35, and 40 GHz are presented in **Figure 10**. Due to the measurement limitation, the measured radiation patterns with low sidelobe levels are presented from −90° to 90°. The simulated and measured results agree well within the bandwidth. Almost equal 3-dB beamwidths have been achieved between two planes within the bandwidth.

CONCLUSION

A broadband dual-polarized corrugated horn antenna incorporated a turnstile orthomode transducer (OMT) has been presented and verified at *K*a-band (26.5–40 GHz). A turnstile OMT is designed to achieve dual polarization with high isolation. A broadband linearly polarized corrugated horn

antenna is designed with five-stage choke rings achieving stable and symmetric radiation patterns within the bandwidth. The antenna system including the turnstile OMT and corrugated horn antenna shows a 50.7% −15 dB impedance bandwidth at two input ports, respectively. The proposed dual-polarized antenna system is a promising candidate for future 5G applications.

DATA AVAILABILITY STATEMENT

The original contributions presented in the study are included in the article/Supplementary Material, further inquiries can be directed to the corresponding authors.

AUTHOR CONTRIBUTIONS

JX: Conceptualization, data curation, formal analysis, funding acquisition, investigation, methodology, project administration, resources, software, supervision, validation, visualization, writing—original draft, writing—review and editing. GT: Conceptualization, formal analysis, investigation, methodology, writing—review and editing. HL: Conceptualization, formal analysis, funding acquisition, investigation, software, writing—review and editing. TD: Conceptualization, investigation, writing—review and editing. QY: Conceptualization, formal analysis, funding acquisition, investigation, methodology, project administration, resources, supervision, writing—review and editing.

FUNDING

This work was supported in part by the Natural Science Foundation of Fujian Province under Grant 2020J05149, Project JAT190298 through the Education Department of Fujian Province, and also supported in part by the National Natural Science Foundation of China under Grant 62071152.

REFERENCES

1. Olk AE, Liu M, Powell DA. Printed Tapered Leaky-Wave Antennas for W-Band Frequencies. *IEEE Trans Antennas Propagat* (2022) 70(2):900–10. doi:10.1109/tap.2021.3111291
2. Xu K-D, Xia S, Jiang Y, Guo Y-J, Liu Y, Wu R, et al. Compact Millimeter-Wave On-Chip Dual-Band Bandpass Filter in 0.15-μm GaAs Technology. *IEEE J Electron Devices Soc* (2022) 10:152–6. doi:10.1109/jeds.2022.3143999
3. Al-Tarifi MA, Filipovic DS. On the Design and Fabrication of W-Band Stabilised-Pattern Dual-Polarised Horn Antennas with DMLS and CNC. *IET Microw Antennas Propag* (2017) 11:1930–5.
4. Zhang L, He W, Donaldson CR, Smith GM, Robertson DA, Hunter RI, et al. Optimization and Measurement of a Smoothly Profiled Horn for a W-Band Gyro-TWA. *IEEE Trans Electron Devices* (2017) 64(6):2665–9. doi:10.1109/ted.2017.2687949
5. Montofré DA, Molina R, Khudchenko A, Hesper R, Baryshev AM, Reyes N, et al. High-Performance Smooth-Walled Horn Antennas for THz Frequency Range: Design and Evaluation. *IEEE Trans Thz Sci Technol* (2019) 9(6):587–97. doi:10.1109/tthz.2019.2938985
6. McKay JE, Robertson DA, Speirs PJ, Hunter RI, Wylde RJ, Smith GM. Compact Corrugated Feedhorns with High Gaussian Coupling Efficiency and $-60\;\text{dB}$ Sidelobes. *IEEE Trans Antennas Propagat* (2016) 64(6):2518–22. doi:10.1109/tap.2016.2543799
7. Sekiguchi S, Sugimoto M, Shu S, Sekimoto Y, Mitsui K, Nishino T, et al. Broadband Corrugated Horn Array with Direct Machined Fabrication. *IEEE Trans Thz Sci Technol* (2017) 7(1):36–41. doi:10.1109/TTHZ.2016.2634321
8. Gonzalez A, Kaneko K, Kojima T, Asayama S, Uzawa Y. Terahertz Corrugated Horns (1.25-- 1.57 THz): Design, Gaussian Modeling, and Measurements. *IEEE Trans Thz Sci Technol* (2017) 7(1):42–52. doi:10.1109/tthz.2017.2758789
9. Agnihotri I, Sharma SK. Design of a 3D Metal Printed Axial Corrugated Horn Antenna Covering Full Ka-Band. *Antennas Wirel Propag Lett* (2020) 19(4):522–6. doi:10.1109/lawp.2020.2967996
10. Qi J-R, Dang Y, Zhang P-Y, Chou H-T, Ju H-S. Dual-Band Circular-Polarization Horn Antenna with Completely Inhomogeneous Corrugations. *Antennas Wirel Propag Lett* (2020) 19(5):751–5. doi:10.1109/lawp.2020.2978878
11. Feng R, Ratni B, Yi J, Zhang H, de Lustrac A, Burokur SN. Versatile Metasurface Platform for Electromagnetic Wave Tailoring. *Photon Res* (2021) 9:1650–9. doi:10.1364/prj.428853
12. Lin M, Liu C, Yi J, Jiang ZH, Chen X, Xu HX, et al. Chirality-intrigged Spin-Selective Metasurface and Applications in Generating Orbital Angular Momentum. *IEEE Trans Antennas Propag., Early Access* (2022). doi:10.1109/tap.2022.3140491
13. Li J, Hu P, Chen J, Xu K-D, Mao C-X, Zhang XY. Dual-polarized Duplex Base-Station Antenna with a Duplexer-Integrated Balun. *Antennas Wirel Propag Lett* (2022) 21(2):317–21. doi:10.1109/lawp.2021.3130032
14. Jacobs OB, Odendaal JW, Joubert J. Quad-Ridge Horn Antenna with Elliptically Shaped Sidewalls. *IEEE Trans Antennas Propagat* (2013) 61(6):2948–55. doi:10.1109/tap.2013.2254436
15. Manafi S, Al-Tarifi M, Filipovic DS. 45-110 GHz Quad-Ridge Horn with Stable Gain and Symmetric Beam. *IEEE Trans Antennas Propagat* (2017) 65(9):4858–63. doi:10.1109/tap.2017.2724069
16. Flygare J, Pantaleev M. Dielectrically Loaded Quad-Ridge Flared Horn for Beamwidth Control over Decade Bandwidth-Optimization, Manufacture, and Measurement. *IEEE Trans Antennas Propagat* (2020) 68(1):207–16. doi:10.1109/tap.2019.2940529
17. Bøifot A, Lier E, Schaug-Pettersen T. Simple and Broadband Orthomode Transducer. *IEE Proc H (Microwaves, Antennas Propagation)* (1990) 137:396–400.
18. Asayama Si., Kamikura M. Development of Double-Ridged Waveguide Orthomode Transducer for the 2 MM Band. *J Infrared Milli Terahz Waves* (2009) 30:573–9. doi:10.1007/s10762-009-9475-9
19. Navarrini A, Nesti R. Symmetric Reverse-Coupling Waveguide Orthomode Transducer for the 3-mm Band. *IEEE Trans Microwave Theor Techn.* (2009) 57(1):80–8. doi:10.1109/tmtt.2008.2008943
20. Leal-Sevillano CA, Reck TJ, Chattopadhyay G, Ruiz-Cruz JA, Montejo-Garai JR, Rebollar JM. Development of a Wideband Compact Orthomode Transducer for the 180-270 GHz Band. *IEEE Trans Thz Sci Technol* (2014) 4(5):634–6. doi:10.1109/tthz.2014.2336540
21. Tribak A, Cano JL, Mediavilla A, Boussouis M. Octave Bandwidth Compact Turnstile-Based Orthomode Transducer. *IEEE Microw Wireless Compon Lett* (2010) 20(10):539–41. doi:10.1109/lmwc.2010.2060261
22. Henke D, Claude S. Minimizing RF Performance Spikes in a Cryogenic Orthomode Transducer (OMT). *IEEE Trans Microwave Theor Techn.* (2014) 62(4):840–50. doi:10.1109/tmtt.2014.2309551
23. Cano JL, Mediavilla A. Quasi-Octave Bandwidth In-phase Three-Layer Platelet Orthomode Transducer Using Improved Power Combiners. *IEEE Microw Wireless Compon Lett* (2018) 28(12):1086–8. doi:10.1109/lmwc.2018.2874160
24. Gomez-Torrent A, Shah U, Oberhammer J. Compact Silicon-Micromachined Wideband 220-330-GHz Turnstile Orthomode Transducer. *IEEE Trans Thz Sci Technol* (2019) 9(1):38–46. doi:10.1109/tthz.2018.2882745
25. Shen J, Ricketts DS. Compact W-Band "Swan Neck" Turnstile Junction Orthomode Transducer Implemented by 3-D Printing. *IEEE Trans Microwave Theor Techn.* (2020) 68(8):3408–17. doi:10.1109/tmtt.2020.2992065

Conflict of Interest: GT was employed by the company Beijing Xibao Electronic Technology Co. Ltd.

The remaining authors declare that the research was conducted in the absence of any commercial or financial relationships that could be construed as a potential conflict of interest.

Publisher's Note: All claims expressed in this article are solely those of the authors and do not necessarily represent those of their affiliated organizations, or those of the publisher, the editors and the reviewers. Any product that may be evaluated in this article, or claim that may be made by its manufacturer, is not guaranteed or endorsed by the publisher.

frontiers | Frontiers in Physics

BRIEF RESEARCH REPORT
published: 27 April 2022
doi: 10.3389/fphy.2022.890356

Highly Efficient Metasurface Polarization Converter at Far-Infrared Range

Ahmed Mahfuz Tamim[1], *Md Mehedi Hasan*[2] *and Mohammad Rashed Iqbal Faruque*[1]*

[1]Space Science Centre (ANGKASA), Universiti Kebangsaan Malaysia, Bangi, Malaysia, [2]Research School of Electrical, Energy, and Materials Engineering, College of Engineering and Computer Science (CECS), The Australian National University, Canberra, ACT, Australia

Controlling the polarization state is an efficient way to enhance the functionalities in sensing, imaging, and communication systems in the microwave and terahertz (THz) spectrum. This study proposed an anisotropic metasurface and numerically explained it as a highly efficient polarization conversion using far-infrared frequency. Structural design, optimization, and results examination of the metasurface are performed using the CST microwave studio electromagnetic simulator. The metasurface was developed surrounding the two individual arrow-shaped metal resonators with two bar resonators on the opposite angular side of the arrow. Aluminum (Al) was used as a metallic resonator, while gallium arsenide (GaAs) was as the substrate. The interference theory was used to describe the co-polarized and cross-polarized reflectance coefficients, where two different mediums and interference layers were considered along with the reflected and transmitted wave. The polarization conversion efficiency yielded over 90% from 282.9 to 302.3 μm (0.987–1.062 THz) and 558.78 to 676.7 μm (0.442–0.537 THz) indicating multiple resonances at 286.7, 298.25, 586.1, and 689.55 μm. In conclusion, the performances and diverse characteristics of the designed metasurface demonstrated potential applications in the far-infrared spectrum as an efficient polarization converter application.

Keywords: metasurface, polarization conversion, terahertz, x-polarized, y-polarized

OPEN ACCESS

Edited by:
Kai-Da Xu,
Xi'an Jiaotong University, China

Reviewed by:
Jie Li,
Tianjin University, China
Ben-Xin Wang,
Jiangnan University, China
Yongzhi Cheng,
Wuhan University of Science and Technology, China
Xiang Wan,
Southeast University, China

***Correspondence:**
Mohammad Rashed Iqbal Faruque
rashed@ukm.edu.my

Specialty section:
This article was submitted to Optics and Photonics, a section of the journal Frontiers in Physics

Received: *05 March 2022*
Accepted: *25 March 2022*
Published: *27 April 2022*

Citation:
Tamim AM, Hasan MM and Faruque MRI (2022) Highly Efficient Metasurface Polarization Converter at Far-Infrared Range. Front. Phys. 10:890356. doi: 10.3389/fphy.2022.890356

INTRODUCTION

The development of metasurfaces has attracted significant attention among researchers as they possess unusual properties that could be useful in artificial composite structures and future innovations for its lightweight, simplified structure, and easy integration with other devices [1]. Comparatively, natural materials do not possess such characteristics. Although microwave and terahertz (THz) metamaterials have a wide range of applications [2–6], 3D metamaterials frequently suffer from drawbacks such as narrow bandwidth, low efficiency, and bulky size [7]. The superior polarization manipulation capabilities of a 2D metasurface, on the other hand, overcome these constraints [8]. Polarization is an essential characteristic in the field of electromagnetic waves, as it plays a fundamental role in many communication systems (antenna, satellite, optical fiber, etc.), contrast imaging microscopy, optical sensing, molecular biotechnology, and controlling, by manipulating the polarization states of electromagnetic waves. Thus, achieving arbitrary control of electromagnetic wave polarization state remains a key problem in microwave and TH) engineering. Some are always being used, such as the optical action of crystals, the Faraday effect, gases, or solutions of chiral molecules (e.g., sugars), helical secondary structure proteins,

and chiral liquid crystals [9]. The major drawbacks of these methods are that they result in bulky volumes, narrow bandwidth, and an incidence-angle-dependent response that limits their use in practical applications [10, 11]. Hence, metasurfaces are being emphasized to overcome these limitations due to their light profile nature, polarization-insensitiveness, and higher efficiency [12, 13]. Metasurfaces are widely used in beam splitting [14], radar cross-section reduction [15], flat lensing [16], real-time holograms [17], absorbers [18], etc. Additionally, the miniaturized polarization converters and various metasurface design schemes were proposed to extend the operating bandwidth or realize multiband and multiple resonances to enhance its practical applicability [19, 20]. Feng et al. developed a polarization rotator using a high impedance surface (HIS) over polarization conversion ratio (PCR) efficiency of 56% from 2 to 3.5 GHz. Their geometrical structure of 20.2 × 18.2 mm^2 was comparatively bigger in terms of only 56% efficiency [21]. Chen et al. developed a polarization conversion metasurface using an arrow-type resonator structure in a microwave where the bandwidth was enhanced through the generation of electric and magnetic resonances [22]. Zhang et al. designed a metasurface with a metallic oval ring resonator with a PCR of 68.6% between 8 and 18 GHz [23]. Meanwhile, the Flame Retardant-4 (FR4) is a highly lossy substrate over 10 GHz in the real-life experiment. The dielectric value changes with increasing frequency, hence resulting in deviations from the simulated results.

Several researchers proposed and developed reflectance-based metasurface for polarization conversion. Cheng et al. proposed a dual-band asymmetric transmission-based multi-layered anisotropic metamaterial working from 0.1 to 0.9 THz [24]. Jiang et al. investigated a reflective linear to circular polarization converter. The unit cell was made of multiple phosphorene layers over a dielectric layer and a gold mirror [25]. At the same time, Zhu et al. proposed a sinusoidally structured graphene-based metasurface that can be tuned using the Fermi energies of the graphene. The metasurface presented polarization conversion from 1.28 to 2.13 THz with a PCR over 85% [26]. Wen et al. developed a polyimide dielectric substrate base metasurface where gold was used as the metasurface resonator array. They claimed a near-unity efficiency from 0.44 to 0.76 THz [27]. On the other hand, Cheng et al. proposed a bilayer chiral metamaterial for linear to circular polarization where incident x-polarized light propagated on the back surface, while y-polarized light was emitted at a frequency range of 2.19–2.147 THz [28]. Ako et al. developed a tri-layered linear polarization converter utilizing the cyclin olefin copolymer (dielectric medium) and gold as a resonator pattern that works between 0.22 and 1.02 THz frequency range with over 80% conversion efficiency [29]. Due to the high demand for THz applications, more investigations are being conducted to develop a polarization converter with higher conversion performance and wider bandwidth in the microwave and THz frequency spectrum [30–32]. In recent years, THz wavefront modulation research is gaining much interest among researchers [33, 34], and THz technology has penetrated the field of biomedical applications such as microfluidic biosensors [35], DNA characterization [36], protein synthesis [37], diagnosis of cancer tissues [38], imaging [39], etc. Thus, a metasurface with highly efficient polarization conversion is still in demand. Research is ongoing to develop a highly efficient metasurface that is of low cost and can be produced using available conventional materials to make a compact-sized single-layered structure for easy fabrication.

This study aimed to design a metasurface structure with significant bandwidth and high polarization conversion efficiency. To serve this purpose, an anisotropic metasurface with a size of 120 × 120 μm^2 was designed and numerically demonstrated from 0.3 to 1.2 THz. Aluminum (Al) was used as a metallic resonator (front and ground), while gallium arsenide (GaAs) was used as a substrate medium. The metasurface yielded a cross-polarization conversion efficiency of up to 90% from 282.9 to 302.3 μm (0.987–1.062 THz) and 558.78–676.7 μm (0.442–0.537 THz) with multiple resonance frequencies at 286.7 μm (1.046 THz), 298.25 μm (1.0055 THz), 586.1 μm (0.5115 THz), and 689.55 μm (0.4554 THz). The single-layered structure makes the design more compact to be used in the THz regime. Thus, the metasurface device is highly suitable for the applications of THz detectors, sensing, biomedical imaging, and potential THz-based devices. A meta lens-based holographic imaging system using the polarization conversion metasurface is one kind of illustration to show the image of the object at suitable distances [40].

METASURFACE DESIGN

The metasurface was designed following a series of optimization to yield better results. The final metasurface structure was designed using two individual arrow-shaped metal resonators surrounded by two bar resonators on the opposite angular sides of the arrow (**Figure 1**). The overall size of the metasurface was 120 × 120 μm^2 with aluminum (Al) as a metallic element (thickness = 11 μm and conductivity = 3.56 × 107 S/m). The Al layers were etched on the front and back of the Gallium Arsenide (GaAs) substrate. The GaAs have a relative permittivity of 12.94 and a loss tangent of 0.0004. The GaAs substrate has some distinct advantages such as higher efficiency, heat and moisture resistance, superior flexibility, etc. In addition, electrons travel faster through its crystalline structure than through silicon. Both the dielectric and metallic lossy mediums were used to ensure the outcomes would match the actual prototype. Inductance (L) was produced by the metal strips of the resonators, whereas capacitance (C) from the splits or gaps of the resonators. The coupling of the inductance and capacitance helps to create resonance frequency. Thus, the resonance frequency comes from [41],

$$f = \frac{1}{2\pi\sqrt{LC}}.$$

The optimized dimensions were A_1 = 61.05 μm, A_2 = 68.45 μm, G_1 = 7.85 μm, G_2 = 7.15 μm, G_3 = 2.2 μm, Ws =

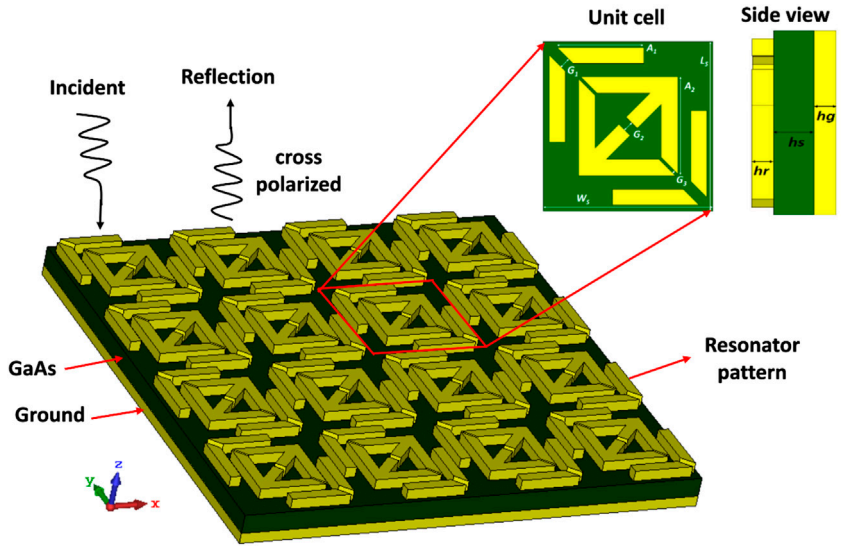

FIGURE 1 | Schematic prototype of the proposed metasurface polarization converter with the front and side views of the unit cell in the inset figure. The dark green and yellow parts represent GaAs and Al, respectively.

120 μm, and Ls = 120 μm; the thickness of GaAs was 20 μm (hs), while the thickness of the metallic resonator was 11 μm (hr, hg).

THEORETICAL ANALYSIS AND SIMULATION METHODOLOGY

Interference theory [42] clarifies the co-polarized and cross-polarized reflectance coefficients. Interference theory can be applied when there is an interface between the metallic resonators and the dielectric substrate medium. The theory for the proposed metasurface polarization converter is depicted in **Figure 2A**. When a y-polarized wave is an incident on interface layer 1, then the polarized wave is transmitted to medium 2 from medium 1. However, some portion of the wave is reflected in medium 1. Since interface layer 1 is the interconnection of the metallic resonator and dielectric medium, it functions as a polarization converter. Thus, the transmitted and reflected waves will yield two components, y to y and y to x components denoting y-polarized and x-polarized waves, respectively. As the second interface layer 2 is grounded, it also serves as an interface layer of the metallic resonator and dielectric medium. Thus, when the transmitted wave is incident, some components will be reflected in the same medium 2 with negative unity, i.e., $r_{23} = -1$. The reflected waves will propagate in medium 2 in a backward direction. When they are incident on interface layer 1, some portion of the waves will be transmitted to medium 1 and some will be reflected into medium 2. Thus, the reflected portions between interface layers 1 and 2 will undergo multiple reflectances and multiple transmissions to medium 2. The reflected (r_{yy}, r_{xy}) and transmitted (t_{yy}, t_{xy}) portions of the waves contain co-polarized and cross-polarized components of both x-polarized and y-polarized waves. Hence, the reflectance coefficient for the y to y is

$$R_{yy} = r_{yy12} + \frac{t_{yy12}\, t_{yy21}\, e^{-j2\psi}}{1 + r_{yy21}\, e^{-j2\psi}} - \frac{t_{xy12}\, t_{yx21}\, e^{-j2\psi}}{1 + r_{xx21}\, e^{-j2\psi}} + \ldots \quad (1)$$

and the reflectance co-efficient for y to x is

$$R_{xy} = r_{xy12} + \frac{t_{yy12}\, t_{xy21}\, e^{-j2\psi}}{1 + r_{yy21}\, e^{-j2\psi}} - \frac{t_{xy12}\, t_{xx21}\, e^{-j2\psi}}{1 + r_{xx21}\, e^{-j2\psi}} + \ldots \quad (2)$$

Similarly, the same occurs when an x-polarized wave incident on interface layer 1. For the x-polarized wave, the reflectance coefficient for x to x is

$$R_{xx} = r_{xx12} + \frac{t_{xx12}\, t_{xx21}\, e^{-j2\psi}}{1 + r_{xx21}\, e^{-j2\psi}} - \frac{t_{yx12}\, t_{xy21}\, e^{-j2\psi}}{1 + r_{yy21}\, e^{-j2\psi}} + \ldots \quad (3)$$

and the reflectance co-efficient for x to y is

$$R_{yx} = r_{yx12} + \frac{t_{xx12}\, t_{yx21}\, e^{-j2\psi}}{1 + r_{xx21}\, e^{-j2\psi}} - \frac{t_{yx12}\, t_{yy21}\, e^{-j2\psi}}{1 + r_{yy21}\, e^{-j2\psi}} + \ldots \quad (4)$$

Equations (1)–(4) were simplified for the clarification of the model where higher-order multiple reflected components are neglected [43, 44]. The terms (r_{yy12}, r_{xx12}) and (r_{xy12}, r_{yx12}) refer to the co-polarized reflectance coefficient and cross-polarized reflectance coefficient exhibited from the metasurface array resonator, respectively. The other terms represent the reflectance that was produced through the superposition of multiple reflectances between interface layers 1 and 2. When destructive interferences occur continuously in the co-polarized reflectance and other multiple reflectances, the reflectance for y to y and x to x becomes so small, i.e., R_{yy}, $R_{xx} = 0$. Therefore, this phenomenon successfully achieved polarization conversation.

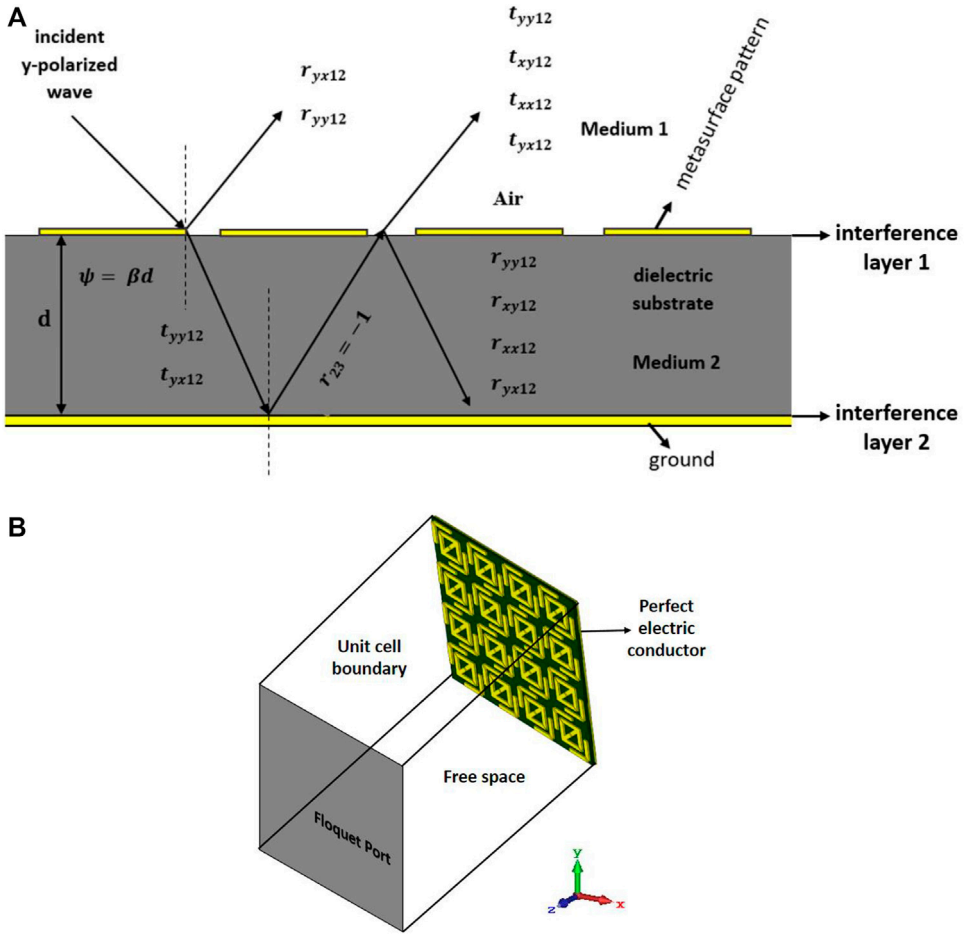

FIGURE 2 | (A) Reflectance and transmission of waves based on interference theoretical model and **(B)** schematic description of simulation.

To control the polarization state of the electromagnetic waves through the metasurface, it is necessary to accurately simulate the metasurface structure. In this regard, the finite integration technique (FIT)-based CST microwave electromagnetic simulator (CST Studio Suite 2019) was used for the design, numerical calculations, and characteristic analysis. During the simulation, the proposed metasurface was placed in the x- and y-direction, where the unit cell boundary conditions were imposed so that infinite unit cells were assumed to make the simulation more accurate. The positive z-direction was set as an open space boundary condition with the applied floquet port, while for the negative z-axis, the perfect electric conductor boundary was used to ensure the occurrences of reflectance only. The boundary condition of the proposed metasurface is depicted in **Figure 2B**. The numerical simulation was performed between 250 and 850 μm wavelength. Adaptive tetrahedral mesh refinement was also applied to get the results more accurately. Moreover, transverse electric (TE) and transverse magnetic (TM) waves have been utilized for the y-polarized and x-polarized wave simulation, respectively.

RESULTS AND DISCUSSION

Based on the extant literature, in a common phenomenon, the intensity of the co-polarized reflectance coefficient should be lower than −3 dB (i.e., $R_{xx} < -3$ dB and $R_{yy} < -3$ dB) and the cross-polarized reflectance coefficient should be opposite of that of the co-polarized reflectance coefficient (i.e., $R_{yx} \geq$ -3 dB and $R_{xy} \geq$ -3 dB), resulting in a cross-polarization conversion performance of 70%. However, if the intensity of co-polarized reflective coefficient falls below -10 dB (i.e., $R_{xx} < -10$ dB and $R_{yy} < -10$ dB) or the cross-polarized reflectance is higher than -2 dB (i.e., $R_{yx} \geq -2$ dB and $R_{xy} \geq -2$ dB), the cross polarizer is deemed to be highly efficient. In this situation, the cross-polarization performance reaches 90% and more [45]. The metasurface achieved dual bandwidth operation because of the multi-resonance characteristics. Multiple resonances were recorded at 286.7 μm (1.046 THz), 298.25 μm (1.0055 THz), 586.1 μm (0.5115 THz), and 689.55 μm (0.4554 THz). In this study, the developed metasurface performed as a polarization plane converter at an efficiency rate of 90%. The co-polarized and cross-polarized reflectance coefficients for both the x-polarized

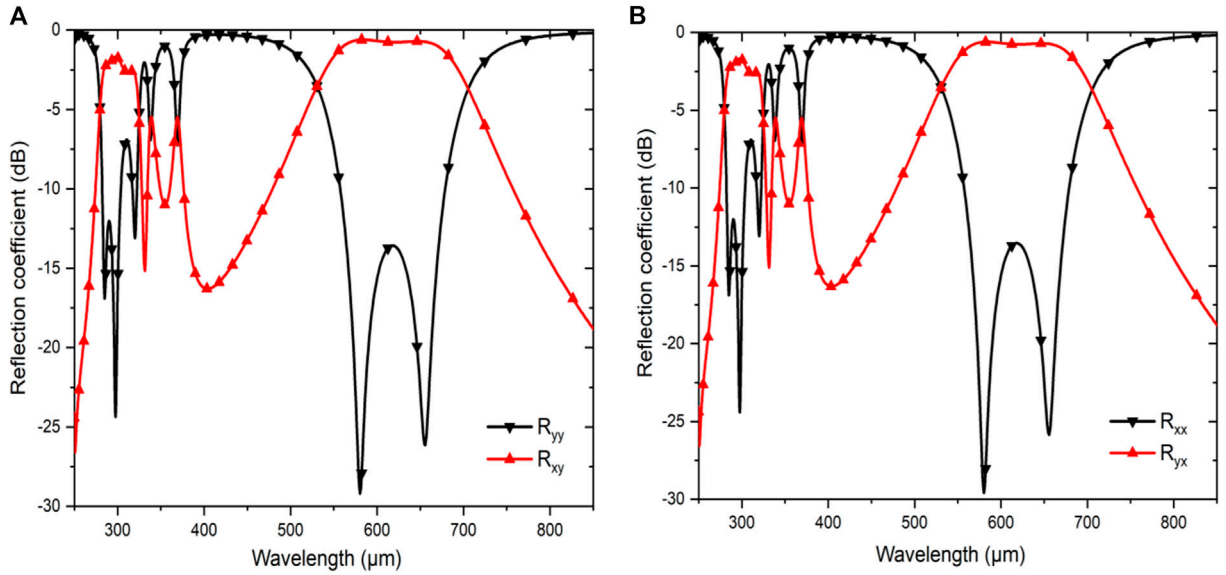

FIGURE 3 | Simulated co- and cross-polarized reflectance coefficients for **(A)** y-polarized and **(B)** x-polarized waves.

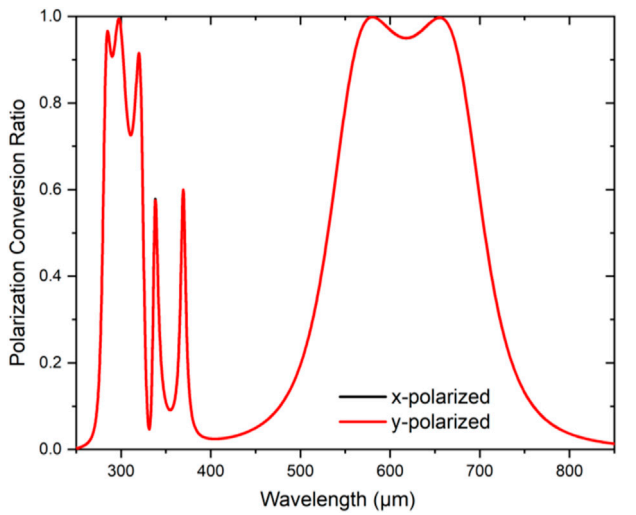

FIGURE 4 | Computed PCR for x- and y-polarized waves.

and y-polarized waves are presented in **Figures 3A,B**, respectively.

Based on **Figure 3**, the co-polarized reflectance coefficients for both the x-polarized and y-polarized waves remained almost the same, i.e., less than −10 dB, whereas the cross-polarized reflectance coefficients for both the x-polarized and y-polarized waves were above −2 dB. Thus, the cross-polarization conversion was achieved from 282.9 to 302.3 μm (0.987–1.062 THz) and 558.78 to 676.7 μm (0.442–0.537 THz), signifying the conversions of the x-polarized wave into the y-polarized wave, and the y-polarized wave into the x-polarized wave, respectively. The cross-polarization efficiency was measured using PCR. The PCR for both the y-polarized and x-polarized waves was calculated as follows:

$$PCR_{y-polarized} = \frac{|R_{xy}|^2}{|R_{xy}|^2 + |R_{yy}|^2},$$

$$PCR_{x-polarized} = \frac{|R_{yx}|^2}{|R_{yx}|^2 + |R_{xx}|^2}.$$

The magnitudes of PCR for the x- and y-polarized waves were plotted versus frequency spectrum as illustrated in **Figure 4**. The developed metasurface yielded above 90% polarization conversion efficiency from 282.9 to 302.3 μm and 558.78 to 676.7 μm. This result indicated that the developed metasurface could be used as an efficient polarization converter at a far-infrared range (0.3–1.2 THz).

To describe the multi resonance behavior of the metasurface for further clarification, the electric field distribution and surface current circulation for both the y- and x-polarized waves were assessed (**Figure 5**). At a higher frequency [i.e., 1.0055 THz (298.25 μm)], the electric charge is concentrated inside the splits of the array resonators. However, at the moderate resonance frequency [0.5115 THz (586.1 μm)], the charge concentration was more spread and concentrated at the corners of the resonators. As the frequency reduced, the electric charge concentration was spread to the corners and gaps [0.4554 THz (689.55 μm)]. However, some portions of resonators were weak in electric charge concentration, indicating decoupling characteristics at those regions. On the other hand, the black circle marks (O) represent the strong electric field, which leads to excellent electromagnetic coupling that defeats the decoupling portions to perform better. The electric charge concentration of the surface current distribution also justified the electric surface

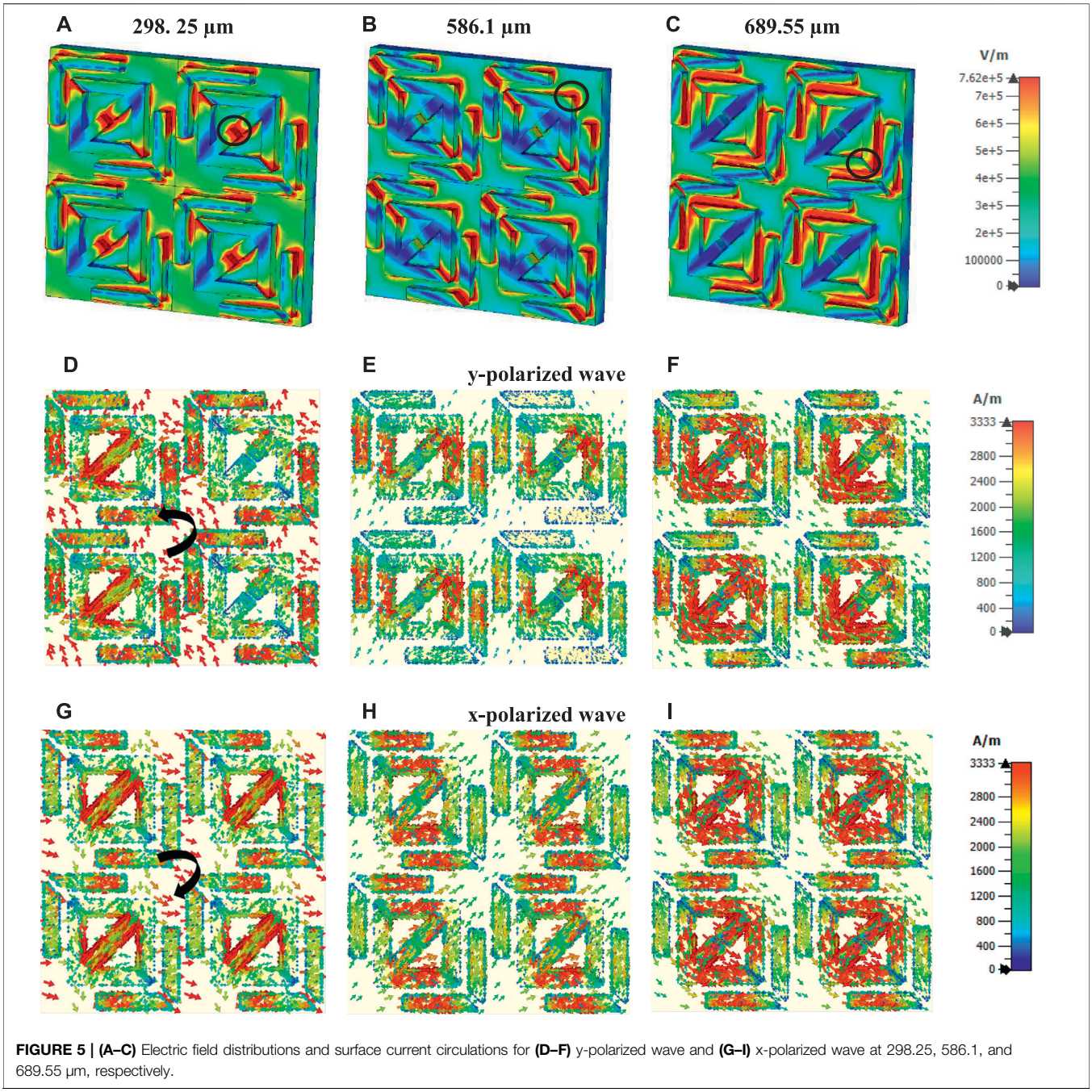

FIGURE 5 | (A–C) Electric field distributions and surface current circulations for **(D–F)** y-polarized wave and **(G–I)** x-polarized wave at 298.25, 586.1, and 689.55 µm, respectively.

current distribution of the metasurface at different frequencies.

To realize the physical phenomena of the polarization conversion, the surface current distributions for the periodic resonator layer at the resonance frequencies were presented in **Figure 5**. **Figures 5D–F** and **Figures 5G–I** present the instantaneously induced current distributions at resonance frequencies of 298.25 µm (1.0055 THz), 586.1 µm (0.5115 THz), and 689.55 µm (0.4554 THz) for both the y- and x-polarized waves, respectively. As depicted in **Figure 5D**, when the y-polarized wave propagated through the metasurface structure, where an anti-clockwise current circulation occurred as indicated by the black sign at a resonance frequency of 298.25 µm. The current circulation can also be termed as anti-parallel current circulation. The anti-parallel current circulation could lead to magnetic dipole moments. The y-components of the induced magnetic field, which were also parallel to the incident electric field, led to the cross-coupling formation between the electric field and magnetic field. Subsequently, cross-polarization conversion from the y- to x-polarized state occurred. This cross-coupling effect was also produced for the resonance frequencies at 586.1 and 689.55 µm, as depicted in **Figures 5E,F**, because the

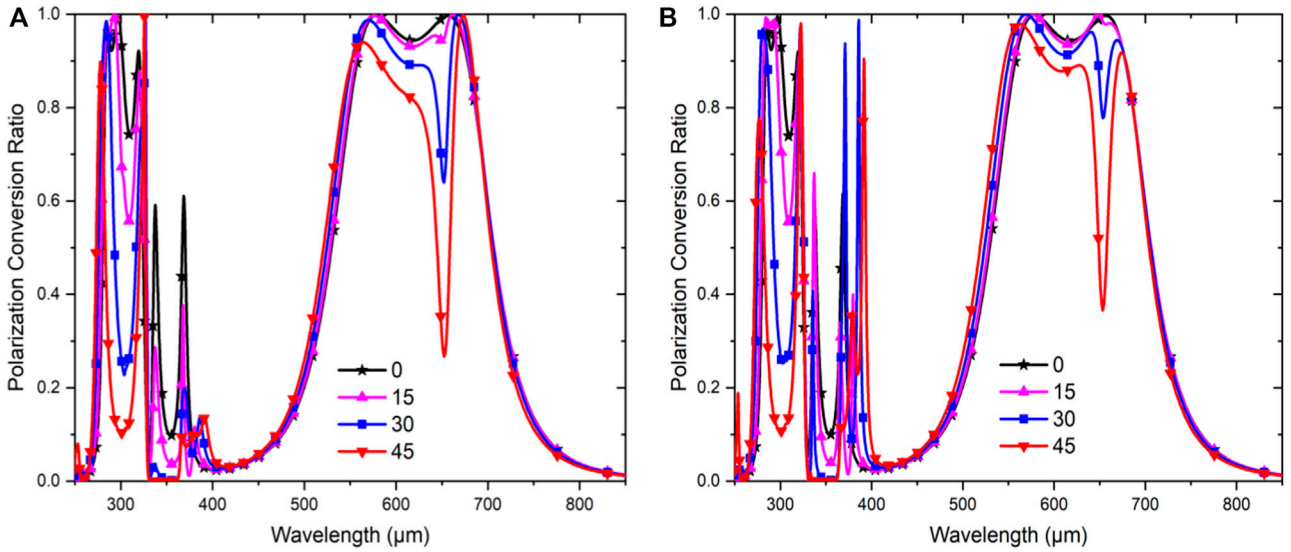

FIGURE 6 | Computed PCR from 0 to 45-degree oblique incidence for **(A)** y-polarized wave and **(B)** x-polarized wave.

y-polarized wave propagated and cross-polarization conversion occurred from the y- to x-polarized state [46]. When the x-polarized wave propagated through the metasurface, the current flowed in a clockwise direction (**Figure 5G**). The x-components of the induced magnetic field, which were perpendicular with the incident electric field, could not initiate cross-polarization conversion because the incident magnetic field was also in the same direction. However, the y-components of the induced magnetic field remained parallel with the incident electric field. Hence, it can induce the x-components perpendicular to the y-components of the electric field. Consequently, the induced x-components of the electric field led to polarization conversion. These phenomena occurred at 586.1 and 689.55 μm resonance frequencies, as depicted in **Figures 5H,I**, as the x-polarized wave was propagating.

The PCR performance of the metasurface was also examined under an increasingly oblique angle from 0 to 45° for the x- and y-polarized waves, as represented in **Figures 6A,B**, respectively. Based on the figures, the performance of the metasurface remained stable for bandwidths 556–679.9 μm (0.441 THz to 0.539 THz), despite the negligible changes. However, higher bandwidth affected the oblique incidence of the wave. The increase in the oblique incident angle (θ) also changed the magnitudes of the PCR due to the increase in the incident angle that greatly affected the reflected wave. The decrease in the cross-polarization component caused this reaction, whereby the bandwidth becomes narrower. However, in this study, angle stability was examined up to 45°, where 90% polarization efficiency was still achievable up to 30°, while the polarization efficiency dropped to 80% up to 45°.

For the proper justification of the metasurface structure, the characteristics of the co-polarized and cross-polarized reflectance coefficients were analyzed against three critical parameters of the metasurface, namely, substrate thickness, split length (spotted at the middle of the two orthogonal arrows joining), and splits of the arrow shape of the square-shaped resonator (**Figures 7A–F**). To achieve the best characteristics of the co- and cross-polarized reflectance coefficients of the metasurface, the dielectric substrate thickness is considered an important parameter. **Figures 7A,B** displayed the co- and cross-polarized reflectance coefficients using the dielectric substrate at different thicknesses. According to the scale invariance of Maxwell, the substrate thickness and resonant frequency are inversely related. At higher frequencies, the substrate must have a minimum thickness for the unit cell to resonate. To achieve cross-polarization conversion over 90%, after a series of optimization processes, the thickness of the substrate was set at 20 μm. Increasing the thickness of the substrate, decrease the dB values of the co-polarized reflectance as well as the cross-polarized reflectance also tend to decrease higher than −2 dB. In those cases, the cross-polarization conversion could not be achieved, which is our main goal. On the other hand, the co-polarized reflectance coefficient lost its resonance at a higher frequency when the thickness of the substrate was reduced.

The split at the middle of the two orthogonal arrows joining is responsible for the metasurface response at higher frequency (i.e., the resonance at 286.7 and 298.25 μm occurred due to the split creation). The split also leads to an increased capacitance of the inside resonator and yields higher frequency resonances. After a series of optimization processes, the split width in this study was set at 55 μm. Moreover, there is an inverse relationship between capacitance and resonant frequency. As depicted in **Figures 7C,D**, we discovered better co-polarized reflectance characteristics with resonance dip at higher frequencies that were valuable in medical imaging applications. The splits at the corner of the square-shaped resonator were also an

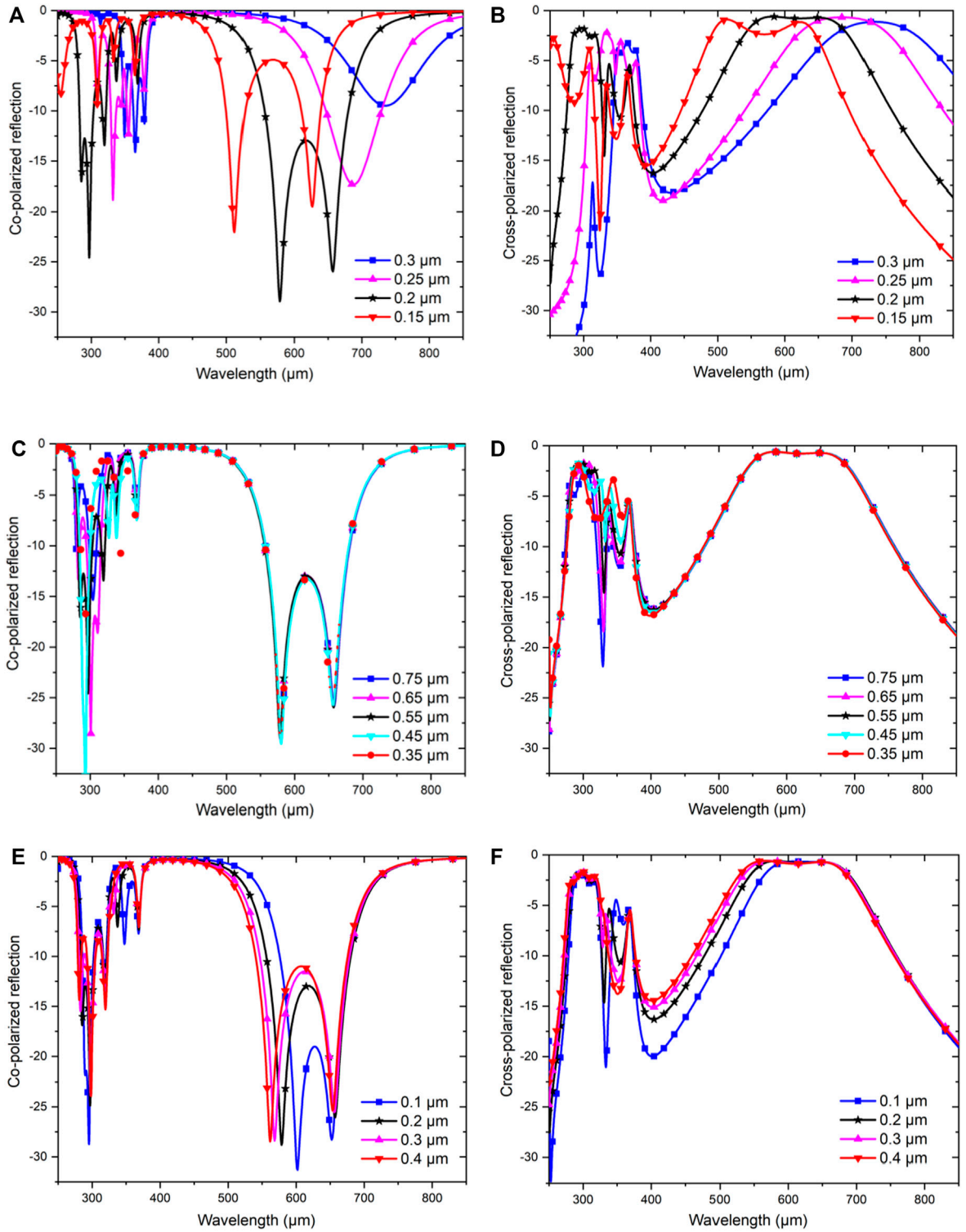

FIGURE 7 | Co- and cross-polarized reflectance responses based on varying **(A,B)** substrate thickness, **(C,D)** split length, and **(E,F)** split gap at the corner of the square-shaped resonator.

TABLE 1 | Summary of the parametric analysis of the proposed metasurface.

Parameters	Size (μm)	Resonance points (μm)	Bandwidth (μm)
Substrate thickness	0.15	512.38, 626.57	490.01–527.58
			610.42–639.92
	0.2	285.4, 297.1	282.8–303.2
		579.1, 657.7	556.2–679.8
	0.25	332.6, 688.47	328.76–336.88
	0.30	365.13	362.4–367.84
			647.49–729.37
Split at the middle	0.35	579.1, 657.7	556.2–679.8
	0.45	293.22, 579.1	284.62–299.94
		657.7	556.2–679.8
	0.55	285.4, 297.1	282.8–303.2
		579.1, 657.7	556.2–679.8
	0.65	300.9, 311.11	294.6–315.72
		579.1, 657.7	556.2–679.8
	0.75	301.24, 579.1	298.5–309.5
		657.7	556.2–679.8
Split at the corner	0.1	295.28, 602.12	285.4–302.08
		652.6	577–679.01
	0.2	285.4, 297.1	282.8–303.2
		579.1, 657.7	556.2–679.8
	0.3	283.05, 298.01	290–304.15
		598.52, 656.9	546.8–679.01
	0.4	281.02, 298.32	292.6–305.3
		562.16, 653.92	540.9–675.68

TABLE 2 | Comparison of the proposed work with the existing literature.

Ref	Materials used	Configurations	Frequency range (THz)	Polarizations achieved	Highest efficiency
Cheng et al. [24]	Benzocyclobutene and copper	Multi-layered	—	Circular	93%
Jiang et al. [25]	Phosphorene and gold	Multi-layered	12.82–23.28, 14.20–23.12	Linear to circular	—
Zhu et al. [26]	Graphene, quartz and gold	Single-layered	1.28–2.13	Cross	97.2%
Wen et al. [27]	Polyimide and gold	Single-layered	0.44–0.76	Linear to orthogonal	Near unity
Cheng et al. [28]	Polyimide and copper	Double-layered	2.19–2.47	Linear to circular	96%
Ako et al. [29]	Cyclin olefin copolymer and gold	Multi-layered	0.22–1.02	Linear to orthogonal	> 80%
Proposed work	Gallium arsenide and aluminum	Single-layered	0.459–0.555, 1.023–1.097	Linear to cross	96%

important factor in creating an arrow-shaped structure. **Figures 7E,F** display the co- and cross-polarized reflectance coefficients for varying gaps of splits. Following numerous analyses, the optimum value for the splits of the corner was set as 0.2 μm. Increasing the gap deteriorates the resonance frequencies due to the decrease in capacitance and gap that reduces the bandwidth.

Table 1 summarizes the analytical results of the crucial parameters of the designed structure. When the substrate thickness changes, the resonance frequencies and bandwidth also changed. The split in the middle, which is responsible for the first two low resonance frequencies, changed with different split lengths, except for two other resonance peaks that were almost stable regardless of the changes. Then, the splits in the two corners, which are responsible for the two upper resonance frequencies, are changing with changes of the split length, and for this case, the lower two frequencies saw minor shifting. Overall, the combination of 0.2 μm substrate thickness, 0.55 μm split at the middle, and 0.2 μm splits at two corners demonstrated that the proposed metasurface yielded the best results for polarization conversion.

Due to the inadequate facilities, the metasurface device could not be fabricated. However, the metasurface polarization converter can be fabricated using ultraviolet (UV) lithography and lift-off process [47, 48]. The steps are given below:

1) At first, a supporting substrate (Si or Ti) needs to fabricate by the e-beam evaporation process so that the whole structure of the metasurface can be fabricated onto it.
2) Second, the ground metallic layers, which was Al, can be evaporated evenly on the skin of the supporting substrate.
3) After that, with the technologies of spin-coating, the middle dielectric layer can be consistently coated over the surface of the Al layer.

4) At last, the top metallic array pattern (Al) can be fabricated by utilizing conventional lithography and lift-off processes of micro-fabrication.

By following these steps, the proposed metasurface device can be fabricated and experimentally measured utilizing the fiber-coupled THz time-domain spectrometer (THz-TDS) system.

Table 2 summarizes and compares the findings from the reported literature with the proposed design. Based on the results, every metasurface that was designed for polarization conversion either involved cross-polarization or linear to circular polarization conversion. Comparatively, previous studies which utilized double-layered or multi-layered designs were complicated to fabricate and were costly as they used materials such as graphene and gold. Thus, the need for a single layer, low-cost, and compact metasurface was still in demand. The proposed work is a suitable candidate for the metasurface resonator array pattern.

CONCLUSION

A proposed metasurface was numerically described for efficient polarization conversion in this study. The interference theory was used to discuss the model. Exhibiting the anisotropy of the metasurface structure, the metasurface yielded a 90% polarization converter from x- to y-polarization, and vice versa from 282.9 to 302.3 μm and 558.78 to 676.7 μm. The metasurface structure was also angle independent up to 30°. The metasurface was examined using different parameters to assess its potentiality as an efficient polarization converter. Finally, the compact size, angular stability performance, and numerous features make the proposed single-layered metasurface a potential candidate for advanced THz applications, including THz detectors, sensing, and many other THz-based devices.

DATA AVAILABILITY STATEMENT

The original contributions presented in the study are included in the article/Supplementary Material, further inquiries can be directed to the corresponding author.

AUTHOR CONTRIBUTIONS

Conceptualization—AT and MH; methodology—AT; software—AT; formal analysis—AT and MH; writing—AT and MH; writing—review and editing—MH, MF; supervision—MF; funding acquisition—MF. All authors have read and agreed to the published version of the manuscript.

FUNDING

This work was supported by the Research Universiti Grant, Universiti Kebangsaan Malaysia, Geran Universiti Penyelidikan (GUP), code: 2021-074.

REFERENCES

1. Holloway CL, Dienstfrey A, Kuester EF, O'Hara JF, Azad AK, Taylor AJ. A Discussion on the Interpretation and Characterization of Metafilms/metasurfaces: The Two-Dimensional Equivalent of Metamaterials. *Metamaterials* (2009) 3:100–12. doi:10.1016/j.metmat.2009.08.001
2. Cheng Y, Fan J, Luo H, Chen F. Dual-band and High-Efficiency Circular Polarization Convertor Based on Anisotropic Metamaterial. *IEEE Access* (2020) 8:7615–21. doi:10.1109/ACCESS.2019.2962299
3. Wang B-X, He Y, Lou P, Zhu H. Multi-band Terahertz Superabsorbers Based on Perforated Square-Patch Metamaterials. *Nanoscale Adv* (2021) 3(2): 455–62. doi:10.1039/D0NA00903B
4. Ahamed E, Faruque MRI, Alam MJ, Mansor MFB, Islam MT. Digital Metamaterial Filter for Encoding Information. *Sci Rep* (2020) 10(1):1–9. doi:10.1038/s41598-020-60170-8
5. Wang B-X, Wu Y, Xu W, Yang Z, Lu L, Pi F. Quad-band Terahertz Metamaterial Absorber Enabled by an Asymmetric I-type Resonator Formed from Three Metallic Strips for Sensing Application. *Sens Diagn* (2022) 1:169–76. doi:10.1039/D1SD00005E
6. Alam MJ, Ahamed E, Faruque MRI, Islam MT, Tamim AM. Left-handed Metamaterial Bandpass Filter for GPS, Earth Exploration-Satellite and WiMAX Frequency Sensing Applications. *PloS one* (2019) 14(11):e0224478. doi:10.1371/journal.pone.0224478
7. Tamim AM, Hasan MM, Faruque MRI, Islam MT, Nebhen J. Polarization-independent Symmetrical Digital Metasurface Absorber. *Results Phys* (2021) 24:103985. doi:10.1016/j.rinp.2021.103985
8. Chen H-T, Taylor AJ, Yu N. A Review of Metasurfaces: Physics and Applications. *Rep Prog Phys* (2016) 79(7):076401. doi:10.1088/0034-4885/79/7/076401
9. Saleh BEA, Teich MC. *Fundamentals of Photonics*. 2nd ed. New Jersey, United States: Wiley (2007).
10. Zhao Y, Alù A. Manipulating Light Polarization With Ultrathin Plasmonic Metasurfaces. *Phys Rev B* (2011) 84(20):205428. doi:10.1103/PhysRevB.84.205428
11. Khan MI, Tahir FA. A Compact Half and Quarter-Wave Plate Based on Bi-layer Anisotropic Metasurface. *J Phys D: Appl Phys* (2017) 50:43LT04. doi:10.1088/1361-6463/aa86d6
12. Chang C-C, Headland D, Abbott D, Withayachumnankul W, Chen H-T. Demonstration of a Highly Efficient Terahertz Flat Lens Employing Tri-layer Metasurfaces. *Opt Lett* (2017) 42:1867. doi:10.1364/ol.42.001867
13. Akram MR, Mehmood MQ, Tauqeer T, Rana AS, Rukhlenko ID, Zhu W. Highly Efficient Generation of Bessel Beams with Polarization Insensitive Metasurfaces. *Opt Express* (2019) 27:9467. doi:10.1364/oe.27.009467
14. Yoon G, Lee D, Nam KT, Rho J. Geometric Metasurface Enabling Polarization Independent Beam Splitting. *Sci Rep* (2018) 8(1):1–8. doi:10.1038/s41598-018-27876-2
15. Su P, Zhao Y, Jia S, Shi W, Wang H. An Ultra-Wideband and Polarization-Independent Metasurface for RCS Reduction. *Sci Rep* (2016) 6(1):1–8. doi:10.1038/srep20387
16. Azad AK, Efimov AV, Ghosh S, Singleton J, Taylor AJ, Chen H-T. Ultra-thin Metasurface Microwave Flat Lens for Broadband Applications. *Appl Phys Lett* (2017) 110:224101. doi:10.1063/1.4984219
17. Huang L, Zhang S, Zentgraf T. Metasurface Holography: From Fundamentals to Applications. *Nanophotonics* (2018) 7(6):1169–1190. doi:10.1515/nanoph-2017-0118
18. Faruque MRI, Hasan MM, Islam MT. Tree-shaped Fractal Meta-Surface with Left-Handed Characteristics for Absorption Application. *Appl Phys A* (2018) 124:1–8. doi:10.1007/s00339-017-1498-9
19. Cheng Y, Zhu X, Li J, Chen F, Luo H, Wu L. Terahertz Broadband Tunable Reflective Cross-Polarization Convertor Based on Complementary Cross-

Shaped Graphene Metasurface. *Physica E: Low-dimensional Syst Nanostructures* (2021) 134:114893. doi:10.1016/j.physe.2021.114893
20. Cheng Y, Wang J. Tunable Terahertz Circular Polarization Convertor Based on Graphene Metamaterial. *Diamond Relat Mater* (2021) 119:108559. doi:10.1016/j.diamond.2021.108559
21. Feng M, Wang J, Ma H, Mo W, Ye H, Qu S. Broadband Polarization Rotator Based on Multi-Order Plasmon Resonances and High Impedance Surfaces. *J Appl Phys* (2013) 114:074508. doi:10.1063/1.4819017
22. Zhang L, Zhou P, Lu H, Chen H, Xie J, Deng L. Ultra-thin Reflective Metamaterial Polarization Rotator Based on Multiple Plasmon Resonances. *Antennas Wirel Propag Lett* (2015) 14:1157–60. doi:10.1109/LAWP.2015.2393376
23. Chen H, Wang J, Ma H, Qu S, Xu Z, Zhang A, et al. Ultra-wideband Polarization Conversion Metasurfaces Based on Multiple Plasmon Resonances. *J Appl Phys* (2014) 115:154504. doi:10.1063/1.4869917
24. Cheng Y, Fan J, Luo H, Chen F, Feng N, Mao X, et al. Dual-band and High-Efficiency Circular Polarization Conversion via Asymmetric Transmission with Anisotropic Metamaterial in the Terahertz Region. *Opt Mater Express* (2019) 9:1365. doi:10.1364/ome.9.001365
25. Jiang Y, Zhao H, Wang L, Wang J, Cao W, Wang Y. Broadband Linear-To-Circular Polarization Converter Based on Phosphorene Metamaterial. *Opt Mater Express* (2019) 9:2088. doi:10.1364/ome.9.002088
26. Zhu J, Li S, Deng L, Zhang C, Yang Y, Zhu H. Broadband Tunable Terahertz Polarization Converter Based on a Sinusoidally-Slotted Graphene Metamaterial. *Opt Mater Express* (2018) 8:1164. doi:10.1364/ome.8.001164
27. Wen X, Zheng J. Broadband THz Reflective Polarization Rotator by Multiple Plasmon Resonances. *Opt Express* (2014) 22:28292. doi:10.1364/oe.22.028292
28. Cheng Z, Cheng Y. A Multi-Functional Polarization Convertor Based on Chiral Metamaterial for Terahertz Waves. *Opt Commun* (2019) 435:178–82. doi:10.1016/j.optcom.2018.11.038
29. Ako RT, Lee WSL, Atakaramians S, Bhaskaran M, Sriram S, Withayachumnankul W. Ultra-wideband Tri-layer Transmissive Linear Polarization Converter for Terahertz Waves. *APL Photon* (2020) 5:046101. doi:10.1063/1.5144115
30. Borgese M, Costa F, Genovesi S, Monorchio A, Manara G. Optimal Design of Miniaturized Reflecting Metasurfaces for Ultra-Wideband and Angularly Stable Polarization Conversion. *Sci Rep* (2018) 8(1):1–11. doi:10.1038/s41598-018-25934-3
31. Fan J, Cheng Y. Broadband High-Efficiency Cross-Polarization Conversion and Multi-Functional Wavefront Manipulation Based on Chiral Structure Metasurface for Terahertz Wave. *J Phys D: Appl Phys* (2020) 53:025109. doi:10.1088/1361-6463/ab4d76
32. Zhang J, Zhang K, Cao A, Liu Y, Kong W. Bi-functional Switchable Broadband Terahertz Polarization Converter Based on a Hybrid Graphene-Metal Metasurface. *Opt Express* (2020) 28:26102. doi:10.1364/oe.397338
33. Li J, Li J, Yang Y, Li J, Zhang Y, Wu L, et al. Metal-graphene Hybrid Active Chiral Metasurfaces for Dynamic Terahertz Wavefront Modulation and Near Field Imaging. *Carbon* (2020) 163:34–42. doi:10.1016/j.carbon.2020.03.019
34. Li J, Zheng C, Li J, Wang G, Liu J, Yue Z, et al. Terahertz Wavefront Shaping with Multi-Channel Polarization Conversion Based on All-Dielectric Metasurface. *Photon Res* (2021) 9(10):1939–47. doi:10.1364/PRJ.431019
35. Serita K, Matsuda E, Okada K, Murakami H, Kawayama I, Tonouchi M. Invited Article: Terahertz Microfluidic Chips Sensitivity-Enhanced with a Few Arrays of Meta-Atoms. *APL Photon* (2018) 3:051603. doi:10.1063/1.5007681
36. Tang M, Zhang M, Yan S, Xia L, Yang Z, Du C, et al. Detection of DNA Oligonucleotides With Base Mutations by Terahertz Spectroscopy and Microstructures. *PLoS One* (2018) 13(1):e0191515. doi:10.1371/journal.pone.0191515
37. Han X, Yan S, Zang Z, Wei D, Cui H-L, Du C. Label-free Protein Detection Using Terahertz Time-Domain Spectroscopy. *Biomed Opt Express* (2018) 9:994. doi:10.1364/boe.9.000994
38. Rahman A, Rahman AK, Rao B. Early Detection of Skin Cancer *via* Terahertz Spectral Profiling and 3D Imaging. *Biosens Bioelectron* (2016) 82:64–70. doi:10.1016/j.bios.2016.03.051
39. Lee K, Jeoung K, Kim SH, Ji Y-b., Son H, Choi Y, et al. Measuring Water Contents in Animal Organ Tissues Using Terahertz Spectroscopic Imaging. *Biomed Opt Express* (2018) 9:1582. doi:10.1364/boe.9.001582
40. Zhao H, Wang X, He J, Guo J, Ye J, Kan Q, et al. High-efficiency Terahertz Devices Based on Cross-Polarization Converter. *Sci Rep* (2017) 7(1):1–9. doi:10.1038/s41598-017-18013-6
41. Ahamed E, Faruque MRI, Mansor MFB, Islam MT. Polarization-dependent Tunneled Metamaterial Structure with Enhanced fields Properties for X-Band Application. *Results Phys* (2019) 15:102530. doi:10.1016/j.rinp.2019.102530
42. Chen H-T. Interference Theory of Metamaterial Perfect Absorbers. *Opt Express* (2012) 20:7165. doi:10.1364/oe.20.007165
43. Gao X, Han X, Cao W-P, Li HO, Ma HF, Cui TJ. Ultrawideband and High-Efficiency Linear Polarization Converter Based on Double V-Shaped Metasurface. *IEEE Trans Antennas Propagat* (2015) 63:3522–30. doi:10.1109/TAP.2015.2434392
44. Kundu D, Mohan A, Chakrabarty A. Reduction of Cross-Polarized Reflection to Enhance Dual-Band Absorption. *J Appl Phys* (2016) 120:205103. doi:10.1063/1.4968569
45. Salman MS, Khan MI, Tahir FA, Rmili H. Multifunctional Single Layer Metasurface Based on Hexagonal Split Ring Resonator. *IEEE Access* (2020) 8:28054–63. doi:10.1109/ACCESS.2020.2971557
46. Grady NK, Heyes JE, Chowdhury DR, Zeng Y, Reiten MT, Azad AK, et al. Terahertz Metamaterials for Linear Polarization Conversion and Anomalous Refraction. *Science* (2013) 340(6138):1304–7. doi:10.1126/science.1235399
47. Huang L, Chowdhury DR, Ramani S, Reiten MT, Luo S-N, Taylor AJ, et al. Experimental Demonstration of Terahertz Metamaterial Absorbers with a Broad and Flat High Absorption Band. *Opt Lett* (2012) 37(2):154–6. doi:10.1364/OL.37.000154
48. Wang B-X, Xu W, Wu Y, Yang Z, Lai S, Lu L. Realization of a Multi-Band Terahertz Metamaterial Absorber Using Two Identical Split Rings Having Opposite Opening Directions Connected by a Rectangular Patch. *Nanoscale Adv* (2022) 4:1359–67. doi:10.1039/D1NA00789K

Conflict of Interest: The authors declare that the research was conducted in the absence of any commercial or financial relationships that could be construed as a potential conflict of interest.

frontiers | Frontiers in Physics

ORIGINAL RESEARCH
published: 09 May 2022
doi: 10.3389/fphy.2022.907718

Synthesis Design of Dual-Band Filtering Power Dividers Based on E-Shape Resonators

Jiwei Shen[1], *Wei Li*[2], *Kang Ping*[2], *Zhuowei Zhang*[2]* *and Minghan Shu*[2]

[1]ZiJin College Nanjing University of Science and Technology, Nanjing, China, [2]Nanjing Normal University, Nanjing, China

In this study, a comprehensive design of dual-band filtering power dividers (FPDs) with arbitrary phase distribution is presented. With a series of analytical equations for the direct synthesis design, the proposed method shows its great capacity of designing dual-band FPDs with any pre-specified responses, arbitrary phase distribution, and high isolation. To verify this design method, a demonstrated dual-band FPD with 90° phase differences between two outputs based on E-shape resonators has been implemented. The emulational results coincide with the measured results well, showing the feasibility of the proposed method.

Keywords: direct synthesis design, filtering power divider, dual-band, phase distribution, isolation

OPEN ACCESS

Edited by:
Kai-Da Xu,
Xi'an Jiaotong University, China

Reviewed by:
Baoping Ren,
East China Jiaotong University, China
Zhi-Chong Zhang,
Jinggangshan University, China

***Correspondence:**
Zhuowei Zhang
zhuowei_zhang@163.com

Specialty section:
This article was submitted to Optics and Photonics, a section of the journal Frontiers in Physics

Received: *30 March 2022*
Accepted: *11 April 2022*
Published: *09 May 2022*

Citation:
Shen J, Li W, Ping K, Zhang Z and Shu M (2022) Synthesis Design of Dual-Band Filtering Power Dividers Based on E-Shape Resonators. Front. Phys. 10:907718. doi: 10.3389/fphy.2022.907718

INTRODUCTION

A bandpass filter (BPF) and power divider (PD) are the indispensable components in various modern wireless communication systems. In general, they often integrate into a single component for miniaturization and improved performance, i.e., filtering power divider (FPD) [1–6], which provides both function of power division and filtering simultaneously. In the meantime, future mobile communication can provide mobile terminal online HD video virtual reality (VR), augmented reality (AR), and such wireless interactive services that require big data traffic and high transmission quality [7, 8]. The phase shifter is the critical component for the multi-polarization and multi-beam technology, which plays an important role in the construction of mobile communication systems with high-speed data transmission and efficient spectrum utilization.

In recent years, there are few research studies on filtering power dividers with an arbitrary phase difference [9–11]. For instance, in [9], a new class of filtering power divider that integrates the filter's PD, phase shifter, and impedance transformer into a single component was proposed, which achieves a good result in filtering power division response and phase difference. Moreover, in [10], a filtering power divider consisting of a Wilkinson power divider (WPD) and N_{th}-order-coupled line bandpass filters was proposed, and closed-form design equations are derived.

Unfortunately, they are only single-band filtering power divider with a phase difference; as the author knows, there are few dual-band filtering power dividers with a phase difference.

In this study, a new synthesis design method of dual-band FPD with arbitrary phase distribution is proposed. Based on a series of analytical equations and synthesis design, a dual-band FPD with any prescribed specifications including filtering power division response, isolation, and phase shifter can be obtained. To verify the proposed design concept, a dual-band FPD with 90° port-to-port phase distribution based on E-shape resonators has been designed and fabricated.

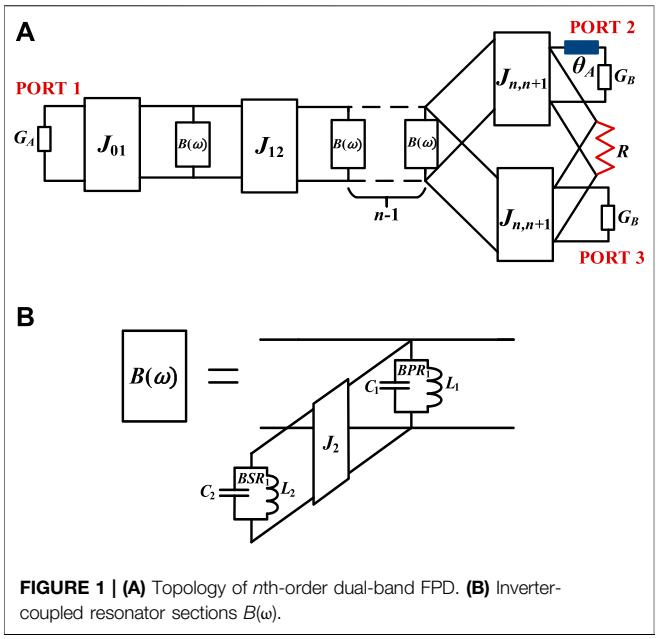

FIGURE 1 | (A) Topology of *n*th-order dual-band FPD. **(B)** Inverter-coupled resonator sections *B*(ω).

DESIGN AND ANALYSIS

Figure 1A describes a new general *n*th-order dual-band FPD topology, which is mainly made up of multiple dual-frequency resonant units B (ω), one branch line θ_A, and one isolation resistor R. Specifically, for dual-number operation bands, every dual-frequency resonant unit consists of one bandpass resonator (BPR_1) and one inverter-coupled bandstop resonators (BSR_1) as shown in **Figure 1B**. The signal comes from port #1, flowing through multiple dual-frequency resonant units, and finally outputs from port #2 and port #3. Due to the branch line and isolation resistor, the two outputs can achieve phase difference and isolation at the same time.

Analysis of Filtering Power Division Response

On the bias of the frequency transformation and prototype synthesis technique, the prescribed dual-band filtering power division response can be obtained step by step. In the first step, the admittance of inverter-coupled resonators in **Figure 1B** viewed from the input/output is derived by:

$$B(\omega) = jT(\omega) = jb_1\left(\frac{\omega}{\omega_{01}} - \frac{\omega_{01}}{\omega}\right) + \frac{J_2}{jb_2\left(\frac{\omega}{\omega_{02}} - \frac{\omega_{02}}{\omega}\right)},$$
$$b_i = \omega_{0i}C_{0i}, \omega_{0i} = 1\Big/\sqrt{C_{0i}L_{0i}}, i = 1, 2, 3...m., \quad (1)$$

where ω_{0i} and b_i represent the angular resonant frequency and susceptance slope parameter of the ith resonator, respectively.

Assuming that the FPD has two passbands of (ω_{L1}, ω_{H1}) and (ω_{L2}, ω_{H2}), the lower limits of the two passbands (ω_{L1}, ω_{L2}) ought to map to −1 in the normalized domain, while the upper limits (ω_{H1}, ω_{H2}) ought to map to +1 in the normalized domain. The parameters that define the transformation (ω_{01}, ω_{02}, b_1, and b_2) can finally be expressed as the functions of the two passband limits (ω_{L1}, ω_{H1}, and ω_{L2}, ω_{H2}) according to the relationship between the roots and the coefficients of the equation of $T(\omega) = 1$. Since the function $U(\omega) = T(\omega)$-1 denotes the ratio of two polynomials, we can further use $Q(\omega)$ to represent the numerator of $U(\omega)$ as:

$$Q(\omega) = \omega^4 + d_3\omega^2 + d_2\omega^2 + d_1\omega + d_0. \quad (2)$$

Once the aforementioned frequencies are prescribed according to specifications in advance, the parameters (ω_{01}, ω_{02}) and (b_1, b_2) can be calculated as:

$$\begin{aligned}\omega_{01} &= \sqrt{-\frac{d_0 d_3}{d_1}},\\ \omega_{02} &= \sqrt{-\frac{d_1}{d_3}},\\ b_1 &= \sqrt{-\frac{d_0}{d_1 d_3}},\\ b_2 &= \sqrt{-\frac{d_1}{d_3}}\,\frac{d_1 d_3^2}{d_1 d_2 d_3 - d_1^2 - d_0 d_3^2}.\end{aligned} \quad (3)$$

Afterward, by mapping the *n*th-order dual-band FPD topology to its corresponding low-pass prototype, the inverters' values can be finally expressed as [12]:

$$J_{01} = \sqrt{\frac{G_A}{g_0 g_1}}, \quad J_{i,i+1} = \sqrt{\frac{1}{g_i g_{i+1}}}, \quad J_{n,n+1} = \sqrt{\frac{G_B}{2g_n g_{n+1}}}. \quad (4)$$

Afterward, the coupling coefficients between the adjacent BPRs can be derived as:

$$k_{i,i+1} = \frac{J_{i,i+1}}{b_1}. \quad (5)$$

Meanwhile, the coupling coefficient between the BSR and BPR can be derived as:

$$k_i = \frac{J_i}{\sqrt{b_1 b_i}}. \quad (6)$$

In addition, the external quality factors can be formulated by:

$$Q_{in} = \frac{b_1 G_A}{J_{01}^2}, Q_{out} = \frac{b_1 G_B}{J_{n,n+1}^2}. \quad (7)$$

After the dual-band filtering power division responses are analyzed, the isolation and phase distribution can be obtained by

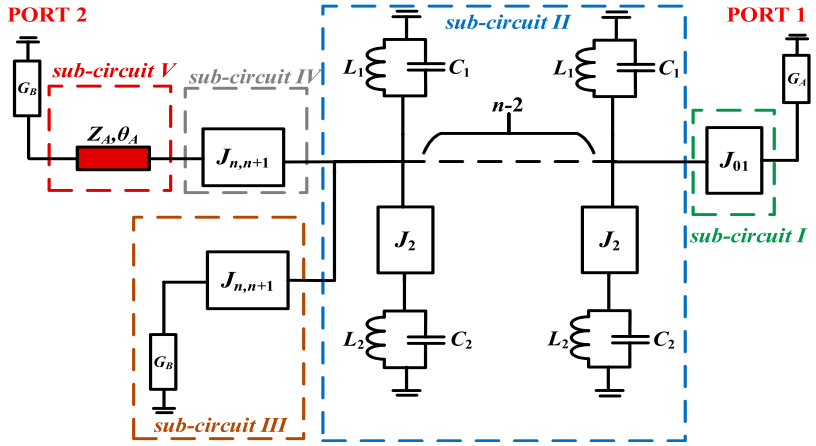

FIGURE 2 | Equivalent circuit diagram for analyzing phase difference between two output ports.

means of the isolation resistor R and the branch lines, respectively.

Analysis of Phase Difference Between Outputs

In order to analyze the phase difference between the output ports of the dual-band filtering power division network topology, the ABCD matrix of the whole circuit is solved through the microwave network analysis method. Furthermore, the insertion phase shifts $\angle S_{12}$ and $\angle S_{13}$ can be deduced.

First, $\angle S_{12}$ is analyzed. Assuming that the incident wave is only introduced in port #1 and output in port #2 ($G_A = G_B = Y_0$), the topology diagram of the dual-band filtering power division network with phase-shifting function in **Figure 1A** is appropriately simplified and redrawn, as shown in **Figure 2**. There are five sub-circuits in this schematic, as denoted by sub-circuit I, sub-circuit II, sub-circuit III, sub-circuit IV, and sub-circuit V.

For dual-frequency resonant units $B(\omega)$, its input admittance P can be represented as:

$$P = P_1 + \frac{J_2^2}{P_2}, \tag{8}$$

where $P_1 = j\omega C_1$ is represented as the square root of capacitances of BPR and BSR in the low-pass prototype, where the value of eac+$1/j\omega L_1$, $P_2 = j\omega C_2$+$1/j\omega L_2$, and P_1 and P_2 are the admittances of the corresponding resonators.

For sub-circuit I, its ABCD matrix can be obtained as:

$$\begin{pmatrix} A_1 & B_1 \\ C_1 & D_1 \end{pmatrix} = \begin{pmatrix} 0 & \frac{1}{jJ_{01}} \\ -jJ_{01} & 0 \end{pmatrix}. \tag{9}$$

For sub-circuit II, its ABCD matrix can be obtained as:

$$\begin{pmatrix} A_2 & B_2 \\ C_2 & D_2 \end{pmatrix} = \begin{pmatrix} 1 & 0 \\ N_1 & 1 \end{pmatrix}, \tag{10}$$

where

$$N_1 = P + \cfrac{J_{n-1,n}^2}{P + \cfrac{J_{n-2,n-1}^2}{P + \ldots}}$$
$$\ddots$$
$$P + \frac{J_{12}^2}{P}$$

Meanwhile, for sub-circuits III, IV, and V, their ABCD matrix can be obtained, respectively, as follows:

$$\begin{pmatrix} A_3 & B_3 \\ C_3 & D_3 \end{pmatrix} = \begin{pmatrix} 1 & 0 \\ \frac{J_{n,n+1}^2}{Y_0} & 1 \end{pmatrix}, \tag{11}$$

$$\begin{pmatrix} A_4 & B_4 \\ C_4 & D_4 \end{pmatrix} = \begin{pmatrix} 0 & \frac{1}{jJ_{n,n+1}} \\ -jJ_{n,n+1} & 0 \end{pmatrix}, \tag{12}$$

$$\begin{pmatrix} A_5 & B_5 \\ C_5 & D_5 \end{pmatrix} = \begin{pmatrix} \cos\theta_A & jZ_A \sin\theta_A \\ \frac{j\sin\theta_A}{Z_A} & \cos\theta_A \end{pmatrix}. \tag{13}$$

Finally, the ABCD matrix of the whole circuit can be solved as follows:

$$\begin{pmatrix} A_6 & B_6 \\ C_6 & D_6 \end{pmatrix}, \tag{14}$$

where

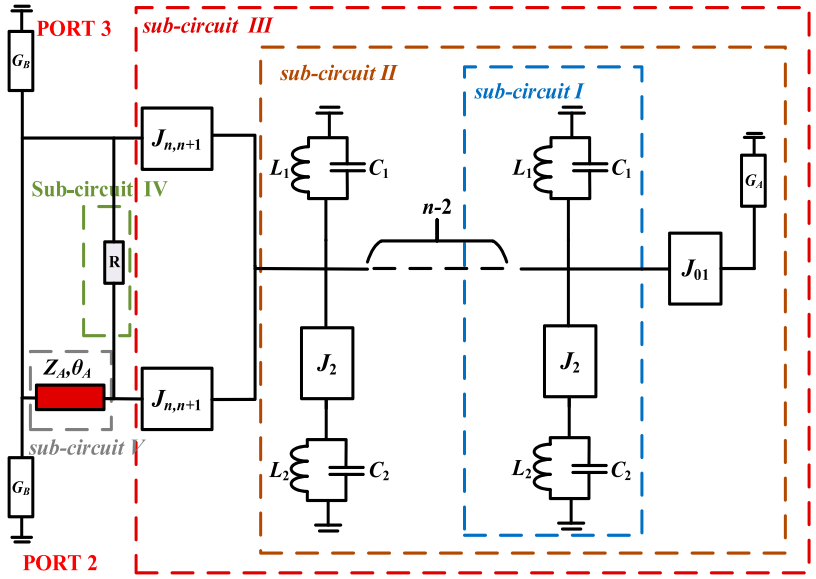

FIGURE 3 | Equivalent circuit diagram for analyzing isolation between two output ports.

$$A_6 = -\frac{J_{n,n+1}\cos\theta_A}{J_{01}} - \frac{j\left(J_{n,n+1}^2/Y_0 + N_1\right)\sin\theta_A}{J_{01}J_{n,n+1}Z_A},$$

$$B_6 = -\frac{\left(J_{n,n+1}^2/Y_0 + N_1\right)\cos\theta_A}{J_{01}J_{n,n+1}} - \frac{jJ_{n,n+1}Z_A\sin\theta_A}{J_{01}},$$

$$C_6 = -\frac{jJ_{01}\sin\theta_A}{J_{n,n+1}Z_A},$$

$$D_6 = -\frac{J_{01}\cos\theta_A}{J_{n,n+1}}.$$

Then, the insertion phase $\angle S_{12}$ can be obtained as:

$$\angle S_{12} = -\tan^{-1}\frac{B_6Y_0 + C_6/Y_0}{j(A_6 + D_6)}. \tag{15}$$

In a similar way, the insertion phase $\angle S_{13}$ can be obtained as:

$$\angle S_{13} = -\tan^{-1}\frac{B_7Y_0 + C_7/Y_0}{j(A_7 + D_7)}, \tag{16}$$

where

$$A_7 = -\frac{J_{n,n+1}}{J_{01}},$$

$$B_7 = -\frac{N_1 + J_{n,n+1}^2\left(1/Y_0 + jZ_A\cos\theta_A\right)}{J_{01}J_{n,n+1}},$$

$$C_7 = \theta_A,$$

$$D_7 = -\frac{J_{01}}{J_{n,n+1}}.$$

Once the phase shifts $\angle S_{12}$ and $\angle S_{13}$ are achieved, the phase difference between the output ports can be finally solved by subtracting the two equations ($\angle S_{12}$ and $\angle S_{13}$). Furthermore, the desired electrical length of the branch line can be obtained.

Analysis of Isolation Between Outputs

After analyzing the phase difference between outputs, the isolation can also be derived by means of the microwave network analysis method [13]. First, assuming that the incident wave is only introduced in port #2 and output in port #3 ($G_A = G_B = Y_0$), the topology diagram of the dual-band filtering power division network with phase-shifting function in **Figure 1A** is appropriately simplified and redrawn, as shown in **Figure 3**.

The equivalent circuit diagram has five sub-circuits, which are represented as sub-circuits I, II, III, IV, and V, respectively. As mentioned earlier, with the calculated admittance N_1 of sub-circuit II, the ABCD matrix of sub-circuit III can be deduced as:

$$\begin{pmatrix} A_1 & B_1 \\ C_1 & D_1 \end{pmatrix} = \begin{pmatrix} -1 & -\frac{N}{J_{n,n+1}^2} \\ 0 & -1 \end{pmatrix}. \tag{17}$$

Then, we can attain the admittance matrix Y_1 of sub-circuit III with the following equation by conveniently transforming the ABCD matrix to its corresponding admittance matrix:

$$\mathbf{Y}_1 = \begin{pmatrix} \frac{D_1}{B_1} & \frac{B_1C_1 - A_1D_1}{B_1} \\ -\frac{1}{B_1} & \frac{A_1}{B_1} \end{pmatrix} = \begin{pmatrix} \frac{J_{n,n+1}^2}{N} & \frac{J_{n,n+1}^2}{N} \\ \frac{J_{n,n+1}^2}{N} & \frac{J_{n,n+1}^2}{N} \end{pmatrix}. \tag{18}$$

In a similar way, the admittance matrix Y_2 of sub-circuit IV can be derived as:

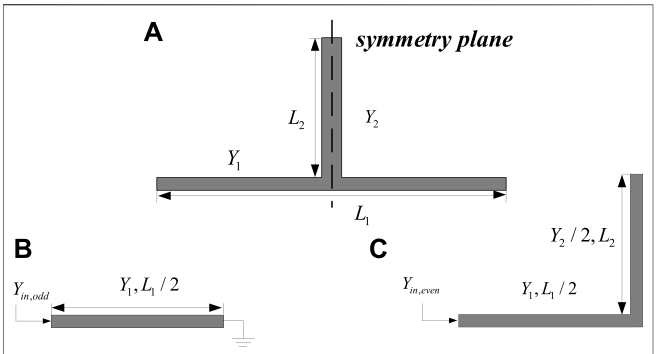

FIGURE 4 | (A) Structure of the employed E-shape resonator. **(B)** Odd-mode equivalent circuit. **(C)** Even-mode equivalent circuit.

$$\mathbf{Y}_2 = \begin{pmatrix} \frac{1}{R} & -\frac{1}{R} \\ -\frac{1}{R} & \frac{1}{R} \end{pmatrix}. \tag{19}$$

In the meantime, the ABCD matrix of sub-circuit V is shown as follows:

$$\begin{pmatrix} A_5 & B_5 \\ C_5 & D_5 \end{pmatrix} = \begin{pmatrix} \cos\theta_A & jZ_A \sin\theta_A \\ \frac{j\sin\theta_A}{Z_A} & \cos\theta_A \end{pmatrix}. \tag{20}$$

Then, the result of $Y_1 + Y_2$ should be converted into an ABCD matrix and cascaded with the ABCD matrix of sub-circuit V to find the whole ABCD matrix of the schematic that has been analytically derived as follows:

$$\begin{pmatrix} A_6 & B_6 \\ C_6 & D_6 \end{pmatrix}, \tag{21}$$

where

$$A_6 = \frac{N_3R\left(N_3 + J_{n,n+1}^2R\right)\cos\theta_A - 4jJ_{n,n+1}^2\left(N_3 - J_{n,n+1}^2R\right)Z_A\sin\theta_A}{N_3R\left(N_3 - J_{n,n+1}^2R\right)},$$

$$B_6 = \frac{N_3R\cos\theta_A + j\left(N_3 + J_{n,n+1}^2R\right)Z_A\sin\theta_A}{N_3 - J_{n,n+1}^2R},$$

$$C_6 = \frac{-4J_{n,n+1}^2\left(N_3 - J_{n,n+1}^2R\right)Z_A\cos\theta_A + jN_3R\left(N_3 + J_{n,n+1}^2R\right)\sin\theta_A}{N_3R\left(N_3 - J_{n,n+1}^2R\right)Z_A},$$

$$D_6 = \frac{\left(N_3 + J_{n,n+1}^2R\right)Z_A\cos\theta_A + jN_3R\sin\theta_A}{\left(N_3 - J_{n,n+1}^2R\right)Z_A}.$$

Till now, the scattering parameter S_{23} can be derived according to the conversion relationship between S parameter and transfer matrix, and then the isolation resistance R can be further obtained by setting $S_{23} = 0$. The solution formula of resistance R can be derived as follows:

$$R = \frac{H_1 + H_2}{H_3}, \tag{22}$$

where

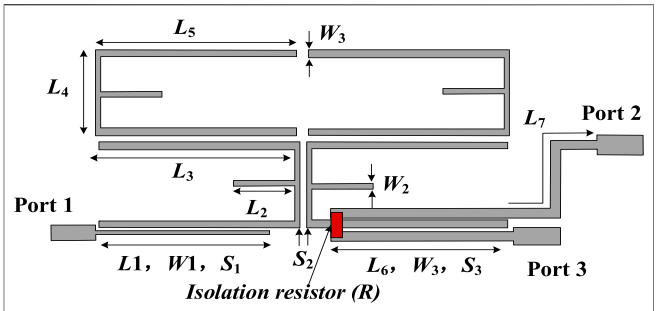

FIGURE 5 | Configuration of the proposed dual-band FPD with physical dimensions: $L_1 = 16.5$, $L_2 = 8.5$, $L_3 = 17$, $L_4 = 7.65$, $L_5 = 17.9$, $L_6 = 16.3$, and $L_7 = 24$, $W_1 = 0.36$, $W_2 = 0.3$, and $W_3 = 1.1$, $S_1 = 0.1$, $S_2 = 0.3$, and $S_3 = 0.1$ (all units: mm), and R = 195Ω. The design targets of the proposed dual-band FPD are given as follows: 1) Passbands 1: 1.87–1.92 GHz; 2) Passbands 2: 2.06–2.11 GHz; 3) Return loss: 20 dB; 4) Isolation: >20 dB; 5) Phase distribution: 90°.

$$H_1 = -2\sqrt{J_{n,n+1}^8 - 2J_{n,n+1}^6N_3} + 2J_{n,n+1}^4\cos^2\theta_A,$$
$$H_2 = -J_{n,n+1}^2N_3\cos^2\theta_A + 2J_{n,n+1}^4\sin^2\theta_A - J_{n,n+1}^2N_3\sin^2\theta_A,$$
$$H_3 = J_{n,n+1}^4\cos^2\theta_A + J_{n,n+1}^4\sin^2\theta_A.$$

When all the design parameters are known, the analytical solution of the required resistance R can be obtained through **Eq. 16**. In the next section, the microstrip E-shape resonator is chosen as the basic resonant element to design a dual-band filtering power divider with 90° phase distribution, which verifies the proposed design method.

IMPLEMENTATION AND RESULTS

To validate this design method, a dual-band FPD prototype was designed and fabricated based on the substrate of Rogers RO4003C with a relative dielectric constant $\varepsilon_r = 3.55$, thickness $h = 0.508$ mm, and loss tangent tan $\delta = 0.0027$.

The L/C resonators are all implemented by E-shape resonators as shown in **Figure 3A**, and the external/internal couplings are all controlled through the gap couplings. Based on the aforementioned analytical equation, the required design parameters can be obtained.

For the E-shape resonators, it can be analyzed by means of even/odd-mode analysis, and the odd-mode and even-mode equivalent circuits are shown in **Figures 4B, C**. Based on the even/odd-mode analysis, the resonant frequency of the odd-mode and even-mode can be obtained as [14]:

$$f_{in,odd} = \frac{c}{4(L_1/2)\sqrt{\varepsilon_{eff}}}, \tag{23}$$

$$f_{in,even} = \frac{c}{4(L_1/2 + L_2)\sqrt{\varepsilon_{eff}}}. \tag{24}$$

The odd-mode resonant frequency of two pairs of E-shape resonators is used to construct the dual-band filtering power divider.

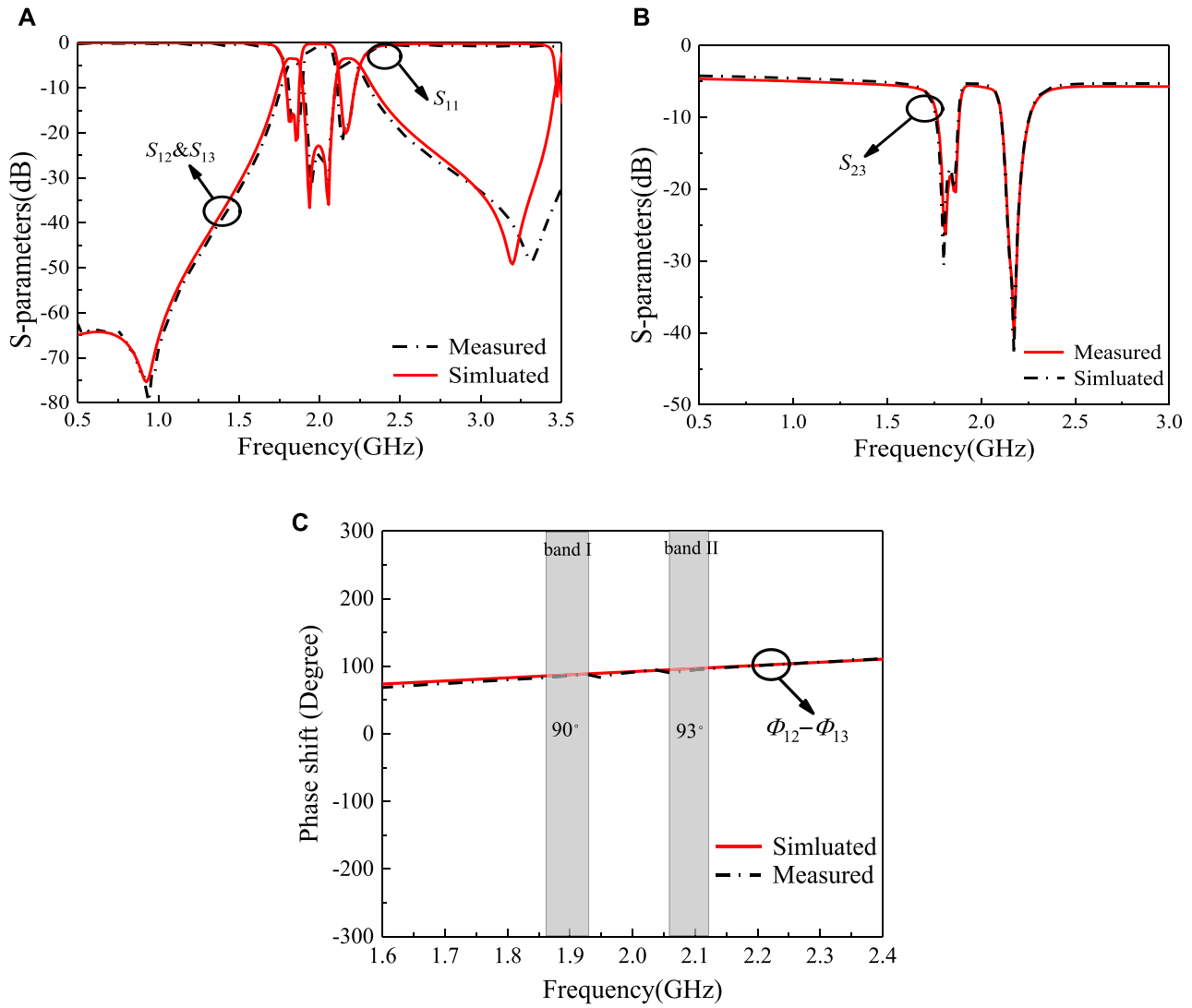

FIGURE 6 | Measured and simulated results of the proposed dual-band FPD. **(A)** Magnitudes of S_{11}, S_{12}, and S_{13}. **(B)** Magnitudes of S_{23}. **(C)** $\angle S_{12}-\angle S_{13}$.

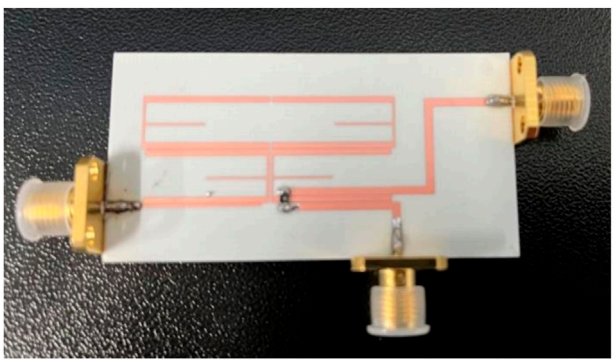

FIGURE 7 | Photograph of the fabricated circuit board.

The whole configuration of the proposed dual-band FPD including corresponding dimensions is shown in **Figure 5**. As observed, there are two pairs of dual-mode resonators between the input port and the output port. The lower pairs of dual-mode resonators are the bandpass resonators, while the upper pairs of dual-mode resonators are the bandstop resonators. The signal is introduced from port #1 and coupled to the arm of the first E-shape resonator. Then, the signal flows through the two pairs of E-shape resonators and is coupled to the two output ports (port #2 and port #3) by the arm of the second bandpass E-shape resonator, which forms a three-coupled line structure. Also, the isolation resistance R is loaded on the front end of the three-coupled line structure to achieve good port–port isolation.

In addition, **Figures 6A, B** exhibit the simulated and measured results of the proposed dual-band FPD. As shown in **Figures 6A, B**, the measured insertion losses are 1.2 and 1.3 dB, respectively, the

measured return losses are all higher than 18 dB, and the measured in-band isolation within two output ports is all higher than 16 dB. Moreover, the phase difference between two outputs within the two passbands is about 90° with less than 3° phase imbalance. The photograph of the fabricated circuit board of the dual-band FPD is shown in **Figure 7**. The overall size of the circuit is $0.67\lambda g \times 0.53\lambda g$, where λg is the relative wavelength of the center frequency. In conclusion, the decent results exhibit the feasibility and effectivity of our proposed design method.

CONCLUSION

This study presented a novel synthesis design method of dual-band FPD including arbitrary phase distribution based on the topology of inverter-coupled L/C resonators. A representative dual-band FPD with 90° phase distribution based on E-shape resonators has been designed and fabricated to verify the design method. It is our belief that the proposed method will be very attractive in future multi-functional wireless communication systems.

DATA AVAILABILITY STATEMENT

The original contributions presented in the study are included in the article/Supplementary Material, further inquiries can be directed to the corresponding author.

AUTHOR CONTRIBUTIONS

JS, WL, KP, ZZ provide the idea and write the paper. MS modify the paper.

REFERENCES

1. Wang K-X, Zhang XY, Hu B-J. Gysel Power Divider with Arbitrary Power Ratios and Filtering Responses Using Coupling Structure. *IEEE Trans Microwave Theor Techn* (2014) 62(3):431–40. doi:10.1109/tmtt.2014.2300053
2. Chau W-M, Hsu K-W, Tu W-H. Filter-based Wilkinson Power Divider. *IEEE Microw Wireless Compon Lett* (2014) 24(4):239–41. doi:10.1109/lmwc.2014.2299543
3. Chen C-J, Ho Z-C. Design Equations for a Coupled-Line Type Filtering Power Divider. *IEEE Microw Wireless Compon Lett* (2017) 27(3):257–9. doi:10.1109/lmwc.2017.2661968
4. Bai YC, Xu. KD. High-performance Filtering Power Divider with Multiple Transmission Zeros. *Microw Opt Technol Lett* (2018) 60(11):2673–6. doi:10.1002/mop.31468
5. Xu KD, Bai Y, Ren X, Xue Q. Broadband Filtering Power Dividers Using Simple Three-Line Coupled Structures. *IEEE Trans Compon., Packag Manufact Technol* (2019) 9(6):1103–10. doi:10.1109/tcpmt.2018.2869077
6. Yu W, Xu L, Zhang XY, Chen J-X. Dual-band Dual-Mode Dielectric Resonator Filtering Power Divider with Flexible Output Phase Difference and Power Split Ratio. *IEEE Trans Microwave Theor Techn.* (2022) 70(1):190–9. doi:10.1109/tmtt.2021.3113654
7. Hong W, Jiang ZH, Yu C, Zhou J, Chen P, Yu Z, et al.Multibeam Antenna Technologies for 5G Wireless Communications. *IEEE Trans Antennas Propagat* (2017) 65(12):6231–49. doi:10.1109/tap.2017.2712819
8. Basavarajappa V, Pellon A, Montesinos-Ortego I, Exposito BB, Cabria L, Basterrechea J. Millimeter-wave Multi-Beam Waveguide Lens Antenna. *IEEE Trans Antennas Propagat* (2019) 67(8):5646–51. doi:10.1109/tap.2019.2916388
9. Lyu Y-P, Zhu L, Cheng C-H. A New Design of Filtering Power Dividers with Arbitrary Constant Phase Difference, Impedance Transformation, and Good Isolation. *IEEE Access* (2019) 7:169495–507. doi:10.1109/access.2019.2955104
10. Kim S, Chaudhary G, Jeong Y. Filtering Power Divider with Arbitrary Prescribed Phase Difference. In: 2020 IEEE Asia-Pacific Microwave Conference (APMC) (2020):421–3.
11. Zhu X, Yang T, Chi P, Xu R. Miniaturized Reconfigurable Filtering Power Divider with Arbitrary Output Phase Difference and Improved Isolation. In: 2021 IEEE MTT-S International Microwave Symposium (IMS) (2021):104–7.
12. Hong J-S. *Microstrip Filters for Rf/microwave Applications*. New York, NY, USA: Wiley (2001).
13. Lee B, Nam S, Lee J. Optimization-free Design Equations for Narrowband Equal-Division Filtering Power Divider with Pre-specified Filtering Response and Wideband Isolation. *IEEE Trans Circuits Syst* (2019) 66(7):2496–507. doi:10.1109/tcsi.2019.2898465
14. Tang L, Zhang X, Jiao F, Liu S, Zhang G, Yang J. Design of a Compact Microstrip Triplexer-Power Divider with E-Shaped Resonator. In: 2019 International Conference on Microwave and Millimeter Wave Technology (ICMMT) (2019):1–2.

Conflict of Interest: The authors declare that the research was conducted in the absence of any commercial or financial relationships that could be construed as a potential conflict of interest.

frontiers | Frontiers in Physics

ORIGINAL RESEARCH
published: 17 May 2022
doi: 10.3389/fphy.2022.862516

A New Triple-Band Four-Way Filtering Power Divider With Highly Improved Performance

Yibing Li[1], Xin Zhou[1,2], Xiaohang Sun[1], Xiaojun Gu[1], Bin Xu[1], Xinde Zhang[1,2] and Kang Ping[1,2]*

[1]Hengdian Electronics Co., Ltd., Nanjing, China, [2]School of Electrical and Automation Engineering, Nanjing Normal University, Nanjing, China

This letter presents a new triple-band four-way filtering power divider (FPD) with greatly improved frequency selectivity and in-band isolation. By elaborately developing a multi-port multi-mode topology between four identical multi-mode resonators and feedlines, a triple-band four-way FPD is attained. In order to validate the feasibility of the proposal, one prototype is designed, fabricated, and measured. Both the simulated and measured results of the designed FPD are provided with a good agreement. Results indicate that this triple-band four-way FPD exhibits not only sharp selective filtering performance, but also satisfactory port-to-port isolations.

Keywords: filtering power divider (FPD), four-way, triple-band, multi-mode, isolation

OPEN ACCESS

Edited by:
Kai-Da Xu,
Xi'an Jiaotong University, China

Reviewed by:
Lei Guo,
The University of Queensland, Australia
Xuedao Wang,
Jinling Institute of Technology, China

****Correspondence:***
Xiaohang Sun
Xiaohang_Sun_hdmw@126.com

Specialty section:
This article was submitted to Optics and Photonics, a section of the journal Frontiers in Physics

Received: *26 January 2022*
Accepted: *16 February 2022*
Published: *17 May 2022*

Citation:
Li Y, Zhou X, Sun X, Gu X, Xu B, Zhang X and Ping K (2022) A New Triple-Band Four-Way Filtering Power Divider With Highly Improved Performance. Front. Phys. 10:862516. doi: 10.3389/fphy.2022.862516

INTRODUCTION

In recent years, with the rapid development of modern wireless communication systems, integrated function RF components have become key devices for multi-communication standards. In the conventional wireless communication system, two indispensable components, power divider [1, 2] and filter [3, 4], are usually cascaded together. However, cascaded devices always lead to large circuit sizes and degraded operating performance. In order to solve this problem, filtering power dividers (FPDs) have received increasing attention, which are multi-function integrated devices that provide both frequency band selection as a filter and power splitting/combining as a power divider. Many FPDs have been proposed, such as microstrip-to-slot transition integrated FPDs [5], substrate integrated waveguide (SIW) resonator cavity based FPDs [6], metamaterial or composite right/left handed transmission lines based FPDs [7], FPD formed by integrating bandpass filter and low-pass filter integrated into a Wilkinson power divider [8], and microstrip multi-mode resonator based FPD [9–11]. However, only a few FPDs with multi-way or multi-band power division have been reported [12–14]. By utilizing the TM_{20} mode of the square patch and the TE_{110} mode of the SIW cavity resonator, a wideband four-way FPD was proposed in [12]. In [13], a four-way FPD was achieved by introducing coupled lines instead of the quarter-wavelength in conventional Wilkinson power divider. To reduce circuit size and improve operation performance, a four-way FPD was realized based on two looped coupled-lines in [14]. For application of multi-passband, a four-way FPD with reconfigurable characteristics is proposed in [15]. By controlling the varactor, the switchable single/dual/wideband filtering response can be adjusted. The aforementioned works have achieved interesting results, but researches about multi-way multi-band FPD are quite few. To meet the up-to-date development trends, it is meaningful and necessary to explore the design of multi-way multi-band FPD.

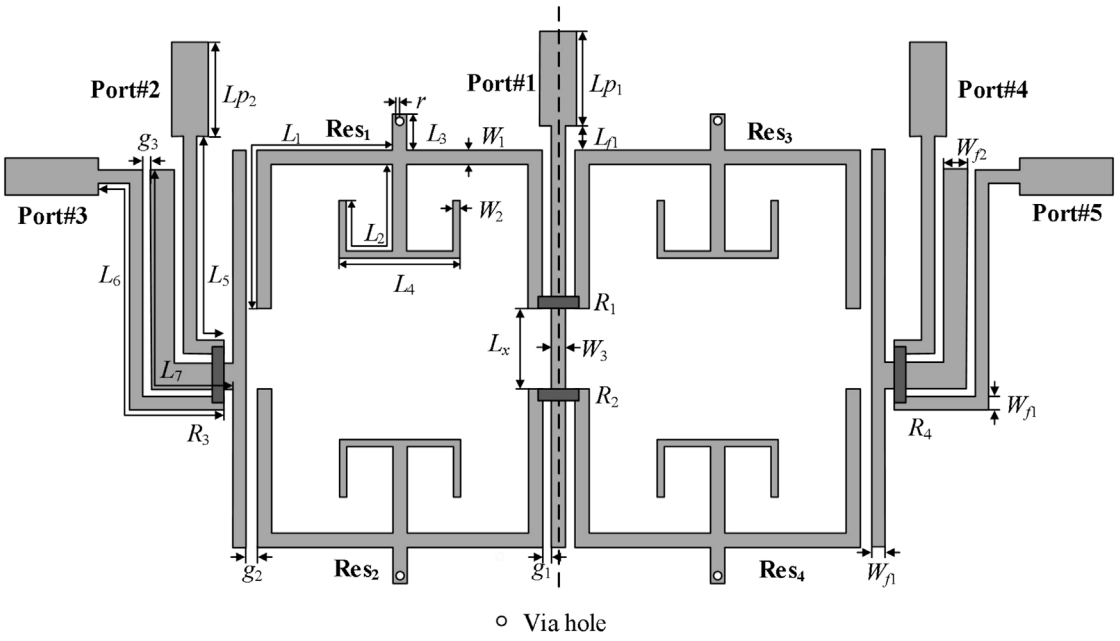

FIGURE 1 | Configuration of proposed four-way triple-band FPD.

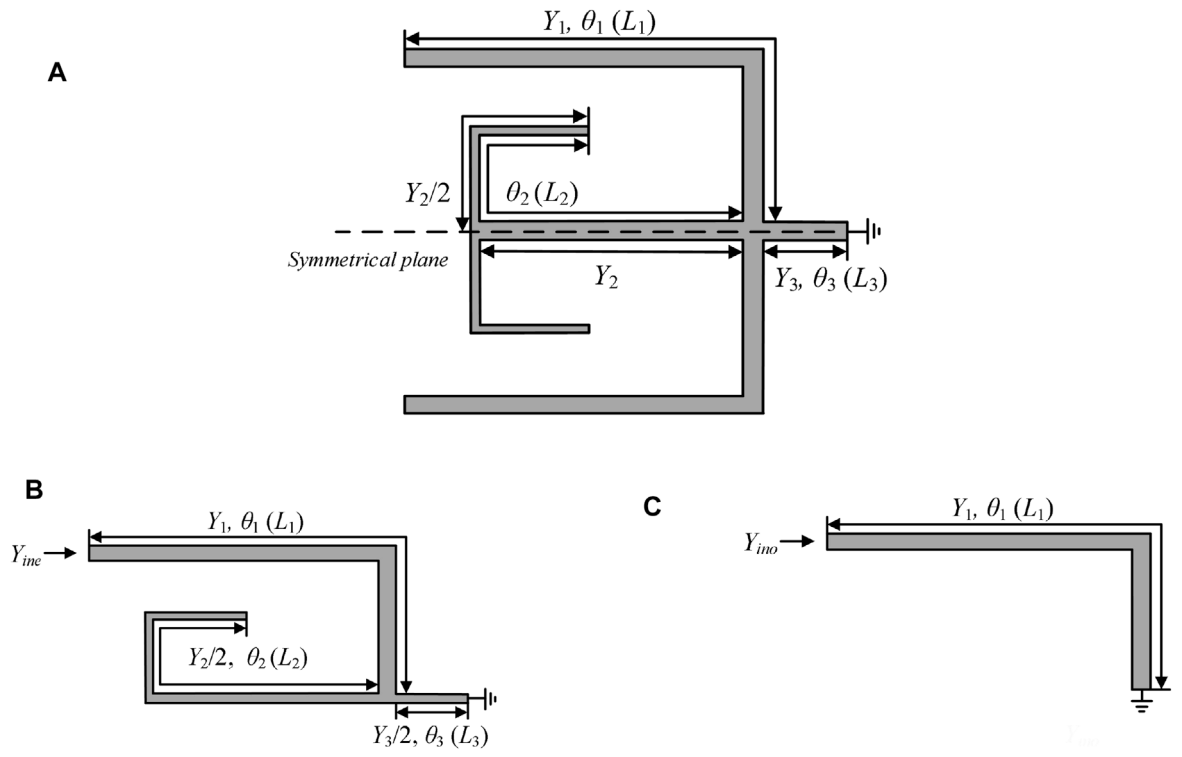

FIGURE 2 | Structure of triple-mode resonator and even-/odd-mode. **(A)** Entire resonator. **(B)** Even-mode equivalent circuit. **(C)** Odd-mode equivalent circuit.

In this letter, a new four-way triple-band FPD with sharp frequency selectivity and high port-to-port isolations is presented. By reasonably distributing the first three resonant modes of four triple-mode resonators for each band, the proposed FPD can be operated at three different frequencies of 1.65, 2, and 2.27 GHz. Meanwhile, favorable isolation

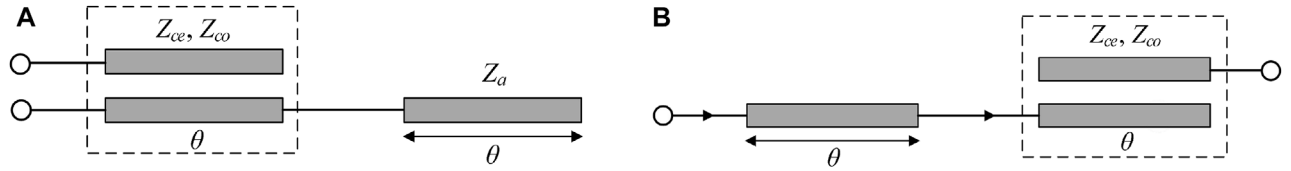

FIGURE 3 | Schematics of two coupled-line prototypes. **(A)** Type A prototype. **(B)** Type B prototype.

performances are attained by loading isolated resistors across output feeding lines and adjacent arms of the adopted resonators. For validation, a prototype is designed, fabricated, and tested. The measured results have a good agreement with the simulated results, which prove the concept of the design.

CONFIGURATION OF THE PROPOSED FOUR-WAY TRIPLE-BAND FPD

The configuration of the proposed four-way triple-band FPD is shown in **Figure 1**. As observed, it is mainly composed of four triple-mode resonators, two T-shaped coupled output lines, five microstrip input/output transmission lines, and four isolation resistors. In particular, the employed four triple-mode resonators are located symmetrically on both sides of the common open-ended input transmission line in this design, and two pairs of output transmission lines are placed at both sides of the two T-shaped coupled output lines, respectively. In addition, two of isolated resistors (R_1, R_2) are loaded between the inner adjacent arms of two pairs of resonators while the other two isolated resistors (R_3, R_4) connect the two open ends of the output line to achieve nice port-to-port isolation. It can distinctly see from the structure that the signal input from Port#1 is first transmitted along the open input line and then evenly coupled to the resonators on both sides of the input line to the T-shaped coupled lines, and finally coupled to output ports (Port#2, Port#3, Port#4, and Port#5) with equal power distribution. Based on the proposed symmetrical circuit structure, the couplings between the resonators and the output lines have the same amplitude and in-phase characteristics. In this way, the desired four-way triple-band filtering power division response can be achieved.

DESIGN AND ANALYSIS OF THE PROPOSED FOUR-WAY TRIPLE-BAND FPD

In this design, as shown in **Figures 2A**, a triple-mode net-type resonator is formed by connecting one net-type open-ended stub, one short-ended stub, and two open-ended stubs, which is

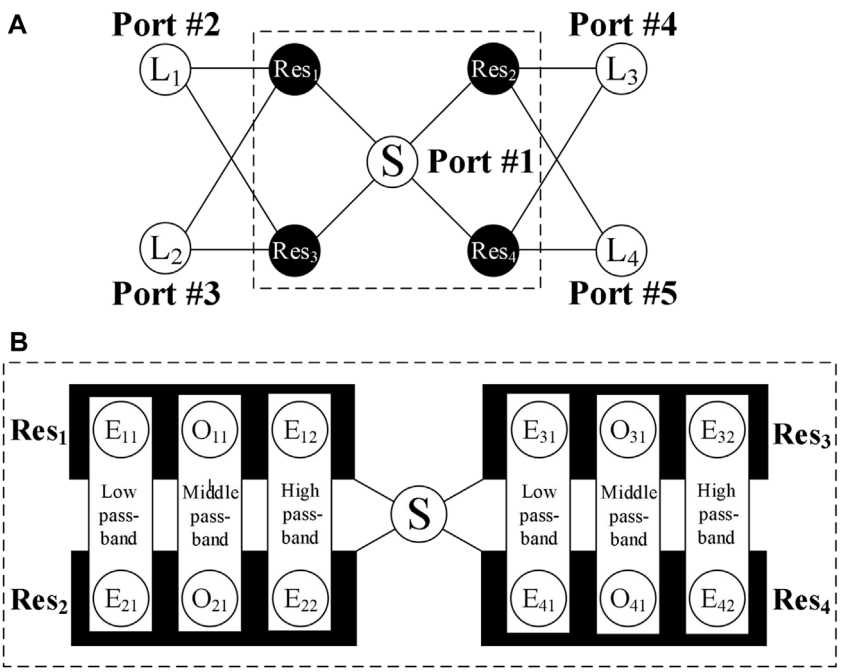

FIGURE 4 | The coupling topology and mode distribution. **(A)** The design coupling scheme of proposed FPD. **(B)** The modes consist of three passbands.

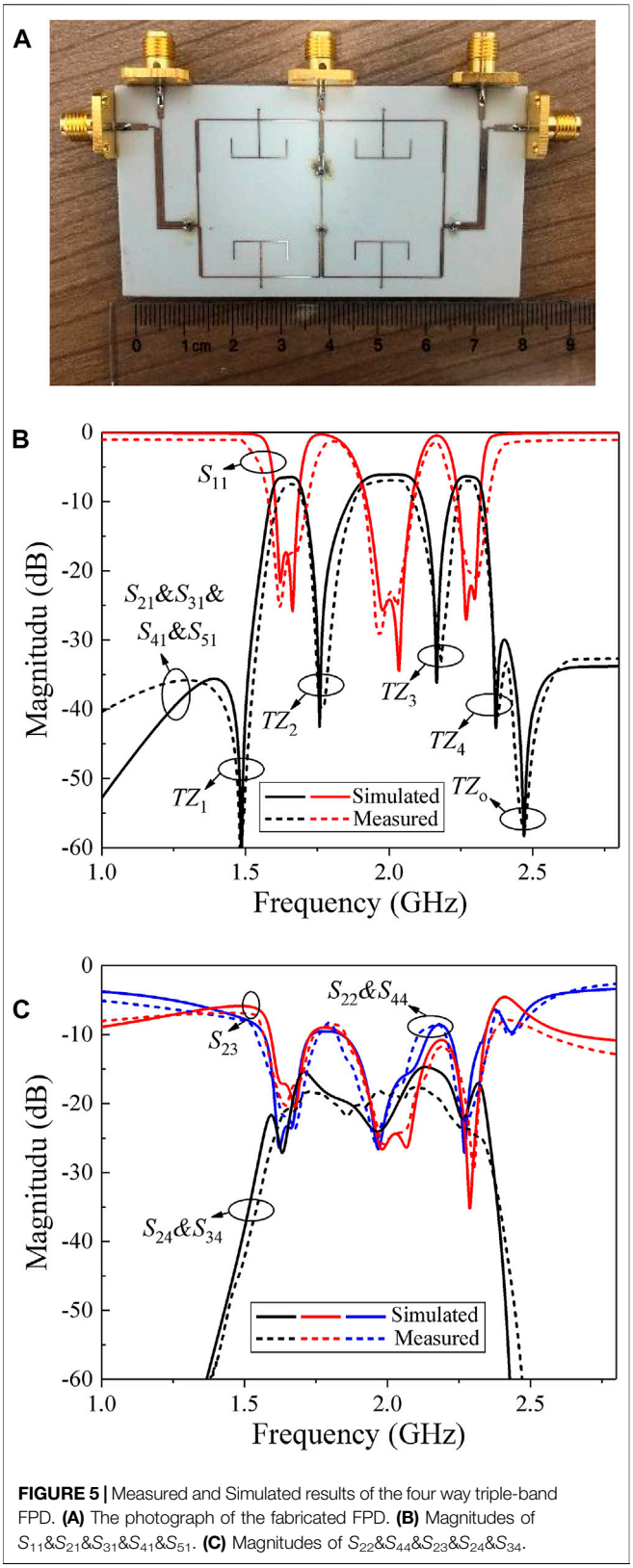

FIGURE 5 | Measured and Simulated results of the four way triple-band FPD. **(A)** The photograph of the fabricated FPD. **(B)** Magnitudes of $S_{11}\&S_{21}\&S_{31}\&S_{41}\&S_{51}$. **(C)** Magnitudes of $S_{22}\&S_{44}\&S_{23}\&S_{24}\&S_{34}$.

inspired by [16, 17]. Because the employed resonator has a symmetrical structure with the reference to the symmetrical plane, the even-/odd-mode analysis method [18] can be applied in analyzing its resonance characteristics. With odd-/even-mode excitation, the symmetrical plane behaves as magnetic/electrical wall. The equivalent circuits for the resonator are shown in **Figures 2B,C**, respectively. According to transmission line theory, the input admittances of odd-/even-mode equivalent circuits are calculated as **Eqs 1**, **2**:

$$Y_{in,odd} = -\mathrm{j}Y_1\cot\theta_1 \tag{1}$$

$$Y_{in,even} = Y_1\frac{-\mathrm{j}Y_3\cot\theta_3 + \mathrm{j}Y_2\tan\theta_1 + \mathrm{j}2Y_1\tan\theta_1}{2Y_1 + Y_3\cot\theta_3\tan\theta_1 - Y_2\tan^2\theta_1} \tag{2}$$

where Y_i $(i = 1, 2, 3)$ denotes the characteristic admittance of each transmission line section. $\theta_i\,(= 2\pi f L_i\sqrt{\varepsilon_{eff}}/c, i = 1, 2, 3)$ represents the related electrical lengths, where c and ε_{eff} are the light speed in free space and the effective dielectric constant of the substrate. Based on **Eqs 1**, **2**, a triple-mode resonator whose first three resonant modes are even mode, odd mode, and even mode can be designed. Its first three resonance frequencies (f_{even1}, f_{odd1} and f_{even2}) are derived as **Eqs 3** and **4** when $Y_{in,odd} = 0$ and $Y_{in,even} = 0$.

$$Y_3\cot\theta_3 - Y_2\tan\theta_2 = 2Y_1\tan\theta_1\,(\mathrm{even-mode}) \tag{3}$$

$$\theta_1 = 90^\circ\,(\mathrm{odd-mode}) \tag{4}$$

Furthermore, the three resonance frequencies of even-/odd-mode can be roughly estimated as **Eq. 5**:

$$f_{\mathrm{even1}} \approx \frac{\pi f_0}{2(\theta_1+\theta_3)}, f_{\mathrm{even2}} \approx \frac{\pi f_0}{\theta_1+\theta_2}, f_{\mathrm{odd}} = \frac{\pi f_0}{2\theta_1} \tag{5}$$

where f_0 is the center frequency. By setting $Y_{in,odd} = Y_{in,even}$, an inherent transmission zero (TZ) frequency can be deduced by $f_{TZ_0} = \frac{\pi f_0}{2\theta_2}$. Besides, the other four additional TZs are introduced by two coupled-line prototypes. **Figure 3** shows two adopted coupled line sections in the design, i.e., Type A and Type B coupled-line prototypes, which are based on anti-parallel and parallel coupling lines. For the Type A protoype, the frequencies of the two transmission zeros TZ_2 and TZ_3 can be deduced by $f_{TZ_2} = \frac{2f_0}{\pi}\arctan\sqrt{\frac{2Z_a}{Z_{ce}+Z_{co}}}$ and $f_{TZ_3} = \frac{2f_0}{\pi}[\pi - \arctan\sqrt{\frac{2Z_a}{Z_{ce}+Z_{co}}}]$. Similarly, the frequencies of other two transmission zeros TZ_1 and TZ_4 can also be established near $\frac{\pi f_0}{2(\theta_1+\theta_3)}$ and $\frac{\pi f_0}{\theta_1+\theta_2}$, respectively.

Figure 4 presents the coupling topology and mode distribution of the proposed four-way triple-band FPD. It can be seen from **Figure 4A** that an incident signal that is fed at Port #1 is divided into two same signals by symmetrically coupling to two pairs of identical triple-mode resonators. Then, by proper exciting the first three resonant modes of the triple-mode resonators and coupling them to the four output ports, four-way filtering power division is realized. In **Figure 4A**, S and $L_{1/2/3/4}$ denote source and loads while $Res_{1/2/3/4}$ represents the employed net-type triple-mode resonators. Among them, resonators $Res_{1/2}$ and resonators $Res_{3/4}$ as well as loads $L_{1/2}$ and $L_{3/4}$ are

TABLE 1 | Comparisons with other previous works

References	No. of bands/No. of ways	Input RL/Output RL, dB	In-band isolation, dB	IL, dB	Size, λ_g^2	TZs
[13]	Single-band Four-way	>15.6/14.7	>12	6.48	0.16 × 0.55	4
[14]	Single-band Four-way	>10.5/16.8	>13	6.8	0.32 × 0.32	4
[15]	Dual-band Four-way	>16.7, 18.5/17.1, 13.8	>21.7/33.2	7.3/8.5	0.38 × 0.34	3
This work	Triple-band Four-way	**>17.3, 23.1, 20.2/17.1, 17.3, 16.3**	**>17.0/16.3/17.8**	**7.44/6.92/7.02**	**0.83 × 0.44**	**5**

IL, insertion loss; RL, return loss; TZs, transmission zeros. Bolded values on the bottom row highlight results from our research.

symmetrically arranged. **Figure 4B** is a schematic diagram of the contents of the dotted frame in **Figure 4A**, which describes detailed mode distribution for multi-band. It can be clearly seen that the corresponding mode contributes to each passband of the triple band. Specifically, each resonator of $Res_{1/2/3/4}$ is composed of three resonance modes, which are even mode E_{11} (E_{21}, E_{31}, E_{41}), odd mode O_{11} (O_{21}, O_{31}, O_{41}), and even mode E_{12} (E_{22}, E_{32}, E_{42}), respectively. Among them, the first even modes E_{11} (E_{31}) and E_{21} (E_{41}) of the resonator Res_1 (Res_3) and Res_2 (Res_4) constitute low passband response. In a similar way, the first odd modes O_{11} (O_{31}) and O_{21} (O_{41}) of the resonator Res_1 (Res_3) and Res_2 (Res_4) constitute middle passband response. Besides, the second even modes E_{12} (E_{32}) and E_{22} (E_{42}) of the resonator Res_1 (Res_3) and Res_2 (Res_4) constitute high passband response. Based on the above the coupling topology and mode distribution, a four-way triple-band filtering power divider can be initially implemented. Meanwhile, for achieving good port-to-port isolations, two isolated resistors are elaborately introduced between the inner adjacent arms of two pairs of resonators while the other two isolated resistors are properly placed between the adjacent output lines as shown in **Figure 1**.

IMPLEMENTATION AND RESULTS

Based on the above analysis, one prototype four-way triple-band FPD was fabricated on a Rogers RO4003C substrate with a relative dielectric constant ε_r = 3.55, thickness h = 0.508 mm, and loss tangent tan δ = 0.0027. The photograph of the fabricated four-way triple-band FPD with size of 66.8 × 35.2 mm^2 ($0.83\lambda_g \times 0.44\lambda_g$) is shown in **Figure 5A**. The final optimal layout parameters (in mm) in **Figure 1** are: L_1 = 21.86, L_2 = 15.62, L_3 = 2.03, L_4 = 10.82, L_5 = 25.44, L_6 = 27.86, L_7 = 25.53, L_p = 6.28, L_{f1} = 1.36, L_x = 10.81, W_1 = 0.22, W_2 = 0.18, W_3 = 0.23, W_{f1} = 0.32, W_{f2} = 0.64, g_1 = 0.14, g_2 = 0.11, g_3 = 0.1, r = 0.1, R_1 = 2000 Ω, R_2 = 1,000 Ω, R_3 = 220 Ω, and R_4 = 220 Ω. The frequency characteristic of the proposed four-way triple-band FPD was studied by the electromagnetic simulator HFSS and the network analyzer Agilent N5244A. The simulation and measured results are shown in **Figures 5B,C**. Due to the connection loss of the SMA connector, there is a certain discrepancy between the simulation results and the measurement ones. Results indicate that the proposed FPD works at the center frequency of 1.67, 2.10, and 2.26 GHz, with corresponding 3-dB fractional bandwidths of 7%, 12%, and 11%. In addition, as expected, five TZs are generated, at 1.48, 1.76, 2.16, 2.37, and 2.47 GHz, ensuring sharp roll-off skirt and out-of-band harmonic suppression. Meanwhile, the measured insertion losses (ILs) are 7.44, 6.92, 7.02 dB while input return losses (RLs) are better than 17.3, 23.1, and 20.2 for the three passbands, respectively. Besides, the output RLs are better than 17.1, 17.3, and 16.3 dB. Moreover, the three passbands exhibit higher than the 17.0, 16.3, and 17.8 dB isolation for each passband, respectively. **Table 1** tabulates the performance comparison between the proposed four-way triple-band FPD and other reported works. It can be seen that our proposed FPD exhibits nice return loss, sharp frequency selectivity with multiple TZs, as well as high port-to-port isolations.

CONCLUSION

In this letter, a novel triple-band four-way FPD with highly improved performance has been presented. After clearly analyzing its working mechanism, a four-way triple-band FPD is implemented with nice multi-band filtering performance and satisfactory port-to-port isolation. It is believed that the proposed design is very attractive for multi-way multi-band application in wireless multi-communication standard systems.

DATA AVAILABILITY STATEMENT

The original contributions presented in the study are included in the article/Supplementary Material, further inquiries can be directed to the corresponding author.

AUTHOR CONTRIBUTIONS

YL conducted extensive analysis and wrote parts of this paper. XZ gave assistance in the measurement and wrote parts of this paper. XS, XG, BX, XZ, and KP revised this paper.

REFERENCES

1. Lei Wu L, Zengguang Sun Z, Yilmaz H, Berroth M. A Dual-Frequency Wilkinson Power Divider. *IEEE Trans Microwave Theor Techn.* (2006) 54: 278–84. doi:10.1109/tmtt.2005.860300
2. Guo L, Zhu H, Abbosh AM. Wideband Tunable In-phase Power Divider Using Three-Line Coupled Structure. *IEEE Microw Wireless Compon Lett* (2016) 26: 404–6. doi:10.1109/lmwc.2016.2562058
3. Xu K-D, Xia S, Jiang Y, Guo Y-J, Liu Y, Wu R, et al. 'Compact Millimeter-Wave On-Chip Dual-Band Bandpass Filter in 0.15-μm GaAs Technology'. *IEEE J Electron Devices Soc* (2022) 10:152–156. doi:10.1109/jeds.2022.3143999
4. Xu K-D, Lu S, Guo Y-J, Chen Q. Quasi-Reflectionless Filters Using Simple Coupled Line and T-Shaped Microstrip Structures. *IEEE J Radio Freq Identif* (2022) 6:54–63. doi:10.1109/jrfid.2021.3106664
5. Zhu H, Cheng Z, Guo YJ. Design of Wideband In-phase and Out-of-phase Power Dividers Using Microstrip-To-Slotline Transitions and Slotline Resonators. *IEEE Trans Microwave Theor Techn.* (2019) 67:1412–24. doi:10.1109/tmtt.2019.2897928
6. Zhang G, Liu Y, Wang E, Yang J. Multilayer Packaging SIW Three-Way Filtering Power Divider with Adjustable Power Division. *IEEE Trans Circuits Syst* (2020) 67(12):3003–7. doi:10.1109/tcsii.2020.2987327
7. Keshavarz. S, Abdipour A, Mohammadi A, Keshavarz R. 'Design and Implementation of Low Loss and Compact Microstrip Triplexer Using CSRR Loaded Coupled Lines'. *Aeu-int J Electron Commun* (2019) 111:1–5. doi:10.1016/j.aeue.2019.152913
8. Chau W-M, Hsu K-W, Tu W-H. Filter-Based Wilkinson Power Divider. *IEEE Microw Wireless Compon Lett* (2014) 24:239–41. doi:10.1109/lmwc.2014.2299543
9. Zhang G, Wang X, Hong J-S, Yang J. A High-Performance Dual-Mode Filtering Power Divider with Simple Layout. *IEEE Microw Wireless Compon Lett* (2018) 28:120–2. doi:10.1109/lmwc.2018.2789821
10. Zhang G, Yang J, Zhao Y. Simple Wideband FPD with Sharp Passband Selectivity and Nice UWB Isolation. *Electron Lett* (2018) 54:217–9. doi:10.1049/el.2017.4213
11. Zhang G, Wang J, Zhu L, Wu W. Dual-Mode Filtering Power Divider with High Passband Selectivity and Wide Upper Stopband. *IEEE Microw Wireless Compon Lett* (2017) 27:642–4. doi:10.1109/lmwc.2017.2711556
12. Yang M, Wang J, Wang X, Wu W. Design of Wideband Four-Way Filtering Power Divider Based on SIW Loaded Square Patch Resonator. *Electron Lett* (2019) 55:389–91. doi:10.1049/el.2018.8058
13. Song K, Mo Y, Fan Y. Wideband Four-Way Filtering-Response Power Divider with Improved Output Isolation Based on Coupled Lines. *IEEE Microw Wireless Compon Lett* (2014) 24:674–6. doi:10.1109/lmwc.2014.2340992
14. Zhu H, Abbosh AM, Guo L. Wideband Four-Way Filtering Power Divider with Sharp Selectivity and Wide Stopband Using Looped Coupled-Line Structures. *IEEE Microw Wireless Compon Lett* (2016) 26:413–5. doi:10.1109/lmwc.2016.2562107
15. Zhu C, Xu J, Wu W. Microstrip Four-Way Reconfigurable Single/Dual/Wideband Filtering Power Divider with Tunable Frequency, Bandwidth, and PDR. *IEEE Trans Ind Electron* (2018) 65:8840–50. doi:10.1109/tie.2017.2787577
16. Zhang G, Qian Z, Yang J, Hong J-S. Wideband Four-Way Filtering Power Divider with Sharp Selectivity and High Isolation Using Coshared Multi-Mode Resonators. *IEEE Microw Wireless Compon Lett* (2019) 29:641–4. doi:10.1109/lmwc.2019.2936138
17. Zhang G, Qian Z, Yang J. Design of a Compact Microstrip Power-Divider Diplexer with Simple Layout. *Electron Lett* (2018) 54:1007–9. doi:10.1049/el.2018.0375
18. Pozar DM. *Microwave Engineering*. New York: John Wiley Sons Press (2005).

Conflict of Interest: YL, XZ, XS, XG, BX, XZ, and KP were employed by Hengdian Electronics Co., Ltd.

Advantages of publishing in Frontiers

OPEN ACCESS
Articles are free to read for greatest visibility and readership

FAST PUBLICATION
Around 90 days from submission to decision

HIGH QUALITY PEER-REVIEW
Rigorous, collaborative, and constructive peer-review

TRANSPARENT PEER-REVIEW
Editors and reviewers acknowledged by name on published articles

Frontiers
Avenue du Tribunal-Fédéral 34
1005 Lausanne | Switzerland

Visit us: www.frontiersin.org
Contact us: frontiersin.org/about/contact

REPRODUCIBILITY OF RESEARCH
Support open data and methods to enhance research reproducibility

DIGITAL PUBLISHING
Articles designed for optimal readership across devices

FOLLOW US
@frontiersin

IMPACT METRICS
Advanced article metrics track visibility across digital media

EXTENSIVE PROMOTION
Marketing and promotion of impactful research

LOOP RESEARCH NETWORK
Our network increases your article's readership